Ageing and the Decay of Beauty

Radiation Hardness of the LHCb Outer Tracker and Time-Dependent CP Violation using $B_s^0 \to J/\psi\,\phi$ Decays

Daan van Eijk

CERN-THESIS-2012-137
//2012

Cover: Lucas Keijning and Daan van Eijk
Printed in 2012 by Ipskamp Drukkers

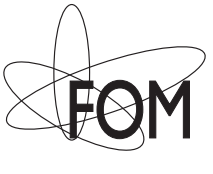

Netherlands Organisation for Scientific Research

This work is part of the research program of the Foundation for Fundamental Research on Matter (FOM), which is part of The Netherlands Organisation for Scientific Research (NWO). It has been supported by the VIDI grant entitled 'No GUTs, no Glory: the Search for Grand Unified Theories with B-decays' of dr. N. Tuning.

VRIJE UNIVERSITEIT

Ageing and the Decay of Beauty

Radiation Hardness of the LHCb Outer Tracker and Time-Dependent CP Violation using $B_s^0 \to J/\psi\,\phi$ Decays

ACADEMISCH PROEFSCHRIFT

ter verkrijging van de graad Doctor aan
de Vrije Universiteit Amsterdam,
op gezag van de rector magnificus
prof.dr. L.M. Bouter,
in het openbaar te verdedigen
ten overstaan van de promotiecommissie
van de Faculteit der Exacte Wetenschappen
op maandag 15 oktober 2012 om 13.45 uur
in de aula van de universiteit,
De Boelelaan 1105

door

Daan van Eijk

geboren te Spijkenisse

promotoren:	prof.dr. M.H.M. Merk
	prof.dr. H.G. Raven
copromotor:	dr. N. Tuning

Einstein: 'Mijn vrouw begrijpt mij niet'

Herman Finkers

Niks subatomairs in het Standaardmodel is zo komisch, althans vind ik

uit Neutrino's, Kees Torn

Contents

Introduction

The two parts of the title and subtitle of my thesis, namely *Ageing: radiation hardness of the LHCb Outer Tracker* and *The decay of beauty: time-dependent CP violation using* $B_s^0 \to J/\psi\,\phi$ *decays* represent its two main subjects. In this introduction, I will first elaborate on the radiation hardness of the LHCb Outer Tracker. Next, I will discuss the subject of time-dependent CP violation in $B_s^0 \to J/\psi\,\phi$ decays. Finally, I will end the introduction with a brief chapter overview.

If you read this, there is a slight chance that you are a non-expert in particle physics. Since the main content of my thesis is quite technical, with this introduction, the summary and the acknowledgements, I aim to give the non-expert readers an impression of my research during the past four years. My hope is, naturally, that particle physicists will read these sections as well and will also find satisfaction in reading the physics chapters.

Ageing: Radiation Hardness of the LHCb Outer Tracker

LHCb is one of the four major experiments at the Large Hadron Collider (LHC) at CERN[1]. The Outer Tracker (OT) is a subdetector of the LHCb experiment. It is used to reconstruct the trajectories of particles through the detector originating from proton-proton collisions. To detect a traversing particle, the OT uses straw tubes filled with an ionization gas that act as cathodes with a central anode wire. It consists of three detection stations and each station comprises 4 detection layers. The OT has a modular design, meaning that it consists of 432 modules of 128 straw tubes, leading to a total of roughly 55 000 straw tubes in the entire OT. The modules are constructed by glueing the straws to the module panels.

After construction and prior to installation of the modules in the LHCb experiment, laboratory tests proved that outgassing of the glue that was used in the module construction reduced the performance of the detector modules. In the context of particle detector technology, effects that gradually reduce detector performance, such as malicious outgassing, are collectively called ageing effects.

The modules that were installed in the LHCb cavern were subjected to several beneficial treatments to reduce or prevent ageing effects. In this thesis, I will describe the results of tests that were performed to monitor the behavior of the OT modules during beam operation. Whereas this part of my thesis is hardware-oriented, the other part presents the analysis of

[1] CERN was founded as *Conseil Européen pour la Recherche Nucléaire*, but is known nowadays as the *European Organization for Nuclear Research*.

proton-proton collisions that contain B_s^0 particles and decay into J/ψ and ϕ particles, which I will explain below.

The Decay of Beauty: Time-Dependent CP Violation using $B_s^0 \to J/\psi\,\phi$ Decays

The main goal of the analysis of $B_s^0 \to J/\psi\,\phi$ decays is to measure a parameter, named the weak phase ϕ_s. The B_s^0 meson is sometimes called a beauty meson, since it consists of one s quark and one so-called beauty quark, $\overline{b}$. As I studied one particular decay mode of these beauty mesons, I decided to adopt the phrase *The Decay of Beauty* as the first part of my title.

The parameter ϕ_s is a measure of the amount of time-dependent CP violation in the interference between mixing and decay in $B_s^0 \to J/\psi\,\phi$ decays. In the Standard Model (SM), ϕ_s is estimated to be close to zero. New Physics models, however, predict that the value of ϕ_s can be enhanced due to so far unknown processes in B_s^0 mixing. Therefore, any significant deviation in ϕ_s from the SM prediction could be an indication of New Physics. The LHCb experiment is well suited to measure this parameter and I will present the most precise measurement of ϕ_s to date.

Chapter Overview

This thesis consists of six chapters. The first two chapters serve as a general introduction to the LHCb experiment (Chap. 2) and to parts of its physics program (Chap. 1). The final four chapters include my own research.

Chapter 1: CP Violation and Physics of B Mesons

This chapter is theoretically oriented and starts with a brief history of the discovery of CP violation and the appearance of CP violation in the Standard Model. Next, I will describe mixing and the decay of B mesons, and a classification of the different types of CP violation. Finally, more specific to $B_s^0 \to J/\psi\,\phi$ decays, I will discuss CP violation in the interference between decays with and without mixing in $b \to c(\overline{c}s)$ transitions.

Chapter 2: The LHCb Experiment

In the second chapter I will give an overview of the LHCb experiment and its various subdetectors. At the end of the chapter, I will discuss the performance of various subdetectors in relation to $B_s^0 \to J/\psi\,\phi$ decays.

Chapter 3: Operation and Performance of the Outer Tracker

This chapter focuses on the Outer Tracker, which is one of the LHCb subdetectors. I will discuss the working principle of the OT and its performance and will also introduce the

concept of hit efficiency. Hit efficiency is used to monitor possible ageing effects in the OT, which is the subject of the subsequent chapter.

Chapter 4: Radiation Hardness of the Outer Tracker

After a brief introduction, this chapter reproduces an article that was published in *Nuclear Instruments and Methods in Physics Research A*. It summarizes the results of methods to monitor ageing of the OT modules during beam operation.

Chapter 5: $B_s^0 \to J/\psi\,\phi$ Formalism

The remaining two chapters will cover the measurement of ϕ_s using $B_s^0 \to J/\psi\,\phi$ decays. This chapter is a continuation of the first chapter and focuses specifically on $B_s^0 \to J/\psi\,\phi$ decays.

Chapter 6: $B_s^0 \to J/\psi\,\phi$ Analysis

The final chapter presents the analysis of $B_s^0 \to J/\psi\,\phi$ decays. I will discuss the event selection and detector effects such as decay-time resolution and angular acceptance. Finally, after a study of systematic uncertainties, I will present a measurement of ϕ_s and other parameters of interest.

CHAPTER

ONE

CP Violation and Physics of B Mesons

In electroweak interactions, an up-type quark u can change its flavour to a down-type quark d via the emission of a charged W boson: $u \to W^+ d$. In the Standard Model (SM) the couplings of these interactions are described by the Cabibbo-Kobayashi-Maskawa (CKM) matrix elements. Flavour physics is the field of particle physics that studies these flavour changing interactions. B mesons contain one b or $\bar{b}$ quark and because of their relatively high mass and long lifetime, B meson decays are particularly well suited to study flavour changing interactions and the structure of the CKM mechanism. Some B meson decays are observed to be not invariant under the combined operation of the charge (C) and parity (P) operators, i.e. they are CP violating. One of the main subjects of this thesis is the search for CP violation in a specific type of B_s^0 meson decays, namely the decay of a B_s^0 meson into a J/ψ meson and a ϕ meson, also indicated as $B_s^0 \to J/\psi\,\phi$ decays. In the SM, CP violation is expected to be tiny in this decay channel, implying that a positive signal indicates the presence of physics beyond the SM. In this chapter, a general introduction to CP violation is given and the physics of neutral B meson decays is discussed.

1.1 History of CP Violation

CP symmetry is the symmetry of the combined operations of P and C, where the charge operator C inverts the charge of particles, and P is the parity operator which inverts all spatial coordinates. Processes that are not invariant under the CP operation are called CP-violating processes. In 1956, Chien-Shiung Wu performed a historical experiment utilizing the decay of ^{60}Co, which demonstrated that P symmetry was violated in the weak interactions [1]. Contrary to expectations, she found that neutrinos occur in one single helicity state only, implying maximal P violation.

Experiments with pion decays [2] revealed that the C symmetry is also maximally violated by the weak interactions. However, no evidence was found that the combined symmetry CP is violated. Indeed, CP seems to be preserved in strong and electromagnetic interactions [3]. But in 1964, James Cronin and Val Fitch performed an experiment using neutral kaon decays [4], in which they observed the (until that time assumed to be) CP-odd K_L particles

decaying to CP-even $\pi^+\pi^-$ final states with a branching fraction of about 0.2%. In other words, they observed that CP is violated in kaon oscillations, but in contrast to C and P violation, the magnitude of the CP violation is small. Cronin and Fitch received the Nobel Prize for their experiment in 1980.

In 1973, Makoto Kobayashi and Toshihide Maskawa postulated that a hypothetical additional third quark family could explain the observed small amount of CP violation through an imaginary phase in their proposed Cabibbo-Kobayashi-Maskawa (CKM) matrix [5, 6]. At that time, only three quarks were known to exist and a fourth quark had been postulated to complete the second quark family. This fourth quark was discovered in November 1974 [7, 8]. The bottom quark, the lightest member of the third quark family and predicted by Kobayashi and Maskawa, was discovered in 1977 at Fermilab [9], for which they were awarded the 2008 Nobel Price, sharing the price with Yoichiro Nambu. Finally, the top quark was discovered in 1995, completing the third quark family [10, 11].

CP violation outside of the kaon system was discovered in the first decade of this century by the so-called B-factories: the BaBar and Belle experiments. Both these experiments found CP violation in the B^0 meson system [12, 13]. The search for CP violation continued at the Tevatron at Fermilab, where the D0 experiment found evidence of CP violation in the mixing of B mesons [14]. The Tevatron was shut down in 2011 and currently the LHCb experiment at CERN plays a leading role in the search for CP violation. In 2012, LHCb reported the first evidence of CP violation in charmed meson decays [15].

The subject of this thesis is the search for time-dependent CP violation in the interference between mixing and decay in $B_s^0 \to J/\psi\,\phi$ decays at LHCb. But in order to explain this type of CP violation and how to search for it, it is necessary first to explain how CP violation is incorporated in the SM.

1.2 CP Violation in the Standard Model

CP violation is incorporated in the SM by the CKM matrix, which appears in the description of the charged current interactions. This matrix arises when diagonalizing the quark mass terms (also known as the Yukawa terms) in the SM Lagrangian:

$$-\mathcal{L}_{\text{Yukawa}} = M^d_{ij}\,\overline{d}^I_{iL}\,d^I_{jR} + M^u_{ij}\,\overline{u}^I_{iL}\,u^I_{jR} \quad . \tag{1.1}$$

Here, (u, d) indicates the quark type, (i, j) stands for the quark generation, (L, R) means left-handed or right-handed chirality states and I indicates the interaction basis. To obtain mass terms, the mass matrices are diagonalized via unitary transformations V_L and V_R, which yields:

$$\begin{aligned} -\mathcal{L}_{\text{Yukawa}} &= \overline{d}^I_{iL}\,M^d_{ij}\,d^I_{jR} + \overline{u}^I_{iL}\,M^u_{ij}\,u^I_{jR} \\ &= \overline{d}^I_{iL}\,V^{d\dagger}_L\,V^d_L\,M^d_{ij}\,V^{d\dagger}_R\,V^d_R\,d^I_{jR} + \overline{u}^I_{iL}\,V^{u\dagger}_L\,V^u_L\,M^u_{ij}\,V^{u\dagger}_R\,V^u_R\,u^I_{jR} \\ &= \overline{d}_{iL}\,(M^d_{ij})_{diag}\,d_{jR} + \overline{u}_{iL}\,(M^u_{ij})_{diag}\,u_{jR} \quad , \end{aligned} \tag{1.2}$$

where in the second equality unitarity is used ($V^\dagger V = \mathbb{1}$), while the third equality is obtained by defining

$$\begin{aligned} d_{iL} &= (V_L^d)_{ij}\, d_{jL}^I \quad , \quad d_{iR} = (V_R^d)_{ij}\, d_{jR}^I \quad , \\ u_{iL} &= (V_L^u)_{ij}\, u_{jL}^I \quad , \quad u_{iR} = (V_R^u)_{ij}\, u_{jR}^I \quad . \end{aligned} \tag{1.3}$$

By construction, these quark states represent the mass eigenstates. Rewriting the charged current interaction terms in the Lagrangian leads to

$$\begin{aligned} \mathcal{L}_{\text{kinetic}} &= \frac{g}{\sqrt{2}}\, \overline{u}_{iL}^I \gamma^\mu\, W_\mu^-\, d_{iL}^I + \frac{g}{\sqrt{2}}\, \overline{d}_{iL}^I \gamma^\mu\, W_\mu^+\, u_{iL}^I \\ &= \frac{g}{\sqrt{2}}\, \overline{u}_{iL}\, \gamma^\mu\, W_\mu^-\, (V_{\text{CKM}})_{ij}\, d_{jL} + \frac{g}{\sqrt{2}}\, \overline{d}_{jL}\, (V_{\text{CKM}})_{ij}^*\, \gamma^\mu\, W_\mu^+\, u_{iL} \quad , \end{aligned} \tag{1.4}$$

where the CKM matrix is given by

$$(V_{\text{CKM}})_{ij} = (V_L^u\, V_L^{d\dagger})_{ij} \quad . \tag{1.5}$$

By convention, the interaction and mass eigenstates are chosen to be the same for the up-type quarks, but are rotated for down-type quarks. This implies, that for the down-type quarks they differ by a unitary transformation:

$$\begin{aligned} u_i^I &= u_j \\ d_i^I &= (V_{\text{CKM}})_{ij}\, d_j \quad . \end{aligned} \tag{1.6}$$

From Eq. 1.4, it follows that the Standard Model Lagrangian is invariant under CP if, and only if, $V_{ij} = V_{ij}^*$. Therefore, a non-vanishing complex phase in the CKM matrix can generate CP violation in the SM. Kobayashi and Maskawa realized, that the presence of a third quark family allows for the existence of such an imaginary degree of freedom. This can be seen from the fact that a general complex $n \times n$ CKM matrix has $2n^2$ real parameters. The unitarity constraints $V^\dagger V = 1$ reduce this number of free parameters by n^2. Subsequently, due to the freedom to choose the phase of the $2n$ quark fields, $2n-1$ relative phases are not observable. This leaves $2n^2 - n^2 - (2n-1) = (n-1)^2$ degrees of freedom.

For a general orthogonal $n \times n$ matrix such as the CKM matrix, there are $\frac{1}{2}n(n-1)$ independent rotation (or Euler) angles. Therefore, out of the $(n-1)^2$ original degrees of freedom, $\frac{1}{2}n(n-1)$ are Euler angles and the remaining $\frac{1}{2}(n-1)(n-2)$ degrees of freedom are independent complex phases. Indeed, for $n = 3$, as Kobayashi and Maskawa proposed, there is one imaginary degree of freedom in the corresponding 3×3 CKM matrix, offering the possibility to describe the observed CP violation.

1.3 Unitarity Triangles

Writing out the quark generation index $i, j = \{u, c, t\}, \{d, s, b\}$, the CKM elements from Eq. 1.6 are written in matrix form as follows:

$$V_{\text{CKM}} = \begin{pmatrix} V_{ud} & V_{us} & V_{ub} \\ V_{cd} & V_{cs} & V_{cb} \\ V_{td} & V_{ts} & V_{tb} \end{pmatrix} \quad . \tag{1.7}$$

Since the CKM matrix is unitary, six orthogonality and three unitarity relations exist. Two of the orthogonality equations are particularly interesting in flavour physics, since the corresponding matrix elements appear in decays involving B mesons:

$$V_{ud}V_{ub}^* + V_{cd}V_{cb}^* + V_{td}V_{tb}^* = 0 \quad (B^0 \text{ system}) \tag{1.8}$$
$$V_{us}V_{ub}^* + V_{cs}V_{cb}^* + V_{ts}V_{tb}^* = 0 \quad (B_s^0 \text{ system}) \quad . \tag{1.9}$$

The orthogonality equations define so-called unitarity triangles in the complex plane. The sides of these unitarity triangles correspond to the various terms in Eq. 1.8 and Eq. 1.9, and their magnitudes are observables that can be related to the (relative) rate of certain B meson decays. In addition, the internal angles of the unitarity triangles are invariant under rephasing of the quark fields and are physical observables. A convenient representation of the two unitarity triangles associated with Eq. 1.8 and Eq. 1.9 is shown in Fig. 1.1, where a phase convention is adopted so that one of their sides is on the real axis, and this side is subsequently normalized to unit length.

The apex of the unitarity triangle for the B_d^0 system (UT) is located at $-V_{ud}V_{ub}^*/V_{cd}V_{cb}^*$ and the interior angles are defined as

$$\alpha \equiv \arg\left[-\frac{V_{td}V_{tb}^*}{V_{ud}V_{ub}^*}\right], \quad \beta \equiv \arg\left[-\frac{V_{cd}V_{cb}^*}{V_{td}V_{tb}^*}\right], \quad \gamma \equiv \arg\left[-\frac{V_{ud}V_{ub}^*}{V_{cd}V_{cb}^*}\right] \quad . \tag{1.10}$$

Similarly, for the unitarity triangle in the B_s^0 system (UT_s), the apex is located at $-V_{us}V_{ub}^*/V_{cs}V_{cb}^*$ and the interior angles in the UT_s are

$$\alpha_s \equiv \arg\left[-\frac{V_{tb}V_{ts}^*}{V_{ub}V_{us}^*}\right], \quad \beta_s \equiv \arg\left[-\frac{V_{cb}V_{cs}^*}{V_{tb}V_{ts}^*}\right], \quad \gamma_s \equiv \arg\left[-\frac{V_{ub}V_{us}^*}{V_{cb}V_{cs}^*}\right] \quad . \tag{1.11}$$

As will be shown in Sec. 5.7, the angle β_s is related to $B_s^0 - \overline{B}_s^0$ mixing through the appearance of the CKM element V_{ts} to leading order, and can be measured using $B_s^0 \to J/\psi\,\phi$ decays.

1.3.1 Wolfenstein Parameterization

As was mentioned before, for three quark families, the CKM matrix can be parameterized using four real parameters. The Wolfenstein parameterization is inspired by the observation that $|V_{cb}| \gg |V_{ub}|$ and $|V_{cb}| \sim |V_{us}|^2$, and takes the following form [16]:

$$\begin{aligned} V_{\mathrm{CKM}} &= V_{\mathrm{CKM}}(\mathcal{O}(\lambda^3)) + \mathcal{O}(\lambda^4) \\ &= \begin{pmatrix} 1-\frac{1}{2}\lambda^2 & \lambda & A\lambda^3(\rho - i\eta) \\ -\lambda & 1-\frac{1}{2}\lambda^2 & A\lambda^2 \\ A\lambda^3(1-\rho-i\eta) & -A\lambda^2 & 1 \end{pmatrix} + \mathcal{O}(\lambda^4) \quad . \end{aligned} \tag{1.12}$$

The four real parameters are A, ρ, η and the expansion parameter λ, with $\lambda \sim 0.225$.

To obtain the imaginary contribution to the coupling V_{ts}, which is important in the

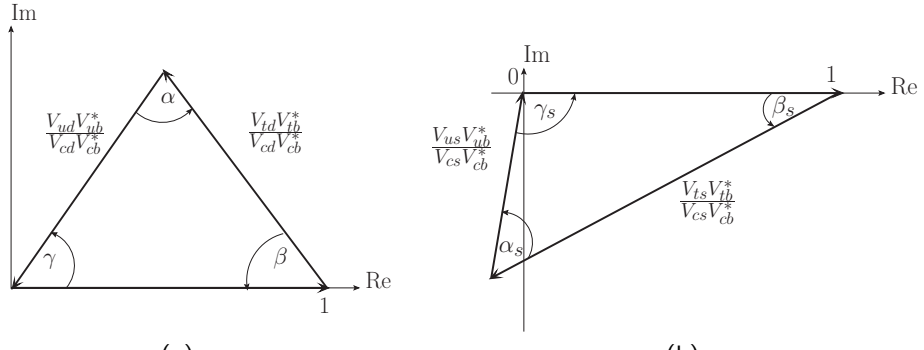

Figure 1.1: *(a) Unitarity triangle in the B_d^0 system, historically known as 'The Unitarity Triangle' (UT). (b) Unitarity triangle in the B_s^0 system. In both pictures the sides are scaled so that one of the sides is on the real axis and equal to one. In the SM, the magnitude of the angle β_s is small, but in this picture it is shown enlarged for the sake of clarity.*

$B_s^0 \to J/\psi\,\phi$ decay, a higher order expansion of the CKM matrix in λ is needed:

$$\begin{aligned} V_{\rm CKM} &= V_{\rm CKM}(\mathcal{O}(\lambda^3)) \\ &+ \begin{pmatrix} -\frac{1}{8}\lambda^4 & 0 & 0 \\ \frac{1}{2}A^2\lambda^5[1-2(\rho+i\eta)] & -\frac{1}{8}\lambda^4(1+4A^2) & 0 \\ \frac{1}{2}A\lambda^5(\rho+i\eta) & \frac{1}{2}A\lambda^4[1-2(\rho+i\eta)] & -\frac{1}{2}A^2\lambda^4 \end{pmatrix} \\ &+ \mathcal{O}(\lambda^6) \quad . \end{aligned} \tag{1.13}$$

From this parameterization it follows that the apex of the UT is located at

$$-\frac{V_{ud}V_{ub}^*}{V_{cd}V_{cb}^*} = (\overline{\rho},\overline{\eta}) \simeq (1-\lambda^2/2)(\rho,\eta) \quad , \tag{1.14}$$

which is in the first quadrant as shown in Fig. 1.1 (a). Similarly, in the case of UT$_s$, the apex is at

$$-\frac{V_{us}V_{ub}^*}{V_{cs}V_{cb}^*} = (\overline{\rho}_s,\overline{\eta}_s) \simeq \frac{-\lambda^2}{1-\lambda^2/2}(\rho,\eta) \quad , \tag{1.15}$$

located in the third quadrant as shown in Fig. 1.1 (b). Using the fact that $\lambda \sim 0.225$, it turns out that this figure is not to scale and β_s is actually very small, $\mathcal{O}(\lambda^2)$.

Using the angles defined in Eq. 1.10 and Eq. 1.11, it follows that, in the phase convention implied by the Wolfenstein parameterization (see Eq. 1.12),

$$\begin{aligned} \beta &= \arg(-1) + \arg(V_{cd}V_{cb}^*) - \arg\left(V_{td}V_{tb}^*\right) = -\arg(V_{td}) \\ \gamma &= \arg(-1) + \arg(V_{ud}V_{ub}^*) - \arg(V_{cd}V_{cb}^*) = \arg(V_{ub}^*) = -\arg\left(V_{ub}\right) \\ \beta_s &= \arg(-1) + \arg(V_{cb}V_{cs}^*) - \arg(V_{tb}V_{ts}^*) = \pi - \arg(V_{ts}^*) = \pi + \arg\left(V_{ts}\right) \quad . \end{aligned}$$

$\mathrm{UT}_{(s)}$ angle	value (°)
α	$91.1^{+4.3}_{-4.3}$
β	$21.85^{+0.80}_{-0.77}$
γ	$67.1^{+4.3}_{-4.3}$
β_s	$1.044^{+0.047}_{-0.046}$

Table 1.1: *Latest results of global fits to the $\mathrm{UT}_{(s)}$ angles from the CKMfitter Group, as of the Moriond 2012 conference [17].*

This implies that the CKM matrix can be written in the following way:

$$V_{\mathrm{CKM}} = \begin{pmatrix} |V_{ud}| & |V_{us}| & |V_{ub}|e^{-i\gamma} \\ -|V_{cd}| & |V_{cs}| & |V_{cb}| \\ |V_{td}|e^{-i\beta} & -|V_{ts}|e^{i\beta_s} & |V_{tb}| \end{pmatrix} + \mathcal{O}(\lambda^5) \quad . \tag{1.16}$$

The Wolfenstein parameterization will be used throughout this thesis, unless explicitly stated otherwise.

1.3.2 CKM Constraints from Experiments

The CKM mechanism in the SM can be tested experimentally by measuring the lengths of the sides and the interior angles of the unitarity triangles. The lengths of the sides of the $\mathrm{UT}_{(s)}$ yield an indirect determination of the angles in the CKM matrix. Direct measurements of the angles can be obtained from CP-violating observables in B decays. The combination of these direct and indirect measurements provides a test of the consistency of the CKM mechanism.

The current constraints on the location of the apex of the UT and UT_s are shown in Fig. 1.2 and the resulting $\mathrm{UT}_{(s)}$ angles are given in Table 1.1. Notice that the location of the apex is defined by only two parameters, $\overline{\rho}_{(s)}$ and $\overline{\eta}_{(s)}$, while there are various physical observables that lead to different constraints, as indicated by the different colored regions in Fig. 1.2. It follows that currently all measurements are consistent with the CKM description of the weak interactions in the SM. That is, both the apex in the UT and the UT_s lie within the uncertainty bounds of all measurements. More accurate measurements are needed to reveal potential tensions in the CKM mechanism and possible deviations from the Standard Model.

1.4 Mixing of Neutral B Mesons

Neutral B mesons have the property that they can oscillate to their antiparticle. This process is called mixing. The flavour eigenstates of the B^0 meson and the B_s^0 meson are

$$\begin{aligned} |B^0\rangle &= |\bar{b}d\rangle \quad , \quad |\overline{B}^0\rangle = |b\bar{d}\rangle \quad , \\ |B_s^0\rangle &= |\bar{b}s\rangle \quad , \quad |\overline{B}_s^0\rangle = |b\bar{s}\rangle \quad . \end{aligned} \tag{1.17}$$

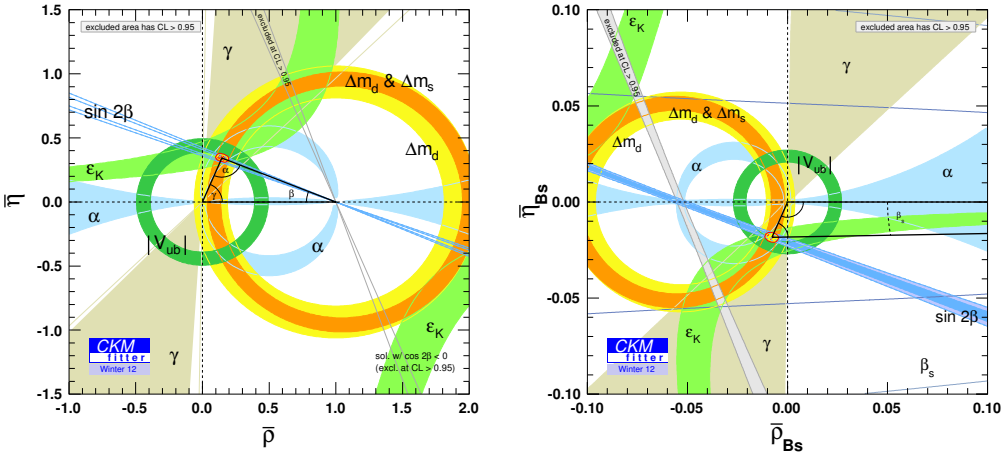

Figure 1.2: *(a) UT constraints. (b) UT$_s$ constraints. Both graphs are the latest results (as of the Moriond 2012 conference) from the CKMfitter Group [17]. Notice that the UT$_s$ is drawn to scale here, unlike the schematic picture in Fig. 1.1 (b).*

For the remainder of this section B will denote any neutral B meson, i.e. either a B_d^0 or a B_s^0 meson.

Since B mesons can oscillate between $|B\rangle$ and $|\overline{B}\rangle$ states, the time evolution of the linear combination $|B(t)\rangle = a(t)\,|B\rangle + b(t)\,|\overline{B}\rangle$ can effectively be described by a two-dimensional Schrödinger equation:

$$i\frac{d}{dt}\begin{pmatrix} a(t) \\ b(t) \end{pmatrix} = \mathbf{H}\begin{pmatrix} a(t) \\ b(t) \end{pmatrix} \quad , \tag{1.18}$$

where the Hamiltonian can be written as

$$\mathbf{H} = \mathbf{M} - \frac{i}{2}\mathbf{\Gamma} \quad , \tag{1.19}$$

with the Hermitian matrices $\mathbf{M}$, the so-called mass matrix, and $\mathbf{\Gamma}$, the decay matrix. Assuming CPT invariance, the masses and decay times of B mesons are equal. This implies that $M_{11} = M_{22} = M$ and $\Gamma_{11} = \Gamma_{22} = \Gamma$. In addition, for the off-diagonal elements, responsible for mixing between $|\overline{B}\rangle$ and $|B\rangle$ eigenstates, $M_{21} = M_{12}^*$ and $\Gamma_{21} = \Gamma_{12}^*$, due to hermiticity [18]. Hence the Hamiltonian can be written as

$$\mathbf{H} = \begin{pmatrix} M - \frac{i}{2}\Gamma & M_{12} - \frac{i}{2}\Gamma_{12} \\ M_{12}^* - \frac{i}{2}\Gamma_{12}^* & M - \frac{i}{2}\Gamma \end{pmatrix} \quad . \tag{1.20}$$

In the off-diagonal elements, M_{12} is dominated by short-distance (virtual) processes, whereas Γ_{12} is dominated by real intermediate states (long-distance processes), to which both the B and the $\overline{B}$ mesons can decay [19, 20].

By diagonalizing the Hamiltonian, the solutions to the Schrödinger equation for the mass eigenstates are found: $|B_H(t)\rangle = e^{-(im_H+\frac{\Gamma_H}{2}t)}|B_H(0)\rangle$ and $|B_L(t)\rangle = e^{-(im_L+\frac{\Gamma_L}{2}t)}|B_L(0)\rangle$ with eigenvalues $m_H - \frac{i}{2}\Gamma_H$ and $m_L - \frac{i}{2}\Gamma_L$, respectively.

In turn, these time-dependent mass eigenstates are linear combinations of the weak flavour eigenstates:

$$|B_{H,L}(t)\rangle = p|B(t)\rangle \mp q|\overline{B}(t)\rangle \quad . \tag{1.21}$$

Solving the eigenvalue equation for either $\lambda_H = H_0 + \sqrt{H_{21}H_{12}}$ with eigenvector $(p,-q)$ or $\lambda_L = H_0 - \sqrt{H_{21}H_{12}}$ with eigenvector (p,q) the ratio $\frac{q}{p}$ is found to be

$$\frac{q}{p} = -\sqrt{\frac{H_{21}}{H_{12}}} = -\sqrt{\frac{M_{12}^* - \frac{i}{2}\Gamma_{12}^*}{M_{12} - \frac{i}{2}\Gamma_{12}}} \quad . \tag{1.22}$$

Expressing the time-dependent flavour eigenstate in Eq. 1.21 in terms of mass eigenstates gives

$$|B(t)\rangle = \frac{|B_L(t)\rangle + |B_H(t)\rangle}{2p} \quad . \tag{1.23}$$

Inserting the time dependence of the mass eigenstates yields

$$|B(t)\rangle \quad = \quad \frac{e^{-(im_L+\frac{\Gamma_L}{2})t}|B_L(0)\rangle + e^{-(im_H+\frac{\Gamma_H}{2})t}|B_H(0)\rangle}{2p} \quad . \tag{1.24}$$

Using the definition

$$g_\pm(t) \equiv \frac{1}{2}(e^{-(im_L+\frac{\Gamma_L}{2})t} \pm e^{-(im_H+\frac{\Gamma_H}{2})t}) \quad , \tag{1.25}$$

it is finally found that

$$|B(t)\rangle = g_+(t)|B\rangle + \frac{q}{p}g_-(t)|\overline{B}\rangle \quad . \tag{1.26}$$

This equation expresses the time-dependent composition in flavour eigenstates of a state $|B(t)\rangle$, initially produced as a $|B\rangle$ state.

Using these expressions, the probability to observe a $|B\rangle$ state in a measurement at time t, provided that the original particle was produced as a $|B\rangle$ state, is given by

$$|\langle B|B(t)\rangle|^2 = |g_+(t)|^2 \quad , \tag{1.27}$$

while the probability to observe a $|B\rangle$ state at time t that was produced as a $|\overline{B}\rangle$ state is

$$|\langle \overline{B}|B(t)\rangle|^2 = \left|\frac{q}{p}\right|^2 |g_-(t)|^2 \quad , \tag{1.28}$$

where

$$|g_\pm(t)|^2 \quad = \quad \frac{e^{-\Gamma t}}{2}\left(\cosh\left(\frac{\Delta\Gamma t}{2}\right) \pm \cos(\Delta m t)\right) \quad , \tag{1.29}$$

and

$$\Delta m \equiv m_H - m_L = 2\mathrm{Re}\sqrt{(M_{12} - \frac{i}{2}\Gamma_{12})(M_{12}^* - \frac{i}{2}\Gamma_{12}^*)} \quad (1.30)$$

$$\Delta\Gamma \equiv \Gamma_L - \Gamma_H = -4\mathrm{Im}\sqrt{(M_{12} - \frac{i}{2}\Gamma_{12})(M_{12}^* - \frac{i}{2}\Gamma_{12}^*)} \quad . \quad (1.31)$$

Moreover, it is useful to define the average mass $m \equiv \frac{m_H+m_L}{2}$ and average width $\Gamma \equiv \frac{\Gamma_H+\Gamma_L}{2}$. By definition $\Delta m > 0$, but $\Delta\Gamma$ can, a-priori, have either sign. LHCb recently determined the sign of $\Delta\Gamma$ to be positive [21] and this will be discussed in more detail in Sec. 6.7.3.

Writing the ratio of M_{12} and Γ_{12} in terms of its magnitude and phase, the convention-independent phase difference $\phi_{M/\Gamma}$ is defined by

$$\frac{M_{12}}{\Gamma_{12}} \equiv -\left|\frac{M_{12}}{\Gamma_{12}}\right| e^{i\phi_{M/\Gamma}} \quad . \quad (1.32)$$

Using the definition of the mixing phase

$$\phi_M = \arg(M_{12}) \quad , \quad (1.33)$$

$\phi_{M/\Gamma}$ is written as

$$\phi_{M/\Gamma} = \phi_M - \arg(-\Gamma_{12}) \quad . \quad (1.34)$$

In terms of the Hamiltonian matrix elements, Δm and $\Delta\Gamma$ can then be written as

$$\Delta m = 2|M_{12}|\left[1 + \mathcal{O}\left(\left|\frac{\Gamma_{12}}{M_{12}}\right|^2\right)\right] \quad (1.35)$$

$$\Delta\Gamma = 2|\Gamma_{12}|\cos\phi_{M/\Gamma}\left[1 + \mathcal{O}\left(\left|\frac{\Gamma_{12}}{M_{12}}\right|^2\right)\right] \quad , \quad (1.36)$$

where $|\Gamma_{12}/M_{12}| \ll 1$ was used [1].

Finally, from Eq. 1.22, $\frac{q}{p}$ can be written as

$$\frac{q}{p} = -e^{-i\phi_M}\sqrt{\frac{|M_{12}| + \frac{i}{2}|\Gamma_{12}|e^{i\phi_{M/\Gamma}}}{|M_{12}| + \frac{i}{2}|\Gamma_{12}|e^{-i\phi_{M/\Gamma}}}} \quad . \quad (1.37)$$

As before, in the limit $|\Gamma_{12}/M_{12}| \ll 1$, this can be written as

$$\frac{q}{p} = -e^{-i\phi_M}[1 - \frac{a_{\mathrm{fs}}}{2}] \quad , \quad (1.38)$$

with the so-called flavour-specific CP asymmetry

$$a_{\mathrm{fs}} \simeq \left|\frac{\Gamma_{12}}{M_{12}}\right| \sin\phi_{M/\Gamma} \quad , \quad (1.39)$$

[1] This follows from experiments that show $\Delta m \gg |\Delta\Gamma|$ and theoretical calculations that show $|\Gamma_{12}| \ll \Delta m$ [22].

where all terms of order $\left(\frac{\Gamma_{12}^2}{M_{12}^2}\right)$ are neglected. The departure of this parameter from zero is a measure of the amount of CP violation in mixing, which is discussed in Sec. 1.7. This parameter can be measured with flavour-specific B decays. An example of these kind of decays are semileptonic B decays, hence this parameter is also referred to as the semileptonic CP asymmetry $a_{\rm sl}$ [14].

1.5 Decay of Neutral B Mesons

After production and mixing, neutral B mesons can decay in several hundreds of modes, with branching fractions in the range $\mathcal{O}(10^{-1} - 10^{-10})$ [23]. The time-dependent decay amplitudes of flavour eigenstates to a final state f are defined as

$$\begin{array}{lll} A_f \equiv \langle f|T|B\rangle & , & \overline{A}_f \equiv \langle f|T|\overline{B}\rangle \quad , \\ A_{\overline{f}} \equiv \langle \overline{f}|T|B\rangle & , & \overline{A}_{\overline{f}} \equiv \langle \overline{f}|T|\overline{B}\rangle \quad , \end{array} \tag{1.40}$$

with T the transition matrix [24]. The decay rate of a B meson decaying to a final state f is therefore

$$\Gamma_{B\to f}(t) = |A_f(t)|^2 = |\langle f|T|B(t)\rangle|^2 \quad . \tag{1.41}$$

Defining the parameter

$$\lambda_f = \frac{q}{p}\frac{\overline{A}_f}{A_f} \quad , \tag{1.42}$$

and using Eq. 1.26, this is rewritten as

$$\Gamma_{B\to f}(t) = |A_f|^2|g_+(t) + \lambda_f\, g_-(t)|^2 \quad . \tag{1.43}$$

The corresponding decay amplitude is

$$A_f(t) = A_f(0)[g_+(t) + \lambda_f g_-(t)] \quad , \tag{1.44}$$

and is graphically represented in Fig. 1.3, which shows an example where the total amplitude for a B meson decay to a final state, accessible to both B and $\overline{B}$, consists of two contributions: a direct decay, and a decay after mixing. Equation 1.43 is expanded as

$$\Gamma_{B\to f}(t) = |A_f|^2\left(|g_+(t)|^2 + |\lambda_f|^2|g_-(t)|^2 + 2\mathrm{Re}[\lambda_f\, g_+^*(t)\, g_-(t)]\right) \quad . \tag{1.45}$$

From the definition of $g_\pm(t)$ it follows that

$$g_+^*(t)g_-(t) = \frac{e^{-\Gamma t}}{2}(-\sinh\frac{\Delta\Gamma t}{2} + i\sin\Delta m t) \quad . \tag{1.46}$$

Using this and Eq. 1.29, the decay rate finally becomes

$$\begin{aligned} \Gamma_{B\to f}(t) \quad = \quad & |A_f|^2\,(1+|\lambda_f|^2)\,\frac{e^{-\Gamma t}}{2}\cdot \\ & (\cosh\frac{\Delta\Gamma t}{2} - D_f\,\sinh\frac{\Delta\Gamma t}{2} + C_f\,\cos\Delta m t - S_f\,\sin\Delta m t)\,, \end{aligned} \tag{1.47}$$

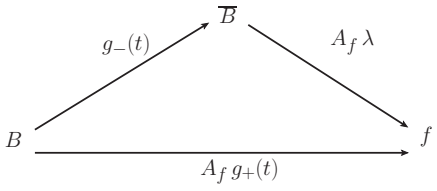

Figure 1.3: *The amplitude of a B meson decaying to a final state f consists of two contributions: the direct decay ($A_f\,g_+(t)$) at the bottom and the decay after mixing ($A_f\,\lambda_f\,g_-(t)$) via the upper path.*

where [25]

$$D_f = \frac{2\,\mathrm{Re}[\lambda_f]}{1+|\lambda_f|^2} \quad , \quad C_f = \frac{1-|\lambda_f|^2}{1+|\lambda_f|^2} \quad , \quad S_f = \frac{2\,\mathrm{Im}[\lambda_f]}{1+|\lambda_f|^2} \quad . \tag{1.48}$$

Equivalently, for the other possible combinations of B and $\overline{B}$ meson decays to a final state f or $\overline{f}$, the decay rates are

$$\begin{aligned}
\Gamma_{B\to\overline{f}}(t) &= |\overline{A}_{\overline{f}}|^2 \left|\frac{q}{p}\right|^2 (1+|\overline{\lambda}_{\overline{f}}|^2)\,\frac{e^{-\Gamma t}}{2}\cdot \\
&\quad (\cosh\frac{\Delta\Gamma t}{2} - \overline{D}_{\overline{f}}\,\sinh\frac{\Delta\Gamma t}{2} - \overline{C}_{\overline{f}}\,\cos\Delta m t + \overline{S}_{\overline{f}}\,\sin\Delta m t) \qquad (1.49)\\
\Gamma_{\overline{B}\to f}(t) &= |A_f|^2 \left|\frac{p}{q}\right|^2 (1+|\lambda_f|^2)\,\frac{e^{-\Gamma t}}{2}\cdot \\
&\quad (\cosh\frac{\Delta\Gamma t}{2} - D_f\,\sinh\frac{\Delta\Gamma t}{2} - C_f\,\cos\Delta m t + S_f\,\sin\Delta m t) \qquad (1.50)\\
\Gamma_{\overline{B}\to\overline{f}}(t) &= |\overline{A}_{\overline{f}}|^2\,(1+|\overline{\lambda}_{\overline{f}}|^2)\,\frac{e^{-\Gamma t}}{2}\cdot \\
&\quad (\cosh\frac{\Delta\Gamma t}{2} - \overline{D}_{\overline{f}}\,\sinh\frac{\Delta\Gamma t}{2} + \overline{C}_{\overline{f}}\,\cos\Delta m t - \overline{S}_{\overline{f}}\,\sin\Delta m t)\,, \qquad (1.51)
\end{aligned}$$

with $\overline{\lambda}_{\overline{f}} = \frac{p}{q}\frac{A_{\overline{f}}}{\overline{A}_{\overline{f}}}$ and

$$\overline{D}_{\overline{f}} = \frac{2\,\mathrm{Re}[\overline{\lambda}_{\overline{f}}]}{1+|\overline{\lambda}_{\overline{f}}|^2} \quad , \quad \overline{C}_{\overline{f}} = \frac{1-|\overline{\lambda}_{\overline{f}}|^2}{1+|\overline{\lambda}_{\overline{f}}|^2} \quad , \quad \overline{S}_{\overline{f}} = \frac{2\,\mathrm{Im}[\overline{\lambda}_{\overline{f}}]}{1+|\overline{\lambda}_{\overline{f}}|^2} \quad . \tag{1.52}$$

1.6 Measurement of Relative Phases

The overall phase of an amplitude can be written as the combination of a phase that flips sign under the CP transformation and a phase that is invariant. The former is referred to as the weak phase ϕ_{weak}, as it originates from weak interactions; the latter typically arises from strong final state interactions. For processes with only one contributing amplitude, the phase of this amplitude is not observable. However, when two amplitudes contribute,

the magnitude of the total amplitude can differ between a process and its CP conjugated process. This can be shown by writing the total amplitude as $A = A_1 + A_2$, where, without loss of generality, the phase of A_1 can be chosen to be zero, and the relative weak and strong phase difference between A_1 and A_2 are indicated by ϕ and δ, respectively:

$$A_1 = |A_1| \quad , \quad \frac{A_2}{A_1} = \frac{|A_2|}{|A_1|} e^{i\delta} e^{i\phi} \quad . \tag{1.53}$$

In that case the total rate equals

$$|A|^2 = |A_1 + A_2|^2 = \left||A_1| + |A_2| e^{i\delta} e^{i\phi}\right|^2 = |A_1|^2 + |A_2|^2 + 2\,|A_1||A_2| \cos(\delta + \phi) \quad , \tag{1.54}$$

whereas the CP-conjugated rate is

$$|\overline{A}|^2 = \left||A_1| + |A_2| e^{i\delta} e^{-i\phi}\right|^2 = |A_1|^2 + |A_2|^2 + 2\,|A_1||A_2| \cos(\delta - \phi) \quad . \tag{1.55}$$

. The CP asymmetry then reads

$$A_{\mathrm{CP}} \equiv \frac{|A|^2 - |\overline{A}|^2}{|A|^2 + |\overline{A}|^2} = \frac{-2 \sin\delta \sin\phi}{|A_1|/|A_2| + |A_2|/|A_1| + 2\cos\delta\cos\phi} \quad . \tag{1.56}$$

This shows that there can be an observable non-zero CP asymmetry, provided there is both a strong and a weak phase difference between the contributing amplitudes.

1.7 Classification of CP Violation

Because Eq. 1.45 has three contributions, there are three ways to break the CP symmetry. Therefore, the following types of CP violation can be distinguished:

1) CP violation in decay
CP violation in decay occurs when the decay rate of a B meson to a final state f differs from the rate of a $\overline{B}$ meson to a final state $\overline{f}$. This type of CP violation occurs when

$$\left| \frac{A_f}{\overline{A}_{\overline{f}}} \right| \neq 1 \quad . \tag{1.57}$$

2) CP violation in mixing
CP violation in mixing occurs when the probability to oscillate from a B meson to a $\overline{B}$ meson is different from the probability to oscillate from a $\overline{B}$ to a B meson. For this to happen, it is required that

$$|\langle B|\overline{B}(t)\rangle|^2 = |\frac{p}{q}|^2 \, |g_-(t)|^2 \neq |\frac{q}{p}|^2 \, |g_-(t)|^2 = |\langle \overline{B}|B(t)\rangle|^2 \quad , \tag{1.58}$$

which follows from Eq. 1.27. It follows that this requirement is satisfied when $|q/p| \neq 1$, or, equivalently when

$$a_- \equiv \left(1 - \left|\frac{p}{q}\right|^2\right) \neq 0 \quad . \tag{1.59}$$

3) CP violation in interference between decays with and without mixing
There is a third type of CP violation which can occur even if there is neither CP violation in mixing nor CP violation in decay. This type of CP violation is caused by the interference between decays with and without mixing and can be observed in decays to a final state that is accessible to both B and $\overline{B}$ mesons.

A special case occurs when the final state is a CP eigenstate: $CP|f_{\rm CP}\rangle = \pm|f_{\rm CP}\rangle$. Then, by definition, the final state can be reached by a direct decay to the final state $B \to f_{\rm CP}$, and via mixing and subsequent decay $B \to \overline{B} \to f_{\rm CP}$. The CP asymmetry between a B meson decaying to a final state $f_{\rm CP}$ and its CP conjugated process is defined as

$$\begin{aligned} A_{\rm CP}(t) &= \frac{\Gamma_{B\to f}(t) - \Gamma_{\overline{B}\to f}(t)}{\Gamma_{B\to f}(t) + \Gamma_{\overline{B}\to f}(t)} \\ &= \frac{a_- \cosh\frac{\Delta\Gamma t}{2} - a_- D_f \sinh\frac{\Delta\Gamma t}{2} + a_+ C_f \cos\Delta m t - a_+ S_f \sin\Delta m t}{a_+ \cosh\frac{\Delta\Gamma t}{2} - a_+ D_f \sinh\frac{\Delta\Gamma t}{2} + a_- C_f \cos\Delta m t - a_- S_f \sin\Delta m t}, \end{aligned} \tag{1.60}$$

where a_- was defined in Eq. 1.59, and a_+ is defined as $a_+ \equiv \left(1 + \left|\frac{p}{q}\right|^2\right)$. Note that, as opposed to the two previous types of CP violation, this CP asymmetry depends on t, because of the dependence on decay time in B mixing.

The two amplitudes that contribute to the total decay amplitude are the direct decay of a B meson to the final state and the decay where the B meson first oscillates before decaying, as indicated in Fig. 1.4. Since now the total decay amplitude is the sum of two amplitudes, their relative weak phase difference can be determined by comparing the decay process and its CP conjugate process[2]. This type of CP violation can be observed in $B_s^0 \to J/\psi\,\phi$ decays, or more generally, in B_s^0 decays via $b \to c\bar{c}s$ transitions.

1.8 CP Violation in Interference between Mixing and $b \to c(\overline{c}s)$ Transitions

In B_s^0 decays that occur through $b \to c\bar{c}s$ transitions to a CP eigenstate, see for example Fig. 1.4, CP violation can manifest itself through interference between decays with and without mixing. Here, $|\lambda_f| = \left|\frac{q}{p}\frac{\overline{A}_f}{A_f}\right| = 1$, if one assumes that there is no CP violation in mixing, i.e. $|q/p| = 1$, and that penguin contributions (see Sec. 5.9) can be ignored, i.e.

[2] In this particular case, the origin of the strong phase difference is the mixing dynamics. For example, in the simplified case where $\Delta\Gamma = 0$, from Eq. 1.25, it follows that mixing generates a phase difference of exactly 90° between $g_+(t)$ and $g_-(t)$.

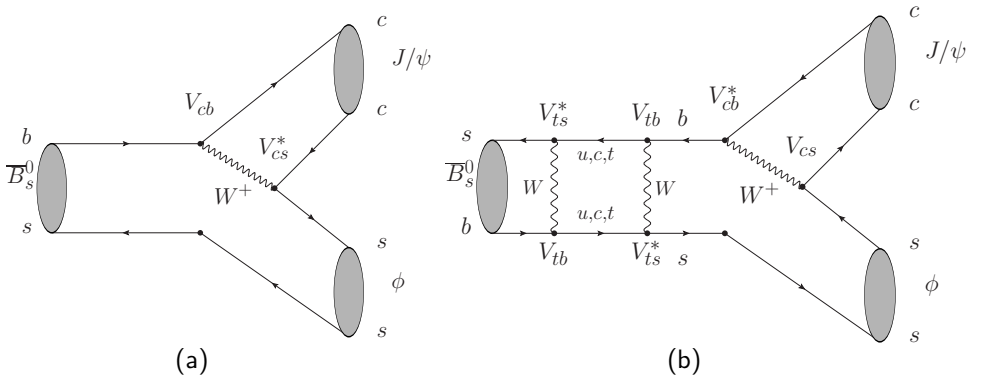

Figure 1.4: *a) An example of a $b \to c(\bar{c}s)$ transition: Feynman diagram of a $\overline{B}{}^0_s \to J/\psi\,\phi$ decay without mixing. b) Feynman diagram of a $\overline{B}{}^0_s \to J/\psi\,\phi$ decay including mixing.*

$|\overline{A}_f/A_f| = 1$. This leads to $C_f = 0$, $a_+ = 2$ and $a_- = 0$, causing the decay time-dependent CP asymmetry from Eq. 1.60 to simplify to

$$A_{\mathrm{CP}}(t) = \frac{-S_f \sin \Delta m t}{\cosh \frac{\Delta\Gamma t}{2} - D_f \sinh \frac{\Delta\Gamma t}{2}} \quad . \tag{1.61}$$

In the case of $B^0_s \to J/\psi\,\phi$ decays, an extra complication occurs because the final state $J/\psi\,\phi$ is an admixture of CP eigenstates with eigenvalues $\eta_f = \pm 1$. The CP asymmetry then becomes

$$A_{\mathrm{CP}}(t) = \frac{-\eta_f \sin \phi_s \sin \Delta m t}{\cosh \frac{\Delta\Gamma t}{2} - \eta_f \cos \phi_s \sinh \frac{\Delta\Gamma t}{2}} \quad . \tag{1.62}$$

In this equation, $\phi_s = \phi_M - 2\,\phi_{c(\bar{c}s)}$ is the relative weak phase difference, see Sec. 1.6, where $\phi_{c(\bar{c}s)}$ is the phase of the $b \to c(\bar{c}s)$ transition. The precise derivation of $S_f = \eta_f \sin \phi_s$ and $D_f = \eta_f \cos \phi_s$ is explained in more detail in Chap. 5. In that chapter, it is also shown that in the SM, the parameter ϕ_s is related to the angle β_s: $\phi_s^{\mathrm{SM}} = -2\,\beta_s$, which is expected to be small. However, the value of ϕ_s can be enhanced by New Physics (NP) models, indicating that the $B^0_s \to J/\psi\,\phi$ decay mode is an important probe for New Physics. Before going into the details of the analysis of $B^0_s \to J/\psi\,\phi$ decays in Chap. 5 and Chap. 6, it is time to introduce the LHCb experiment.

CHAPTER
TWO

The LHCb Experiment

The Large Hadron Collider beauty experiment (LHCb) is a dedicated heavy-flavour physics experiment at the Large Hadron Collider (LHC) at CERN, Geneva. The primary goal of the experiment is to look for indirect evidence of New Physics (NP) in the heavy-flavour sector, in particular by studying CP violation and rare decays of beauty and charm hadrons. First, a description of the LHC itself is given, after which the design of the various LHCb subdetectors is presented.

2.1 The Large Hadron Collider

The LHC is located in a 27 km long almost circular tunnel about 100 m underground on average (the deepest point is at 175 m below the surface, the most shallow point at 50 m below the surface). Before LHC construction, the 3.8 m diameter tunnel accommodated its predecessor, the LEP collider.

The LHC collides two proton beams or two heavy ion beams, while collisions of protons with lead ions are also foreseen. LHCb has only taken data in proton-proton collision mode so far and was switched off during lead-lead collisions due to too high final state flux in the forward direction. The possibility to collect data in proton-lead collisions is being investigated.

Protons are injected into the LHC at an energy of 450 GeV, using the pre-accelerators on the CERN premises. A schematic picture of the accelerator complex is shown in Fig. 2.1. The LHC consists of over 1600 superconducting magnets that generate the magnetic field to keep the accelerated particles in their orbit. These superconducting magnets operate at a temperature of 1.9 K using a cryostat with liquid helium. During the acceleration of the beams from 450 GeV to the final collision energy of 3.5 TeV, the magnetic field is increased to approximately 4 T [26].

At four distinct points in the LHC ring, the proton beams collide in caverns that house the four major LHC experiments: ATLAS, CMS, ALICE and LHCb. ATLAS and CMS are general purpose detectors and ALICE is designed specifically to study Pb-Pb collisions. In addition, two smaller dedicated small angle experiments, TOTEM and LHCf complete

the LHC physics program. TOTEM makes use of collisions in the CMS interaction region to measure the total proton-proton cross section, while LHCf is located near the ATLAS detector and performs experiments to calibrate collision processes in large scale cosmic ray experiments.

During the 2010 and 2011 runs, the proton-proton center-of-mass collision energy was 7 TeV. This is only half the LHC design value, which is a safety precaution after the incident in one of the LHC magnets on 19 September 2008. In the 2012 run the LHC will be operated at $\sqrt{s} = 8\,\text{TeV}$ and after upgrading the machine during a technical stop in 2013, LHC is expected to operate at its design center-of-mass energy of 14 TeV in 2014.

The proton beams are not continuous, but spaced in bunches of about 10^{11} protons each. At design luminosity the LHC is filled with 2808 bunches, providing a bunch-bunch collision rate of 40 MHz and a maximum instantaneous luminosity of $10^{34}\,\text{cm}^{-2}\text{s}^{-1}$.

During the LHC startup in 2009, initially only two proton bunches collided. This was gradually increased to 1320 colliding bunches by the end of 2011. In addition, the bunch spacing was decreased from 75 ns in 2010, to 50 ns during the 2011 run and, finally, in a test run at the end of 2011, to 25 ns. The implications of the bunch spacing for the Outer Tracker subdetector of LHCb is discussed in section 3.4.5. Most of the data described in this thesis is taken with the 50 ns bunch spacing.

2.1.1 LHC Environment at LHCb

Because of their relatively long lifetime, B mesons travel a macroscopic distance in the detector, typically in the order of a centimeter, before decaying into final state particles. In LHCb, B meson decays are identified by their flight distance, their invariant mass and their decay into a specific final state. The flight distance is measured by reconstructing the pp interaction point, called the primary vertex and the point where the B meson decays, called the secondary vertex. In order to limit combinatoric backgrounds and to avoid incorrect association between primary and secondary vertices, LHCb is designed to run at an instantaneous luminosity in the range of $2 - 5 \cdot 10^{32}\,\text{cm}^{-2}\text{s}^{-1}$, where the number of single pp interactions per bunch crossing is close to maximal.

In order to limit the instantaneous luminosity at the LHCb interaction point, the LHC beams are displaced and defocussed. In this way LHCb can operate simultaneously to the general purpose experiments ALTAS and CMS, but with reduced instantaneous luminosity. Towards the end of 2011 the luminosity had reached $4 \cdot 10^{32}\,\text{cm}^{-2}\text{s}^{-1}$, an optimal value to maximize event yields while ensuring efficient track reconstruction in high occupancy events. The average number of visible pp interactions per bunch crossing was 1.5 at the end of 2011. The total recorded integrated luminosity in 2011 was $1.1\,\text{fb}^{-1}$, as shown in Fig. 2.2.

LHCb measured the total $b\bar{b}$ cross section at $\sqrt{s} = 7\,\text{TeV}$ to be $288 \pm 4\,(\text{stat.}) \pm 48\,(\text{syst.})\,\mu\text{b}$ [27]. This implies a total amount of $3 \cdot 10^{11}$ produced $b\bar{b}$ pairs at the LHCb interaction point in 2011.

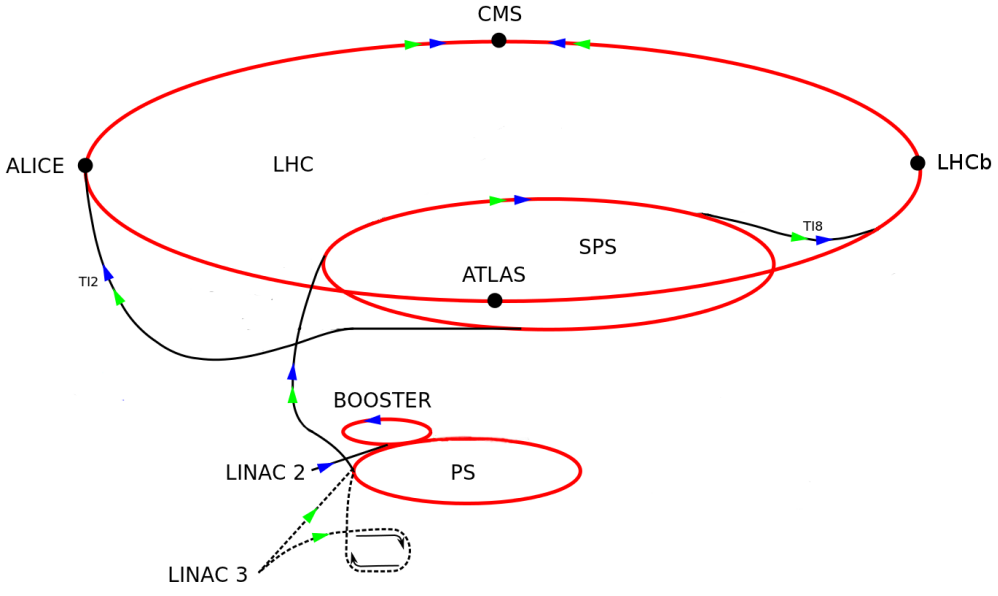

Figure 2.1: *Schematic picture of the CERN accelerator complex. Indicated by blue arrows are protons that collide in the LHC experiments. They begin their journey in LINAC2 (a linear accelerator), and are subsequently accelerated in the BOOSTER, the PS, the SPS and finally in the LHC. Lead ions are indicated by green arrows and are coming from LINAC3 before being injected to the BOOSTER. The four large LHC experiments are also indicated: ATLAS, CMS, ALICE and LHCb.*

2.2 LHCb Requirements

Not only must LHCb be able to select $b\bar{b}$ events out of a minimum bias rate of 40 MHz, but in addition, from this large set of events, it must identify specific (and often rare) B-hadron decays. This requires an efficient trigger, which must be sensitive to many different final states of interest.

The decay-time resolution must be good enough to resolve the rapid oscillations in the $B_s^0 - \overline{B}_s^0$ system. This requires a precise vertex reconstruction. Sufficient momentum resolution (directly related to mass resolution) is required to reduce combinatorial backgrounds. Both these requirements are of crucial importance in the reconstruction and selection of $B_s^0 \to J/\psi\,\phi$ decays.

In addition, to differentiate between different B decay modes, the LHCb experiment needs the ability to identify particle types in particular decays. For example, in the case of $B_s^0 \to J/\psi\,\phi$ decays, it is important to correctly identify charged kaons and muons, since the J/ψ meson decays to $\mu^+\mu^-$ and the ϕ meson decays to K^+K^-. The design of the LHCb subdetectors is discussed below.

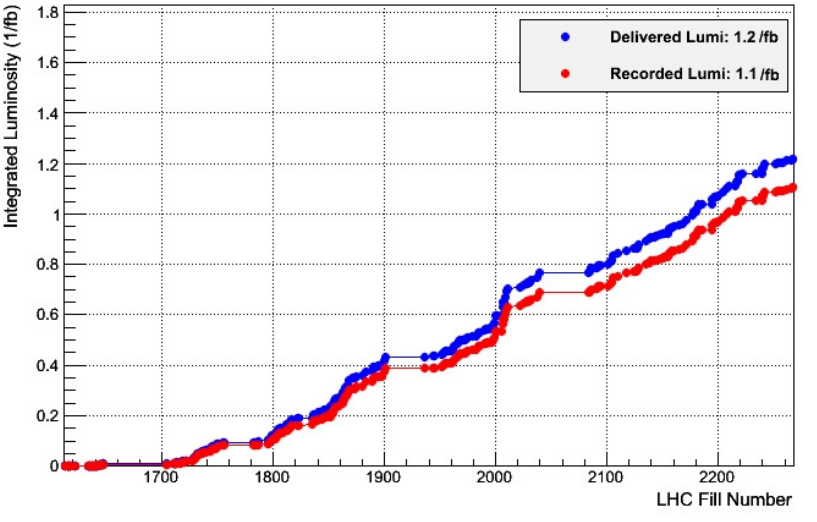

Figure 2.2: *LHCb integrated luminosity at 3.5 TeV in 2011. The blue line is the delivered integrated luminosity, the red line is the recorded integrated luminosity. The average recording efficiency was 90.8%.*

2.3 The LHCb Detector

LHCb is a single-arm spectrometer with an angular coverage of 10-300 mrad in the bending plane of the dipole magnet and 10-250 mrad in the non-bending plane. This particular choice of detector geometry is justified by the fact that at high energies both the b and $\overline{b}$ hadrons are mainly produced in the same forward or backward cone. A schematic picture of LHCb is shown in Fig. 2.3 and an event display showing a selected $B_s^0 \to J/\psi\,\phi$ candidate with all the hits and tracks traversing the detector is shown in Fig. 2.4.

The LHCb subdetectors can be subdivided according to two main functionalities: the tracking system (VELO, ST, OT and the dipole magnet) which serves to reconstruct charged particle tracks through the detector and the particle identification system (RICH, ECAL, HCAL, MUON system).

The LHCb trigger consists of a hardware component (L0) and a software component (HLT). The subdetectors and the trigger of LHCb are briefly described in this chapter. More detailed information on the various subsystems can be found in [26].

2.3.1 Beam Pipe

The beam pipe of the LHC in the LHCb experimental region is composed of beryllium, up to $z = 13\,\mathrm{m}$. Although beryllium is expensive, toxic and fragile, the main advantage of beryllium is its large radiation length (little interaction with traversing particles).

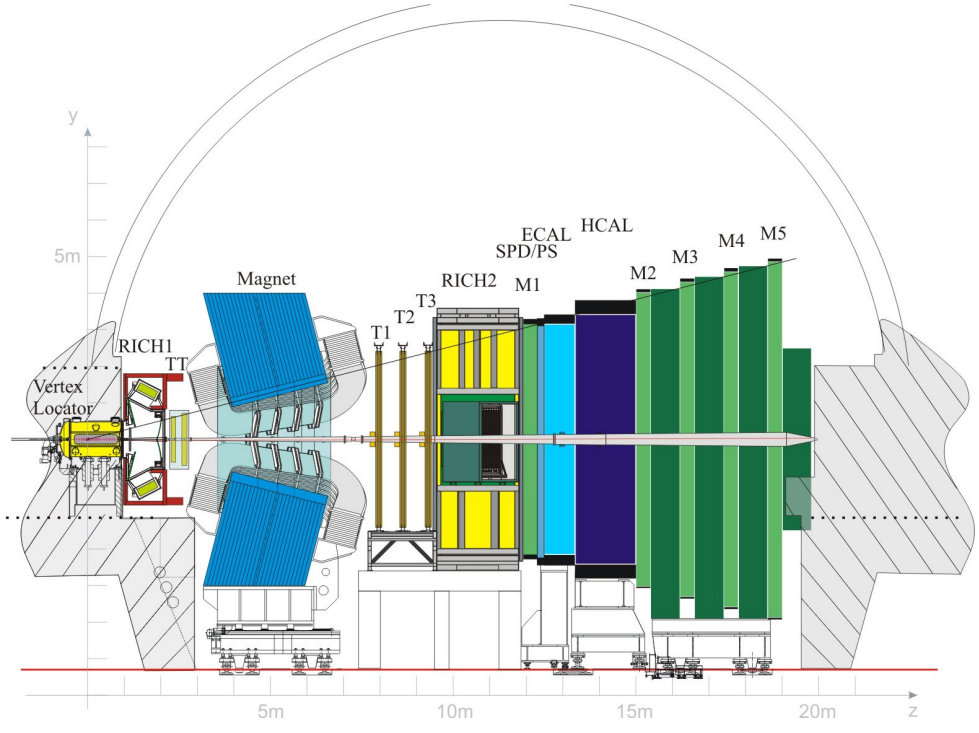

Figure 2.3: *Schematic picture of the LHCb detector with all its subdetectors. A right-handed coordinate system is chosen with the z-axis from left to right along the beam line, and the y-axis pointing upwards in the vertical plane. The x-axis completes the right-handed coordinate system.*

2.4 Tracking System

Precise vertex and momentum reconstruction are needed to reconstruct $B_s^0 \to J/\psi\,\phi$ events, since these two aspects provide the ingredients for the mass, angular and decay-time distributions that are used in the trigger, offline selection and the final $B_s^0 \to J/\psi\,\phi$ decay analysis.

The tracking system in LHCb consists of a large dipole magnet and the tracking subdetectors: the vertex locator (VELO) and the Tracker Turicensis (TT) upstream of the magnet, and three tracking stations downstream of the magnet. The three downstream tracking stations consist of the Inner Tracker (IT) stations covering the central region close to the beam pipe and the Outer Tracker (OT) stations covering the outside region. The TT and IT were developed in a common project called the Silicon Tracker (ST).

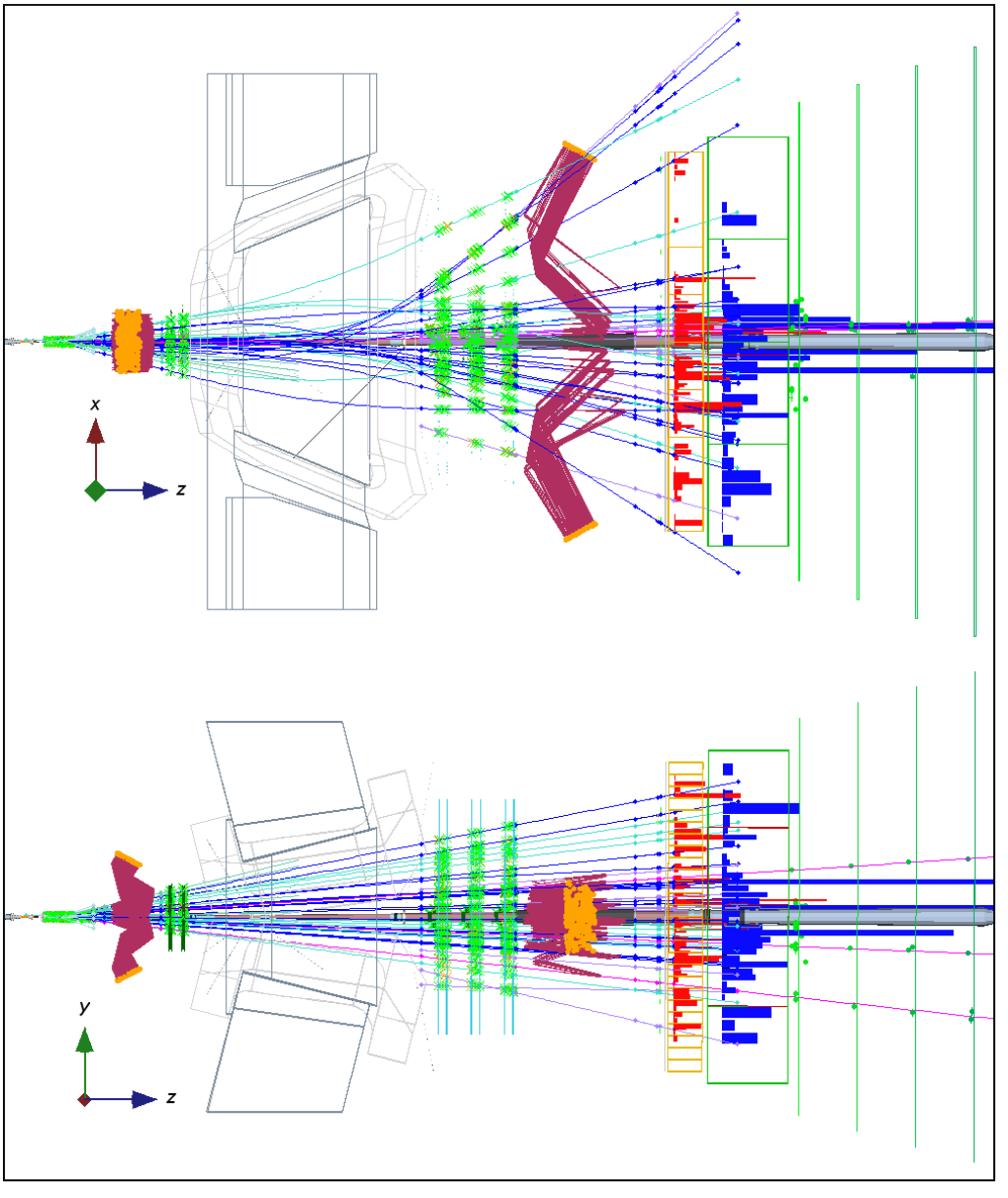

Figure 2.4: *LHCb event display showing all the hits and tracks through the detector in an event recorded on August 17, 2011, in xz projection (upper) and in yz projection (lower). The green crosses indicate detector hits in the tracking stations, the red and blue histograms represent detector energy in the ECAL and HCAL and the orange circles are detected photons in the RICH. Reconstructed charged particle tracks are drawn in blue (in pink for muon tracks). The purple zig-zag lines are the trajectories of Cherenkov photons in the RICH.*

2.4.1 LHCb Magnet

To measure the momentum of charged particles, the LHCb spectrometer consists of a warm dipole magnet with an integrated magnetic field of 4 Tm. The magnet has saddle-shaped coils in a window-frame yoke with sloping poles outside the LHCb acceptance. The principal field component is in the vertical direction (y direction). The magnet weighs 1600 tons and measures 11 m$\times$8 m$\times$5 m. The integrated magnetic field allows to measure particle momenta up to 200 GeV/c with a resolution between 0.3% and 0.5%. Figure 2.5 shows a photograph of the LHCb magnet.

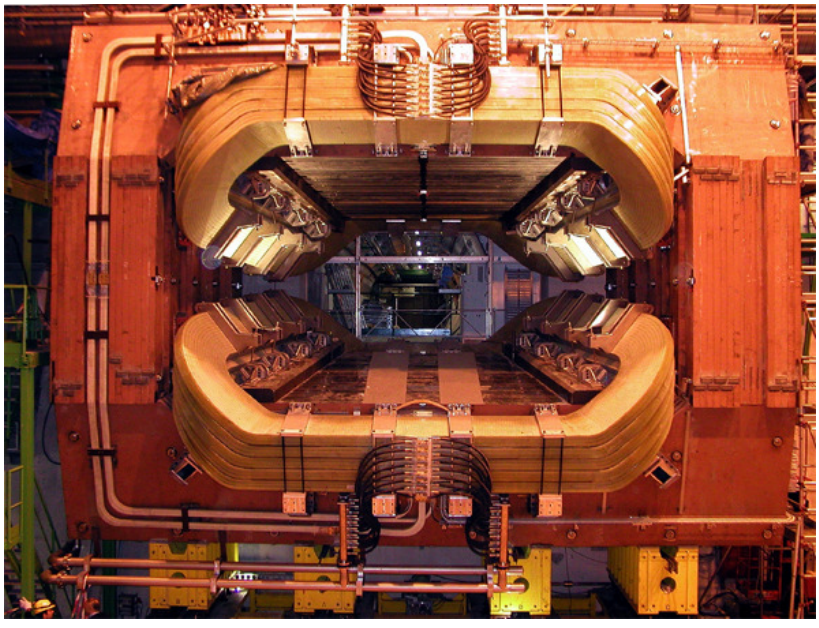

Figure 2.5: *The LHCb magnet prior to detector installation, consisting of the window-frame yoke and saddle-shaped coils. The particles pass through the opening in the center.*

2.4.2 VELO

The VELO measures track coordinates close to the interaction region. These measurements are used to identify primary and displaced secondary vertices, which are a distinctive feature of b and c hadron decays.

The VELO consists of an array of modules with silicon strip detectors. One VELO module consists of two sensors which are glued back-to-back: one to measure the azimuthal ϕ-coordinate and one to measure the radial r-coordinate. The r-sensors consist of semicircular silicon strips, whereas the ϕ-sensors contain straight silicon strips. The strips in the inner and outer region of the ϕ-sensor have a different angle with respect to the radial to improve the pattern recognition capability. In addition, adjacent ϕ-sensors have opposite skew in the

inner and outer regions. A schematic picture of the VELO sensors is shown in Fig. 2.6. Two VELO modules (one on each side of the beam pipe) comprise one VELO station. The

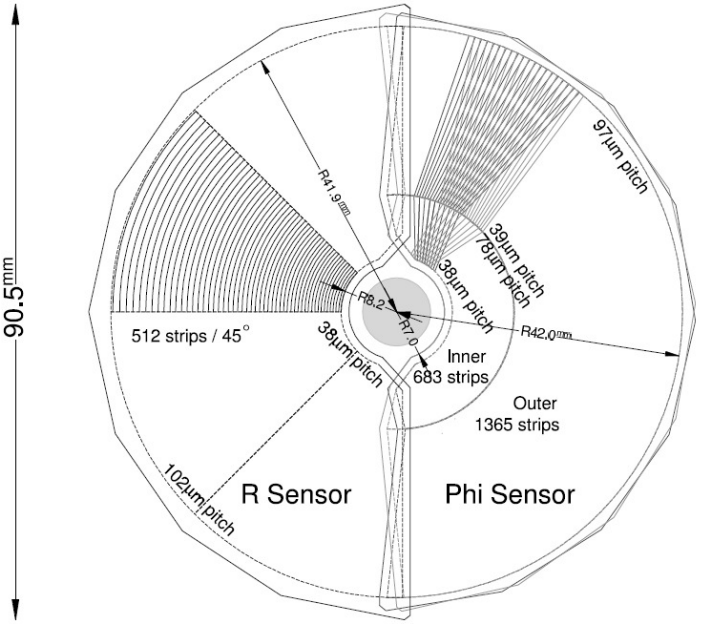

Figure 2.6: *Schematic layout of the VELO sensors. An r-sensor is shown on the left. The ϕ-sensor on the right shows the silicon strips of two adjacent modules superimposed, to indicate the different angle with respect to the radial. In addition, the different orientation of the strips in the inner and outer region is shown.*

minimal reconstructable track polar angle is 15 mrad for particles traversing at least three VELO stations, as shown in Fig. 2.7.

Two detector planes at the upstream end of the VELO are called the pile-up (PU) subdetector. The PU consists of r-sensors only, and has a dedicated 40 MHz readout, as it is used in the Level-0 (L0) trigger. Originally, the PU was designed to veto events with multiple pp interactions in one bunch crossing. Currently, the PU is used in the L0 trigger to detect beam-gas interactions. These are collisions of protons with gas atoms that are left in the beam pipe vacuum. The PU distinguishes between beam-gas collisions coming from LHC beam 1 and LHC beam2.

The silicon sensors of the VELO are placed at a distance of 8 mm from the interaction point. Since this distance is smaller than the beam aperture of the LHC beams during injection, the VELO sensors are retractable over a distance of 30 mm. The sensors are mounted in a vessel that maintains a secondary vacuum around the sensors. The sensors are separated from the primary LHC vacuum by a thin aluminum box called the RF-box, to guarantee ultra-high vacuum and to prevent RF pickup from the LHC beams. The design of the RF-foil, the top layer in between the beam and the VELO sensors, is such that it

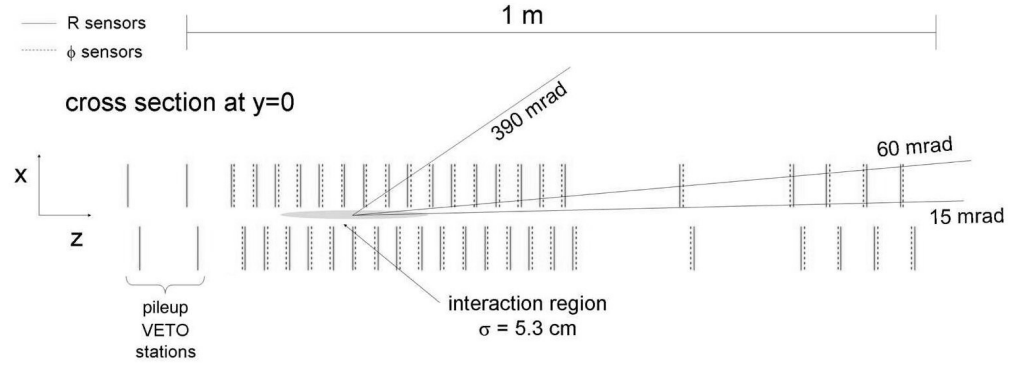

Figure 2.7: *Schematic layout of the VELO modules. This view is a cross section in the (x, z) plane at $y = 0$. The two upstream (small z) module pairs are the modules of the pile-up detector. 15 mrad is the minimal reconstructable track angle for which at least three VELO stations are crossed. The maximal reconstructable angle is 390 mrad for the same condition.*

minimizes the amount of material traversed by particles and also allows the z-staggered VELO sensors of a station to overlap in the closed position to obtain full azimuthal coverage around the beam pipe.

2.4.3 Silicon Tracker (ST)

The ST consists of the Tracker Turicensis (TT) and Inner Tracker (IT), which both use silicon microstrip detectors. The TT is located upstream of the LHCb magnet, whereas the IT is placed downstream of the magnet.

Tracker Turicensis (TT)

The TT is approximately 160 cm wide and 130 cm high with an active area of about 8.4 m^2. Its four detection layers are arranged in two pairs that are separated by 27 cm along the beam axis. The four layers are constructed in x-u-v-x configuration, with vertically orientated detection strips in the first and last layer (so-called x orientation), and strips rotated by -5° (u orientation) and $+5^\circ$ (v orientation) with respect to the vertical in the second and third layer, respectively. This so-called stereo configuration is also used in the IT stations and the OT stations which are discussed later. A schematic picture of the TT is shown in Fig. 2.8.

Track candidates formed by the VELO and the tracking stations downstream of the magnet are confirmed by hits in the TT upstream of the LHCb magnet to reduce the number of fake track combinations. The TT also serves to measure track parameters of long-lived particles that decay after the VELO, e.g. K^0_S and Λ. In addition, the TT detects slow

particles that are bent out of the LHCb acceptance before they reach the region downstream of the magnet.

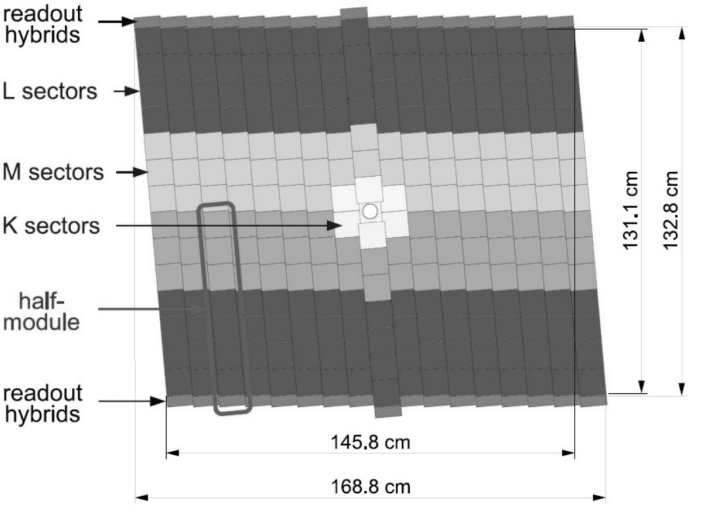

Figure 2.8: *Schematic picture of TT layer 3, which is the stereo layer in v-configuration. The various readout sectors are indicated by different shadings.*

Inner Tracker (IT)

The IT is located downstream of the dipole magnet and consists of three four-layer tracking stations. The layers in each IT station are constructed in the same x-u-v-x configuration as used in the TT. The IT covers the region closest to the beam pipe in the center of the downstream tracking system with a total active area of approximately $4.0\,\mathrm{m}^2$. The dimensions of the IT are shown in Fig. 2.9.

The four layers in each station are housed in 4 detector boxes which are separated by 4 mm in z and have a 3 mm overlap in y to avoid detector gaps and to facilitate detector alignment.

2.4.4 Outer Tracker (OT)

The OT covers an area of about $5 \times 6\,\mathrm{m}^2$, surrounding the IT. It is a gaseous straw-tube detector and consists of stand-alone, gas-tight detector modules containing two layers of straw-tube drift cells. The OT consist of three OT stations, T1, T2 and T3, each of which consists of four detection layers of OT modules, arranged in the same x-u-v-x configuration as the IT and TT.

There are two main types of modules in the OT: F-modules which span the entire height of the OT and S-modules which are installed below and above the IT. There are three different

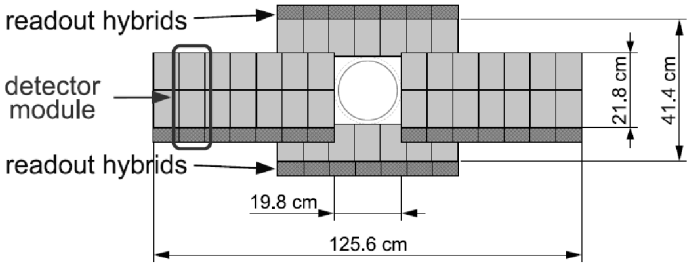

Figure 2.9: *Schematic picture of an IT x-detection layer in the second IT station.*

S-modules types: S1-modules have the same width but are smaller in length compared to F-modules, while S2-modules are yet shorter and installed only on the OT A-side (positive LHCb x-coordinate). Finally, S3-modules are half the width of the other OT modules and installed only on the C-side (negative LHCb x-coordinate). A schematic picture of the OT, including the position of the various module types, is shown in Fig. 2.10. The Outer Tracker is discussed in greater detail in Chap. 3.

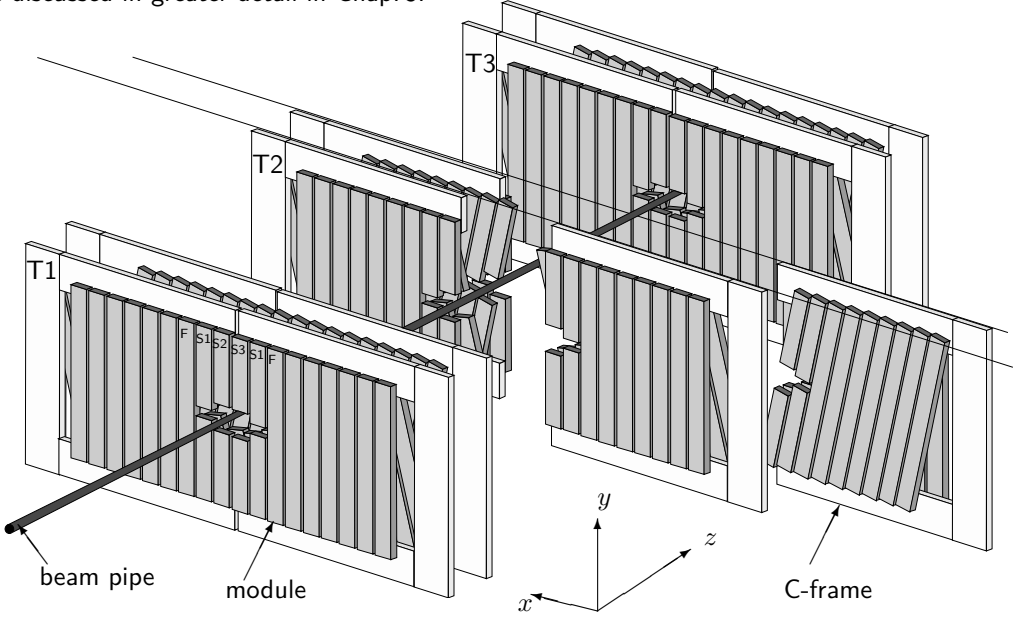

Figure 2.10: *Schematic picture of the Outer Tracker. The three tracking stations T1, T2 and T3 each accommodate four layers of detector modules in x-u-v-x configuration. The module type (F, S1, S2, S3) is indicated for modules in the first layer of T1. The supporting C-frames can move in and out of the detector acceptance for service tasks.*

2.5 Particle Identification

The particle identification (PID) subdetectors in LHCb are the RICH system, the calorimeter system and the muon system. These serve to identify charged pions and kaons (RICH), electrons and photons (ECAL and HCAL) as well as muons (MUON). For the $B_s^0 \to J/\psi\,\phi$ decay, PID information is used to identify the two muons and the two kaons in the final state. In addition, the PID detectors are used to identify single muon, electron or kaon tracks that tag the B meson flavour at the time of production. This so-called tagging procedure is of vital importance in the $B_s^0 \to J/\psi\,\phi$ analysis and is explained in more detail in Sec. 6.4.

2.5.1 RICH

Ring Imaging CHerenkov (RICH) detectors measure the radius of so-called Cherenkov rings from which the velocity v of a particle is derived. When a relativistic particle traverses a medium (often called a radiator) at a velocity larger than the speed of light in that medium, Cherenkov light is emitted in a cone around the particle trajectory. The angle of this cone, combined with the index of refraction of the radiator yields the velocity of the particle:

$$\cos\theta_c = \frac{1}{n\,\beta} \quad , \tag{2.1}$$

with θ_c the angle of the cone, n the index of refraction of the radiator and $\beta = v/c$. By comparing the velocity to the measured momentum of a particle, its mass is determined.

In LHCb, at large polar angles the particle momentum spectrum is relatively soft, while at small polar angles the momentum spectrum is relatively hard. To cover the entire momentum range, two RICH detectors are installed. RICH1, located upstream of the magnet, covers the low momentum range (1-60 GeV/c) and uses aerogel and C_4F_{10} as radiators, whereas RICH2, downstream of the magnet, covers the high momentum range (up to approximately 100 GeV/c) and uses CF_4 as radiator.

In both detectors spherical and flat mirrors reflect the Cherenkov light out of the LHCb acceptance and focus it on Hybrid Photon Detectors (HPDs) to detect the Cherenkov rings. A schematic picture and an event display of RICH1 are shown in Fig. 2.11.

Particle identification using the RICH detectors is based on a log-likelihood (LL) method [28] which matches the observed pattern of hit pixels in the HPDs of the RICH to that expected from the reconstructed tracks under a given set of particle hypotheses.

2.5.2 Calorimeter

The calorimeter system provides particle identification by means of energy and position measurements of hadrons, electrons and photons. The L0 trigger uses the CALO system to select events with high transverse energy E_T.

The layout of the calorimeter system is a classic configuration of an electromagnetic calorimeter (ECAL) followed by a hadronic calorimeter (HCAL). Both consist of alternating layers of absorber and detector material. Incident particles interact with the absorber material (lead in the ECAL, iron in the HCAL), creating a shower of secondary particles. These particles induce light when passing through the scintillation detector material. This

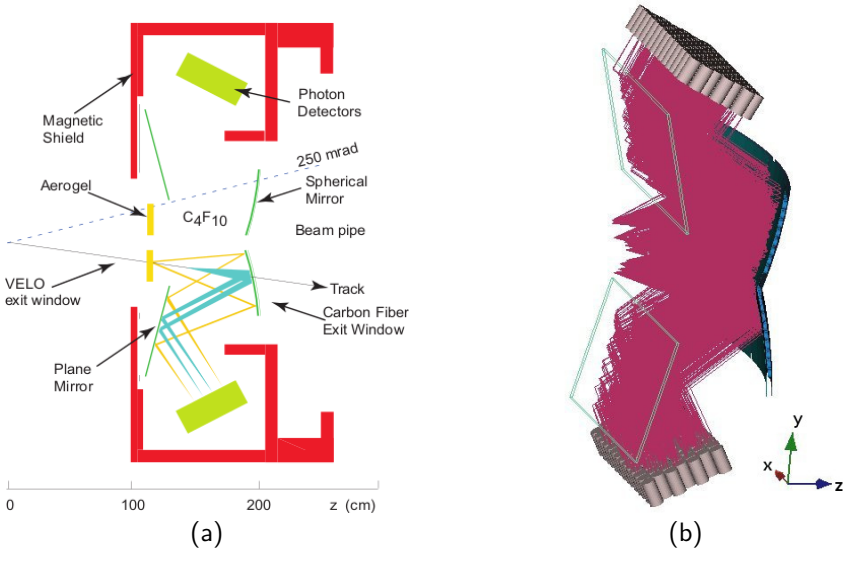

Figure 2.11: *(a) Schematic picture of RICH1, side view. (b) Graphical representation of an event recorded on August 17, 2011, as detected by RICH1. The lines represent the reconstructed trajectories of the Cherenkov photons. The orientation in the LHCb coordinate system is indicated on the right.*

scintillation light is subsequently collected by photo-multiplier tubes (PMTs). The amount of light is a measure of the energy of the incident particles.

Two additional subdetectors of the CALO system are located in front of the ECAL. The Scintillating Pad Detector (SPD) detects charged particles, which together with the information from the ECAL is used to separate electrons from uncharged particles such as photons and π^0's.

The Preshower (PS) detector is separated from the SPD by a 15 mm thick lead layer to induce electromagnetic showers. Light hadrons, like charged pions, leave less energy in the PS than electrons, allowing them to be distinguished from electrons.

2.5.3 Muon System

The most downstream subdetector is the muon system, which consists of five muon stations named M1 to M5. The muon system is used to trigger on muons with high p_T in the L0 trigger and is also used in later trigger stages and in the offline analysis.

Traversing muons are detected using multi-wire proportional chambers. Only in the inner region of M1, where hit densities are high, triple Gas Electron Multiplier (GEM) detectors are used. Iron absorbers of 80 cm thick are placed in between M2-M5 and behind M5 to remove hadronic backgrounds, and select penetrating muons. M1 is placed in front of the calorimeter system to provide a measurement point before muons undergo multiple scattering

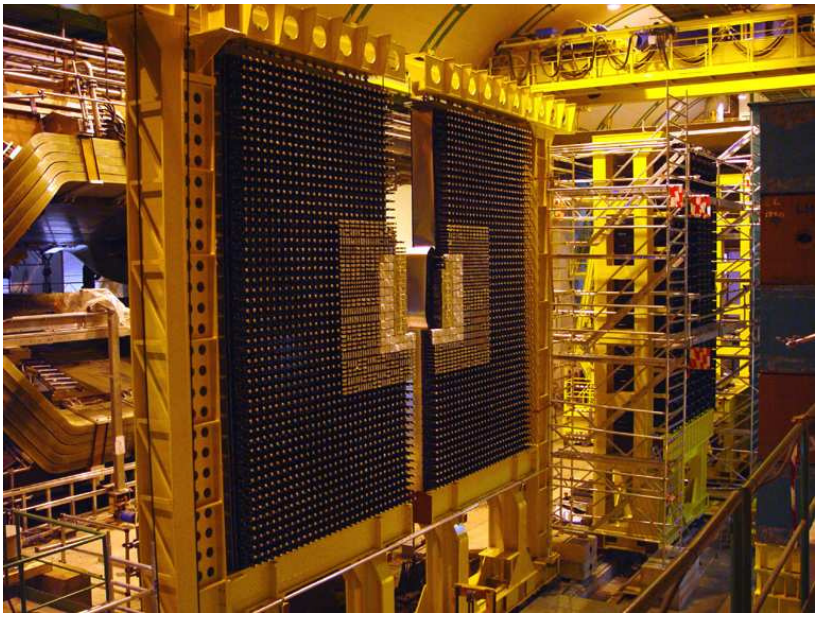

Figure 2.12: *Photograph of the ECAL detector after installation in the LHCb experiment.*

in the calorimeter and to provide a larger lever arm to optimize the p_T measurement in the L0 trigger. Stations M1-M3 have high spatial resolution in the bending plane. They are used to define the track direction and to calculate the p_T of the candidate with a resolution of 20%. Station M4 and M5 are mainly used for candidate confirmation and have limited spatial resolution. The L0 trigger uses the muon chambers for a stand-alone muon track reconstruction and p_T measurement.

2.6 Trigger

The task of the trigger is to reduce the 40 MHz bunch crossing rate, to the output event rate of 3 kHz, at which events are written to tape for offline analysis. This is achieved by dividing the trigger in two levels: the hardware Level-0 (L0) trigger and the software High Level Trigger (HLT), where the latter is subdivided in two stages: HLT1 and HLT2. A diagram of the trigger flow in LHCb, and various classes of so-called trigger lines are shown in Fig. 2.14.

2.6.1 L0

The L0 trigger is a hardware trigger that uses custom electronics. This trigger operates synchronously to the 40 MHz LHC bunch crossing clock and reduces the rate to 1 MHz, which is the input rate for the next trigger level, the HLT. Since B mesons have a relatively

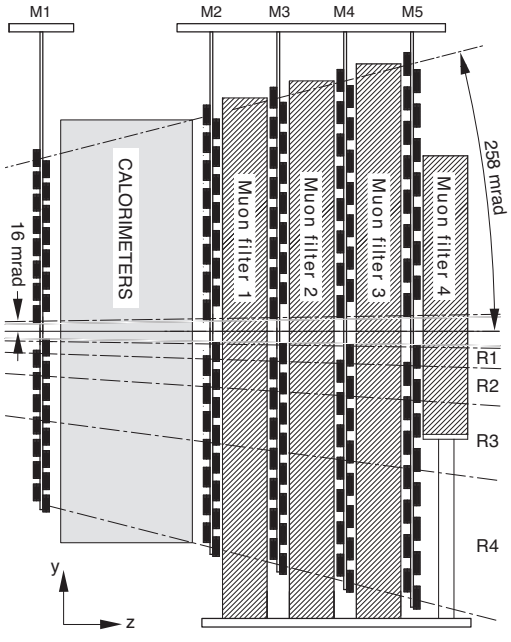

Figure 2.13: *Schematic picture (side view) of the muon stations M1 to M5, including the iron absorbers placed in between the stations.*

large mass, their decay particles tend to have large transverse momentum (p_T) or transverse energy (E_T). These properties are used in the L0 trigger.

First of all, to veto busy events, the L0 trigger requires a maximal number of 600 hits in the SPD detector. Then, the global L0 decision is the logical OR of several requirements: either the hadron E_T is required to be at least 3.5 GeV, or the electromagnetic E_T is at least 2.5 GeV, or the muon p_T is at least 1.48 GeV/c. In addition to this latter requirement on a single muon, there is also a di-muon requirement in the L0, which asks for at most 900 hits in the SPD and $p_{T_1} p_{T_2} > 1.68\,\text{GeV}^2/c^2$. On a positive L0 decision, all detector information is read out into the data acquisition system (DAQ).

2.6.2 HLT

In order to further reduce the L0 output rate from 1 MHz to 3 kHz, the L0 accepted events are processed by the HLT. The HLT is a software trigger running on a processor farm, asynchronously to the LHC clock. The HLT is subdivided in two stages: HLT1 and HLT2.

The HLT1 reduces the event rate to 50 kHz. As indicated in Fig. 2.14, HLT1 trigger lines can be grouped in various classes: e.g. technical trigger lines (including minimum bias triggers), one-track trigger lines (asking for a track with high impact parameter), single muon trigger lines and di-muon trigger lines. The global HLT1 decision is the logical OR of all the HLT1 trigger lines. HLT1-accepted events are subsequently processed by the HLT2.

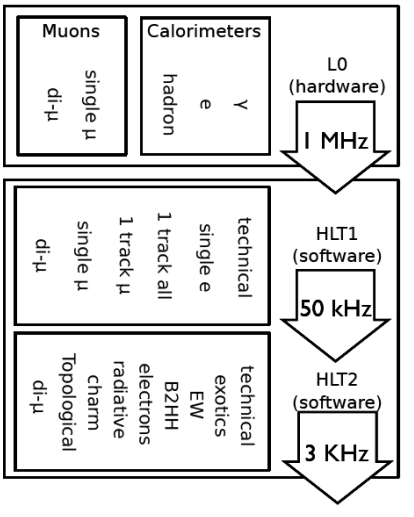

Figure 2.14: *Trigger flow in LHCb showing the event output rate after each trigger step. For each trigger step, various classes of trigger lines are indicated. For the $B_s^0 \to J/\psi\,\phi$ decay analysis, only di-muon trigger lines are considered.*

The input rate for HLT2 is sufficiently reduced to use the full event information and perform online track reconstruction. These tracks are used to reconstruct and select composite particles. Using requirements on variables such as invariant mass and decay time, inclusive and exclusive event selection algorithms are implemented to select events for each of the LHCb physics programs. This is reflected by the names of the various HLT2 trigger line classes indicated in Fig. 2.14. The global HLT2 decision is the logical `OR` of all the HLT2 trigger lines. On a positive global HLT2 decision the event is written to disk. If the HLT output rate is too high, individual HLT1 and HLT2 trigger lines can be prescaled or postscaled by randomly selecting a subset of events.

In the $B_s^0 \to J/\psi\,\phi$ decay analysis, only the class of di-muon trigger lines is considered. Two types of these di-muon HLT lines are used: so-called decay-time unbiased trigger lines and decay-time biased trigger lines. In the first category of trigger lines, no explicit and implicit selection cuts on decay time or impact parameter are made, and therefore these trigger lines are not expected to introduce a bias in the decay-time distribution of the selected events. However, the allowed output rate requires the application of a prescale factor leading to a low efficiency. As an example, the `Hlt2DiMuonJPsi` unbiased trigger line, important for the $B_s^0 \to J/\psi\,\phi$ decay analysis, was prescaled by a factor five during the second half of 2011.

Alternatively, in the decay-time biased trigger lines, impact parameter (IP) cuts are made, introducing a non-uniform efficiency in the decay-time distribution, but resulting in a larger efficiency for B mesons with large decay times. In physics analyses that are using events triggered by biased trigger lines, the time-dependent acceptance needs to be known and taken into account. The trigger lines used in the analysis of $B_s^0 \to J/\psi\,\phi$ as well as their

prescale factors and decay-time dependence, are discussed in more detail in Chap. 6.

2.7 Performance

In order to study CP violation in $B_s^0 \to J/\psi\,\phi$ decays, the following requirements must be met: good decay-time resolution to observe the fast oscillations in B_s^0 mixing, good mass resolution to reconstruct the B_s^0 invariant mass and to suppress combinatorial background, and particle identification to identify the muons and kaons in the final state. These three aspects are discussed here to illustrate the performance of the LHCb subdetectors.

2.7.1 Decay-Time Resolution

Track reconstruction software uses hits in the VELO, TT, IT and OT subdetectors to reconstruct charged particle trajectories. These tracks are used to reconstruct the primary vertex (PV) where the pp collision took place, and any secondary vertices (SV) of long-living particles, notably B mesons. The decay time of a B meson is calculated from the distance between the PV and the SV together with its reconstructed momentum. For each event, the true decay time is slightly altered in the experimental measurement leading to a decay-time distribution that is convoluted with a resolution factor. This decay-time resolution can be obtained from Monte Carlo simulations by studying the difference between true decay time and reconstructed decay time.

However, the decay-time resolution can also be determined from data itself, by looking at so-called prompt particles. These are particles that are created at zero decay time. For a perfect detector, the decay-time distribution of these particles would be a delta function at zero decay time. In LHCb, however, the decay-time distribution of promptly produced particles will show a spread around zero decay time and the width of the distribution is a measure of the decay-time resolution. Fig. 2.15 shows the decay-time resolution of fake, prompt $B_s^0 \to J/\psi\,\phi$ decays. These are promptly produced J/ψ and ϕ particles which happen to have a reconstructed mass close to the B_s^0 mass. The observed decay-time resolution of ~ 50 fs is fairly constant over the momentum range and close to the expected value of 40 fs from the MC.

2.7.2 Mass Resolution

The mass resolution of reconstructed B decays is related to the momentum resolution of the tracking system. The di-muon invariant mass distribution in Fig. 2.16 shows reconstructed resonances over two orders of magnitude in $m(\mu^+\mu^-)$. The mass resolutions of the J/ψ resonance and the $\Upsilon(1S)$ resonance are 14 MeV/c^2 and 53.9 MeV/c^2, respectively. These numbers increase roughly linearly with mass, since momentum resolution in LHCb is only mildly momentum dependent [29]. The width of the Z boson peak is dominated by its intrinsic width.

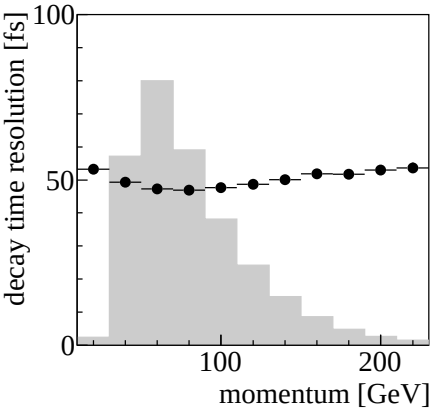

Figure 2.15: *Decay-time resolution as a function of B_s^0 momentum of fake, prompt $B_s^0 \to J/\psi\,\phi$ decays. The data points represent the observed resolution, while the superimposed histogram shows the momentum distribution on an arbitrary vertical scale.*

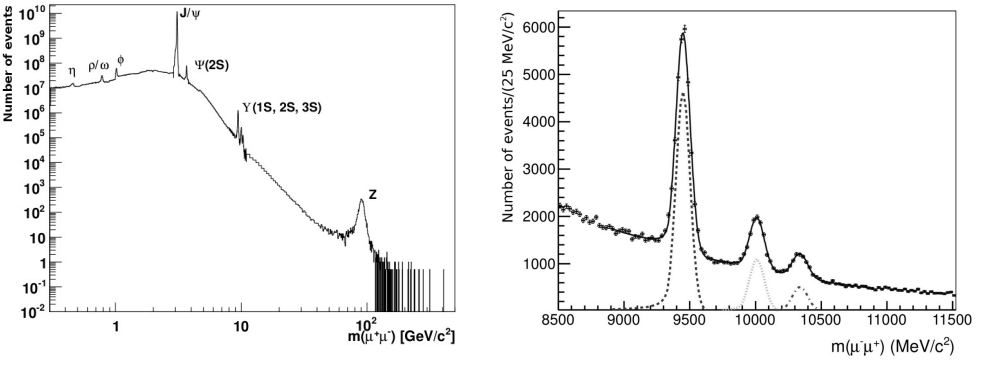

(a) (b)

Figure 2.16: *Di-muon invariant mass spectrum (a) and a zoom-in of the resonances $\Upsilon(1S)$, $\Upsilon(2S)$ and $\Upsilon(3S)$ (b). The dotted lines indicate the signal components of the respective resonances.*

2.7.3 PID Performance

The background-suppression capability of the PID system and the RICH detector in particular, is illustrated in Fig. 2.17, which shows the invariant mass distribution of two charged particles. In Fig. 2.17 (a), there are no PID requirements on the particles and the $\phi(1020)$

resonance is not visible above the background. In Fig. 2.17 (b), the two particles are required to be positively identified as kaons by the RICH detectors. By doing this, the background is strongly suppressed, revealing the $\phi(1020)$ resonance.

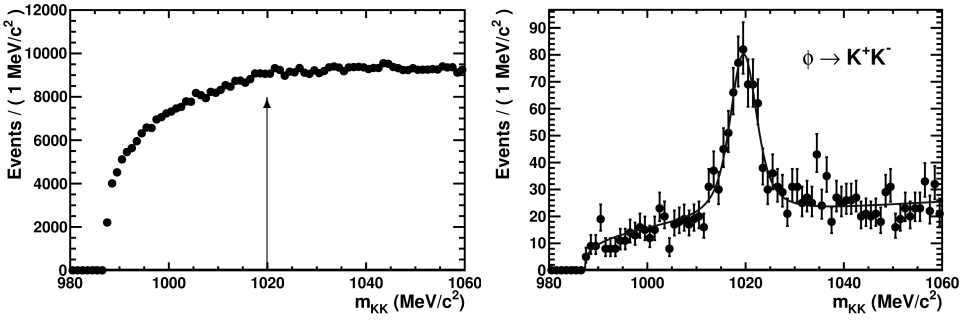

Figure 2.17: *(a) Invariant K^+K^- mass distribution without PID information, only applying kinematic cuts. (b) Invariant K^+K^- mass distribution including PID information. Both tracks are required to have $LL(K) - LL(\pi) \equiv DLL(K\pi) > 15$, where the log-likelihood LL was described in Sec. 2.5.1. The background is strongly suppressed by adding PID information, revealing the $\phi(1020)$ resonance. The data shown has been recorded in 2010, with $\sqrt{s} = 900\,\mathrm{GeV}$.*

2.7.4 Reconstructed $B_s^0 \to J/\psi\,\phi$ Mass

As a preview to Chap. 6, where the $B_s^0 \to J/\psi\,\phi$ analysis will be discussed, the reconstructed B_s^0 mass is shown in Fig. 2.18. In total 21217 $B_s^0 \to J/\psi\,\phi$ events are selected from a dataset of 1.0 fb^{-1} of integrated luminosity. The fitted B_s^0 mass is $5368.23 \pm 0.05\,\mathrm{MeV}/c^2$ with a resolution of $6.28 \pm 0.05\,\mathrm{MeV}/c^2$.

In addition, a $B_s^0 \to J/\psi\,\phi$ candidate in one particular LHCb event is shown in Fig. 2.19. Indicated are its associated primary vertex, the reconstructed secondary vertex and the daughter tracks. The flight distance of this B_s^0 candidate is 19.2 mm, corresponding to a decay time of 3.2 ps.

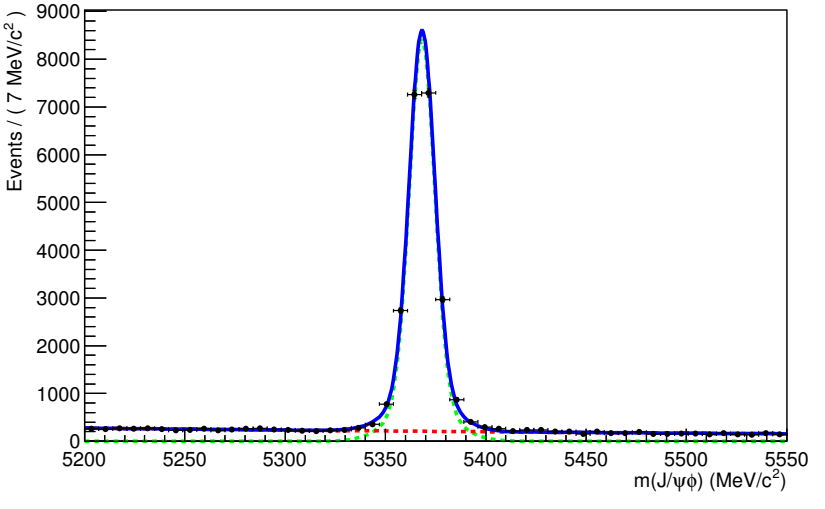

Figure 2.18: *Reconstructed B_s^0 mass distribution fitted with a double Gaussian. The resolution of the second Gaussian is taken as a scale factor times the fitted resolution of the first Gaussian, where the scale factor as well as the fraction between the two Gaussians is obtained from MC. The background component is a single exponential. The signal component is the dashed green line, the background component is the dashed red line and the sum is the solid blue line. In total, 21217 $B_s^0 \to J/\psi\,\phi$ events are selected.*

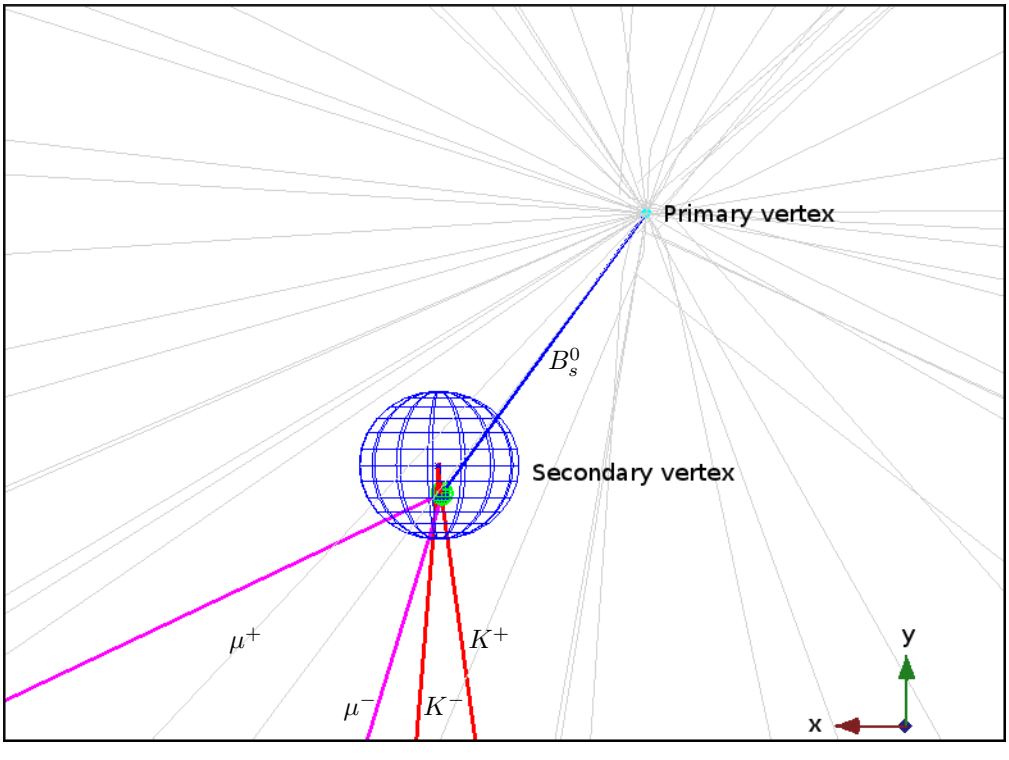

Figure 2.19: *Graphical representation of a $B_s^0 \to J/\psi\,\phi$ candidate in an event recorded on August 17, 2011. The flight distance of the B_s^0 candidate between the primary vertex and the secondary vertex (blue line) is 19.2 mm, corresponding to a decay time of 3.2 ps. The K^+ meson and K^- meson are indicated by red lines and join in the reconstructed ϕ meson vertex, indicated by the blue sphere. The μ^+ and the μ^- are indicated by pink lines and join in the reconstructed J/ψ meson vertex indicated by the green sphere.*

CHAPTER

THREE

3

Operation and Performance of the Outer Tracker

The performance of the Outer Tracker (OT) detector is presented in detail in this chapter. First, the working principle of an OT straw drift cell is reviewed. Subsequently, the design and the geometry of the modules are described, as well as the components of the front-end electronics. Finally, the operational performance of the OT during the 2009, 2010 and 2011 running periods is described.

3.1 Working Principle of the Outer Tracker

The OT is a gaseous straw-tube detector. The cells consist of a cathode straw and an anode wire in the center. The drift cell is filled with a counting gas, and a high voltage (HV) of 1550 V is applied to the anode wire to create a large electric field between anode and cathode.

When a minimum-ionizing particle traverses the cell and the gas therein, the gas is ionized if the energy transfer from the particle to a gas molecule is higher than the ionization potential of the gas. The so-called primary electrons that are produced in this process can be emitted with an energy larger than the ionization potential, liberating additional, secondary, electrons. The primary and secondary electrons form a so-called ionization cluster which drifts to the anode wire under the influence of the electric field.

The number of ionization clusters created depends strongly on the gas mixture. The OT was designed to operate using a gas mixture of 70% Ar and 30% CO_2. However, to prevent ageing effects [30], in January 2010 the gas mixture was changed by adding an oxygen component. The current gas mixture is $Ar/CO_2/O_2$ (70%/28.5%/1.5%), in which under standard conditions (0° C, 101.325 kPa) a minimum ionizing particle produces about 31 clusters per centimeter. The ionization clusters of a minimum ionizing particle (MIP) consist of 3 electron-ion pairs on average [31].

The heavier ions drift slowly to the cathode, while the electrons drift to the anode. The kinetic energy of the electrons increases due to the increase of the electric field E towards

the anode wire:

$$E(r) = \frac{U}{r \ln \frac{R}{r_a}} \quad , \tag{3.1}$$

where U is the potential difference between the anode and cathode, r is the position in the cell, R is the straw radius and r_a is the diameter of the anode wire. At a certain radius to the wire the kinetic energy of the drifting electrons reaches the ionization energy of the gas, producing new electron-ion pairs through collisions with gas molecules. The liberated electrons in turn can generate new pairs. This process results in an avalanche of electrons drifting to the anode wire. The region where this avalanche occurs is called the gas amplification region. The gas gain is defined as the ratio of the electric charge deposited on the anode wire and the primary liberated charge. At the nominal HV value of 1550 V, the gas gain is in the order of 5×10^4. The large number of electrons reaching the anode wire and the slow drift of the ions in the opposite direction induce a measurable electric pulse. A schematic picture of the cross section of an OT cell is shown in Fig. 3.1.

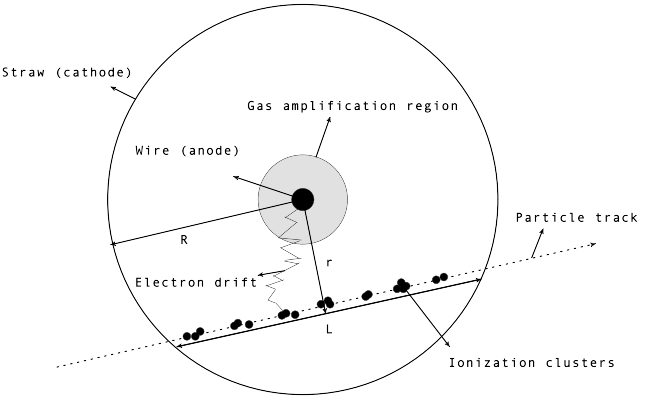

Figure 3.1: *Schematic picture of an OT drift cell. L is the path length of the particle through the straw, R is the straw diameter and r is the distance of closest approach of the track to the anode wire. The ionization clusters consist of primary and secondary electrons liberated in the gas. These clusters drift to the anode wire and create an avalanche in the gas amplification region.*

In order to reconstruct charged particle tracks, the distance of closest approach to the anode wire is determined by measuring the drift time. Therefore, drift time resolution is directly related to the spatial resolution.

3.2 Design of the OT Modules

The layout of the OT and the location of different module types were shown in Fig. 2.10. A cross section of an OT module is shown in Fig. 3.2 (a). An F-module consists of two

monolayers of 64 straw tubes. To limit the hit occupancy, the channels are electrically disconnected around $y = 0$ (the two monolayers are staggered in y to prevent insensitive detector areas). The lower 128 channels are read out at the bottom and the upper 128 channels at the top of the module. One monolayer of straws is glued on a Rohacell [1] panel, and two of these panels are joined with sidewalls to form a stand-alone gas-tight detector module. The module panels and sidewalls are covered with 25 μm Kapton and laminated with 12.5 μm aluminum, to ensure gas tightness and to provide a closed Faraday cage. The anode wire is made of 25 μm gold plated tungsten. The cathode consists of an inner foil of 40 μm electrically conducting carbon-doped Kapton-XC and an outer foil of 25 μm Kapton XC, laminated with 12.5 μm aluminum. A schematic picture of the straw winding is shown in Fig. 3.2 (b).

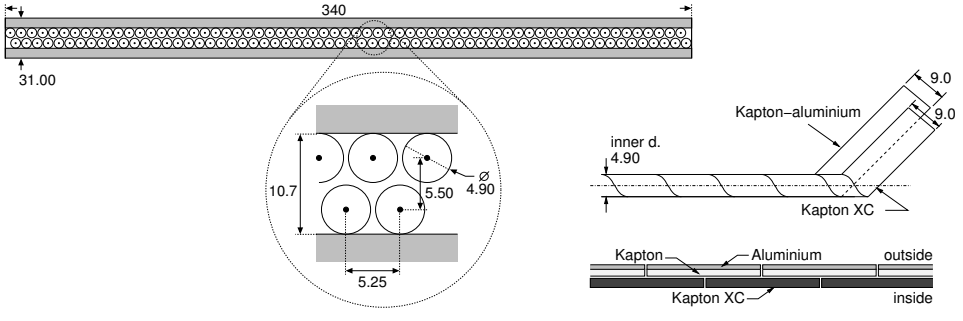

(a) (b)

Figure 3.2: *(a) OT module cross section, dimensions in mm. (b) Straw winding of the drift straw tubes, dimensions in mm. The straws are wound using two foils, Kapton-XC and a laminate of Kapton and aluminum.*

The S1-modules and S2-modules, as described in Sec. 2.4.4, contain 128 channels and are half the length of the F-modules. Finally, the S3-modules contain 64 channels (32 per monolayer) and are half the width of the other module types. Table 3.1 gives a summary of the different types of OT modules. The OT has 53760 readout channels in total.

module type	dimensions (mm^3)	number of channels	quantity
F	$4900 \times 340 \times 31$	256	168
S1	$2375 \times 340 \times 31$	128	48
S2	$2275 \times 340 \times 31$	128	24
S3	$2275 \times 170 \times 31$	64	24

Table 3.1: *Geometry and channel count of the OT modules.*

[1] Rohacell® is a lightweight structural foam, produced by Evonik industries.

3.3 Front-End Electronics

The distance of closest approach to the anode wire is determined by detecting the pulse induced by the first cluster at the anode wire. The time of arrival of this pulse with respect to the LHC bunch-crossing clock is determined by the front-end (FE) electronics.

The FE electronics read out the hit signals from the straw tubes, determine their timing with respect to the LHC bunch clock and, if a positive L0 decision is received, ship them to the off-detector readout electronics. These functionalities are implemented in various service boards that are all housed in so-called FE boxes. One FE box contains 4 HV boards, 8 ASDBLR pre-amplifier boards, 4 OTIS TDC boards and 1 GOL/AUX board.

FE box

Front-end boxes are mounted on the top and/or bottom of the modules and are covered by an aluminum chassis which serves as shielding and grounding for the straws. An FE box services 128 straw tubes, with the exception of FE boxes for S3-modules, which serve 64 channels. A photograph of the inside of an FE box and all its electronic components is shown in Fig. 3.3.

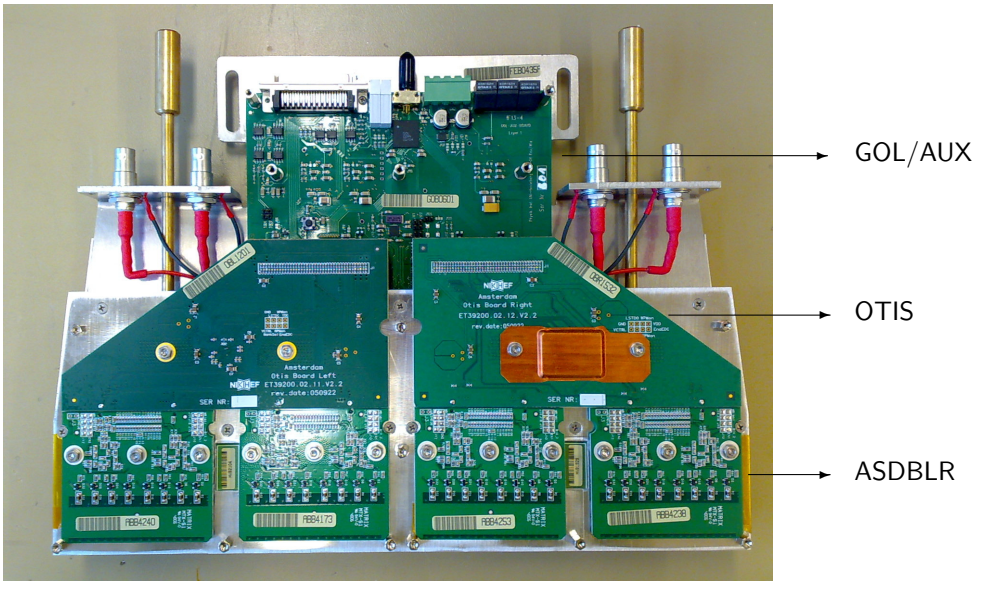

Figure 3.3: *Picture of an Outer Tracker FE box without aluminum cover showing the electronics components. From top to bottom: GOL/AUX board, two OTIS boards and 4 ASDBLR boards. Two more OTIS and four more ASDBLR boards are located on the backside of the FE box. The 4 HV boards are not visible, since they are installed on the inside of the aluminum chassis beneath the ASDBLR boards.*

HV Board

The HV board serves to supply positive high voltage to the anode wires. Another function of the HV board is to decouple the HV supply from the pre-amplifier chip (ASDBLR, discussed in the next section), through 330 pF insulation capacitors. A schematic picture of the electronic straw tube connections is shown in Fig. 3.4.

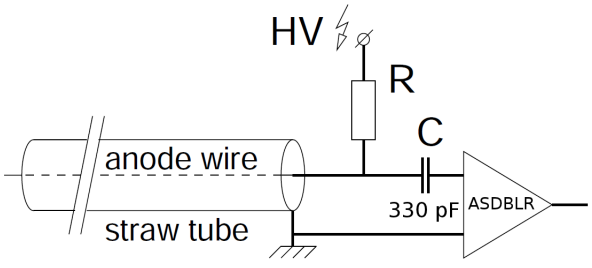

Figure 3.4: *Schematic picture of the electronic straw tube connections. High voltage is supplied to the anode wires and the cathode straw tubes are grounded. The pre-amplifier ASDBLR chip is separated from the HV by insulation capacitors of 330 pF.*

Amplifier and Discriminator: ASDBLR chip

The Amplifier-Shaper-Discriminator with BaseLine Restoration (ASDBLR) board contains two ASDBLR chips that amplify and shape the signals from the anode wires to eliminate their slow ion tails. Subsequently these signals are discriminated against a threshold value. The shaping time of the ASDBLR chip is fast: its peaking time is roughly 7 ns [32], which, compared to the maximal drift time of 35 ns (see Sec. 3.4.2), has potential performance consequences such as double pulses, as explained in Sec. 3.4.4.

Time-to-Digital Converter: OTIS chip

The hit signals from two ASDBLR boards are sent to one OTIS (Outer Tracker Time Information System, [33]) time-to-digital (TDC) chip which operates synchronously to the LHC bunch crossing clock to digitize the 'time-over-threshold' of the hit with respect to the bunch crossing (collision) time. The time is encoded in 6 bits, resulting in a granularity of about 0.4 ns.

In addition, the OTIS chip provides the threshold voltages for the ASDBLR chips. These are the electronic amplifier thresholds that are varied when performing a so-called OT threshold layer scan to monitor possible gain loss, as explained in Chap. 4,

Finally, the OTIS chip provides intermediate data storage in its 4 μs pipeline buffer. On a positive L0 decision, the chip transfers the corresponding event data to the GOL serializer chip on the GOL/AUX board.

Gigabit Optical Link: GOL/AUX board

Each FE box contains one GOL/AUX board. It contains a Gigabit Optical Link (GOL) chip which receives the output of four OTIS chips. Optical fibers transport the data to the off-detector counting house at an output rate of 1.3 Gbit/s. The GOL/AUX board also provides the bias voltage to the OTIS and ASDBLR chips through radiation-hard voltage regulators and distributes the slow and fast control signals.

3

3.4 Drift Time, Dead Time and Spillover

3.4.1 Drift Time

The front-end electronics measure the timing of hits with respect to the LHC bunch crossing clock. The raw detection time t_{TDC} is the sum of various contributions:

$$t_{\mathrm{TDC}} = t_{\mathrm{tof}} + t_{\mathrm{drift}} + t_{\mathrm{prop}} + t_0 \quad , \tag{3.2}$$

where t_{tof} is the time-of-flight of the particle from the collision point to the drift cell, t_{drift} is the drift time in the cell, which is used in the track reconstruction, t_{prop} is the signal propagation time through the anode wire and t_0 is an offset, specific to each FE box.

3.4.2 Readout Window

The maximum drift time in a cell is about 35 ns. Adding the maximum propagation time of 10 ns, the spread in time-of-flight and the t_0 fluctuations between individual FE boxes, the maximal detection time exceeds 50 ns. Given that the LHC provides colliding bunches every 25 ns, the readout window of the OT is taken to be three bunch crossings wide to accommodate the latest arriving signals.

The readout window, or gate, starts at different times t_{gate} for the three OT stations to correct for average time-of-flight differences. By doing so, the rising edge in the raw drift spectrum, or TDC spectrum, will occur around the same TDC value for all stations. This leads to the following expression for the detection time inside the active gate:

$$t_{\mathrm{TDC,T}} = t_{\mathrm{tof}} + t_{\mathrm{drift}} + t_{\mathrm{prop}} + t_0 - t_{\mathrm{gate,T}} \quad , \tag{3.3}$$

where T stands for station number and $t_{\mathrm{gate,T1}} = 20.8\,\mathrm{ns}, t_{\mathrm{gate,T2}} = 22.8\,\mathrm{ns}, t_{\mathrm{gate,T3}} = 24.8\,\mathrm{ns}$.

In 2010 and the beginning of 2011 LHC delivered colliding bunches every 75 ns. Typical TDC spectra for this bunch configuration are shown in Fig. 3.5, where one TDC unit equals 0.4 ns. For this particular run, t_{gate} was set equal for the three OT stations, which appears as a shift in the TDC spectra due to time-of-flight differences between T1, T2 and T3. The small peak in bin 0, 63 and 127 of the TDC spectra is always observed, due to a characteristic of the OTIS chip [34].

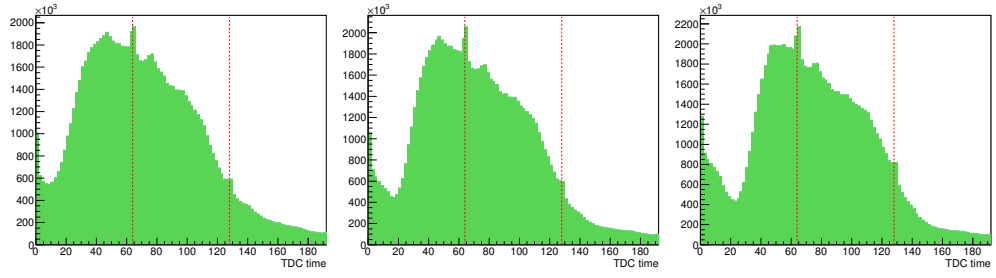

(a) (b) (c)

Figure 3.5: *TDC spectrum for station T1 (a), T2 (b) and T3 (c), for run 87880, recorded on March 22 2011, with 75 ns bunch spacing. 1 TDC unit corresponds to 0.4 ns. Due to equal t_{gate} for the three stations in this run, the TDC spectra are shifted for T2 and T3 with respect to T1 due to time-of-flight differences.*

3.4.3 Dead Time

After the detection of a hit, for a certain amount of time (called the dead time), no second hit can be detected. Firstly, the shaping of analog signals in the ASDBLR chips leads to a typical analog dead time of roughly 7 ns (as mentioned already in Sec. 3.3). Secondly, an effective dead time is introduced by the OTIS chip readout. In the single-hit readout mode, only the first hit in the readout window is recorded, which leads to an effective dead-time as high as 75 ns for early hits. In multiple-hit mode, one hit per 25 ns can be recorded. Single-hit mode is the default readout mode of the OTIS chips in the OT.

3.4.4 Double Pulse

Due to the operation of the OTIS chips in single hit mode, only the first hit in the readout window is recorded. In reality, one traversing particle can give rise to more than one electric pulse. These so-called double pulses can be induced by reflections of the signal in the anode wire [35] or by arrival of late ionization clusters (i.e. later than the analogue dead time of the amplifier chip) of the same traversing particle [32, 36]. Finally, another source of double pulses is so-called photon feedback [37]. This effect is induced by photons that are created in the avalanche region. When these photons hit the cathode, they release electrons that in turn will start drifting to the anode wire.

The combined effect of the short analog ASDBLR dead time and the single-hit mode OTIS readout, causes double pulses from the previous readout window to contribute to the TDC spectrum of the current readout window. This explains why the shoulder at the left side of the TDC spectra in Fig. 3.5 is higher than the tail on the far right side. In the MC simulation, the double pulse probability is assumed to be 30%, while recent studies on data reveal that this number might be as high as 40% [38].

3.4.5 Spillover

The LHC is designed to collide bunches every 25 ns. Since the readout window of the OT is three bunch crossings wide to accommodate late signals, events from the previous and subsequent bunch crossings will contribute to the TDC spectra of the bunch crossing under consideration. These so-called spillover hits will appear in the TDC spectrum in the case of hits corresponding to long drift times in the previous bunch crossing or short drift times in the subsequent bunch crossing.

In 2011, the 75 ns LHC bunch spacing was reduced to 50 ns. The corresponding TDC spectrum is shown in Fig. 3.6 (a). At the time of this run, the t_{gate} values for the three OT stations were corrected for time-of-flight differences. The hits with $t_{\mathrm{TDC}} \gtrsim 128$, or 50 ns, mainly originate from a collision in the next bunch crossing.

Finally, at the end of 2011 a test run was performed with 25 ns bunch spacing. The TDC spectrum is shown in Fig. 3.6 (b). Three major contributions can be distinguished: one from the current bunch crossing (1<TDC<64), one from the next bunch crossing (65<TDC<128) and finally the so-called next-to-next bunch crossing (129<TDC<192).

Note that the contributions of the different spills are not equal. This is due to the fact that the current bunch crossing caused a positive L0 trigger decision, leading to more contributing hits to the drift time spectrum, compared to the spillover bunch crossings.

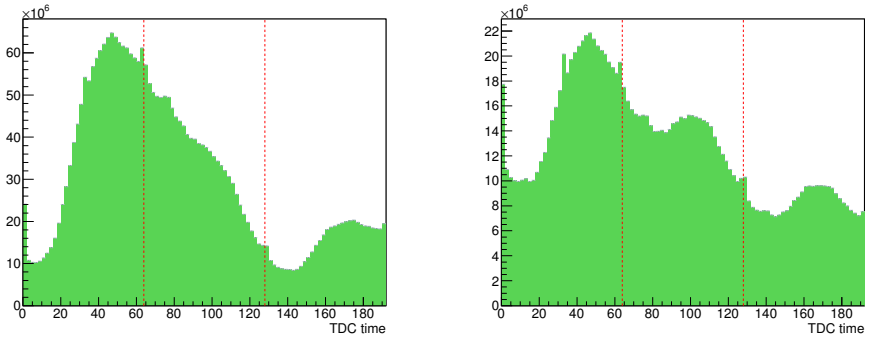

Figure 3.6: *(a) TDC spectrum for run 96759, recorded on July 22 2011, with 50 ns bunch spacing. 1 TDC unit corresponds to 0.4 ns. Notice the contribution from the next bunch crossing in the tail of the spectrum. This TDC spectrum is integrated over the entire OT. (b) TDC spectrum for run 103053, recorded on October 7 2011, with 25 ns bunch spacing. Notice the contributions from the next bunch crossing and the next-to-next bunch crossing.*

3.5 rt-Relation and Outer Tracker Resolution

The unbiased distance of closest approach (DOCA) of a traversing particle is the predicted track distance to the wire, where the hit under consideration is not used in the track recon-

struction. The drift time t_{drift} is calculated from the measured TDC time t_{TDC} according to Eq. 3.3 as $t_{\mathrm{drift}} = t_{\mathrm{TDC}} - t_{\mathrm{tof}} - t_{\mathrm{prop}} - t_0 + t_{\mathrm{gate,T}}$. The relation between drift time and distance, called the rt-relation, is given by a fit of a quadratic function to the distribution of measured drift time versus the unbiased DOCA.

A set of good-quality reference tracks is defined as long tracks (tracks that are reconstructed in both the VELO and the tracking system), with momentum $p > 10\,\mathrm{GeV}$ and $\chi^2/\mathrm{nDOF} < 2$. The rt-relation for a set of reference tracks is shown in Fig. 3.7 (a).

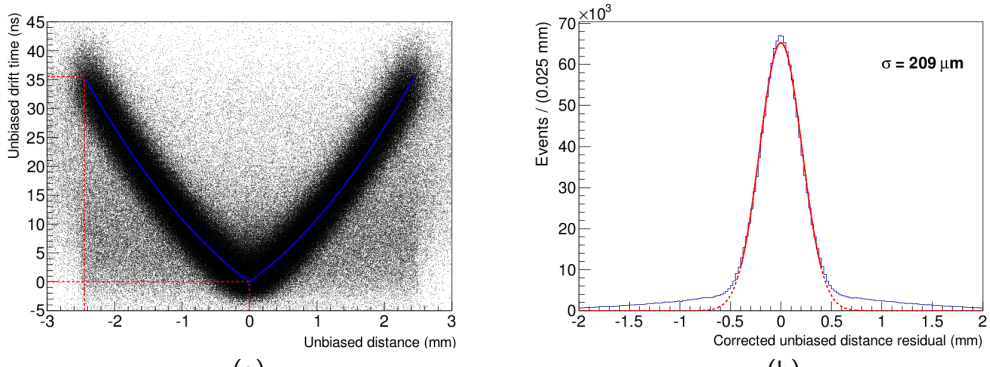

(a) (b)

Figure 3.7: *(a) Unbiased drift time versus unbiased track distance of good quality tracks. The rt-relation is fitted as a quadratic function. (b) Unbiased distance residuals for the reference tracks as explained in the text. A Gaussian fit in the range [-0.4 mm, 0.4 mm] yields a single hit resolution of $209\,\mu\mathrm{m}$. Data for both pictures is taken from LHCb run 89350.*

The track reconstruction uses the rt-relation to minimize the unbiased residuals defined as $r_{\mathrm{DOCA}} - r(t_{\mathrm{drift}})$. Here, r_{DOCA} is the DOCA of the track and $r(t_{\mathrm{drift}})$ is the drift distance as calculated from the rt-calibration curve using the measured drift time. A Gaussian fit to the distribution of the unbiased residuals is shown in Fig. 3.7 (b) for the reference tracks. The fitted width of 209 μm is the OT single hit resolution, close to the OT design value of 200 μm [39].

3.6 Occupancy and Track Distribution

3.6.1 Occupancy

The occupancy of a detector is defined as the number of observed hits divided by the total number of channels in the detector. The occupancy fluctuates from event to event and depends strongly on the average number of visible pp interactions per bunch crossing, μ. When operating the experiment at higher values of μ, more particles will traverse the detector per bunch crossing causing the occupancy to increase. The OT occupancy distribution for events passing the HLT2 trigger (therefore B meson-enriched), recorded in a typical run in

2011, with $\mu = 1.29$, a 50 ns bunch spacing and $L = 3.1 \cdot 10^{32}\,\mathrm{cm}^{-2}\mathrm{s}^{-1}$, is shown in Fig. 3.8.

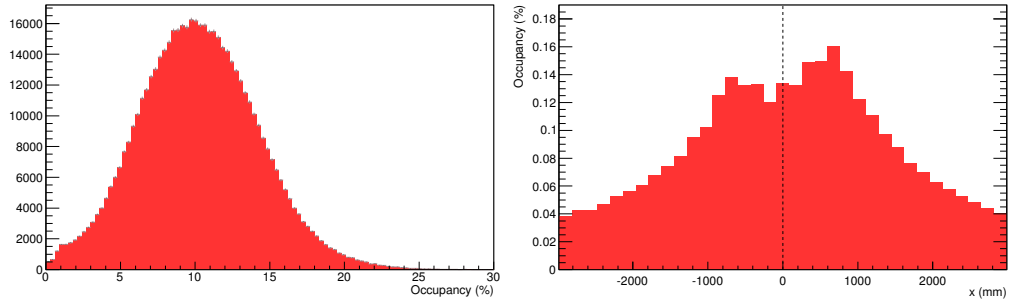

(a) (b)

Figure 3.8: *(a) Occupancy histogram for run 96759 recorded on July 22 2011, with 50 ns bunch spacing and $L = 3.1 \cdot 10^{32}\,\mathrm{cm}^{-2}\mathrm{s}^{-1}$. The average μ for this particular run is 1.29. (b) Occupancy as a function of LHCb-coordinate x for the same run.*

3.6.2 Track Distribution

To determine the track distribution in the transverse plane, a set of reference tracks is defined as long tracks with $\chi^2/\mathrm{nDOF} < 2$ and at least 15 hits in the OT. In addition, these tracks are required to pass close to the wire: $\mathrm{DOCA} < 1.25\,\mathrm{mm}$, to ensure that the OT hits are on the hit efficiency plateau (see Sec. 3.8.1). The track distribution for these reference tracks is shown in Fig. 3.9. One entry in this figure corresponds to the x and y position of one track, extrapolated to the OT layer most distant from the interaction point. The bin size is 85 mm in x, corresponding to one quarter of an OT module and 56 mm in y.

When normalizing the number of entries to the number of events, the track density is calculated as roughly $1 \cdot 10^{-3}$ tracks per cm per straw per event in the hottest area around the beampipe [2].

3.7 Noise and Crosstalk

3.7.1 Noise

Noise in the readout electronics gives rise to random signals that increase the number of unphysical reconstructed tracks (also called ghost tracks). Noise in the readout electronics is estimated by recording hits in the absence of input charge. A channel is considered noisy if it exceeds 10% occupancy at the nominal amplifier threshold of 800 mV, which corresponds to a noise rate of approximately 4 MHz. About 0.5 % of the OT channels were noisy in 2011.

[2] This number has been corrected with a factor 5.25 mm/2.5 mm, to compensate for the narrow DOCA requirement of ± 1.25 mm compared to the cell pitch of 5.25 mm.

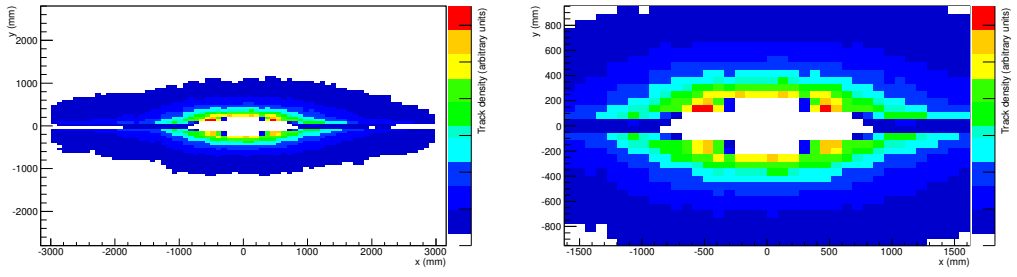

Figure 3.9: *(a) Track distribution in the OT layer that is most distant from the interaction point for a set of reference tracks as defined in the text. Data is taken from run 96759, recorded on July 22 2011, with a 50 ns bunch spacing and an average μ of 1.29. (b) Zoom of the central region.*

Studies revealed that these noisy channels always appeared in groups in similar channel numbers within an FE box. The cause for these groups of noisy channels were traced to improper grounding of the insertion pins that connect the FE boxes to the OT modules. All the noisy FE boxes were repaired during the 2011-2012 winter shutdown.

3.7.2 Crosstalk

Two types of crosstalk are distinguished: crosstalk inside OT modules, for example the electric pick-up of signals in neighboring straws and crosstalk in the electronic components, such as pick-up from neighboring channels on the ASDBLR board. First data recorded in 2009 revealed that crosstalk levels were as low as 0.5% in neighboring cells. The occurrence of cross talk has been implemented accordingly in the MC simulations.

3.8 Efficiency

3.8.1 Single Cell Efficiency

The primary ionizations in a straw tube follow Poisson statistics. Therefore, if n_p is the average number of primary ionizations, the probability for k actual ionizations in one event is

$$P(k) = \frac{n_p^k}{k!} e^{-n_p} \quad . \tag{3.4}$$

The average number of primary ionizations is given by $n_p = \rho l$. Here l is the actual path length of the particle through the straw and ρ is the average number of primary ionizations per unit length. In the OT gas mixture, on average 31 ionization clusters per cm are expected: $\rho = 3.1/\mathrm{mm}$, see Sec. 3.1. The corresponding single drift cell efficiency $\epsilon(l)$ is defined as the probability of having at least one ionization cluster: $\epsilon(l) = 1 - P(0) = 1 - e^{-\rho l}$.

When fitting the single drift cell efficiency to the data, an inefficiency factor $\epsilon_{\text{plateau}}$ is introduced to take into account detector gain loss or dead channels and ρ is changed to an effective number of primary ionization per unit length ρ_{eff}, since electrons might be lost during their drift due to attachment [40]. Rewriting the path length l through the wire as $l = 2\sqrt{R^2 - x^2}$, with x the shortest distance to the wire and R the straw radius, the expression for the average single cell efficiency becomes

$$\epsilon(x) = \epsilon_{\text{plateau}} \left(1 - \exp(-2\,\rho_{\text{eff}}\,\sqrt{R^2 - x^2})\right) \quad . \tag{3.5}$$

At the straw edges, where x is close to R, the efficiency drops, because the path length through the cell becomes shorter, hence reducing the probability of having at least one primary ionization.

The single cell efficiency profile is obtained from data by studying the hit efficiency for reconstructed tracks. For a given track, the straw closest to the predicted track position in a monolayer, and its neighboring straws, are inspected. The binary hit information (hit found $= 1$, hit not found $= 0$) for all tracks is summed and averaged as a function of unbiased track position in each cell, where the unbiased track position is the extrapolated track position without using the hit under consideration in the track reconstruction. An example of the average cell efficiency profile is shown in Fig. 3.10, which shows a comparison between 2009 data and MC simulated data.

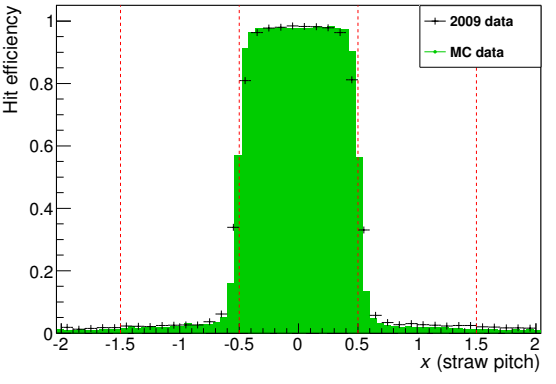

Figure 3.10: *Comparison between data recorded in 2009 and Monte Carlo simulated data of the hit efficiency versus x in units of straw pitch. The data shown is for every module in the OT that is located at the fourth position as counted from the beam pipe. Crosstalk levels were set to 0.5% on both sides in the MC simulation, for a good agreement with the data. The drop in hit efficiency around $|x| \approx 0.5$ is broadened due to finite track resolution.*

The cell efficiency profile in Fig. 3.10 is parameterized as

$$f(x) = 1 - [1 - (\epsilon * G)(x)]\,(1 - \omega) \quad , \tag{3.6}$$

where $\epsilon(x)$ is the predicted cell efficiency from Eq. 3.5, convoluted with a Gaussian $G(x|0,\sigma)$, representing the track reconstruction resolution and ω the occupancy. Fitting this curve to the hit efficiency profile using a representative data sample in 2011 yields an average $\rho_{\text{eff}} = 1.3/\text{mm}$ and $\epsilon_{\text{plateau}}$ in the range of 98.6% - 99.4%. Notice that, when assuming an optimally working detector ($\epsilon_{\text{plateau}} = 1$) and $\rho_{\text{eff}} = 1.3/\text{mm}$, there is an average efficiency of 99.7% in the range $|x| < 1.25\,\text{mm}$ from the wire, i.e. a 0.3% inefficiency due to Poisson statistics alone. This corresponds to the intrinsic efficiency limit on the plateau region.

3.8.2 Gain Loss Monitoring using Hit Efficiency

The concept of hit efficiency is used to monitor possible gain loss in the Outer Tracker. In this case the hit efficiency is only considered in the plateau region defined as $|x| < 1.25\,\text{mm}$. The hit efficiency plateau height is studied as a function of amplifier threshold of the front-end electronics. This procedure is discussed in detail in the next chapter.

CHAPTER

FOUR

Radiation Hardness of the Outer Tracker

4

In laboratory tests, Outer Tracker modules have shown to suffer from ageing effects that cause gain losses. These ageing effects are due to outgassing of the glue used to construct the modules [30] and occur at moderate radiation intensities, i.e. moderate collected charge per unit time.

Before the LHC startup in 2009 the installed OT modules were subjected to several treatments in order to prevent or reduce ageing effects:

- Heating of the installed modules using heating blankets, to speed up glue outgassing [41].
- Continuous flushing of the modules with the counting gas, to transport away the vapours originating from outgassing of the glue [30].
- Addition of O_2 to the counting gas, to increase the concentration of chemically reactive radicals, such as atomic oxygen and ozone [42].

The effects of these treatments are tested by deliberately irradiating and scanning modules using a dedicated scanning setup which is installed in front of the modules. The results of these tests are summarized in Appendix A.

Two methods have been devised to monitor gain stability in the OT: firstly, the module response is measured with radioactive sources using the same scanning setup as mentioned before. These scans are recorded manually in the LHCb experimental hall and can therefore only be performed when the LHC is not operational. The second method uses charged particle tracks produced by LHC collisions to study hit efficiency as a function of amplifier threshold. These so-called threshold scans are performed while the LHC is operational, producing collisions with tracks in the LHCb detector.

A paper with the results of the OT gain stability monitoring after the LHC startup has been published in Nuclear Instruments and Methods in Physics Research A and is reproduced on the following pages.

Nuclear Instruments and Methods in Physics Research A 685 (2012) 62–69

Contents lists available at SciVerse ScienceDirect

Nuclear Instruments and Methods in Physics Research A

journal homepage: www.elsevier.com/locate/nima

Radiation hardness of the LHCb Outer Tracker

D. van Eijk [a,*], S. Bachmann [b], Th. Bauer [a], Ch. Färber [b], A. Bien [b], V. Coco [a], M. Deckenhoff [d], F. Dettori [a], R. Ekelhof [d], E. Gersabeck [b], T.M. Karbach [d], R. Koopman [a], A. Kozlinskiy [a], Ch. Langenbruch [b], Ch. Linn [b], M. Merk [a], M. Meissner [b], P. Morawski [e], A. Pellegrino [a], N. Serra [f], P. Seyfert [b], B. Spaan [d], S. Swientek [d], B. Storaci [a], M. Szczekowski [c], N. Tuning [a], U. Uwer [b], E. Visser [a], D. Wiedner [b], M. Witek [e]

[a] Nikhef, Amsterdam, The Netherlands
[b] Physikalisches Institut, Heidelberg, Germany
[c] A. Soltan Institute for Nuclear Studies, Warsaw, Poland
[d] Technische Universität Dortmund, Germany
[e] H. Niewodniczanski Institute of Nuclear Physics, Cracow, Poland
[f] Physik-Institut, Universität Zürich, Switzerland

4

ARTICLE INFO

Article history:
Received 9 March 2012
Received in revised form
3 May 2012
Accepted 3 May 2012
Available online 22 May 2012

Keywords:
Gas detectors
Ageing
Gain loss
Hit efficiency

ABSTRACT

This paper presents results on the radiation hardness of the LHCb Outer Tracker (OT) during LHC operation in 2010 and 2011. Modules of the OT have shown to suffer from ageing effects that lead to gain loss, after irradiation in the laboratory. Under irradiation at moderate intensities an insulating layer is formed on the anode wire of the OT straw cells. This ageing effect is caused by contamination of the counting gas due to outgassing of the glue used in the construction of the OT modules. Two methods to monitor gain stability in the OT are presented: module scans with radioactive sources and the study of hit efficiency as a function of amplifier threshold. No gain loss is observed after receiving 1.3 fb^{-1} of integrated luminosity corresponding to an integrated charge of 0.055 C/cm in the hottest spot of the detector.

1. The LHCb Outer Tracker

The LHCb experiment is a single arm spectrometer, located at the LHC, designed to measure CP violation and rare B-decays. The tracking system consists of silicon strip detectors and straw-tube detectors around a large dipole magnet. The large area behind the magnet is covered by the Outer Tracker (OT) detector, as indicated in Fig. 1. The OT is a gaseous straw-tube detector [1] consisting of 53 760 straw tubes and covering an area of approximately $5 \times 6\ m^2$ with 12 detection layers. Every detection layer consists of a double layer of straw tubes as indicated in Fig. 2(a).

The straw tubes are 2.4 m long and 4.9 mm in diameter, and are filled with the gas mixture $Ar/CO_2/O_2$ (70%/28.5%/1.5%) at an exchange rate of about 0.2 volumes per hour. The O_2 component is added to the gas mixture for its beneficial effect on the ageing rate [2]. A high voltage of 1550 V is applied to the anode wire, corresponding to a gain of about 5×10^4 [3]. The anode is made of gold-plated tungsten wire of 25 μm diameter, whereas the cathode consists of an inner foil of electrically conducting carbon doped Kapton-XC[1] and an outer foil consisting of Kapton-XC laminated with a layer of aluminium. The straws are glued to panels and sealed with sidewalls, resulting in a gas-tight box enclosing a stand-alone detector module. A sketch of the module layout is shown in Fig. 2.

2. Ageing of OT modules

2.1. Laboratory tests

Laboratory tests with radioactive sources revealed that, despite extensive ageing tests in the R&D phase, the OT modules suffer from gain loss after moderate irradiation (i.e. moderate collected charge per unit time), corresponding to approximately 2 nA/cm. Gain losses of 5–25% were observed after 20 h of irradiation. The origin of the gain loss was traced to an insulating layer containing carbon on the anode wire [2], which is caused by glue outgassing components inside the gas volume [4].

The characteristic feature of this ageing phenomenon is a small area of gain loss upstream the radioactive source position. No gain loss is observed downstream the source, presumably due to the formation of ozone in the high intensity region [2]. The contaminated wires have shown to recover the gain after applying a large high voltage of about 1900 V to the anode wire, inducing large

* Corresponding author. Tel.: +31 205922147.
E-mail address: dveijk@nikhef.nl (D. van Eijk).
[1] Kapton® is a polyimide film developed by DuPont.

0168-9002/$ - see front matter © 2012 Elsevier B.V. All rights reserved.
http://dx.doi.org/10.1016/j.nima.2012.05.033

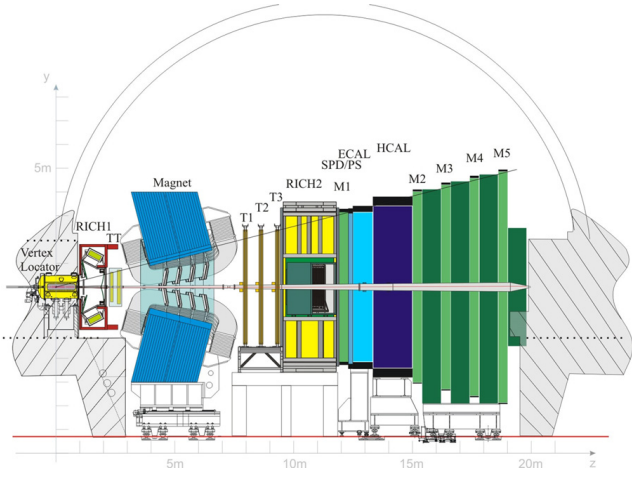

Fig. 1. Schematic picture of the LHCb experiment and all its subdetectors. The interaction point is located in the Vertex Locator on the left. The OT consist of three tracking stations indicated by T1, T2 and T3 and covers the region behind the magnet.

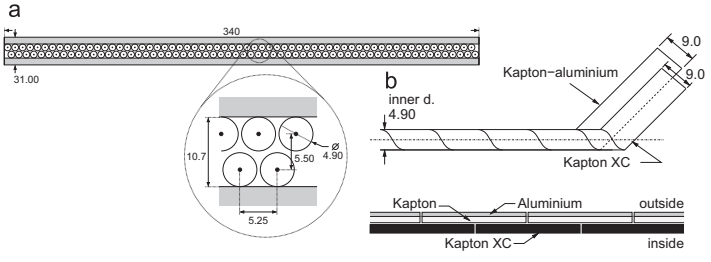

Fig. 2. (a) Cross-section of an OT module containing 2 × 64 straw cells. (b) The straws are wound using two foils, Kapton-XC and a laminate of Kapton and aluminium. All dimensions are given in mm.

dark currents, or by applying a large high voltage of 1860 V while irradiating with a radioactive source [4].

2.2. Conditions during LHC operation

During most of the 2011 running period, LHCb was operating at an instantaneous luminosity of 3.5×10^{32} cm^{-2} s^{-1}, which corresponds to a current of 700 nA in the straws located closest to the beam line. The central region of the detector is subject to the largest intensity, corresponding to 14 nA/cm. The LHC delivered a total integrated luminosity of 1.3 fb^{-1} to LHCb in 2011, which translates in a total accumulated dose at the hottest spot of the OT of 0.055 C/cm.

Two methods to monitor gain stability in the OT will be discussed: scans of the module response with radioactive sources and the study of hit efficiency as a function of amplifier threshold.

3. Scans with radioactive sources

3.1. Setup

The responses of OT modules to radioactive sources before and after LHC operation are performed manually in the LHCb cavern and hence only when the LHC is not in operation. A picture of the setup is shown in Fig. 3(a). It consists of a frame installed in front of the OT modules accommodating a source holder and a step motor used to move the source holder vertically along the modules. The detector response is determined using two 74 MBq ^{90}Sr sources by measuring the induced current through the wires with a stand-alone current meter. The radiation damage in terms of gain loss is quantified by comparing the 2-dimensional current profiles before and after irradiation by LHC operation. The ratio of the currents is expected to be close to unity if no insulating layer is formed on the anode wire.

3.2. Results

The lower half of nine modules, corresponding to a quarter of a detector layer (see Fig. 3(b)) were scanned before and after LHC operation in 2011. The current variation in one wire as a function of the source position is shown in Fig. 4(a). The ratio of currents for all 64 wires in one monolayer and for all positions is shown in Fig. 4(b). The variations in the relative detector response of $\pm 10\%$ over the width of the module are attributed to small changes in the source profile between the two scans.

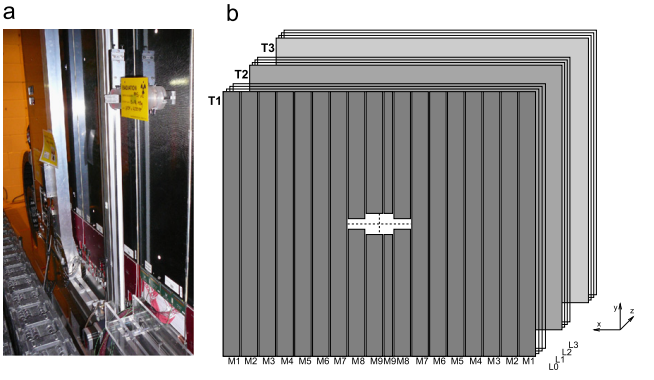

Fig. 3. (a) Picture of the scanning setup. The OT modules are visible, as well as the two ^{90}Sr sources in the source holder, which is mounted on the scanning frame. The front-end electronics at the bottom of the scanned module are replaced by a stand-alone current meter. (b) Schematic picture of the arrangement of the modules in the LHCb detector.

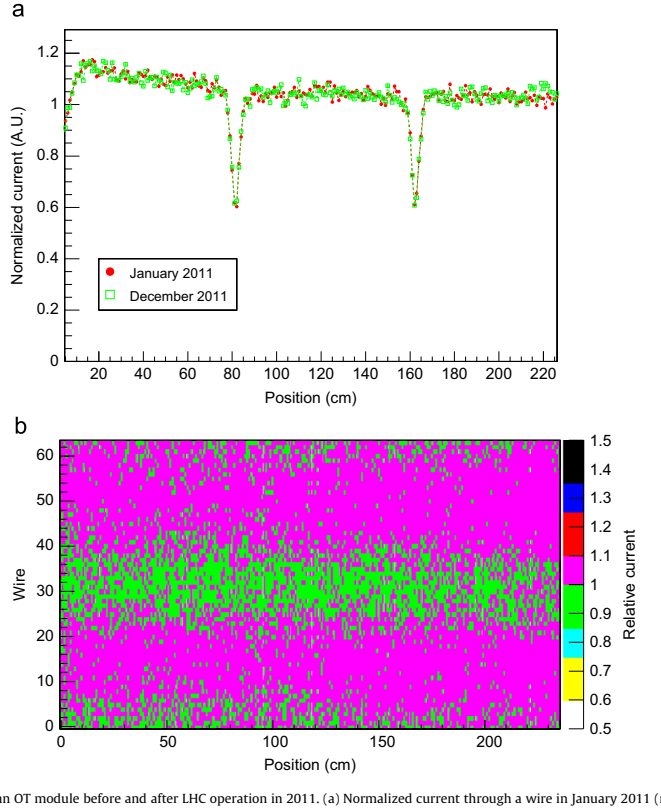

Fig. 4. Gain stability scans of an OT module before and after LHC operation in 2011. (a) Normalized current through a wire in January 2011 (red circles) and in December 2011 (open green squares). The current drop at positions 80 cm and 160 cm is due to wire locators inside the straw. (b) Relative detector response between January 2011 and December 2011 as a function of wire and position on the module. (For interpretation of the references to color in this figure caption, the reader is referred to the web version of this article.)

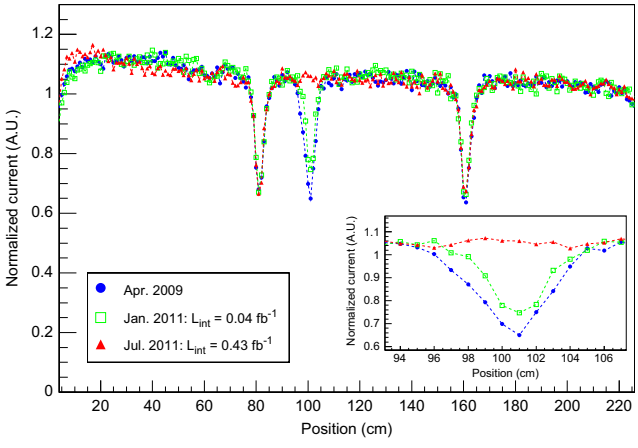

Fig. 5. Normalized current as a function of position along a wire in April 2009 (blue circles), January 2011 (open green squares) and July 2011 (red triangles). The current loss around position 100 cm in April 2009 is caused by a deliberate irradiation (inset: zoom of irradiated area). This loss is partly recovered in January 2011 due to LHC operation in 2010 and fully recovered in July 2011 after an additional six months of LHC operation. The current drop at positions 80 cm and 160 cm is due to wire locators in the module.

The average change in detector response between January 2011 and December 2011 amounts to −3%, after correcting for changes in the atmospheric pressure. This is mainly attributed to the natural decay of ^{90}Sr, which results in a lower detector current of about 3% after 1 year.

3.3. Curing

Before LHC operation, in February 2009, the radiation hardness of the OT modules was studied by irradiating a module with a single 74 MBq ^{90}Sr source during 84 h. The source was collimated with a hole of 6 mm diameter, resulting in an irradiated area of about 4×4 cm^2, with a maximum dose of 0.015 C/cm. A maximum gain loss of 38 % was observed. The module was scanned again in January 2011 and July 2011 after LHC operation which corresponds to a delivered integrated luminosity of 0.042 fb^{-1} and 0.434 fb^{-1}, respectively.

The irradiated area is located 1.2 m below the beam axis where the intensity induced by the LHC is approximately 0.15 nA/cm. The corresponding total accumulated dose from the LHC in the irradiated area amounts to about 0.2 mC/cm. The irradiated area shows a partial recovery of about 10% in January 2011 and a complete recovery of the gain in July 2011. The current in one wire of this module is shown in Fig. 5. The observed effect is similar to the curing effect after applying high voltage [4]. It is unclear whether the underlying microscopic mechanism is related to plasma sputtering of the wire surface or to chemical reactions with radicals such as ozone. An attempt was made to reproduce this curing effect in January 2012, but no gain loss could be provoked after 350 h of irradiation with a single 74 MBq ^{90}Sr source.

4. Amplifier threshold scan

The scans with radioactive sources can only be performed when the LHC is not operational, and only a small selection of modules can be studied. Therefore, a method to monitor gain stability in the entire OT and during LHC operation was devised. The readout electronics of the OT is designed to accurately determine the time of the hit, but not the charge of the hit. However, by studying the hit efficiency as a function of amplifier threshold during LHC operation, gain variations can be monitored.

4.1. Method

The nominal amplifier threshold is 800 mV, corresponding to a charge collection of approximately 4 fC. The amplifier threshold for a given detection layer is increased in steps from the nominal value of 800 mV to 1450 mV for one OT layer, while all other layers are operated at nominal threshold, in order to properly reconstruct charged particle tracks. This procedure is repeated for all 12 layers.

The hit efficiency is determined using tracks with at least 20 hits in the layers operated at nominal threshold. The hit efficiency is defined as the number of found hits, divided by the total number of predicted hits, for tracks passing within 1.25 mm from the wire. The hit efficiency is measured in 85 mm wide bins of the horizontal coordinate x and 56 mm high bins of the vertical coordinate y. The bin size in x corresponds to one quarter of the width of an OT module.

The hit efficiency as a function of amplifier threshold is shown in Fig. 6. This characteristic S-curve can be parameterized using the error function erf(x) as

$$\epsilon_{\mathrm{hit}}(V_{\mathrm{thr}}) = \frac{1}{2}(P+T) - \frac{1}{2}(P-T)\,\mathrm{erf}\left(\frac{V_{\mathrm{thr}}-H}{\sqrt{2}\sigma}\right). \quad (1)$$

The parameters P and T describe the plateau and the tail of the S-curve, respectively. The parameter H is the so-called half-efficiency point, the amplifier threshold at which the efficiency has dropped to $\frac{1}{2}(P+T)$, while σ accounts for noise.

Initially, only eight threshold steps per layer were recorded. Since the hit efficiency was poorly constrained in the tail, two points at 1600 mV and 1800 mV were added in the threshold scans recorded from June 2011 onwards. The hit efficiency at 1600 mV and 1800 mV is observed to be essentially zero and therefore the tail parameter T is fixed to zero in the S-curve fit. For a fair comparison between S-curve fits in different threshold

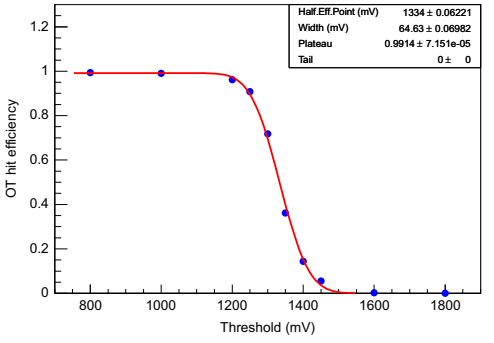

Fig. 6. S-curve fit to data from a threshold scan recorded in October 2011, for the OT detection layer closest to the interaction point. The tail T is fixed to 0, P is found to be 0.99 and H is fitted as 1334 mV. Notice that the two points at 1600 mV and 1800 mV are not taken into account in the fit, for fair comparison between all threshold scans.

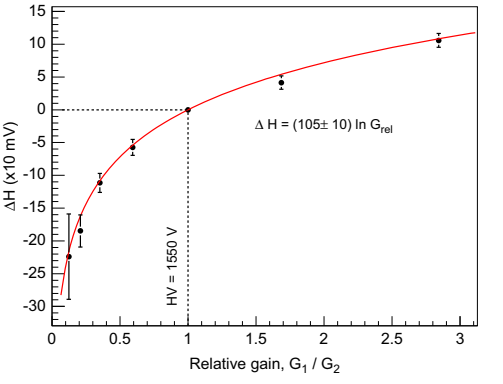

Fig. 7. Calibration curve of the shift in half-efficiency point H versus the relative gain. The data points and uncertainties are obtained from the average shift in H of the 64 wires in the module under test.

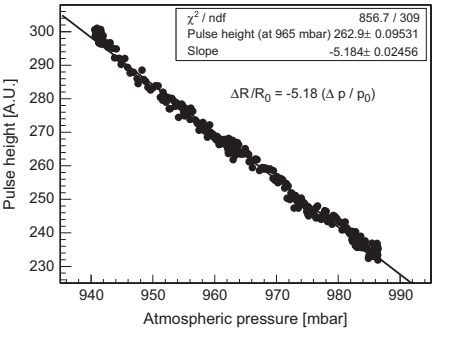

Fig. 8. Pulse height, R, versus atmospheric pressure, p, as measured on a test module in the LHCb cavern.

scans, only the eight measurements below 1600 mV are taken into account in the fit. The result of the fit of Eq. (1) to the hit efficiency as a function of the threshold is shown by the continuous curve in Fig. 6.

Ageing in the OT would reduce the charge amplification, due to the insulating layer on the anode wires. This would lead to an S-curve shifted to lower values of the amplifier threshold, resulting in a smaller half-efficiency point. The stability of the half-efficiency point between threshold scans is used to monitor gain variations in any layer and at any position in x and y. The threshold scans are performed on a regular basis, such that possible ageing in the OT can be detected at an early stage, before the hit efficiency under nominal conditions is affected.

4.2. Gain variations in the OT

To relate shifts in half-efficiency point to gain variations, the shift in H as a function of high voltage was measured [3,5]. Since the relation between gain and HV is known, the shift in half-efficiency point $\Delta H = H_2 - H_1$ as a function of the relative gain $G_{\rm rel} = G_2/G_1$, was determined, and parameterized as (Fig. 7)

$$G_{\rm rel} = \exp\left(\frac{\Delta H\,[\rm mV]}{105\ \rm mV}\right). \tag{2}$$

A correction for the atmospheric pressure p is determined from the pulse height (R) variation as a function of atmospheric pressure shown in Fig. 8, which is obtained from a dedicated test module which is constantly irradiated by a radioactive ^{55}Fe source. Since gain is proportional to pulse height the relative gain is equal to the relative pulse height, which is found to be

$$\frac{\Delta G}{G} = \frac{\Delta R}{R_0} = -5.18\frac{\Delta p}{p_0}. \tag{3}$$

4.3. Threshold scan results

Throughout the 2010 and 2011 run periods, OT threshold scans were performed at regular intervals, corresponding to about 200 pb^{-1} of delivered integrated luminosity. The duration of one threshold scan is approximately 1 h, collecting about 1.5×10^5 events (corresponding to roughly 3×10^6 good quality tracks) at each threshold setting.

The half-efficiency point H is obtained from a fit of the S-curve in every bin, as parameterized in Eq. (1), and is shown in bins of x and y in Fig. 9 for two threshold scans. The first scan is recorded in August 2010, before nominal LHC operation and the second scan is recorded in October 2011.

The values for H in every bin from the scans in August 2010 and October 2011 are subtracted, and the relative gain per bin is calculated using the calibration of Eq. (2) and corrected for the atmospheric pressure. The pressure-corrected relative gain per bin in x and y is shown in Fig. 10. Apart from bin-to-bin fluctuations, no areas with gain loss (relative gain smaller than 1) are observed. The statistical accuracy degrades towards the edges of the OT resulting in larger bin-to-bin fluctuations.

To increase sensitivity, the hit efficiency is averaged over regions of the OT in x and y. Six regions in (x,y) coordinates are studied, averaged over all 12 layers. The inner region is defined as the region within ±60 cm in both x and y from the beam pipe and is subject to the highest particle intensity. The outer region is the region outside ±60 cm in x and y from the beam pipe. The lower (upper) region is defined as $y<-60$ cm ($y>60$ cm). The region closest to the gas inlet and outlet are defined as $y<-200$ cm and $y>200$ cm, respectively.

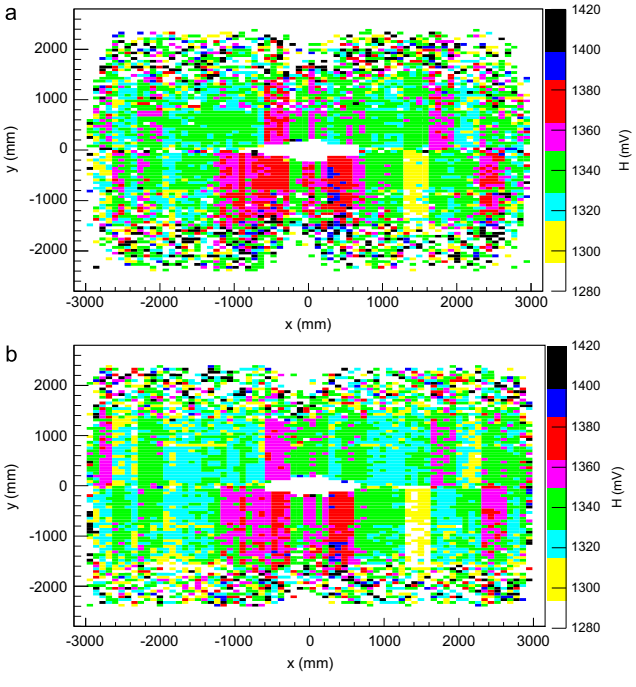

Fig. 9. Fitted half-efficiency point H in mV as a function of x and y for OT layer 8 in August 2010 (a) and October 2011 (b). Differences in threshold characteristics of the individual readout electronics units result in the observed module-to-module variations.

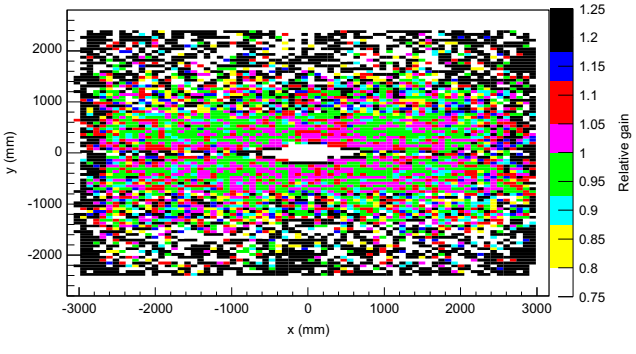

Fig. 10. Pressure-corrected relative gain in bins of x and y for layer 8 of the OT between October 2011 and August 2010.

As an example, the S-curves for the inner region are shown in Fig. 11. The shift in fitted half-efficiency point between the two S-curves is $\Delta H = -3.7$ mV, with a negligible statistical uncertainty, which corresponds to an uncorrected relative gain of 0.965. Correcting for atmospheric pressure differences during the two scans, 975.0 hPa and 985.3 hPa in August 2010 and October 2011, respectively, this number changes to 1.021. The pressure-corrected relative gain variation is thus $+2.1\%$ for the inner region from August 2010 to October 2011. The results for the other regions, integrated over the entire OT, are presented in Table 1, showing a uniform response over the OT surface.

4.4. Systematic uncertainties

To estimate the systematic uncertainty of the method, the fit and the comparison procedures have been varied. For every systematic change, the analysis of the scans in August 2010 and October 2011 is repeated for all regions and the largest deviation

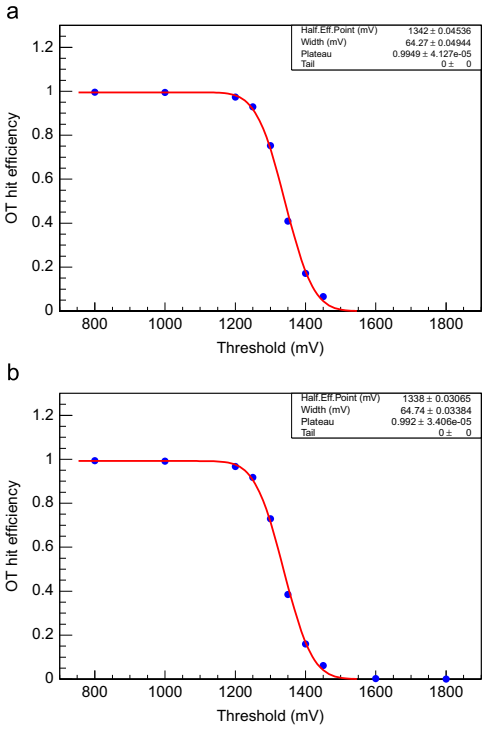

Fig. 11. S-curve for August 2010 (a) and October 2011 (b) for the inner region, defined as ± 60 cm in x and ± 60 cm in y from the central beam pipe, summed over all OT layers. (Notice that the threshold scan in October 2011 contains two extra data points up to 1800 mV which are not used in the fit for fair comparison between threshold scans.)

Table 1
Relative gain variation between August 2010 and October 2011 for various OT regions, summed over all 12 layers and corrected for the change in atmospheric pressure. The various regions are indicated by their coordinates in x and y.

Region	Coordinates (x_1, x_2), (y_1, y_2) (cm)	Pressure-corrected relative gain variation (%)
Entire OT	$(-300, 300)$ $(-250, 250)$	$+1.3$
Inner	$(-60, 60)$ $(-60, 60)$	$+2.1$
Outer	Outside of $(-60, 60)$ $(-60, 60)$	$+0.9$
Lower	$(-300, 300)$ $(60, 250)$	-0.2
Upper	$(-300, 300)$ $(-250, -60)$	$+0.2$
Gas inlet	$(-300, 300)$ $(200, 250)$	$+0.8$
Gas outlet	$(-300, 300)$ $(-250, -200)$	-2.0

in relative gain variation with respect to the nominal analysis is taken as the systematic uncertainty.

The first check is to float the value of the tail parameter T in the fit. A second check is to constrain $P=1$, in addition to $T=0$. Subsequently, the correction for the atmospheric pressure is varied by a relative $\pm 10\%$. The fitted parameter of the calibration curve of ΔH versus relative gain was varied by $\pm 1\sigma$ and the biggest difference is assigned as systematic error. In addition, the definition of H is changed to the threshold at which the hit efficiency is 0.5 instead of $\frac{1}{2}(P+T)$.

The largest difference in relative gain variation per region for each systematic check is summarized in Table 2. The systematic uncertainties of all checks are added in quadrature and a total systematic uncertainty of 2.2% is assigned to the method.

Table 2
Changes to the fit and to the scan comparisons were applied to estimate the systematic uncertainty. The right column shows the largest deviation in relative gain variation from the nominal analysis in the various regions. The total systematic uncertainty is the quadratic sum.

Systematic check	Largest difference in relative gain variation per region (%)
T free	$+1.2$
Fix $P=1$	± 0.0
Pressure correction	$+0.4$
Calibration curve $\pm 1\sigma$	$+0.6$
	-0.8
Definition H	-0.4
Double Gaussian fit	$+1.5$
Total	± 2.2

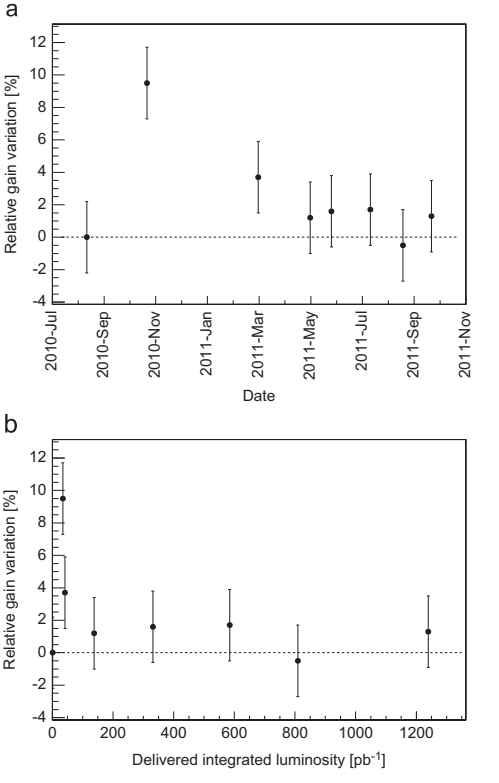

Fig. 12. Relative gain variation averaged over the entire OT, compared to August 2010 (indicated by the dashed line) versus date (a) and versus delivered integrated luminosity (b). The error bars indicate the total systematic uncertainty from Table 2 and are fully correlated between the points.

4.5. Time trend of relative gain variation

In total, eight full threshold scans have been recorded in 2010 and 2011. Using the scan from August 2010 as a reference, the relative gain variation as a function of date and as a function of delivered integrated luminosity, averaged over the entire OT is shown in Fig. 12(a) and (b), respectively.

The observed gain increase for the scan in October 2010 with respect to August 2010 (corresponding to a delivered integrated luminosity of 0.031 fb^{-1}) is not well understood. Overall relative gain variations could be due to variations in the gas mixture. However, the gas mixture is controlled at a level nominally better than 0.2%, which would result in a maximum gain variation of 2% and hence could not explain the observed change in detector response. Relative gain variations could also be caused by different run conditions. For example, the average number of pp interactions per bunch crossing is directly correlated to the event occupancy, which influences the hit efficiency. However, no relation is found between run conditions and the observed relative gain variations. For the scans taken after October 2010, no significant time dependence is observed.

5. Conclusion

Gain stability in the LHCb Outer Tracker is monitored using two techniques: scanning OT modules with a radioactive source and studying hit efficiency as a function of amplifier threshold. The first method compares the module response to ^{90}Sr sources and can only be applied to a small set of modules in periods in which the LHC is not operational. No significant gain loss (about -3%) is observed in the ^{90}Sr scans between January 2011 and December 2011, which is attributed to the decrease of the source strength. The second technique uses the OT readout electronics to study hit efficiency as a function of amplifier threshold during LHC operation. Using this method, the relative gain variation averaged over the entire OT between August 2010 and October 2011 is $(+1.3 \pm 2.2)\%$. This indicates that no gain loss is observed in the OT after LHC operation in 2010 and 2011.

Acknowledgments

We would like to thank Roel Aaij, Johannes Albrecht and Gerhard Raven for their help on the trigger configuration used in the threshold scans. In addition we would like to thank Rainer Schwemmer and Richard Jacobsson for their help in recording the threshold scans in a proper way and for providing additional information on run conditions during the threshold scans.

References

[1] LHCb Collaboration, Journal of Instrumentation 3 (2008) S08005.
[2] S. Bachmann, et al., Nuclear Instruments and Methods A 617 (2010) 202.
[3] G. Apeldoorn, et al., Avalanche and streamer production in Ar/$CO_2$2 mixtures, LHCb-2005-038, 2005.
[4] N. Tuning, et al., Nuclear Instruments and Methods A 656 (2011) 45.
[5] E.L. Visser, Preventing, monitoring and curing the ageing in the LHCb Outer Tracker, CERN-THESIS-2010-094, 2010.

CHAPTER

FIVE

$B_s^0 \to J/\psi\,\phi$ Formalism

In Chap. 1 the general time-dependent decay equations for neutral B mesons were derived. However, the analysis of $B_s^0 \to J/\psi(\mu^+\mu^-)\,\phi(K^+K^-)$ decays involves an additional complication due to the fact that the final state can have contributions from different CP eigenvalues. These contributions from different CP eigenstates are statistically disentangled by performing an angular analysis of the final state particles K^+K^- and $\mu^+\mu^-$ in terms of polarization amplitudes. In this chapter the angular and time dependence of the differential decay rate for $B_s^0 \to J/\psi\,\phi$ decays in terms of these polarization amplitudes is derived.

5.1 CP Eigenstates

The state $|J/\psi\,\phi\rangle$ is a CP eigenstate with eigenvalues $\eta_f = \pm 1$, depending on the angular momentum L of the two vector mesons:

$$\mathrm{CP}|J/\psi\,\phi\rangle = \eta_f |J/\psi\,\phi\rangle = (-1)^L |J/\psi\,\phi\rangle \quad . \tag{5.1}$$

The decaying B_s^0 meson is spinless and thus has total angular momentum $J = 0$. Conservation of angular momentum imposes that the total angular momentum J of the final state must also be zero. J is equal to the sum of the spin S and the orbital angular momentum L: $J = L + S$. The $|J/\psi\,\phi\rangle$ state consists of two vector mesons, each with intrinsic spin equal to 1. This implies that both vector mesons have spin projections $S_z \in \{-1, 0, 1\}$. Adding the spins of the two vector mesons yields the total spin of the $|J/\psi\,\phi\rangle$ state: $S \in \{0, 1, 2\}$. In order to preserve total angular momentum $J = 0$, the spin S must be compensated by the orbital angular momentum L which will therefore have values $L \in \{0, 1, 2\}$, such that $L + S = 0$.

The different orbital angular-momentum states change the CP eigenvalues for the $|J/\psi\,\phi\rangle$ state: the $L = 0$ and $L = 2$ final states are CP-even, whereas the $L = 1$ state is CP-odd. It turns out, as will be shown later, that the CP-even and CP-odd eigenstates contribute to the CP asymmetry (from which the parameter ϕ_s is determined) with opposite sign. Therefore the CP-even and odd components have to be disentangled in order to measure ϕ_s.

The statistical separation between CP-even and CP-odd states is achieved by calculating their relative magnitudes as a function of the observed angular distributions. Two frameworks are commonly used to disentangle CP-even and CP-odd amplitudes. In the helicity framework, spins of stable particles are projected on the momentum direction of the resonant vector mesons and decay amplitudes are decomposed in terms of helicity amplitudes. On the other hand, in the transversity framework, linear polarization amplitudes are used to decompose decay amplitudes.

The conversion from the helicity framework to the transversity framework is closely related to photon helicity and photon polarization, where a photon beam with helicity ± 1 is said to be transversely polarized. In this thesis the transversity framework is adopted, unless specifically stated otherwise. The transversity framework has an associated coordinate system and decay angle definition that will be discussed now.

5.2 The Transversity Framework

A schematic drawing of the coordinate system associated with the transversity framework is shown in Fig. 5.1. In the rest frame of the J/ψ meson, the K^+K^- decay plane defines the xy-plane. The x-axis is defined as the direction of the momentum vector of the ϕ meson in the J/ψ meson rest frame. The y-axis is defined such that $p_y(K^+) > 0$, and finally the z-axis (also called the transversity axis, since it is transverse to the K^+K^- decay plane) completes the right-handed transversity coordinate system.

The angular distribution of $B_s^0 \to J/\psi\,\phi$ decays is described by three decay angles in this coordinate system. The angle ψ_{tr} is the angle of the K^+ candidate with the x-axis in the ϕ meson rest frame. The remaining two angles are defined as the spherical coordinates of the μ^+ in a right-handed system in the J/ψ rest frame. The polar angle and the azimuthal angle are referred to as θ_{tr} and ϕ_{tr} respectively. In the remainder of this thesis the subscript 'tr' will be dropped and the decay angles in the transversity frame will be referred to as ψ, θ and ϕ.

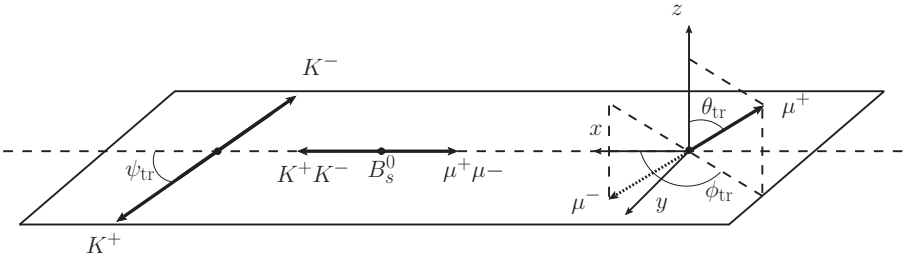

Figure 5.1: *Definition of the transversity frame. In the middle, the rest frame of the B_s^0 is shown. The frames on the left and the right are the center of mass systems of the two kaons and the two muons, respectively.*

Conventionally, the angular distributions of the final state are derived in the helicity framework, after which a transformation to the transversity framework is applied, since

the total decay amplitude of $B_s^0 \to J/\psi\,\phi$ decays is usually decomposed in transversity amplitudes. In this thesis, a different approach is used. It turns out that the $B_s^0 \to J/\psi\,\phi$ decay rate in the transversity framework can be written in the following elegant way:

$$\frac{\mathrm{d}^4\Gamma}{\mathrm{d}t\,\mathrm{d}\cos\psi\,\mathrm{d}\cos\theta\,\mathrm{d}\phi} = \sum_i^6 T_i(t) f_i(\cos\psi, \cos\theta, \phi) = |\vec{A}(t) \times \hat{n}|^2 \quad , \tag{5.2}$$

where the $T_i(t)$ are time-dependent functions and the $f_i(\cos\psi, \cos\theta, \phi)$ are angular-dependent functions. In the following sections, Eq. 5.2 is derived in the transversity framework, as well as the vectors $\vec{A}(t)$ and $\hat{n}$.

5.3 Angular Distributions

In the transversity framework, instead of using the orbital angular momentum eigenstates with $L = \{0, 1, 2\}$ as a basis, decay amplitudes are decomposed using three independent linear polarization states of the vector mesons. The polarization vectors are either longitudinal (labelled by 0) or transverse to the direction of motion of the vector mesons. In the latter case, the polarization vectors are either parallel (labelled by $\|$) or perpendicular ($\perp$) to each other. The different polarization configurations are shown in Fig. 5.2.

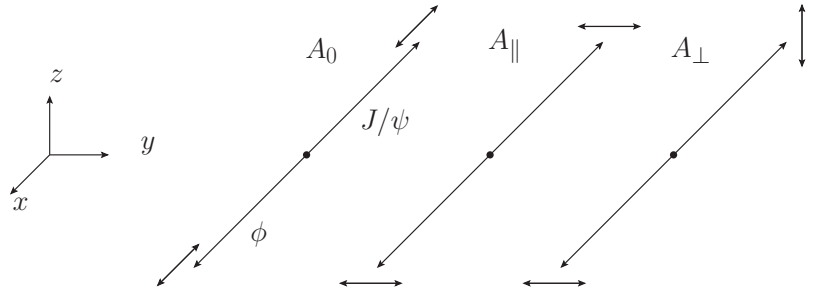

Figure 5.2: *Polarization configurations in the transversity basis, with the transversity axes indicated by the coordinate system on the left. The arrows originating from the vertices are the momentum vectors of the vector mesons in the B_s^0 rest frame, whereas the arrows drawn at the tip of the momentum vectors indicate the possible directions of the linear polarization vectors.*

The $B_s^0 \to J/\psi\,\phi$ decay is a decay to two vector mesons (both the J/ψ meson and the ϕ meson are spin-1 particles). Both (outgoing) vector mesons have an associated polarization four-vector ϵ_μ^*. The most general Lorentz-invariant decomposition of an amplitude $A(B \to$

$V_1\,V_2$), where V_1 and V_2 have momenta p_1 and p_2 and masses m_1 and m_2 is[1] [43, 44]:

$$A(B \to V_1\,V_2) = \epsilon^*_{1,\mu}(\vec{p}_1)\epsilon^*_{2,\nu}(\vec{p}_2)\left[ag^{\mu\nu} + \frac{b}{m_1 m_2}p_2^\mu p_1^\nu + i\frac{c}{m_1 m_2}\epsilon^{\mu\nu\alpha\beta}p_{1,\alpha}p_{2,\beta}\right] \quad . \tag{5.3}$$

The V_1 meson is identified with the J/ψ meson and the V_2 meson is identified with the ϕ meson. In the rest frame of the J/ψ meson, $p^\nu_{J/\psi} = (m_{J/\psi}, \vec{0})^\nu$ and $\epsilon^*_{J/\psi,\mu} = (0, \vec{\epsilon}^*_{J/\psi})_\mu$ and the amplitude becomes

$$A(B \to J/\psi\,\phi) = \epsilon^*_{J/\psi,\mu}(\vec{0})\epsilon^*_{\phi,\nu}(\vec{p}_\phi)\left[ag^{\mu\nu} + \frac{b}{m_\phi}p_\phi^\mu\delta_0^\nu + i\frac{c}{m_\phi}\epsilon^{\mu\nu 0\beta}p_{\phi,\beta}\right] \quad . \tag{5.4}$$

Let $\hat{p}_\phi$ be the unit vector in the direction of motion of the ϕ in the J/ψ rest frame, coinciding with the x-axis in the transversity framework by definition. In the J/ψ rest frame, the polarization vector of the J/ψ meson is decomposed in a component along $\hat{p}_\phi$ and a component transverse to $\hat{p}_\phi$:

$$\epsilon^*_{J/\psi,\mu}(\vec{0}) = (0, \epsilon^{*L}_{J/\psi}\,\hat{p}_\phi + \vec{\epsilon}^{*T}_{J/\psi}) \quad , \tag{5.5}$$

5

where $\epsilon^{*L}_{J/\psi} \equiv \hat{p}_\phi \cdot \vec{\epsilon}^*_{J/\psi}$. In the rest frame of the ϕ meson, accordingly, the polarization vector of the ϕ meson is

$$\epsilon^*_{\phi,\mu}(\vec{0}) = (0, \epsilon^{*L}_\phi\,\hat{p}_\phi + \vec{\epsilon}^{*T}_\phi) \quad . \tag{5.6}$$

Boosting the polarization vector of the ϕ meson back to the J/ψ rest frame, one obtains[2]

$$\epsilon^*_{\phi,\mu}(\vec{0}) = (0, \epsilon^{*L}_\phi\hat{p}_\phi + \vec{\epsilon}^{*T}_\phi) \to \epsilon^*_{\phi,\mu}(\vec{p}_\phi) = \left(\frac{|\vec{p}_\phi|}{m_\phi}\epsilon^{*L}_\phi, \frac{\omega_\phi(\vec{p}_\phi)}{m_\phi}\epsilon^{*L}_\phi\hat{p}_\phi + \vec{\epsilon}^{*T}_\phi\right) \quad . \tag{5.7}$$

Using the expression for the polarization vector of the J/ψ meson in the J/ψ mass frame (Eq. 5.5) and the expression for the boosted polarization vector of the ϕ meson in the J/ψ rest frame (Eq. 5.7), Eq. 5.4 can be written as[3] [45, 46]:

$$\begin{aligned} A(t) &= -a(\vec{\epsilon}^{*T}_{J/\psi}\cdot\vec{\epsilon}^{*T}_\phi) - a\frac{\omega_\phi(\vec{p}_\phi)}{m_\phi}(\vec{\epsilon}^{*L}_{J/\psi}\vec{\epsilon}^{*L}_\phi) \\ &\quad -b\frac{|\vec{p}_\phi|^2}{m_\phi^2}(\vec{\epsilon}^{*L}_{J/\psi}\vec{\epsilon}^{*L}_\phi) - ic\frac{|\vec{p}_\phi|}{m_\phi}(\vec{\epsilon}^{*T}_{J/\psi}\times\vec{\epsilon}^{*T}_\phi)\cdot\hat{p}_\phi \\ &= A_0(t)\epsilon^{*L}_{J/\psi}\epsilon^{*L}_\phi - \frac{1}{\sqrt{2}}A_{||}(t)\vec{\epsilon}^{*T}_{J/\psi}\cdot\vec{\epsilon}^{*T}_\phi - i\frac{1}{\sqrt{2}}A_\perp(t)(\vec{\epsilon}^{*T}_{J/\psi}\times\vec{\epsilon}^{*T}_\phi)\cdot\hat{p}_\phi \end{aligned} \quad . \tag{5.8}$$

The last identity mathematically shows what was depicted in Fig. 5.2: A_0 is associated with the longitudinal components of the two polarization vectors (i.e. aligned in the x-direction),

[1] The most general expression can loosely be written as (ignoring proportionality factors in front of each term) $\epsilon^*_{1,\mu}\epsilon^*_{2,\nu}p_{1,\alpha}p_{2,\beta}[g^{\alpha\beta}g^{\mu\nu} + g^{\alpha\mu}g^{\beta\nu} + g^{\alpha\nu}g^{\beta\mu} + \epsilon^{\mu\nu\alpha\beta}]$. The second term, proportional to $\epsilon^*_{1,\mu}\epsilon^*_{2,\nu}p_1^\mu p_2^\nu$, disappears, because of the restriction $\epsilon^\mu p_\mu = 0$ for vector fields.

[2] For a boost of a general four-vector $a^\mu = (0, \vec{a})$ by $\beta = -\vec{p}/\omega(\vec{p})$, where $\omega(\vec{p})$ is the energy and $\gamma = \omega(\vec{p})/m$, the component $a^L = \hat{p}\cdot\vec{a}$ that is longitudinal to $\hat{p}$ is boosted to $\left(\frac{|\vec{p}|}{m}a^L, \frac{\omega(\vec{p})}{m}a^L\hat{p}\right)$, whereas the transverse component is unaffected by the boost.

[3] Using the metric $g^{\mu\nu} = \mathrm{diag}(1,-1,-1,-1)$.

$A_\parallel$ is associated with the dot product of the transverse components (i.e. purely $A_\parallel$ if the two transverse components are aligned) and finally, $A_\perp$ is associated with the cross product of the transverse components (i.e. purely $A_\perp$ if the two transverse components are perpendicular to each other).

The so-called transversity amplitudes A_0, $A_\parallel$ and $A_\perp$ are related to a, b and c as follows:

$$A_0 = -a\frac{\omega_\phi(\vec{p}_\phi)}{m_\phi} - b\frac{|\vec{p}_\phi|^2}{m_\phi^2} \quad (5.9)$$

$$A_\parallel = a\sqrt{2} \quad (5.10)$$

$$A_\perp = c\sqrt{2}\frac{|\vec{p}_\phi|}{m_\phi} \quad . \quad (5.11)$$

Notice that, by counting powers of $\hat{p}_\phi$ in Eq. 5.8, it follows that A_0 and $A_\parallel$ are CP-even, whereas $A_\perp$ is the CP-odd polarization amplitude, since $\hat{p}_\phi$ changes sign under the parity transformation.

Until now, only the decay $B_s^0 \to J/\psi\,\phi$ was considered. However, also the subsequent decays $\phi \to K^+K^-$ and $J/\psi \to \mu^+\mu^-$ should be taken into account. When considering the former, the ϕ meson couples to K^+K^- through an amplitude $A_{(\phi\to K^+K^-)} \propto \epsilon_\phi(p_{K^+} - p_{K^-})$[4]. In the rest frame of the ϕ meson, this becomes $A_{(\phi\to K^+K^-)} \propto 2\vec{\epsilon}_\phi\cdot\vec{p}_{K^+}$, where it was used that the two kaons are back-to-back ($\vec{p}_{K^-} = -\vec{p}_{K^+}$) and, as before, $\epsilon_{\phi,\mu}(\vec{0}) = (0, \vec{\epsilon}_\phi)_\mu$.

Since the two kaons are spinless, spin conservation requires that the spin of the ϕ meson is compensated by orbital angular momentum of the two kaons perpendicular to the decay plane, indicating that the linear polarization vector of the ϕ meson must lie in the xy-plane. Again, when decomposing $\vec{\epsilon}_\phi$ in a component along and perpendicular to $\vec{p}_\phi$, the amplitude becomes

$$\begin{aligned} A_{(\phi\to K^+K^-)} \propto 2\vec{\epsilon}_\phi\cdot\vec{p}_{K^+} &= 2(\epsilon_\phi^L, \epsilon_\phi^T, 0)\cdot(|\vec{p}_{K^+}|\cos\psi, |\vec{p}_{K^+}|\sin\psi, 0) \\ &\propto \epsilon_\phi^L\cos\psi + \epsilon_\phi^T\sin\psi \quad . \end{aligned} \quad (5.12)$$

Thus, by writing

$$\begin{aligned} \vec{\epsilon}_\phi^{\,L} &= (\cos\psi, 0, 0) \\ \vec{\epsilon}_\phi^{\,T} &= (0, \sin\psi, 0) \quad , \end{aligned} \quad (5.13)$$

the angular dependence arising from the coupling of the ϕ meson to the K^+K^- system is taken into account.

For the J/ψ meson, in its rest frame, each transversity amplitude has a single linear polarization state:

$$\begin{aligned} A_0 &: \quad \vec{\epsilon}_{J/\psi} = (1,0,0) = \hat{x} \\ A_\parallel &: \quad \vec{\epsilon}_{J/\psi} = (0,1,0) = \hat{y} \\ A_\perp &: \quad \vec{\epsilon}_{J/\psi} = (0,0,1) = \hat{z} \quad . \end{aligned} \quad (5.14)$$

[4] In general, the amplitude takes the form $A = A^\mu\epsilon_\mu = [f(p_{K^+} + p_{K^-})^\mu + g(p_{K^+} - p_{K^-})^\mu]\epsilon_\mu$, with arbitrary f and g, but from the vector field constraint, $(p_{K^+} + p_{K^-})^\mu\epsilon_\mu = P^\mu\epsilon_\mu = 0$ (where $P^\mu = (p_{K^+} + p_{K^-})^\mu$ is the four momentum of the ϕ meson), and therefore $A \propto \epsilon_\phi(p_{K^+} - p_{K^-})$.

In other words:

$$\begin{aligned} \vec{\epsilon}^{\,L}_{J/\psi} &= (1,0,0) \\ \vec{\epsilon}^{\,T}_{J/\psi} &= (0,1,1) \quad . \end{aligned} \tag{5.15}$$

Using Eq. 5.13 and Eq. 5.15 the total decay amplitude in Eq. 5.8 simplifies to

$$A(t) = A_0(t)\cos\psi - \frac{1}{\sqrt{2}}A_{||}(t)\sin\psi + i\frac{1}{\sqrt{2}}A_{\perp}(t)\sin\psi \quad . \tag{5.16}$$

Since Eq. 5.15 associates the x, y and z direction with the polarizations $0, \parallel$ and $\perp$, respectively, Eq. 5.16 can also be written as a vector:

$$\vec{A}(t) = \left(A_0(t)\cos\psi, -\frac{1}{\sqrt{2}}A_{\parallel}(t)\sin\psi, \frac{i}{\sqrt{2}}A_{\perp}(t)\sin\psi \right) \quad . \tag{5.17}$$

Now the coupling of the J/ψ meson to the $\mu^+\mu^-$ final state must be considered. In general, the total decay rate is written as

$$\frac{\mathrm{d}^4\Gamma_{B_s^0\to J/\psi\,\phi}}{\mathrm{d}t\,\mathrm{d}\cos\psi\,\mathrm{d}\cos\theta\,\mathrm{d}\phi} \equiv \frac{\mathrm{d}^4\Gamma}{\mathrm{d}t\,\mathrm{d}\vec{\Omega}} \propto \sum_{r,s} A_i^{\dagger}(t)[\overline{u}(s)\gamma_i v(r)]^{\dagger} A_j(t)[\overline{u}(s)\gamma_j v(r)] \quad , \tag{5.18}$$

where $\vec{\Omega}$ is a shorthand notation for $(\cos\psi, \cos\theta, \phi)$ and $[\overline{u}(s)\gamma_i v(r)]$ is the Dirac fermion current representing the muons, with s and r the muon spins. The indices i and j indicate spatial components, and thus the A_i are the components of the polarization amplitude vector in Eq. 5.17.

The direction of the μ^+ in the J/ψ rest frame is defined as (see Fig. 5.1)

$$\hat{n} = (\sin\theta\cos\phi, \sin\theta\sin\phi, \cos\theta) \quad . \tag{5.19}$$

The sum over the muon spins in Eq. 5.18, in the zero muon-mass limit, gives rise to a tensor with spatial components L_{ij}[5]:

$$\sum_{r,s}[\overline{u}(s)\gamma_i v(r)]^{\dagger}[\overline{u}(s)\gamma_j v(r)] \propto L_{ij} \equiv \delta_{ij} - n_i n_j \quad , \tag{5.20}$$

[5] In the zero muon-mass limit, $\sum_{r,s}[\overline{u}(s)\gamma_i v(r)]^{\dagger}[\overline{u}(s)\gamma_j v(r)] = k_{\alpha}^1 k_{\beta}^2 \mathrm{tr}(\gamma^{\mu}\gamma^{\nu}\gamma^{\alpha}\gamma^{\beta})\delta_{i\mu}\delta_{j\nu}$, with $k_{\mu}^{1,2}$ the muon momenta. In the J/ψ mass frame, defining $\vec{k}^1 = \hat{n}|\vec{k}|$ and $\vec{k}^2 = -\hat{n}|\vec{k}|$, this reduces to

$$k_{\alpha}^1 k_{\beta}^2 \mathrm{tr}(\gamma^{\mu}\gamma^{\nu}\gamma^{\alpha}\gamma^{\beta})\delta_{i\mu}\delta_{j\nu} = 4\left(k_i^1 k_j^2 - (k_{\mu}^1 k^{2,\mu})(-\delta_{ij}) - k_i^1 k_j^2\right) = -4|\vec{k}|^2\left(-2n_i n_j + \frac{(k_{\mu}^1 k^{2,\mu})}{|\vec{k}|^2}\delta_{ij}\right) \quad .$$

Finally, using $k_{\mu}^1 k^{2,\mu} = \omega(k^1)\omega(k^2) - |\vec{k}|^2(-\hat{n}\cdot\hat{n}) = 2|\vec{k}|^2$, it is found that [47]

$$\sum_{r,s}[\overline{u}(s)\gamma_i v(r)]^{\dagger}[\overline{u}(s)\gamma_j v(r)] \propto \delta_{ij} - n_i n_j \quad .$$

	$T_i(t) f_i(\vec{\Omega})$	
i	time-dependent product of polarization amplitudes, $T_i(t)$	angular distribution, $f_i(\vec{\Omega})$
1	$\lvert A_0(t)\rvert^2$	$\cos^2\psi(1-\sin^2\theta\cos^2\phi)$
2	$\lvert A_\parallel(t)\rvert^2$	$\frac{1}{2}\sin^2\psi(1-\sin^2\theta\sin^2\phi)$
3	$\lvert A_\perp(t)\rvert^2$	$\frac{1}{2}\sin^2\psi\sin^2\theta$
4	$\mathrm{Re}(A_0^*(t)A_\parallel(t))$	$\frac{1}{2\sqrt{2}}\sin(2\psi)\sin^2\theta\sin(2\phi)$
5	$\mathrm{Im}(A_0^*(t)A_\perp(t))$	$\frac{1}{2\sqrt{2}}\sin(2\psi)\sin(2\theta)\cos\phi$
6	$\mathrm{Im}(A_\parallel^*(t)A_\perp(t))$	$-\frac{1}{2}\sin^2\psi\sin(2\theta)\sin\phi$

Table 5.1: *Tabular representation of the six terms ($i = 1, ..., 6$) in the $B_s^0 \to J/\psi\,\phi$ signal PDF $|\vec{A}(t) \times \hat{n}|^2$, showing their angular dependence $f_i(\vec{\Omega})$. The expression for the signal PDF is found by multiplying the entries in one row: $T_i(t) f_i(\vec{\Omega})$, and summing all the rows.*

and Eq. 5.18 becomes

$$\frac{\mathrm{d}^4\Gamma}{\mathrm{d}t\,\mathrm{d}\vec{\Omega}} \propto A_i(t)A_j(t)^* L_{ij} = |\vec{A}(t) \times \hat{n}|^2 \quad . \tag{5.21}$$

The $B_s^0 \to J/\psi\,\phi$ differential decay rate results in the sum of six terms:

$$\frac{\mathrm{d}^4\Gamma}{\mathrm{d}t\,\mathrm{d}\vec{\Omega}} \propto |\vec{A}(t) \times \hat{n}|^2 = \sum_i^6 T_i(t) f_i(\vec{\Omega}) \quad , \tag{5.22}$$

which are summarized in Table 5.1. From now on, this object is referred to as the $B_s^0 \to J/\psi\,\phi$ signal probability distribution function (PDF) or simply signal PDF[6].

For completeness, the expressions for the charge conjugate $\overline{B}_s^0 \to J/\psi\,\phi$ decays are written as

$$\vec{\overline{A}}(t) = (\overline{A}_0(t)\cos\psi, -\frac{\overline{A}_{||}(t)}{\sqrt{2}}\sin\psi, i\frac{\overline{A}_\perp(t)}{\sqrt{2}}\sin\psi) \quad , \tag{5.23}$$

and

$$\frac{\mathrm{d}^4\overline{\Gamma}}{\mathrm{d}t\,\mathrm{d}\vec{\Omega}} = |\vec{\overline{A}}(t) \times \hat{n}|^2 = \sum_i^6 \overline{T}_i(t) f_i(\vec{\Omega}) \quad . \tag{5.24}$$

5.4 Time Dependence

In the previous section, the angular dependence of the differential decay rates has been derived. In this section, the time dependence of the $A_i(t)$ will be derived.

[6] Strictly speaking, the differential decay rate is not a PDF, because it needs to be normalized by the total decay rate. Proper normalization of the PDF is implicitly assumed here and is addressed in Sec. 5.6.

The time dependence of the polarization amplitudes is obtained by rewriting the general time dependence of a B mixing decay amplitude, starting from Eq. 1.44:

$$A_f(t) = A_f(0)[g_+(t) + \lambda_f g_-(t)] \quad , \tag{5.25}$$

where

$$\lambda_{J/\psi\,\phi} = \frac{q}{p}\frac{\overline{A}_{J/\psi\,\phi}}{A_{J/\psi\,\phi}} \equiv \eta_{J/\psi\,\phi}\lambda \quad . \tag{5.26}$$

The appearance of the CP eigenvalue $\eta_{J/\psi\,\phi}$ of the final state will be explained in Sec. 5.7 when $\lambda_{J/\psi\,\phi}$ is explicitly calculated. In the following, the CP eigenvalue $\eta_{J/\psi\,\phi} = \pm 1$ is chosen to be absorbed in the time dependence of the PDF.

There are three different quantities λ_i, corresponding to the three different polarization amplitudes A_i, with $i \in \{0, \|, \perp\}$. Their CP eigenvalues η_i are given by

$$\eta_i = \begin{cases} +1 \;\text{ if }\; i = 0, \| \\ -1 \;\text{ if }\; i = \perp \end{cases} \quad . \tag{5.27}$$

The three λ_i are assumed to be the same. In particular, all three magnitudes $|\lambda_i|$ are assumed to be equal, which implies that there is either no, or equal amounts of CP violation in decay for all three amplitudes. In other words, all three values for $|\overline{A}_i/A_i|$ are assumed to be equal. This still allows for CP violation in mixing ($|q/p| \neq 1$), but all three $|\lambda_i|$ would be affected in the same way. From here onwards, the λ_i are generically referred to as λ:

$$\lambda_{J/\psi\,\phi} = \eta_i\lambda_i \to \eta_i\lambda \quad . \tag{5.28}$$

Using the identities for S, D and C defined in Eq. 1.48, λ is rewritten in terms of S, D and C:

$$D(\lambda) \equiv \frac{2\mathrm{Re}\lambda}{1+|\lambda|^2} \quad , \quad S(\lambda) \equiv \frac{2\mathrm{Im}\lambda}{1+|\lambda|^2} \quad , \quad C(\lambda) \equiv \frac{1-|\lambda|^2}{1+|\lambda|^2} \quad . \tag{5.29}$$

From these definitions, it follows that $D^2 + S^2 = 1 - C^2$ and

$$\lambda = \frac{D+iS}{1+C} \quad , \quad \frac{1}{\lambda} = \frac{D-iS}{1-C} \quad , \quad |\lambda|^2 = \frac{1-C}{1+C} \quad . \tag{5.30}$$

The decay amplitudes (see Eq. 5.25) then become

$$\begin{aligned} A_i(t) &= [g_+(t) + \eta_i\lambda g_-(t)]\, a_i && (5.31)\\ &= \left[g_+(t) + \eta_i\frac{D+iS}{1+C}g_-(t)\right] a_i && (5.32)\\ \overline{A}_i(t) &= \left[g_+(t) + \frac{1}{\eta_i\lambda}g_-(t)\right] \eta_i a_i && (5.33)\\ &= \left[\eta_i g_+(t) + \frac{D-iS}{1-C}g_-(t)\right] a_i \quad , && (5.34) \end{aligned}$$

where $a_i \equiv A_i(t=0)$ and thus $\overline{a}_i = \eta_i a_i$. The functions $g_\pm(t)$ were defined in Eq. 1.25, from which the following identities were found:

$$|g_\pm(t)|^2 = \frac{e^{-\Gamma_s t}}{2}\left[\cosh\left(\frac{\Delta\Gamma_s t}{2}\right) \pm \cos\left(\Delta m_s t\right)\right] \tag{5.35}$$

and

$$g_+(t)^* g_-(t) = \frac{e^{-\Gamma_s t}}{2}\left[-\sinh\left(\frac{\Delta\Gamma_s t}{2}\right) + i\sin\left(\Delta m_s t\right)\right] \quad . \tag{5.36}$$

The decay amplitudes are written in a more symmetrical way as follows:

$$A_i(t) = \frac{1}{1+C}\left[(1+C)g_+(t) + \eta_i(D+iS)g_-(t)\right]a_i \tag{5.37}$$

$$\overline{A}_i(t) = \frac{1}{1-C}\left[(1-C)g_+(t) + \eta_i(D-iS)g_-(t)\right]\eta_i a_i \quad . \tag{5.38}$$

In this representation the differences in time dependence between B_s^0 decays and $\overline{B}_s^0$ decays are clear: depending on whether the produced meson is a B_s^0 meson or a $\overline{B}_s^0$ meson, the following substitutions are made:

$$B_s^0 \leftrightarrow \overline{B}_s^0 \quad \Leftrightarrow \quad (S \leftrightarrow -S,\, C \leftrightarrow -C,\, a_\perp \leftrightarrow -a_\perp) \quad . \tag{5.39}$$

These substitutions are written even more compactly when defining the flavour tag observable $q_T = \pm 1$ (+1 for a produced B_s^0 meson, -1 for a produced $\overline{B}_s^0$ meson). In LHCb, this flavour tag is assigned with a certain probability by so-called tagging algorithms. With this variable, the substitutions to obtain the time dependence of $\overline{B}_s^0$ decays from the time dependence of B_s^0 decays are

$$(S, C, a_\perp) \to (q_T S, q_T C, q_T a_\perp) \quad \text{with} \quad q_T = \begin{cases} +1 & \text{if tagged as } B_s^0 \\ -1 & \text{if tagged as } \overline{B}_s^0 \end{cases} \quad . \tag{5.40}$$

It is observed from Table 5.1 that the time-dependent decay-rate functions $T_i(t)$ all consist of products of decay amplitudes. Considering the case $q_T = 1$ and thus using Eq. 5.37, these products of decay amplitudes take the following form:

$$\begin{aligned} A_i^*(t)A_j(t) \quad &= \tfrac{a_i^* a_j}{1+C} \quad \Big[(1+C)|g_+(t)|^2 + \eta_i\eta_j(1-C)|g_-(t)|^2 \\ &\qquad +\eta_j(D+iS)g_+^* g_- + \eta_i(D-iS)g_+ g_-^*\Big] \end{aligned} \tag{5.41}$$

$$\begin{aligned} &= \tfrac{a_i^* a_j e^{-\Gamma_s t}}{1+C} \quad \Big[\left(\frac{1+\eta_i\eta_j}{2} + \frac{1-\eta_i\eta_j}{2}C\right)\cosh\left(\frac{\Delta\Gamma_s t}{2}\right) \\ &\qquad + \left(\frac{1-\eta_i\eta_j}{2} + \frac{1+\eta_i\eta_j}{2}C\right)\cos(\Delta m_s t) \\ &\qquad + \left(-\frac{\eta_i+\eta_j}{2}D + \frac{\eta_i-\eta_j}{2}iS\right)\sinh\left(\frac{\Delta\Gamma_s t}{2}\right) \\ &\qquad + \left(-\frac{\eta_i+\eta_j}{2}S - \frac{\eta_i-\eta_j}{2}iD\right)\sin(\Delta m_s t)\Big] . \end{aligned} \tag{5.42}$$

The resulting expressions for the time-dependence of the six terms $T_i(t)$ in the signal PDF, after substituting Eq. 5.40, are summarized in Table 5.2.

		$T_i(t) = \mathcal{F}_i \left(a_i \cosh\left(\frac{\Delta\Gamma_s t}{2}\right) + b_i \cos(\Delta m_s t) + c_i \sinh\left(\frac{\Delta\Gamma_s t}{2}\right) + d_i \sin(\Delta m_s t)\right)$				
i	$T_i(t)$	$\mathcal{F}_i$	a_i	b_i	c_i	d_i
1	$\lvert A_0(t)\rvert^2$	$\frac{\lvert a_0\rvert^2 e^{-\Gamma_s t}}{1+q_T C}$	1	$q_T\, C$	$-D$	$-q_T\, S$
2	$\lvert A_\parallel(t)\rvert^2$	$\frac{\lvert a_\parallel\rvert^2 e^{-\Gamma_s t}}{1+q_T C}$	1	$q_T\, C$	$-D$	$-q_T\, S$
3	$\lvert A_\perp(t)\rvert^2$	$\frac{\lvert a_\perp\rvert^2 e^{-\Gamma_s t}}{1+q_T C}$	1	$q_T\, C$	D	$q_T\, S$
4	$\mathrm{Re}(A_0^*(t)A_\parallel(t))$	$\frac{\mathrm{Re}(a_0^* a_\parallel) e^{-\Gamma_s t}}{1+q_T C}$	1	$q_T\, C$	$-D$	$-q_T\, S$
		$\frac{\mathrm{Im}(a_0^* a_\parallel) e^{-\Gamma_s t}}{1+q_T C}$	0	0	0	0
5	$\mathrm{Im}(A_0^*(t)A_\perp(t))$	$\frac{\mathrm{Re}(a_0^* a_\perp) e^{-\Gamma_s t}}{1+q_T C}$	0	0	S	$-q_T\, D$
		$\frac{\mathrm{Im}(a_0^* a_\perp) e^{-\Gamma_s t}}{1+q_T C}$	C	q_T	0	0
6	$\mathrm{Im}(A_\parallel^*(t)A_\perp(t))$	$\frac{\mathrm{Re}(a_\parallel^* a_\perp) e^{-\Gamma_s t}}{1+q_T C}$	0	0	S	$-q_T\, D$
		$\frac{\mathrm{Im}(a_\parallel^* a_\perp) e^{-\Gamma_s t}}{1+q_T C}$	C	q_T	0	0

Table 5.2: *Tabular representation of the time dependence of the six combinations of polarization amplitudes in the signal PDF. For every i, the time dependence is found by multiplying the factor $\mathcal{F}$ in the third column with the sum of four terms, as indicated in the top row. Since the product of two time dependent polarization amplitudes is itself an imaginary object, the three interference terms split in the sum of a real and an imaginary part.*

5.5 S-Wave Contribution

The spinless kaons in the K^+K^- system in $B_s^0 \to J/\psi\,\phi$ decays must necessarily be in an $L = 1$ state to conserve total angular momentum in the decay of the ϕ vector meson. This $L = 1$ state is also called a P-wave, following the nomenclature from atomic orbitals.

In addition to the P-wave, there might be a contribution from $B_s^0 \to J/\psi\, K^+K^-$ decays, where the invariant mass of the K^+K^- system is in the vicinity of the ϕ meson mass. In this case, the non-resonant, spinless kaons in the K^+K^- system can be in an $L = 0$ state, which is referred to as an S-wave. This S-wave contribution to $B_s^0 \to J/\psi\,\phi$ decays might also arise from $B_s^0 \to J/\psi\, f_0(K^+K^-)$ decays, since the f_0 meson is a scalar meson leading to an S-wave K^+K^- system. The $B_s^0 \to J/\psi\, f_0$ final state is a CP eigenstate with eigenvalue equal to -1. This implies that no angular analysis is needed to measure ϕ_s in this decay. Although this decay has a smaller branching fraction compared to $B_s^0 \to J/\psi\,\phi$ decays, it is also used to measure ϕ_s [48, 49].

The angular and time dependence of a possible S-wave contribution to $B_s^0 \to J/\psi\,\phi$ decays is obtained in a similar way as the P-wave contribution. The $J/\psi\, K^+K^-$ final state is CP-odd:

$$\begin{aligned} \mathrm{CP}|J/\psi\, K^+K^-\rangle &= \eta(J/\psi) \times \eta(K^+K^-) \times (-1)^{L_{K^+K^-}} \times (-1)^{L_{J/\psi\, KK}} \\ &= (1) \times (1) \times (-1)^0 \times (-1)^1 \\ &= -1 \quad . \end{aligned} \tag{5.43}$$

	$T_i(t) f_i(\vec{\Omega})$	
i	time-dependent product of polarization amplitudes, $T_i(t)$	angular distribution, $f_i(\vec{\Omega})$
7	$\lvert A_S(t)\rvert^2$	$\frac{1}{3}\,(1-\sin^2\theta\cos^2\phi)$
8	$\mathrm{Re}(A_0(t)^* A_S(t))$	$\frac{2}{3}\sqrt{3}\,\cos\psi(1-\sin^2\theta\cos^2\phi)$
9	$\mathrm{Re}(A_\parallel(t)^* A_S(t))$	$\frac{1}{6}\sqrt{6}\,\sin\psi\sin^2\theta\sin(2\phi)$
10	$\mathrm{Im}(A_\perp(t)^* A_S(t))$	$-\frac{1}{6}\sqrt{6}\,\sin\psi\sin(2\theta)\cos\phi$

Table 5.3: *Tabular representation of the four terms ($i = 7, 8, 9, 10$) in the signal PDF related to the S-wave component, showing their angular dependence $f_i(\vec{\Omega})$. The four terms are found by multiplying the entries in every row: $T_i(t) f_i(\vec{\Omega})$.*

Here, by definition, $L_{K^+K^-} = 0$ because of the S-wave, and $L_{J/\psi\,K^+K^-} = 1$ is the angular momentum of the $J/\psi\,K^+K^-$ system, needed to compensate for the spin of the J/ψ vector meson in the spinless B_s^0 decay.

An S-wave polarization amplitude A_S has to be added to account for the non-resonant S-wave contribution. In $B_s^0 \to J/\psi\,K^+K^-$ decays the J/ψ meson is the only vector meson involved in the decay, which, as a result of spin conservation, means it is necessarily longitudinally polarized. This implies that the pure S-wave amplitude vector is written as

$$\vec{S}(t) = (A_S(t), 0, 0) \quad , \tag{5.44}$$

in accordance with Eq. 5.17, where the first element of the vector also represents the longitudinal direction.

The differential decay rate for $B_s^0 \to J/\psi\,\phi$ decays, Eq. 5.22, is modified as follows to include an S-wave component:

$$\frac{\mathrm{d}^4\Gamma}{\mathrm{d}t\,\mathrm{d}\vec{\Omega}} \quad \propto \quad \left|\left(\vec{A}(t) + \frac{1}{\sqrt{3}}\vec{S}(t)\right) \times \hat{n}\right|^2 \quad , \tag{5.45}$$

where the factor $\frac{1}{\sqrt{3}}$ is chosen such that the integral of the unnormalized PDF is proportional to the sum of all amplitudes: $|A_0(t)|^2 + |A_\parallel(t)|^2 + |A_\perp(t)|^2 + |A_S(t)|^2$. When calculating the cross product, four extra angular-dependent and time-dependent terms related to the S-wave component are introduced which are summarized in Table 5.3 and Table 5.4, respectively.

5.6 Combining Time Dependence and Angular Dependence

In the previous sections, the angular dependence and the time dependence for both the P-wave component and the S-wave component in the signal PDF were derived. The signal PDF is written as

$$\frac{\mathrm{d}^4\Gamma}{\mathrm{d}t\,\mathrm{d}\vec{\Omega}} \propto \sum_i^{10} T_i(t|\vec{\Pi})\, f_i(\vec{\Omega}) \quad , \tag{5.46}$$

		$T_i(t) = \mathcal{F}_i \left(a_i \cosh\left(\frac{\Delta\Gamma_s t}{2}\right) + b_i \cos(\Delta m_s t) + c_i \sinh\left(\frac{\Delta\Gamma_s t}{2}\right) + d_i \sin(\Delta m_s t)\right)$				
i	$T_i(t)$	$\mathcal{F}_i$	a_i	b_i	c_i	d_i
7	$\lvert A_S(t)\rvert^2$:	$\frac{\lvert a_S\rvert^2 e^{-\Gamma_s t}}{1+q_T C}$	1	$q_T\, C$	D	$q_T\, S$
8	$\mathrm{Re}(A_0(t)^* A_S(t))$:	$\frac{\mathrm{Re}(a_0^* a_S) e^{-\Gamma_s t}}{1+q_T C}$	C	q_T	0	0
		$\frac{\mathrm{Im}(a_0^* a_S) e^{-\Gamma_s t}}{1+q_T C}$	0	0	S	$-q_T\, D$
9	$\mathrm{Re}(A_\parallel(t)^* A_S(t))$:	$\frac{\mathrm{Re}(a_\parallel^* a_S) e^{-\Gamma_s t}}{1+q_T C}$	C	q_T	0	0
		$\frac{\mathrm{Im}(a_\parallel^* a_S) e^{-\Gamma_s t}}{1+q_T C}$	0	0	S	$-q_T\, D$
10	$\mathrm{Im}(A_\perp(t)^* A_S(t))$:	$\frac{\mathrm{Re}(a_\perp^* a_S) e^{-\Gamma_s t}}{1+q_T C}$	0	0	0	0
		$\frac{\mathrm{Im}(a_\perp^* a_S) e^{-\Gamma_s t}}{1+q_T C}$	1	$q_T\, C$	D	$q_T\, S$

Table 5.4: *Tabular representation of the time dependence of the four combinations of polarization amplitudes in the signal PDF related to the S-wave component. For every i, the time dependence is found by multiplying the factor $\mathcal{F}$ in the third column with the sum of four terms, as indicated in the top row. Since the product of two time dependent polarization amplitudes is itself an imaginary object, the three interference terms split in the sum of a real and an imaginary part.*

5

with $\vec{\Pi}$ the set of physics parameters, i.e. $\vec{\Pi} = (\Gamma_s, \Delta\Gamma_s, \Delta m_s, \phi_s, a_0, a_\parallel, a_\perp, a_S)$. Conventionally, the $T_i(t|\vec{\Pi})$ are not written in terms of the real and imaginary parts of the complex parameters a_j ($j \in (0, \parallel, \perp)$), but in terms of their absolute values and phases δ_j. The real and imaginary part of the product of two amplitudes $a_i^* a_j$ are written as

$$\mathrm{Re}(a_i^* a_j) = \mathrm{Re}(|a_i||a_j| e^{(i(\delta_j - \delta_i)}) = |a_i||a_j| \cos(\delta_j - \delta_i) \quad (5.47)$$

$$\mathrm{Im}(a_i^* a_j) = \mathrm{Im}(|a_i||a_j| e^{(i(\delta_j - \delta_i)}) = |a_i||a_j| \sin(\delta_j - \delta_i) \quad . \quad (5.48)$$

As an example, the first term in the PDF, $T_1(t) f_1(\vec{\Omega})$ is explicitly given here in the case of $q_T = 1$:

$$\begin{aligned} T_1(t) f_1(\vec{\Omega}) &= \frac{|a_0|^2 e^{-\Gamma_s t}}{1+C} \\ &\times \left(\cosh\left(\frac{\Delta\Gamma_s t}{2}\right) + C\cos(\Delta m_s t) - D\sinh\left(\frac{\Delta\Gamma_s t}{2}\right) - S\sin(\Delta m_s t)\right) \\ &\times \cos^2\psi(1 - \sin^2\theta\cos^2\phi) \quad . \end{aligned} \quad (5.49)$$

All ten terms of the signal PDF are given explicitly in Appendix D, using the angular functions $f_i(\vec{\Omega})$ (as given in Table 5.1 for the P-wave component and Table 5.3 for the S-wave component) and the time-dependence of the $T_i(t|\vec{\Pi})$ (as given in Table 5.2 for the P-wave component and Table 5.4 for the S-wave component).

The properly normalized signal PDF $P_{B_s^0 \to J/\psi\,\phi}$ is the normalized sum of products of the time-dependent functions $T_i(t|\vec{\Pi})$, and angular functions $f_i(\vec{\Omega})$:

$$P_{B_s^0 \to J/\psi\,\phi} = \frac{\sum_{i=1}^{10} T_i(t|\vec{\Pi})\, f_i(\vec{\Omega})}{\int\int \sum_{i=1}^{10} T_i(t|\vec{\Pi})\, f_i(\vec{\Omega})\, \mathrm{d}t\, \mathrm{d}\vec{\Omega}} \quad . \tag{5.50}$$

In the next section, finally, C, D and S are expressed in terms of the B_s^0 mixing phase ϕ_s.

5.7 Sensitivity to ϕ_s in $B_s^0 \to J/\psi\,\phi$ decays

When deriving the angular-dependent and time-dependent terms in the $B_s^0 \to J/\psi\,\phi$ signal PDF in the previous sections a general approach was used. In this section, $\lambda_{J/\psi\,\phi} = \frac{q}{p}\frac{\overline{A}_{J/\psi\,\phi}}{A_{J/\psi\,\phi}}$ (Eq. 5.26) is explicitly calculated. The value of $\lambda_{J/\psi\,\phi}$ is calculated by inspecting the Feynman diagrams with and without B_s^0 mixing, as shown in Fig. 5.3.

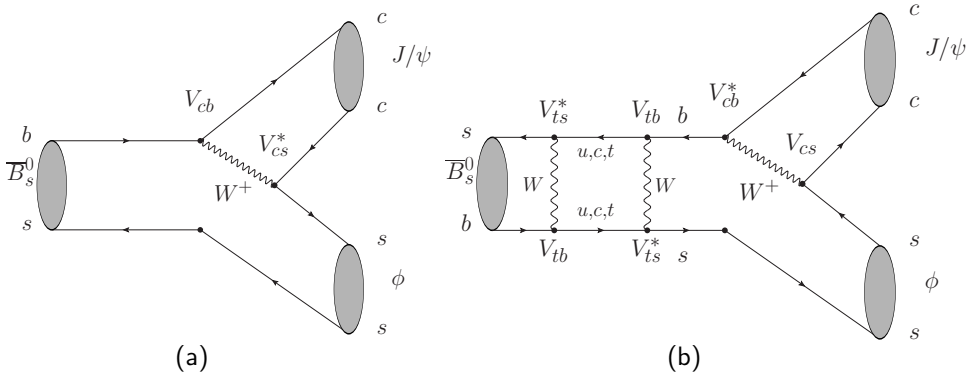

Figure 5.3: *$\overline{B}_s^0 \to J/\psi\,\phi$ decay without (a) and including (b) mixing.*

The expression for q/p was derived in Eq. 1.38:

$$\frac{q}{p} \;=\; -e^{-i\phi_M}[1 - \frac{a_{\mathrm{fs}}}{2}] \quad , \tag{5.51}$$

using $a_{\mathrm{fs}} \simeq \left|\frac{\Gamma_{12}}{M_{12}}\right| \sin\phi_{M/\Gamma}$, where contributions of order $\mathcal{O}((\Gamma_{12}/M_{12})^2)$ are ignored. Since $|\Gamma_{12}| \ll |M_{12}|$, a_{fs} is estimated to be small ($a_{\mathrm{fs}} = (2.06 \pm 0.57) \cdot 10^{-5}$ [19]), and therefore the following approximation is justified:

$$\frac{q}{p} \approx -e^{-i\phi_M} \quad . \tag{5.52}$$

Notice that in this approximation, $|q/p| = 1$. From Fig. 5.3 (b) it follows that, in the phase convention used, $\phi_M = \arg(M_{12}) = \arg[(V_{tb}V_{ts}^*)^2]$.

In addition[7],

$$\frac{\overline{A}_{J/\psi\,\phi}}{A_{J/\psi\,\phi}} = -\eta_{J/\psi\,\phi}\, e^{2i\phi_{c(\overline{c}s)}} \quad , \tag{5.53}$$

where $\phi_{c(\overline{c}s)}$ is the weak phase in the decay coming from the $b \to c(\overline{c}s)$ transition. It follows that $\left|\frac{\overline{A}_{J/\psi\,\phi}}{A_{J/\psi\,\phi}}\right| = 1$, where it is assumed that only one single weak phase contributes to the decay amplitude. This assumption is no longer valid when allowing for penguin contributions, although these are expected to be small, see Sec. 5.9.

Notice the appearance of the CP eigenvalue $\eta_{J/\psi\,\phi}$ that was already absorbed in the time dependence derived in Sec. 5.4. In the phase convention used, the phase $\phi_{c(\overline{c}s)}$ equals

$$\phi_{c(\overline{c}s)} = \arg\left(V_{cb}V_{cs}^*\right) \quad , \tag{5.54}$$

as indicated in Fig. 5.3. Combining the results for q/p (Eq. 5.52) and $\frac{\overline{A}_f}{A_f}$ (Eq. 5.53) and using the definition $\lambda_{J/\psi\,\phi} = \eta_{J/\psi\,\phi}\lambda$ (Eq. 5.26), it is found that

$$\lambda = e^{-i\phi_M} e^{2i\phi_{c(\overline{c}s)}} = e^{-i\phi_s} \quad , \tag{5.55}$$

where $\phi_s = \phi_M - 2\phi_{c(\overline{c}s)}$, independent of any phase convention. Notice that, using the approximations $|q/p| = 1$ and $\left|\frac{\overline{A}_{J/\psi\,\phi}}{A_{J/\psi\,\phi}}\right| = 1$, also $|\lambda| = 1$, see also Sec. 6.7.

Substituting the values for ϕ_M and $\phi_{c(\overline{c}s)}$ in terms of CKM matrix elements, in the SM one finds

$$\begin{aligned}
\phi_s &= \phi_M - 2\phi_{c(\overline{c}s)} \\
&= \arg[(V_{tb}V_{ts}^*)^2] - 2\arg\left(V_{cb}V_{cs}^*\right) \\
&= 2\arg\left(\frac{V_{tb}V_{ts}^*}{V_{cb}V_{cs}^*}\right) \\
&= -2\beta_s \quad ,
\end{aligned} \tag{5.56}$$

where β_s is the angle in one of the Unitarity Triangles as defined in Eq. 1.11[8]. Using $\lambda = e^{-i\phi_s}$ it follows that $|\lambda_{J/\psi\,\phi}| = |\eta_{J/\psi\,\phi}\lambda| = 1$ and subsequently

$$D = \mathrm{Re}\,\lambda = \cos\phi_s \quad , \quad C = 0 \quad , \quad S = \mathrm{Im}\,\lambda = -\sin\phi_s \quad . \tag{5.57}$$

[7] To calculate $\frac{\overline{A}_{J/\psi\,\phi}}{A_{J/\psi\,\phi}}$, it is used that

$$\begin{aligned}
\frac{\overline{A}_f}{A_f} &= \frac{\langle f|H|\overline{B}\rangle}{\langle f|H|B\rangle} = \frac{\langle f|(CP^\dagger CP)H(CP^\dagger CP)|\overline{B}\rangle}{\langle f|H|B\rangle} \\
&= -\eta_f \frac{\langle f|(CP)H(CP^\dagger)|B\rangle}{\langle f|H|B\rangle} = -\eta_f e^{2i\phi_W} \quad ,
\end{aligned}$$

using the convention $\mathrm{CP}|\overline{B}\rangle = -|B\rangle$, $\mathrm{CP}|f\rangle = \eta_f|f\rangle$. The Hamiltonian H can be written as the sum of a CP-conserving (so-called strong) part H_S and a CP-violating (so-called weak) part H_W: $H = H_S + H_W$. In that case, $(CP)H_S(CP^\dagger) = H_S$ and $(CP)H_W(CP^\dagger) = e^{2i\phi_W}H_W$, with ϕ_W the weak phase that flips sign under a CP transformation and finally $(CP)H(CP^\dagger) = e^{2i\phi_W}H$.

[8] Eq. 1.11 defines $\beta_s \equiv \arg\left(-\frac{V_{cb}V_{cs}^*}{V_{tb}V_{ts}^*}\right)$. Equivalently, $\beta_s = \arg(-1) - \arg\left(\frac{V_{tb}V_{ts}^*}{V_{cb}V_{cs}^*}\right)$. From the last equation, one finds $\phi_s = 2\arg\left(\frac{V_{tb}V_{ts}^*}{V_{cb}V_{cs}^*}\right) = 2(\arg(-1) - \beta_s) = -2\beta_s$.

Here, S, C and D do not depend on $\eta_{J/\psi\,\phi}$, as this parameter was absorbed in the time-dependence, contrary to what is usually found in literature.

As an example, when substituting S, C and D, the first term in the signal PDF from Eq. 5.49 becomes:

$$\begin{aligned} T_1(t) f_1(\vec{\Omega}) &= |a_0|^2 e^{-\Gamma_s t} \\ &\times \left(\cosh\left(\frac{\Delta\Gamma_s t}{2}\right) - \cos\phi_s \sinh\left(\frac{\Delta\Gamma_s t}{2}\right) + \sin\phi_s \sin(\Delta m_s t) \right) \\ &\times \cos^2\psi (1 - \sin^2\theta \cos^2\phi) \quad . \end{aligned} \tag{5.58}$$

5.8 $\phi_{M/\Gamma}$ versus ϕ_s

The parameter $\phi_{M/\Gamma}$ was defined in Eq. 1.34 as $\phi_{M/\Gamma} = \phi_M - \arg(-\Gamma_{12})$ and reflects the CP violation in mixing as can be measured via the parameter $a_{\rm sl}$ [14]. Alternatively, the parameter $\phi_s = \phi_M - 2\,\phi_{c(\overline{c}s)}$ is sensitive to CP violation in the interference between decays with and without mixing. This parameter can be measured using $B_s^0 \to J/\psi\,\phi$ decays. There is a relation between ϕ_s and $\phi_{M/\Gamma}$ that can be summarized as follows:

- $\phi_s = \phi_M - 2\,\phi_{c(\overline{c}s)}$: As shown in Sec. 5.7, $\phi_s = -2\beta_s = \arg\left[\frac{(V_{tb}V_{ts}^*)^2}{(V_{cb}V_{cs}^*)^2}\right]$. Here, in the convention used, $\phi_M = \arg[(V_{tb}V_{ts}^*)^2]$ originates from mixing and $\phi_{c(\overline{c}s)}$ is the weak phase that originates from the calculation of $\frac{\overline{A}_{J/\psi\,\phi}}{A_{J/\psi\,\phi}}$.

- $\phi_{M/\Gamma} = \phi_M - \arg(-\Gamma_{12})$: In this parameter, again, ϕ_M gives rise to a phase $\arg[(V_{tb}V_{ts}^*)^2]$. The contribution of $\arg(-\Gamma_{12})$ includes all possible on-shell $b \to q(\overline{q}s)$ transitions and thus can be written as $\arg(\kappa_c V_{cs}^* V_{cb} + \kappa_u\, V_{us}^* V_{ub})^2$, with $\kappa_{c,u}$ real numbers that represent the relative contributions of $b \to c(\overline{c}s)$ and $b \to u(\overline{u}s)$ transitions, respectively. As a result,

$$\begin{aligned} \phi_{M/\Gamma} &= \arg\left(\frac{M_{12}}{-\Gamma_{12}}\right) = \arg\left(\frac{(V_{tb}V_{ts}^*)^2}{(\kappa_c\, V_{cs}^* V_{cb} + \kappa_u\, V_{us}^* V_{ub})^2}\right) \\ &= \arg\left(\frac{(V_{tb}V_{ts}^*)^2}{(\kappa_c\, V_{cs}^* V_{cb}[1 + \frac{\kappa_u}{\kappa_c}\frac{V_{us}^* V_{ub}}{V_{cs}^* V_{cb}}])^2}\right) \\ &= \arg\left(\frac{(V_{tb}V_{ts}^*)^2}{(\kappa_c\, V_{cs}^* V_{cb}[1 + \frac{\kappa_u}{\kappa_c}\lambda^2\, e^{-i\gamma}])^2}\right) \quad , \end{aligned} \tag{5.59}$$

  where λ is the Wolfenstein parameter and γ is the phase appearing in V_{ub}.

If, in the denominator of Eq. 5.59, $(\kappa_c\, V_{cs}^* V_{cb}[1 + \frac{\kappa_u}{\kappa_c}\lambda^2\, e^{-i\gamma}])^2$, the term proportional to λ^2 is neglected, one finds $\phi_{M/\Gamma} = \phi_M - \arg(-\Gamma_{12}) = \phi_M - 2\,\phi_{c(\overline{c}s)}$ [19] and thus $\phi_{M/\Gamma} = \phi_s$. Indeed, both $\phi_{M/\Gamma}$ and ϕ_s are expected to be small in the SM [50, 51]:

$$\begin{aligned} \phi_{M/\Gamma} &= (0.0041 \pm 0.0008)\,\text{rad} = (0.24 \pm 0.04)^\circ \\ \phi_s &= -2\beta_s = -(0.036 \pm 0.002)\,\text{rad} = -(2.1 \pm 0.1)^\circ \quad . \end{aligned}$$

However, they do differ numerically, indicating that this approximation is not justified[9]. Any short-distance New Physics contribution in B_s^0 oscillations will affect ϕ_M and thus both $\phi_{M/\Gamma}$ and ϕ_s.

5.9 Penguin Contributions

In the Standard Model, using only tree-level diagrams as shown in Fig. 5.3, it was derived in Eq. 5.56 that $\phi_s^{\rm SM} = -2\beta_s$. However, loop diagrams, specifically so-called penguin diagrams as shown in Fig. 5.4, contribute to the total $\bar{b} \to \bar{c}c\bar{s}$ decay amplitude:

$$\begin{aligned} A(\bar{b} \to \bar{c}c\bar{s}) &= V_{cs}V_{cb}^*(T_c + P_c) + V_{us}V_{ub}^* P_u + V_{ts}V_{tb}^* P_t \\ &= V_{cs}V_{cb}^*(T_c + P_c - P_t) + V_{us}V_{ub}^*(P_u - P_t) \quad , \end{aligned} \tag{5.60}$$

where, after the CKM elements have been explicitly factored out, T_c is the tree contribution and P_i the penguin contribution with a quark $i \in \{u, c, t\}$ in the loop. In addition, unitarity of the CKM matrix is used: $V_{ts}V_{tb}^* = -V_{us}V_{ub}^* - V_{cs}V_{cb}^*$. The second term in Eq. 5.60 is doubly Cabibbo-suppressed with respect to the first term ($|V_{us}V_{ub}^*| \sim \lambda^4$ versus $|V_{cs}V_{cb}^*| \sim \lambda^2$). The first term, proportional to $V_{cs}V_{cb}^*$, includes both tree and penguin contributions, but these penguin contributions have the same phase as the tree contribution and thus do not change the value of ϕ_s.

The Cabibbo suppressed penguin contributions are difficult to calculate from QCD, but due to their different weak phase might result in a value for $\sin\phi_s$ as large as -0.1 [53], compared to $\sin\phi_s \sim -0.03$, assuming negligible penguin contributions. Therefore, these penguin contributions should be measured experimentally. It has been proposed [53] to do this by analyzing $B_s^0 \to J/\psi \overline{K}^{*0}$ decays, which are also indicated in Fig. 5.4. Applying SU(3) flavour symmetry arguments, the decay amplitude of these decays are written in a similar way as Eq. 5.60, replacing the quark index s by d:

$$A(\bar{b} \to \bar{c}c\bar{d}) = V_{cd}V_{cb}^*(T_c + P_c - P_t) + V_{ud}V_{ub}^*(P_u - P_t) \quad . \tag{5.61}$$

In this case, however, the second term, $V_{ud}V_{ub}^*(P_u - P_t)$, is not Cabibbo suppressed with respect to the first term, since both $|V_{ud}V_{ub}^*|$ and $|V_{cd}V_{cb}^*|$ are of order λ^3. This means that the relative size of the first term with respect to the second term, $\frac{P_u - P_t}{T_c + P_c - P_t}$ can be determined by analyzing $B_s^0 \to J/\psi \overline{K}^{*0}$ decays. Including penguin contributions, the parameter ϕ_s is rewritten as

$$\phi_s^{\rm SM} = -2\beta_s + \phi_{\rm penguin}^{\rm SM} \quad . \tag{5.62}$$

[9] In the B_d^0-system the corresponding difference between these parameters is more pronounced: $\phi_{M/\Gamma}^d = -5.2^\circ\,^{+1.5^\circ}_{-2.1^\circ}$ [52], whereas $\phi_d = -2\beta = 43.7^\circ\,^{1.6^\circ}_{1.5^\circ}$ [17].

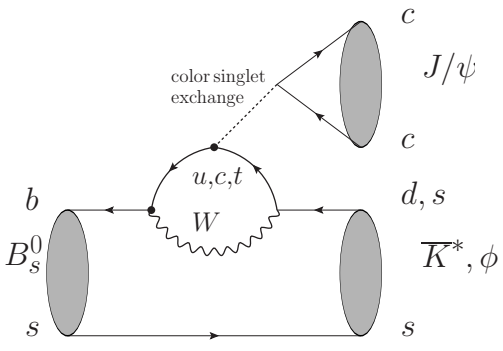

Figure 5.4: *Penguin contributions to $B_s^0 \to J/\psi\,\phi$ decays and the decay $B_s^0 \to J/\psi\,\overline{K}^*$, depending on the flavour of the outgoing quark, $\overline{s}$ or $\overline{d}$, respectively.*

5.10 New Physics Contributions

New Physics (NP) can contribute both at the decay amplitude level and to the amplitude of B_s^0 oscillations [54]. At the decay amplitude level, NP effects must be small, since they have not been observed in $B^0 \to J/\psi K_S$ decays, for example. New Physics could still contribute to B_s^0 oscillations, since heavy, virtual, NP particles can contribute to loop diagrams. This will affect M_{12} and in particular ϕ_M. Including NP effects, Γ_{12} remains unchanged and M_{12} generically changes as [50]

$$M_{12} \to M_{12}^{\rm SM}\Delta_s = M_{12}^{\rm SM}|\Delta_s|e^{i\phi^{\Delta_s}} \quad , \tag{5.63}$$

where Δ_s is a complex number representing the deviation factor. Accordingly, ϕ_M changes to

$$\phi_M = \arg(M_{12}) \to \arg(M_{12}^{\rm SM}\Delta_s) = \phi_M^{\rm SM} + \phi^{\Delta_s} \quad . \tag{5.64}$$

Finally, the observable ϕ_s is modified as follows:

$$\phi_s = \phi_s^{\rm SM} + \phi^{\Delta_s} \quad , \tag{5.65}$$

where, as before, $\phi_s^{\rm SM} = -2\beta_s + \phi_{\rm penguin}^{\rm SM}$.

In the SM, ignoring penguin contributions, the value of ϕ_s is small, $\phi_s = -2\beta_s = -0.036 \pm 0.002$ [17], indicating that any significant deviation of ϕ_s from zero is a strong indication of New Physics. This is the main motivation to measure ϕ_s. This measurement is discussed in the following chapter.

CHAPTER

SIX

$B_s^0 \to J/\psi\,\phi$ Analysis

The B_s^0 mixing phase ϕ_s is a sensitive probe for New Physics. In this chapter, the measurement of ϕ_s is presented. The decay of B_s^0 mesons to the final state $J/\psi(\mu^+\mu^-)\,\phi(K^+K^-)$ was first observed by the CDF collaboration [55] and the branching ratio has been measured by both the CDF collaboration [56] and the Belle collaboration [57].

The CDF collaboration and the D0 collaboration (both situated at the Tevatron accelerator at Fermilab) have published results on the measurement of ϕ_s using datasets of $5.2\,\text{fb}^{-1}$ [58] and $8\,\text{fb}^{-1}$ [59] of integrated luminosity, respectively. The LHCb collaboration has published its first results on ϕ_s using $0.37\,\text{fb}^{-1}$ of integrated luminosity [60]. Although the LHCb dataset corresponds to a smaller integrated luminosity, the number of $B_s^0 \to J/\psi\,\phi$ candidates is larger in LHCb due to the larger production cross section at the LHC, as compared to the Tevatron. The dataset for the analysis presented here is three times larger than the one in [60] and corresponds to $1.0\,\text{fb}^{-1}$ of integrated luminosity. As a result, this analysis leads to the most accurate measurement of ϕ_s to date.

6.1 Candidate Selection

The analysis presented in this chapter is based on $B_s^0 \to J/\psi\,\phi$ candidates recorded during the 2011 LHC running period at a center-of-mass energy of $\sqrt{s} = 7\,\text{TeV}$. The event selection of $B_s^0 \to J/\psi\,\phi$ candidates is performed in three steps: first the online trigger selection (L0, HLT1 and HLT2), followed by the stripping pre-selection and finally the offline selection.

6.1.1 Trigger Selection

The first stage in the extraction of $B_s^0 \to J/\psi\,\phi$ candidates is the trigger selection. As discussed in Sec. 2.6, the level-0 (L0) hardware trigger selects muon candidates with large transverse momentum p_T. Subsequently, the software trigger selects events in two stages: HLT1 and HLT2. In this analysis, only those events that are explicitly triggered on the two muons of the J/ψ candidate are used.

In the HLT1[1], a partial event reconstruction is performed and $\mu^+\mu^-$ candidates are required to have two well-identified muons whose trajectories have a distance of closest approach to each other smaller than 0.2 mm, a good vertex fit, i.e. $\chi^2_{\rm vertex}/{\rm nDoF} < 25$, and an invariant mass of at least 2.7 GeV/c^2 [61]. Note that there are no explicit requirements that affect the decay-time distribution, hence no decay-time acceptance is introduced in this HLT1 line[2].

In the HLT2[3], the J/ψ candidates reconstructed from di-muon pairs are required to have a minimum p_T of 1.5 GeV/c, and only candidates with a reconstructed mass within 120 MeV/c^2 from the nominal J/ψ meson mass (3096 MeV/c^2 [23]) are accepted: $2976\,{\rm MeV}/c^2 < m(\mu^+\mu^-) < 3216\,{\rm MeV}/c^2$. In addition, two cuts are applied to reject short-lived candidates where the largest background contribution is expected: for each muon, there is a cut on the χ^2 of the impact parameter (IP) with respect to the PV, i.e. $\chi^2_{\rm IP}(\mu) > 9$, and in addition there is a di-muon vertex separation cut with respect to the closest PV (decay length significance (DLS) > 3 [61]). Note that these cuts affect the decay-time distribution of the $B^0_s \to J/\psi\,\phi$ event candidates, which will introduce a non-trivial efficiency as a function of decay time in the analysis.

6.1.2 Stripping and Selection Cuts

After offline reconstruction, a so-called stripping procedure is applied to obtain manageable datasets[4]. The final selection is applied to these so-called stripped datasets to obtain the sample of $B^0_s \to J/\psi\,\phi$ candidates used for the determination of ϕ_s.

In the final dataset, muon candidates are each required to have $p_T > 0.5\,{\rm GeV/c}$. Muons are distinguished from pions by requiring a difference of the particle ID log-likelihood $LL(\mu) - LL(\pi) \equiv DLL(\mu\pi) > 0$ (see Sec. 2.5.1). The corresponding J/ψ candidates are created from pairs of oppositely charged muons that have a common vertex which satisfies $\chi^2_{\rm vertex}/{\rm nDoF}(J/\psi) < 16$. The reconstructed di-muon mass is required to be in the range $3030\,{\rm MeV}/c^2 < m(\mu^+\mu^-) < 3150\,{\rm MeV}/c^2$.

The ϕ meson candidates are selected by requiring two oppositely charged kaon candidates with $DLL(K\pi) > 0$, originating from a common vertex with $\chi^2_{\rm vertex}/{\rm nDoF}(\phi) < 16$. In addition, the p_T of the ϕ meson candidate is required to be larger than 1 GeV/c^2. The reconstructed invariant mass should be within 12 MeV/c^2 from the nominal ϕ meson mass [23]: $1008\,{\rm MeV}/c^2 < m(K^+K^-) < 1032\,{\rm MeV}/c^2$.

B^0_s candidates are selected from combinations of J/ψ meson candidates and ϕ meson candidates with an invariant mass in the range $5200\,{\rm MeV}/c^2 < m(J/\psi\,K^+K^-) < 5550\,{\rm MeV}/c^2$. The invariant mass of the B^0_s candidate is computed with the invariant mass of the $\mu^+\mu^-$ pair constrained to the nominal J/ψ mass. The decay time is obtained from a kinematic fit [62]. This algorithm constrains the $B^0_s \to \mu^+\mu^-K^+K^-$ candidate to originate from the PV by imposing a B^0_s vertex cut ($\chi^2_{\rm vertex}/{\rm nDoF}(B^0_s) < 10$), an impact parameter cut ($\chi^2_{\rm IP}(B^0_s) < 25$) and finally a cut on the χ^2 of the kinematic fit itself

[1] The HLT1 trigger line used in this analysis is the decay time unbiased trigger line `Hlt1DiMuonHighMass`.
[2] Assuming that the track reconstruction in the VELO is independent of the decay time, see Sec. 6.3.2.
[3] The HLT2 trigger line used in this analysis is the decay time biased trigger line `Hlt2DiMuonDetachedJpsi`.
[4] The $B^0_s \to J/\psi\,\phi$ candidates used in this analysis are processed using reconstruction version `Reco12` and stripping version `Stripping17`.

decay mode	cut parameter	stripping	selection
all tracks	$\chi^2_{\rm track}/{\rm nDoF}$	< 5	< 4
	clone distance	> 5000	-
$J/\psi \to \mu^+\mu^-$	$DLL(\mu\pi)$	> 0	-
	$p_T(\mu)$	$> 0.5\,{\rm GeV}/c$	-
	$\chi^2_{\rm vertex}/{\rm nDoF}(J/\psi)$	< 16	-
	$\chi^2_{\rm DOCA}(J/\psi)$	< 20	-
	$m(\mu^+\mu^-)$	$\in [3010, 3170]\,{\rm MeV}/c^2$	$\in [3030, 3150]\,{\rm MeV}/c^2$
$\phi \to K^+K^-$	$DLL(K\pi)$	> -2	> 0
	$p_T(\phi)$	$> 0.5\,{\rm GeV/c}$	$> 1\,{\rm GeV/c}$
	$\chi^2_{\rm track}/{\rm nDoF}(K)$	< 4	-
	$\chi^2_{\rm vertex}/{\rm nDoF}(\phi)$	< 16	-
	$\chi^2_{\rm DOCA}(\phi)$	< 30	-
	$m(K^+K^-)$	$\in [980, 1050]\,{\rm MeV}/c^2$	$\in [1008, 1032]\,{\rm MeV}/c^2$
$B_s^0 \to J/\psi\,\phi$	$\chi^2_{\rm vertex}/{\rm nDoF}(B_s^0)$	< 10	-
	$\chi^2_{\rm kin.fit(B+PV)}/{\rm nDoF}(B_s^0)$	-	< 5
	$\chi^2_{\rm IP}(B_s^0)$	-	< 25
	$\chi^2_{\rm IP,next}(B_s^0)$	-	> 50
	$m(J/\psi\,\phi)$	$\in [5200, 5550]\,{\rm MeV}/c^2$	$\in [5200, 5550]\,{\rm MeV}/c^2$
	$t^{(*)}$	$> 0.2\,{\rm ps}$	$\in [0.3, 14]\,{\rm ps}$

Table 6.1: *Stripping and selection criteria for $B_s^0 \to J/\psi\,\phi$ candidates. (*): the stripping decay time and offline decay time are calculated from different algorithms.*

($\chi^2_{\rm kin.fit(B+PV)}/{\rm nDoF} < 5$). In case of multiple candidates per event[5], only the candidate with the smallest $\chi^2_{\rm kin.fit(B+PV)}/{\rm nDoF}$ is kept. Finally, in order to prevent misassociation of the B_s^0 candidate with the next-best PV, which would clearly result in an incorrect decay time, the B_s^0 candidate must have an impact parameter $\chi^2_{\rm IP}$ to the next-best PV in the event greater than 50. This enforces the B_s^0 candidate to be inconsistent with coming from this next-best PV.

Only $B_s^0 \to J/\psi\,\phi$ candidates with a decay time within $0.3 < t < 14\,{\rm ps}$ are considered in the analysis. The lower decay-time cut suppresses a large fraction of the prompt combinatorial background, while losing little in sensitivity to ϕ_s. The upper decay-time cut avoids the use of pathological events (misreconstructed or associated to a wrong PV) while losing only very few signal events. A summary of the stripping and selection cuts is given in Table 6.1.

To illustrate the mass resolution and small background levels, the mass distributions of the reconstructed J/ψ and ϕ meson candidates, after applying all selection criteria, are given in Fig. 6.1. The small background in the di-muon invariant-mass distribution suggests that the main background contribution originates from events containing genuine J/ψ mesons.

[5]The average number of candidates per event is 1.10 with an average number of primary vertices of 2.42.

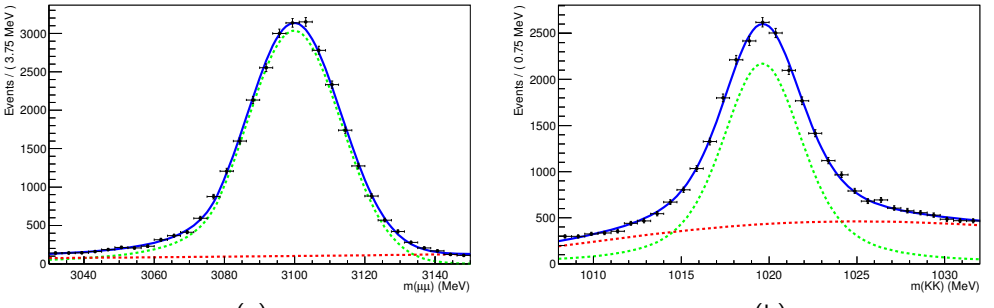

(a) (b)

Figure 6.1: *(a) Invariant mass distribution of the J/ψ meson candidates after applying all selection criteria. (b) Invariant mass distribution of the ϕ meson candidates after applying all selection criteria.*

parameter	value
β_s	0.02
Γ_s	0.6793 ps^{-1}
$\Delta\Gamma_s$	0.060 ps^{-1}
Δm_s	17.8 ps^{-1}
$\lvert A_0(0)\rvert^2$	0.60
$\lvert A_\perp(0)\rvert^2$	0.16
$\lvert A_\parallel(0)\rvert^2$	0.24
δ_0	0
$\delta_\perp$	-0.17
$\delta_\parallel$	2.50

Table 6.2: *Decay model parameters for the simulated sample of $B_s^0 \to J/\psi\,\phi$ events. The values for the transversity amplitudes and strong phases are taken from [63].*

6.2 Angular Acceptance

The detector geometry and the selection criteria introduce an acceptance effect as a function of the decay angles, which must be accounted for in the angular analysis. It is estimated and corrected for by using Monte Carlo simulated data.

6.2.1 MC Dataset

The MC dataset consists of five million simulated $B_s^0 \to J/\psi\,\phi$ events[6]. The parameters of the decay model used to generate these events are given in Table 6.2.

[6]Events are processed by `Sim05-Reco12-Stripping17` (also known as MC11A). The HLT configuration used is TCK 0x40760037, which is representative for the data recorded during and after summer 2011

6.2.2 Reparameterization in Terms of Basis Functions

The distribution of $B_s^0 \to J/\psi\,\phi$ events in terms of decay angles as presented in Table 5.1 and Table 5.3 can be re-expressed in terms of associated Legendre polynomials $P_i(\cos\psi)$ and spherical harmonics $Y_l^m(\cos\theta,\phi)$, where ψ, θ and ϕ are the decay angles in the transversity frame. The reason to do so is that the orthogonality properties of these functions will simplify the implementation of the angular acceptance in the fitting procedure. The basis functions $P_i(\cos\psi)$ and $Y_l^m(\cos\theta,\phi)$, as well as the resulting expressions for the angular dependence of the differential decay rate are given in Appendix E.

While writing the angular-acceptance function as an expansion in terms of the same basis functions $P_i(\cos\psi)$ and $Y_l^m(\cos\theta,\phi)$, the coefficients of this expansion can be calculated from a MC simulated data sample as will be shown in the following section.

6.2.3 Angular-Acceptance Correction

The angular acceptance is implemented in the analysis by multiplying the signal PDF with the angular-acceptance function $\epsilon(\cos\psi,\cos\theta,\phi)$:

$$P_{\text{corrected}}(t,\cos\psi,\cos\theta,\phi) = P_{\text{uncorrected}}(t,\cos\psi,\cos\theta,\phi)\cdot\epsilon(\cos\psi,\cos\theta,\phi) \quad . \tag{6.1}$$

The angular-acceptance function is written as an expansion in terms of associated Legendre polynomials $P_i(\cos\psi)$ and spherical harmonics $Y_l^m(\cos\theta,\phi)$:

$$\epsilon(\vec{\Omega}) = \sum_{i,l,m} c_{lm}^i\, P_i(\cos\psi)\, Y_{lm}(\cos\theta,\phi) \quad , \tag{6.2}$$

where $\vec{\Omega} = (\cos\psi,\cos\theta,\phi)$. The coefficients c_{lm}^i of the expansion are calculated from simulated events as follows.

The simulated data sample is generated according to the theoretical $B_s^0 \to J/\psi\,\phi$ decay distribution $g(\vec{\Omega})$. For an efficiency $\epsilon(\vec{\Omega})$, and a general function $h(\vec{\Omega})$, the following equation holds (following the concept of MC integration):

$$\int \epsilon(\vec{\Omega})h(\vec{\Omega})g(\vec{\Omega})\mathrm{d}\vec{\Omega} \simeq \frac{1}{N_{\text{gen}}}\sum_{e\in\{\text{generated}\}}\epsilon(\vec{\Omega}_e)h(\vec{\Omega}_e) = \frac{1}{N_{\text{gen}}}\sum_{e\in\{\text{accepted}\}}h(\vec{\Omega}_e) \quad . \tag{6.3}$$

Here, the integral is rewritten as a finite sum over the generated events ($\sum_{e\in\{\text{generated}\}}$). As the event is either accepted or not accepted, the per-event efficiency $\epsilon(\vec{\Omega}_i)$ is ±1 and the sum over generated events is rewritten as a sum over accepted events only ($\sum_{e\in\{\text{accepted}\}}$).

It is now argued that an appropriate choice of the function $h(\vec{\Omega})$ allows the calculation of the coefficients c_{lm}^i of the expansion of the angular-acceptance function. Substituting the expansion of the acceptance function from Eq. 6.2 yields

$$\int \sum_{n,j,k} c_{jk}^n P_n(\cos\psi)\, Y_{jk}(\cos\theta,\phi)h(\vec{\Omega})g(\vec{\Omega})\mathrm{d}\vec{\Omega} = \frac{1}{N_{\text{gen}}}\sum_{e\in\{\text{accepted}\}}h(\vec{\Omega}_e) \quad . \tag{6.4}$$

When choosing

$$h(\vec{\Omega}) = \frac{2i+1}{2} \frac{P_i(\cos\psi)\, Y_{lm}(\cos\theta, \phi)}{g(\vec{\Omega})} \quad , \tag{6.5}$$

the orthonormality of the basis functions $P_i(\cos\psi)\, Y_{lm}(\cos\theta, \phi)$ (see Appendix E.4) can be used to find

$$\int g(\vec{\Omega}) \mathrm{d}\vec{\Omega}\, c^n_{jk} P_n(\cos\psi)\, Y_{jk}(\cos\theta, \phi) \cdot \left[\frac{2i+1}{2} \frac{P_i(\cos\psi)\, Y_{lm}(\cos\theta, \phi)}{g(\vec{\Omega})} \right] = c^i_{lm} \quad , \tag{6.6}$$

and hence, using Eq. 6.4

$$c^i_{lm} \quad = \quad \frac{1}{N_{\mathrm{gen}}} \sum_{e \in \{\mathrm{accepted}\}} \frac{2i+1}{2} \frac{P_i(\cos\psi_e)\, Y_{lm}(\cos\theta_e, \phi_e)}{g(\vec{\Omega}_e)} \quad . \tag{6.7}$$

In other words, the coefficients c^i_{lm} are calculated as a finite sum over accepted Monte Carlo events of the function $h(\vec{\Omega}_e)$, as defined in Eq. 6.5. These coefficients fully determine the shape of the acceptance function $\epsilon(\vec{\Omega})$. The decay distributions of the signal events are multiplied with this angular-acceptance function to correct for angular acceptance effects.

Results

6

Using the MC dataset mentioned in Sec. 6.2.1, which is assumed to be representative for the real data (see Sec. 6.7.5 for differences between the MC dataset and the real dataset) used in this analysis, the coefficients of the expansion of the angular-acceptance function are calculated and the acceptance function is projected on the three transversity angles in the upper three figures of Fig. 6.2. In this figure, 41 coefficients c^i_{lm} are used in the expansion[7]. In addition, in the lower three figures of Fig. 6.2, the MC data is shown, together with the theoretical decay distributions of the signal events and the decay distributions corrected for angular acceptance.

6.2.4 Comparison with Normalization-Weights Method

Another method to correct for angular acceptance effects is to calculate ten so-called normalization weights corresponding to the ten angular functions $f_i(\vec{\Omega})$, using Eq. 6.3 and using these weights to normalize the PDF [64]. The two methods can be compared and checked by reconstructing the ten normalization weights from (a subset of) the coefficients c^i_{lm}. This comparison also demonstrates that only a subset of c^i_{lm} actually matters for the minimization in the final fit. The comparison of the two methods is shown in detail in Appendix F. The advantage of the expansion method compared to the normalization-weights method is that the shape of the acceptance function is known, as shown in Fig. 6.2. Another advantage of the expansion method is that no assumption is made on the similarity of the angular-acceptance function between signal and background, while in the normalization-weights method this

[7] In the final analysis, only four coefficients are taken into account, since no difference in the final fit result is observed when using these four coefficients instead of 41 coefficients. The only coefficients used in the final analysis are c^0_{00}, c^0_{22}, c^0_{20} and c^2_{00}.

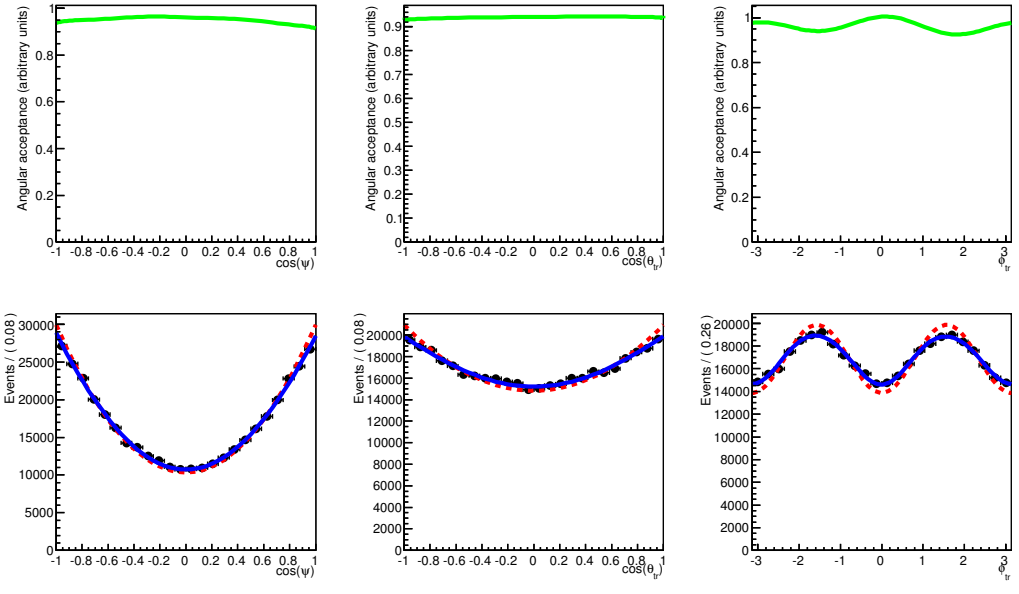

Figure 6.2: *Upper figures: projection of angular-acceptance function on the three decay angles* $\cos\psi$, $\cos\theta$ *and* ϕ *from left to right. Lower figures: MC data (black points), theoretical decay distributions that are used for generation (red dashed curves) and the decay distributions corrected for angular acceptance (blue solid curves).*

assumption is made by construction. Finally, using the expansion method allows to plot differential distributions, which is impossible if only normalization weights are known.

6.3 Decay-Time Acceptance

6.3.1 Acceptance for Small Decay Time

As mentioned in Sec. 6.1, the HLT1 trigger line used in this analysis does not explicitly affect the decay-time distribution of the B_s^0 candidates, whereas the HLT2 line does reject short-living B_s^0 candidates. To quantify this effect, events selected with a similar, prescaled, HLT2 trigger without decay-time biasing cuts are studied. A non-parametric description, i.e. a histogram, of the HLT2 decay-time acceptance is produced from the overlap between events triggered by the unbiased and biased HLT2 lines and is shown in Fig. 6.3. The structure around $t = 2\,\mathrm{ps}$ is understood as so-called vertex splitting [65], when the secondary vertex is unjustly reconstructed as a primary vertex, with respect to which the J/ψ vertex does not pass the DLS cut in the HLT2 trigger as described in Sec. 6.1.1, therefore losing the event. This effect only occurs for moderate decay times, since both at low decay times and at high decay times, no second PV will be reconstructed from the tracks originating from the secondary vertex. The drop in decay-time acceptance is also observed in MC

simulated data. The decay-time acceptance is implemented in the analysis by multiplying the theoretical decay-time distribution with the acceptance histogram.

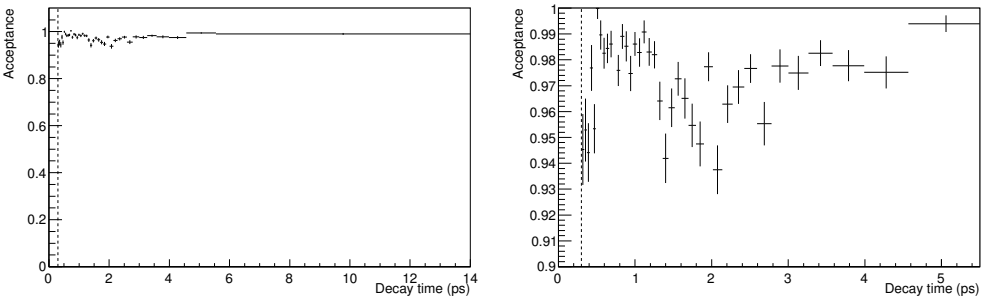

Figure 6.3: *(a) The decay-time acceptance of the biased HLT2 trigger line, determined from the overlap between events triggered by the unbiased and biased HLT2 lines. (b) Zoom-in of the low-lifetime region. Notice the adjusted scale on the y-axis. The offline decay-time cut at 0.3 ps is indicated by the dashed line. The structure around $t = 2\,\mathrm{ps}$ is understood as vertex splitting (see text).*

6

6.3.2 Acceptance for Large Decay Time

From MC studies, a linear drop in acceptance is observed for large decay time, which is attributed to a reduced track-finding efficiency for tracks originating from vertices that are radially displaced from the beam axis. The acceptance is parameterized as $\epsilon(t) = 1 + \beta\, t$, with $\beta = -0.0112 \pm 0.0013\,\mathrm{ps}$. By performing two fits to the data, one including and the other not including this decay-time acceptance, it is found that only the average lifetime Γ_s is affected. Therefore, in the final analysis, the acceptance for large decay time is not explicitly taken into account, but the parameter Γ_s is corrected analytically a posteriori[8].

6.4 Flavour Tagging

The CP-violation phase ϕ_s can be measured thanks to the interference between a direct decay amplitude and a decay amplitude which includes oscillation, which results in a differ-

[8] The corrected value Γ_s is obtained from the fitted value $\Gamma_{s,\mathrm{fit}} = \frac{1}{\tau_{s,\mathrm{fit}}}$, where $\tau_{s,\mathrm{fit}}$ is assumed to be the average of the decay-time distribution $\langle t \rangle$, in the following way:

$$\frac{1}{\Gamma_{s,\mathrm{fit}}} = \langle t \rangle = \frac{\int_0^\infty t(1+\beta t)e^{-\Gamma_s t}}{\int_0^\infty (1+\beta t)e^{-\Gamma_s t}} = \frac{2\beta + \Gamma_s}{\Gamma_s(\beta + \Gamma_s)} \quad , \tag{6.8}$$

which yields

$$\Gamma_s = \frac{\Gamma_{s,\mathrm{fit}}}{2}\left(1 - \beta/\Gamma_{s,\mathrm{fit}} + \sqrt{(1 + 6(\beta/\Gamma_{s,\mathrm{fit}}) + (\beta/\Gamma_{s,\mathrm{fit}})^2)}\right) \quad . \tag{6.9}$$

ence in decay rates between B_s^0 and $\overline{B}_s^0$ initial states. Therefore, the identification of the initial flavour (at production) of the reconstructed B_s^0 candidate is a crucial element in the ϕ_s analysis. The flavour tag q_T, which takes the values -1 for $\overline{B}_s^0$, +1 for B_s^0 and 0 for untagged events, is assigned by combining different tagging algorithms [66]. The combination procedure assigns an estimate of the per-event mistag probability η. In this thesis, only so-called opposite-side (OS) tagging algorithms are used that exploit the following features in the decay of the other, accompanying (non-signal) B hadron:

- the charge of a muon or electron with large transverse momentum produced by semileptonic B decays,
- the charge of a kaon from a subsequent charmed hadron decay,
- the momentum-weighted charge of all tracks included in the inclusively reconstructed decay vertex.

These three different OS taggers are illustrated by a schematic picture of a $B_s^0 \to J/\psi\,\phi$ decay in Fig. 6.4. For this analysis, the so-called same-side (SS) kaon tagger that uses the

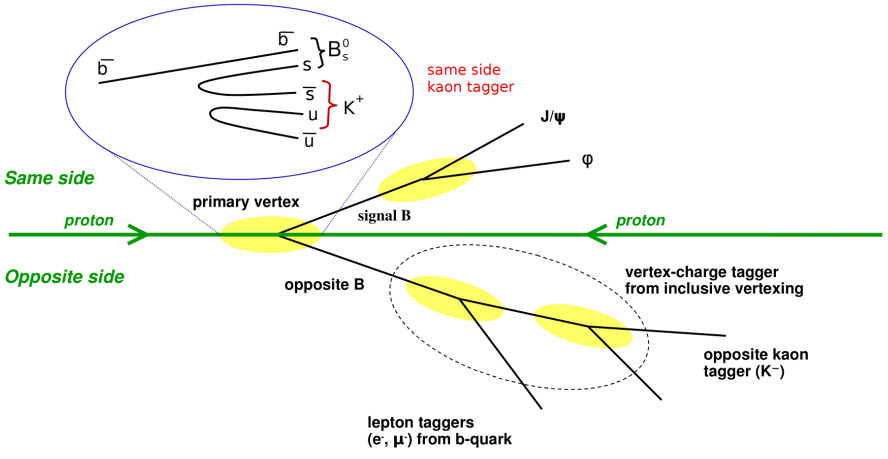

Figure 6.4: *Illustration of the different taggers used in LHCb. For this analysis, only the opposite-side (OS) taggers are used.*

charged kaons originating from the hadronization of the signal B_s^0 meson, is not used.

The tagging algorithms are calibrated by comparing the estimated mistag probability to the measured mistag probability in so-called self-tagging decays (e.g. $B^+ \to J/\psi\,K^+$ decays). A linear dependence is assumed between the estimated mistag probability η and the actual mistag probability w:

$$w = p_0 + p_1(\eta - \langle\eta\rangle) \quad , \tag{6.10}$$

parameter	value
p_0	0.392 ± 0.009
p_1	1.035 ± 0.024
$< \eta >$	0.391

Table 6.3: *Fitted calibration parameters for the combined OS taggers, obtained from a $B^+ \to J/\psi\, K^+$ sample.*

with p_0 and p_1 calibration parameters and $\langle\eta\rangle$ the average estimated mistag probability in the calibration sample. If p_1 is found to be close to 1 and p_0 close to $\langle\eta\rangle$, then this indicates that the estimated mistag probability based on information from simulated data is already close to the actual value ($w \simeq \eta$). A correct estimation of w is important, since it directly affects the determination of ϕ_s.

The calibration parameters p_0 and p_1 are obtained from a background-subtracted $B^+ \to J/\psi\, K^+$ sample as shown in Fig. 6.5 and the results are summarized in Table 6.3. The found values of $p_0 \simeq \langle\eta\rangle$ and $p_1 \simeq 1$ indicate indeed that the estimated mistag probability η is close to the real mistag probability w.

The uncertainties in the tagging calibration parameters p_0 and p_1 are implemented as Gaussian constraints in the final analysis, allowing the tagging calibration parameters p_0 and p_1 to vary within their uncertainties in the maximum likelihood fit for ϕ_s.

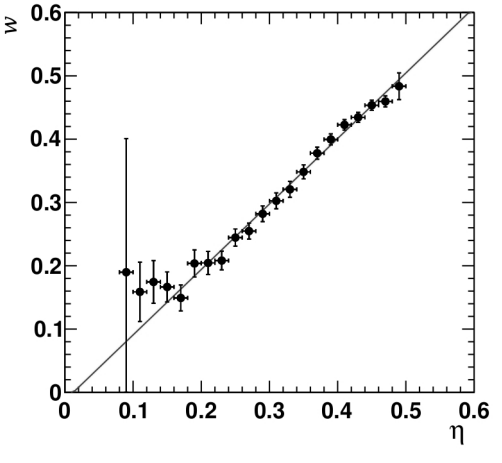

Figure 6.5: *Actual mistag probability w versus estimated mistag probability η for a background-subtracted $B^+ \to J/\psi\, K^+$ sample. The fit parameters are given in Table 6.3.*

The fact that the mistag probability w is non-zero, i.e. that the tag decision q_T is not perfect, leads to so-called dilution factors in the signal PDF. When considering terms with a tag decision $q_T = 1$, there is a contribution P from events that are tagged as B_s^0 with

probability $1-w$, but also a contribution $\overline{P}$ from events that are true $\overline{B}_s^0$ but mis-tagged as B_s^0 with probability w. The resulting expression for terms in the signal PDF with $q_T = 1$ becomes

$$\begin{aligned} P(q_T = 1) &= (1+w)P + w\overline{P} \\ &= (1-w)(U+T) + w(U-T) = U + (1-2w)T\,, \end{aligned} \tag{6.11}$$

where U indicates the untagged terms that do not involve q_T and T denotes the tagged terms that do involve q_T. For example, looking back at Table 5.2, the columns labelled by a_i and c_i represent the untagged terms, while the columns labelled by b_i and d_i represent the tagged terms that indeed flip sign in the $\overline{B}_s^0$ PDF due to the appearance of q_T. From Eq. 6.11 it follows that all the terms in the PDF involving q_T are replaced by Dq_T, where $D \equiv (1-2w)$ is the so-called dilution factor. Untagged events are accounted for by setting their mistag probability to $w = 0.5$.

The raw CP asymmetry A_{CP} is multiplied by the effective dilution D_{eff} to find the observed CP asymmetry:

$$A_{\text{observed}} = D_{\text{eff}} A_{CP} \quad . \tag{6.12}$$

The sensitivity to the observed CP asymmetry (and thus to ϕ_s) is written as

$$\sigma(A_{CP}) = \frac{1}{D_{\text{eff}}}\sigma(A_{\text{observed}}) \propto \frac{1}{D_{\text{eff}}}\frac{1}{\sqrt{\epsilon_T N}} = \frac{1}{\sqrt{\epsilon_T D_{\text{eff}}^2 N}} \equiv \frac{1}{\sqrt{QN}} \quad , \tag{6.13}$$

where ϵ_T is the tagging efficiency. In other words, the effective statistical power of the data sample scales with QN. The effective dilution D_{eff} of the full data sample is defined as

$$D_{\text{eff}}^2 = \frac{1}{N}\sum D_i^2 = \frac{1}{N}\sum_{i\in\text{tagged}} (1-2w_i)^2 \equiv (1-2w_{\text{eff}})^2 \quad . \tag{6.14}$$

From the calibration parameters in Table 6.3 and the distribution of η in the $B_s^0 \to J/\psi\,\phi$ dataset, the effective mistag probability is calculated as $w_{\text{eff}} = (36.8 \pm 0.2\,(\text{stat.}) \pm 0.7\,(\text{syst.}))\%$. The fraction of tagged events in the sample is $\epsilon_T = (32.99 \pm 0.33)\%$. This leads to an effective tagging power $Q = \epsilon_T D_{\text{eff}}^2 = (2.29 \pm 0.07\,(\text{stat.}) \pm 0.26\,(\text{syst.}))\%$.

6.5 Unbinned Likelihood Fits

The fit model that will be described in the following sections will finally result in a PDF that depends on several parameters (including the physics parameters that were introduced in the signal PDF, see Sec. D) and aims at describing the data on a per-event level. Using the PDF and the observed data, the so-called likelihood function is constructed:

$$L(\vec{\Pi};\vec{\mathcal{O}}) \equiv \prod_{i=1}^{n} \text{PDF}(\vec{\mathcal{O}}_i, \vec{\Pi}) \quad , \tag{6.15}$$

where $\vec{\mathcal{O}}$ is the set of observables, $\vec{\Pi}$ is the set of parameters and $\text{PDF}(\vec{\mathcal{O}}_i, \vec{\Pi})$ is the value of the PDF for event i, given the set of parameters $\vec{\Pi}$. The parameters $\vec{\Pi}$ are found by

maximizing the likelihood function (or equivalently, by minimizing the negative log-likelihood function), choosing the parameter set such that the observed data is as likely as possible for this PDF. All fit results in this thesis are obtained from unbinned minimum log-likelihood fits, using RooFit [67].

6.6 Fit Model

In Chap. 5, the differential $\overset{(-)}{B}{}^0_s \to J/\psi\,\phi$ decay rate as a function of the decay time and decay angles was derived. In Sec. 6.4 two more observables were introduced, i.e. the tagging observables q_T and η. In the PDF, both q_T and η are treated as conditional parameters. Choosing q_T as a conditional parameter effectively implies that the PDF for $q_T = 1$ and the one for $q_T = -1$ are normalized separately. The advantage of this choice is that it reduces the impact of a possible $B^0_s - \overline{B}^0_s$ production asymmetry when measuring the time-dependent CP asymmetry[9].

In this section, the full differential decay distribution (in terms of normalized probability density functions (PDF)) are discussed, as a function of $t, \cos\psi, \cos\theta, \phi$, the tagging observables q_T and η, the reconstructed B^0_s mass, m, and finally, the per-event decay-time error, σ_t. The full PDF consists of a signal component and a background component and is written accordingly as

$$P(\vec{\mathcal{O}}) = \left(\frac{N_{\rm signal}}{N_{\rm signal} + N_{\rm bkg}}\, P_{\rm signal}(\vec{\mathcal{O}}) + \frac{N_{\rm bkg}}{N_{\rm signal} + N_{\rm bkg}}\, P_{\rm bkg}(\vec{\mathcal{O}}) \right) P_{\rm Poisson}(N_{\rm signal}+N_{\rm bkg}) \quad , \tag{6.16}$$

where $P_{\rm Poisson}(N_{\rm signal} + N_{\rm bkg})$ is a Poisson term that is included because of the choice to fit for both $N_{\rm bkg}$ and $N_{\rm signal}$[10]. Here, $\vec{\mathcal{O}}$ is a shorthand notation for all observables, $P_{\rm signal}$ and $P_{\rm bkg}$ are the signal and background PDF, respectively and $N_{\rm signal}$ and $N_{\rm bkg}$ are the number of signal and background events, respectively.

6.6.1 Signal Component of the PDF

The signal component of the PDF, $P_{\rm signal}(\vec{\mathcal{O}})$, that appears in Eq. 6.16, is written as

$$P_{\rm signal}(\vec{\mathcal{O}}) = P_{\rm signal}(m)\, P_{\rm signal}(t, \cos\psi, \cos\theta, \phi \,|\, q_T, \eta)\, P_{\rm signal}(q_T)\, P_{\rm signal}(\eta) \quad , \tag{6.17}$$

where the observables right of the vertical bar (|) indicate conditional parameters. In this equation, only the PDFs for the reconstructed B^0_s mass, m, and the tagging observables q_T and η have not been addressed yet:

- $P_{\rm signal}(m)$ is modelled as the sum of two Gaussians $f_1 G_1(\mu, \sigma_1) + (1 - f_1) G_2(\mu, \sigma_2)$, with the same mean μ, centered around the reconstructed B^0_s mass, but with different

[9] A priori, the difference between the number of B^0_s and $\overline{B}^0_s$ mesons is expected to be small when ϕ_s is close to zero. Any source of $B^0_s - \overline{B}^0_s$ asymmetry (e.g. a production asymmetry) can influence the fitted value of ϕ_s when normalizing the entire PDF (i.e. not choosing q_T as a conditional parameter) instead of separately normalizing the PDF for B^0_s and $\overline{B}^0_s$.

[10] The addition of the Poisson term is needed to correctly estimate the errors on $N_{\rm bkg}$ and $N_{\rm signal}$ (as opposed to fitting for only the fraction of signal events $f_{\rm signal}$ when this term is not needed).

width and $\sigma_2/\sigma_1 = 2.258$ fixed from MC simulated events. In addition, also the fraction $f_1 = 0.803$ is fixed from MC. The only free parameters are μ and σ_1. Studies reveal that possible peaking backgrounds from similar final states such as $B_d^0 \to J/\psi\,K^{*0}$ are negligible [60].

- $P_{\text{signal}}(q_T)$: The PDF for the tag decision q_T (where q_T is equal to either ± 1 or 0) is written as

$$P_{\text{signal}}(q_T) = \begin{cases} 1 - \epsilon_{T,\text{signal}} & \text{if } q_T = 0 \\ \frac{1}{2}\epsilon_{T,\text{signal}}(1 + q_T \delta_{T,\text{signal}}) & \text{if } q_T = \pm 1 \end{cases} . \tag{6.18}$$

  Here, $\epsilon_{T,\text{signal}}$ is the tagging efficiency for signal events and $\delta_{T,\text{signal}}$ is the so-called signal tagging-efficiency asymmetry between the tags $q_T = 1$ and $q_T = -1$.

- $P_{\text{signal}}(\eta)$ is modelled in a non-parametric way. The PDF is sampled from the distribution of η of a weighted dataset that represents the signal component of the data (see Sec. 6.6.3) and is shown in Fig. 6.6.

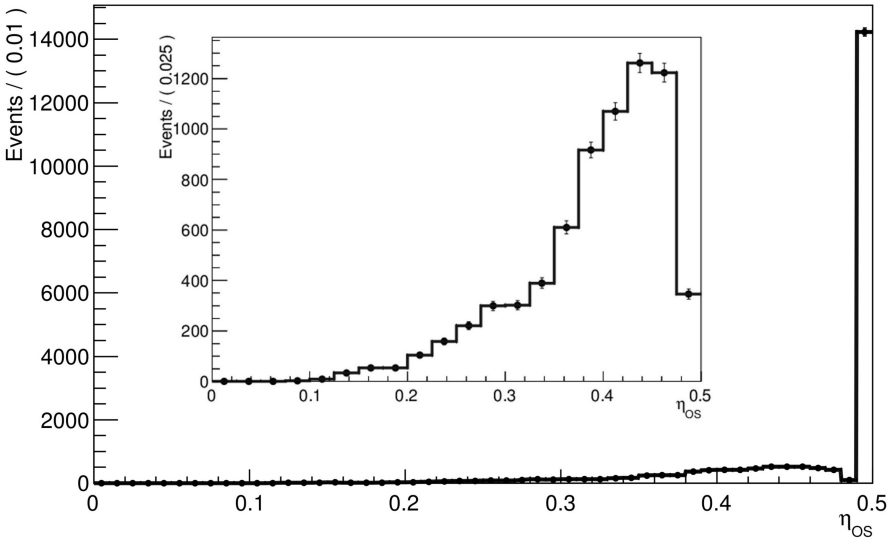

Figure 6.6: *Distribution of η for weighted data representing the signal component of the data (black points). The PDF $P_{\text{signal}}(\eta)$ is indicated by the solid line. The events in the last bin at $\eta = 0.5$ represent the untagged events with $q_T = 0$, and correspond to about 67% of the events. Inset: identical, but with the untagged events at $\eta = 0.5$ removed.*

6.6.2 Background Component of the PDF

The background component of the PDF, $P_{\rm bkg}(\vec{\mathcal{O}})$, that appears in Eq. 6.16, is written as

$$P_{\rm bkg}(\vec{\mathcal{O}}) = P_{\rm bkg}(t)\, P_{\rm bkg}(\cos\psi, \cos\theta, \phi)\, P_{\rm bkg}(m)\, P_{\rm bkg}(q_T)\, P_{\rm bkg}(\eta) \quad . \tag{6.19}$$

The various distributions of the observables are modelled as follows:

- $P_{\rm bkg}(t)$ is modelled as the sum of two exponentials:

$$P_{\rm bkg}(t) = f_{\rm LL} P_{\rm LL}(t) + (1 - f_{\rm LL}) P_{\rm SL}(t) \quad , \tag{6.20}$$

  where LL stands for long-living and SL stands for short-living and $f_{\rm LL}$ is the fraction between the two components. In this model, the three free parameters are the fraction f_{LL} and the lifetimes τ_{SL} and τ_{LL}. Since the final analysis is performed in the range $0.3 < t < 14\,\text{ps}$, the largest background component, the so-called prompt peak around $t = 0$, can be safely ignored. The projection on t for the data in the reconstructed B_s^0 mass sidebands (defined as $5200\,\text{MeV}/c^2 < m < 5330\,\text{MeV}/c^2$ and $5410\,\text{MeV}/c^2 < m < 5550\,\text{MeV}/c^2$) of the full PDF, is shown in Fig. 6.7.

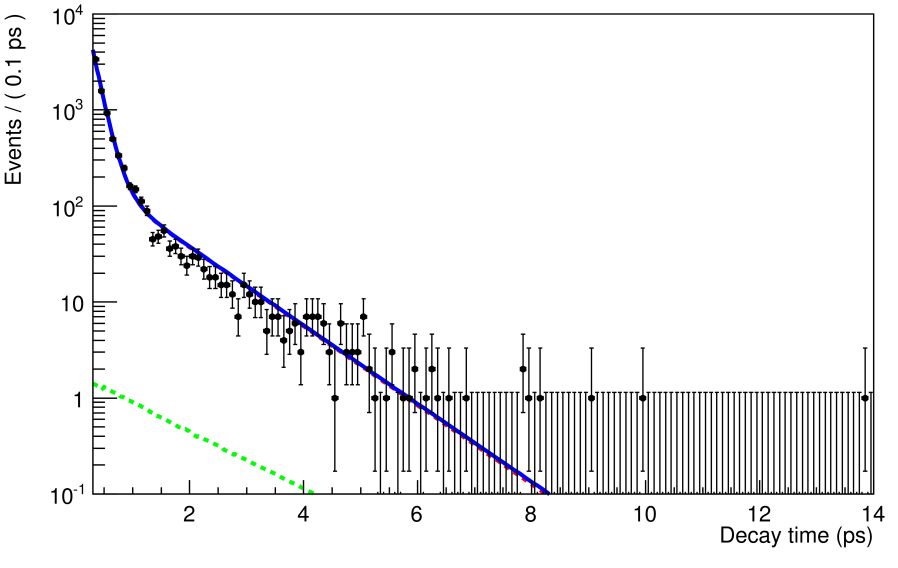

Figure 6.7: *Data in the B_s^0 mass sidebands as defined in the text (black points) and the projection of the full PDF (blue solid line) on the decay time t. The signal component outside the signal mass window is small and indicated by the dashed green line, whereas the double-exponential decay-time PDF $P_{\rm bkg}(t)$ is shown as the red dashed line (almost fully covered by the full PDF, due to the small signal component).*

- $P_{\rm bkg}(\cos\psi, \cos\theta, \phi)$ is modelled in a non-parametric way. To account for the difference in shape, the number of histogram bins is optimized for each variable: five, seven and nine for $\cos\psi$, $\cos\theta$ and ϕ, respectively. The angular distributions are shown in Fig. 6.8 for the data in the B_s^0 mass sidebands. Shown in blue is a rebinned histogram of the same data, representing the PDF $P_{\rm bkg}(\cos\psi, \cos\theta, \phi)$.

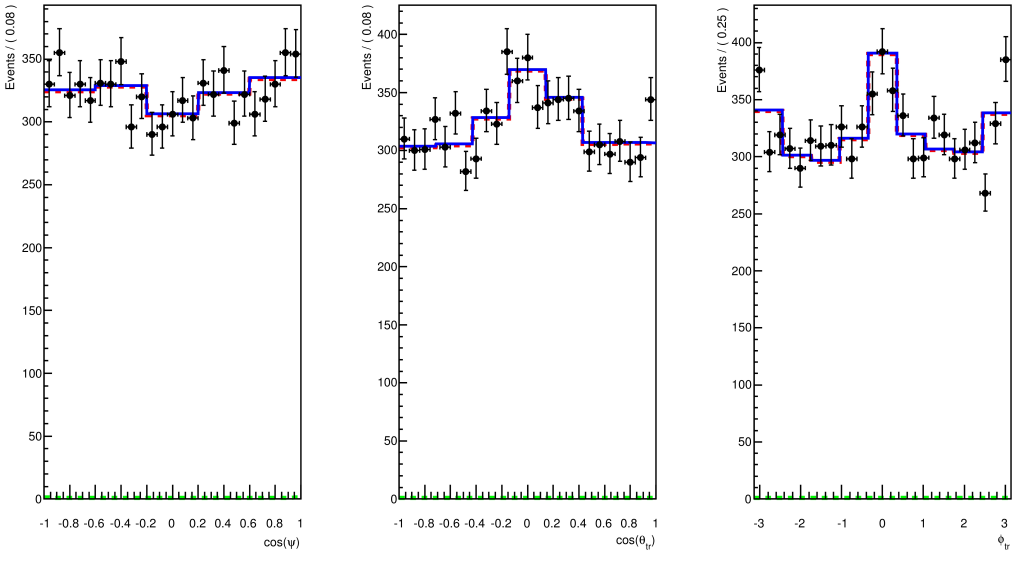

Figure 6.8: *Data in the B_s^0 mass sidebands as defined in the text (black points) and the projection of the full PDF (blue solid line) on the decay angles $\cos\psi$, $\cos\theta$ and ϕ. The signal component is indicated by the dashed green line, whereas the background component $P_{\rm bkg}(\cos\psi, \cos\theta, \phi)$ is shown as the red dashed line (almost fully covered by the full PDF, since the signal component is negligible in the mass sideband). Notice that the events in the peaking structure in $\cos\theta$ and ϕ are correlated. These are events where the two final state muons are along the decay axis of the B_s^0 meson candidate.*

- $P_{\rm bkg}(m)$ is modelled as a simple exponential, with the exponent as free parameter.
- $P_{\rm bkg}(q_T)$: The background PDF for the tag decision q_T is written in the same way as the signal component, but with different parameters $\epsilon_{T,\rm bkg}$ and $\delta_{T,\rm bkg}$:

$$P_{\rm bkg}(q_T) = \begin{cases} 1 - \epsilon_{T,\rm bkg} & \text{if } q_T = 0 \\ \frac{1}{2}\epsilon_{T,\rm bkg}(1 + q_T\delta_{T,\rm bkg}) & \text{if } q_T = \pm 1 \end{cases} . \tag{6.21}$$

- $P_{\rm bkg}(\eta)$ is modelled in a non-parametric way. The PDF is sampled from a distribution of η of the weighted dataset that represents the background component of the data (see Sec. 6.6.3) and is shown in Fig. 6.9.

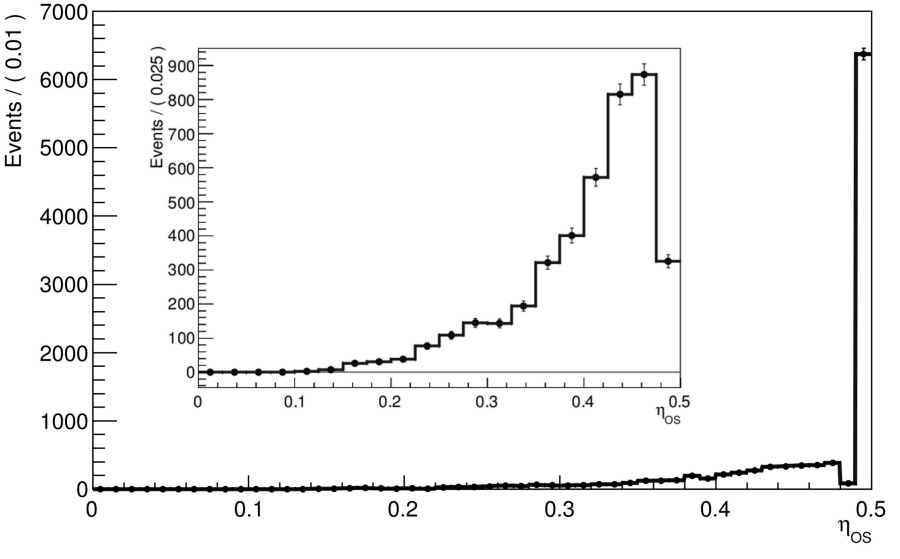

Figure 6.9: *Distribution of η for weighted data representing the background component of the data (black points). The PDF $P_{\mathrm{bkg}}(\eta)$ is indicated by the solid line. The events in the last bin at $\eta = 0.5$ represent the so-called untagged events with $q_T = 0$. Inset: identical, but with the untagged events at $\eta = 0.5$ removed.*

parameter	value
N_{signal}	21217 ± 153
N_{bkg}	10439 ± 112
μ_{signal}	$5368.23 \pm 0.05\,\text{MeV}/c^2$
σ_{signal}	$6.28 \pm 0.05\,\text{MeV}/c^2$
α_{bkg}	$(-1.63 \pm 0.10) \cdot 10^{-3}$

Table 6.4: *Fit results for the five free parameters in the PDF for the reconstructed B_s^0 mass, m, in the range $5200 < m < 5550\,\text{MeV}/c^2$.*

6.6.3 Signal and Background Yields and Weighted Datasets

Since q_T and η are treated as conditional parameters in the analysis, the distributions of q_T and η must be included for both the signal and the background component in order to obtain the full PDF[11]. In the case of η, the signal and background distributions are obtained using the sPlot technique [68]. This is a method that uses information based on a discriminating observable (m in this case) to infer the behavior of the signal and background component with respect to other observables (such as η, in this case). The two datasets that represent the signal component and the background component of the data are weighted according to the the yields N_{signal} and N_{bkg} that are obtained from a fit of the mass-only PDF $P(m)$ to the data. This PDF is given by

$$P(m) = \left(\frac{N_{\text{signal}}}{N_{\text{signal}} + N_{\text{bkg}}}\, P_{\text{signal}}(m) + \frac{N_{\text{bkg}}}{N_{\text{signal}} + N_{\text{bkg}}}\, P_{\text{bkg}}(m) \right) P_{\text{Poisson}}(N_{\text{signal}} + N_{\text{bkg}}) \quad , \tag{6.22}$$

where the PDFs $P_{\text{signal}}(m)$ and $P_{\text{bkg}}(m)$ were explained in Sec. 6.6.1 and Sec. 6.6.2, respectively. The mass PDF $P(m)$ in Eq. 6.22 has five free parameters: the number of signal and background events, N_{signal} and N_{bkg}, the mean μ_{signal} and width σ_{signal} of the Gaussian $P_{\text{signal}}(m)$ and the exponential α_{bkg} from $P_{\text{bkg}}(m)$. The PDF is fitted to the data in the range $5200\,\text{MeV}/c^2 < m < 5550\,\text{MeV}/c^2$ and is shown in Fig. 6.10. The fit results are given in Table 6.4.

6.6.4 Decay-Time Resolution Model

The decay-time resolution needs to be taken into account by convolving all time-dependent functions with the decay-time resolution model, as it dilutes the amplitude of the time-dependent asymmetry. This model is assumed to be the sum of a number of Gaussian functions:

$$R(t, \sigma_t) = \sum_{i=1}^{k} f_i \frac{1}{\sqrt{2\,\pi} s_i \sigma_t} \exp\left(-\frac{(t-d)^2}{2(s_i\,\sigma_t)^2} \right) \quad , \tag{6.23}$$

where f_i is the fraction and s_i is the scale factor of Gaussian i (where $\sum_i f_i = 1$) and d is a common mean value. In addition, σ_t is the per-event decay-time error, determined from

[11] Note that a general PDF $P(x|y)$ that is a function of x and that is conditional on y, should be multiplied with the PDF for y, $P(y)$, to obtain a PDF that depends on both x and y: $P(x, y) = P(x|y)P(y)$.

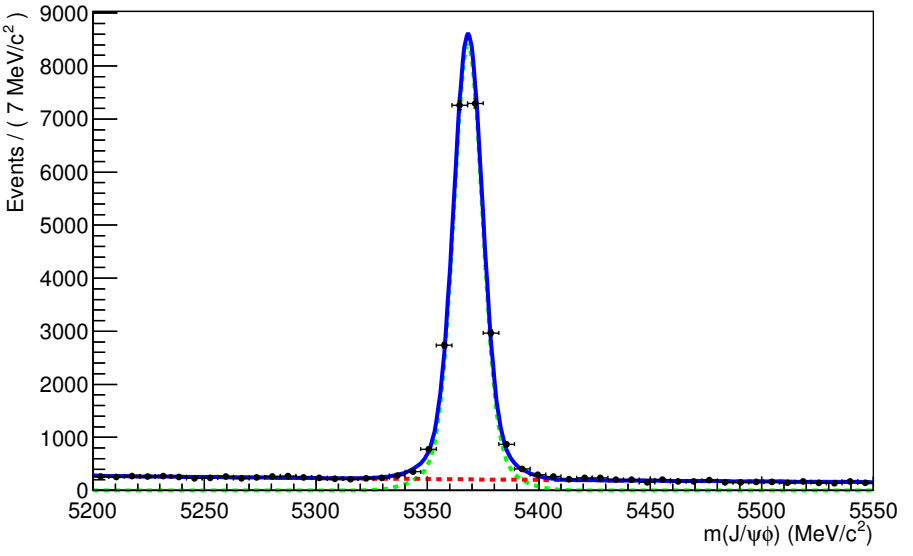

Figure 6.10: *Reconstructed B_s^0 mass distribution (black points) and projection of fitted PDF $P(m)$ in blue. The signal component is shown as the green dashed line, whereas the background component is the red dashed line. The number of signal events is 21217 ± 153.*

6

the decay vertex and decay length uncertainty.

The parameters of this model are obtained from a fit to the decay-time distribution of events in the range $[-1.5, 8.0]\,\mathrm{ps}$, from a dedicated sample obtained using trigger, stripping and selection requirements that are not biased with respect to the decay time. Given the a-priori large amount of background, these events are prescaled, both in the trigger and in the stripping. Only (fake) prompt B_s^0 candidates are considered, formed from a prompt J/ψ and two random tracks. The non-J/ψ background (i.e. a background component outside the J/ψ mass window in J/ψ mass) is subtracted using the sPlot technique. Long-lived (non-prompt) events are modelled by the sum of two exponentials, as was indicated in Sec. 6.6.2. Studies [69] reveal that the data is reasonably well described by two Gaussians ($k = 2$), as shown in Fig. 6.11. When increasing the number of Gaussians to three, the fit parameters change, but the effective dilution[12] remains the same.

Since in the final analysis only the effective dilution due to decay-time resolution matters, the double Gaussian decay-time resolution is transformed into a single Gaussian model with the same effective dilution. This single Gaussian model uses per-event decay-time errors and has parameters $d = 0$ and scale factor $S_{\sigma_t} = 1.45 \pm 0.06$. All time-dependent functions in

[12]For a single Gaussian proper time resolution with width σ_t, the dilution is $\mathcal{D} = \exp(-\Delta m_s^2 \sigma^2/2)$ and the effective power $\mathcal{P} = \mathcal{D}^2$. If the resolution model is the sum of j Gaussians, the effective power becomes $\mathcal{P} = [\sum_j f_j \exp(-\Delta m_s^2 \sigma_j^2/2)]^2$. When using a per-event decay-time error $\sigma_{j,e}$, the average power of the model is $\langle \mathcal{P} \rangle = \sum_e \mathcal{P}_e / N$, where $\mathcal{P}_e$ is the per-event power.

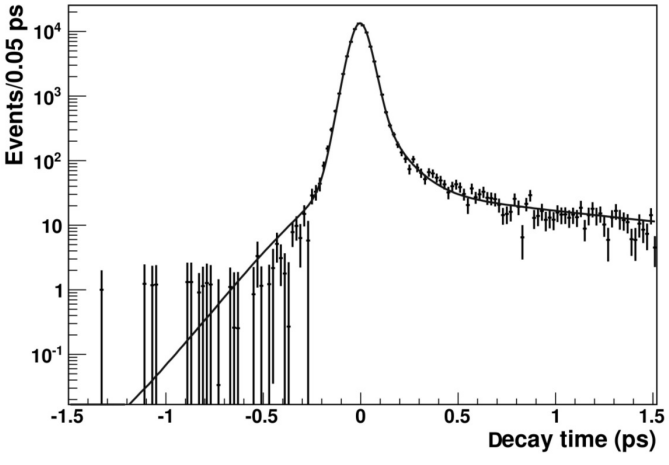

Figure 6.11: *Decay-time distribution in the prompt region (black points) and fitted PDF using a resolution model consisting of the sum of two Gaussians with a per-event decay-time error.*

the final analysis are convolved with this resolution model.

Given the fact that the average of the decay-time error distribution is 32 fs, the effective decay-time resolution is 32 fs $\times$ 1.45 $=$ 46 fs. The scale factor of 1.45 implies that, on average, the decay-time resolution is about 45% worse than estimated from the uncertainties on the track parameters. The assigned uncertainty of 0.06 on S_{σ_t} accounts for possible differences in the decay-time resolution between prompt $J/\psi \to \mu^+\mu^-$ background events and long-lived $B_s^0 \to J/\psi\,\phi$ events and corresponds to a variation of the effective dilution by 2.5%. S_{σ_t} is constrained to vary within its uncertainty in the final fit.

6.6.5 Angular Resolution

Angular resolution has been studied on simulated events [64]. No biases on the physics parameters were found when neglecting angular resolution, and therefore it is ignored in the analysis.

6.7 Results

The shape of the distribution for all variables in the full PDF has been discussed. Using this, a fit to the data is performed, from which physics parameters are extracted. Among these parameters are the amplitudes, strong phases, lifetimes and the weak phase ϕ_s. The following set of physics parameters $\vec{\Pi}_{\rm phys}$ is distinguished:

$$\vec{\Pi}_{\rm phys} = (|A_0|^2,\, |A_\perp|^2,\, |A_\parallel|^2,\, |A_S|^2,\, \delta_0,\, \delta_\perp,\, \delta_\parallel,\, \delta_S,\, \Gamma_s,\, \Delta\Gamma_s,\, \Delta m_s,\, \phi_s) \quad . \qquad (6.24)$$

The overall scaling of the $|A_i|^2$ drops out of the PDF due to the normalization, hence one degree of freedom must be eliminated. The amplitude $|A_S|^2$ is expected to be dependent on the K^+K^- invariant mass, while the other transversity amplitudes are not. Therefore, the sum of the P-wave contributions is normalized to one:

$$|A_0|^2 + |A_\perp|^2 + |A_\parallel|^2 = 1 \quad . \tag{6.25}$$

Consequently, the free parameters in the fit are chosen to be $|A_0|^2$ and $|A_\perp|^2$ and it follows that $|A_\parallel|^2 = 1 - |A_0|^2 - |A_\perp|^2$. Subsequently, the amplitude $|A_S|^2$ is replaced by f_S, the fraction of the S-wave component:

$$f_S = \frac{|A_S|^2}{|A_0|^2 + |A_\perp|^2 + |A_\parallel|^2 + |A_S|^2} = \frac{|A_S|^2}{1 + |A_S|^2} \quad . \tag{6.26}$$

Because only strong phase differences between individual amplitudes enter the PDF, without loss of generality, the strong phase related to the transversity amplitude A_0 is taken to be constant and zero: $\delta_0 = 0$. The final set of physics parameters that is determined in the fit is:

$$\vec{\Pi}_{\text{phys}} = (|A_0|^2,\, |A_\perp|^2,\, f_S,\, \delta_\perp,\, \delta_\parallel,\, \delta_S,\, \Gamma_s,\, \Delta\Gamma_s,\, \Delta m_s,\, \phi_s) \quad . \tag{6.27}$$

The parameter Δm_s is constrained in the fit to $\Delta m_s = 17.63 \pm 0.11\,\text{ps}^{-1}$, as measured by LHCb in $B_s^0 \to D_s^-(3)\pi$ decays [70].

A final remark should be made about the parameter λ as introduced in Eq. 5.55. By writing $\lambda = e^{-i\phi_s}$, it was assumed that $|q/p| = 1$ (no CP violation in mixing) and $\left|\frac{\overline{A}_{J/\psi\,\phi}}{A_{J/\psi\,\phi}}\right| = 1$ (no CP violation in decay), and it follows that $|\lambda| = 1$. This assumption is used in the fit as well.

6.7.1 Fit Results

The fit results of the physics parameters are given in Table 6.5. In particular, it is found that

$$\begin{aligned} \phi_s &= 0.00 \pm 0.10 \\ \Gamma_s &= 0.658 \pm 0.005\,\text{ps}^{-1} \\ \Delta\Gamma_s &= 0.115 \pm 0.018\,\text{ps}^{-1} \end{aligned}$$

The quoted uncertainties are statistical only[13]. Systematic uncertainties are determined in Sec. 6.7.5. The fitted values of the other free parameters in the fit are given in Table 6.6. Note in particular that the values of the parameters that occur in the mass-only PDF as presented in Table 6.4 change slightly in the full fit.

The projections of the fitted PDF, as well as its two components are shown in Fig. 6.12 for the decay time t and in Fig. 6.13 for the decay angles. The observed time-dependent CP asymmetry defined as

$$A_{\text{observed}}(t) = \frac{N_{B\to f}(t) - N_{\overline{B}\to f}(t)}{N_{B\to f}(t) + N_{\overline{B}\to f}(t)} = D_{\text{eff}} A_{\text{CP}}(t) \quad , \tag{6.28}$$

[13] Rounding rules are applied as indicated in [23].

parameter	value
ϕ_s	0.00 ± 0.10
Γ_s	$0.658 \pm 0.005\,\text{ps}^{-1}$
$\Delta\Gamma_s$	$0.115 \pm 0.018\,\text{ps}^{-1}$
Δm_s (*)	$17.59 \pm 0.09\,\text{ps}^{-1}$
$\lvert A_0\rvert^2$	0.522 ± 0.007
$\lvert A_\perp\rvert^2$	0.247 ± 0.010
f_S	0.022 ± 0.011
$\delta_\perp$	2.89 ± 0.34
$\delta_\parallel$	3.33 ± 0.21
δ_S	2.89 ± 0.34

Table 6.5: *Fit results for physics parameters. The parameter Δm_s, indicated by (*) is constrained to external measurements in the fit.*

	parameter	value
signal	N_{signal}	21203 ± 151
	μ_{signal}	$5368.20 \pm 0.05\,\text{MeV}/c^2$
	σ_{signal}	$6.27 \pm 0.04\,\text{MeV}/c^2$
background	N_{bkg}	10453 ± 110
	α_{bkg}	$(-1.63 \pm 0.10) \cdot 10^{-3}\,c^2/\text{MeV}$
	f_{LL}	0.213 ± 0.010
	τ_{LL}	$1.06 \pm 0.04\,\text{ps}$
	τ_{SL}	$0.1507 \pm 0.0029\,\text{ps}$
tagging	$\delta_{T,\text{bkg}}$	-0.033 ± 0.016
	$\epsilon_{T,\text{bkg}}$	0.397 ± 0.005
	$\delta_{T,\text{signal}}$	0.000 ± 0.012
	$\epsilon_{T,\text{signal}}$	0.3296 ± 0.0033
	p_0 (*)	0.392 ± 0.009
	p_1 (*)	1.036 ± 0.024
decay-time resolution	S_{σ_t} (*)	1.45 ± 0.06

Table 6.6: *Fit results for other parameters, grouped by component (signal/background) or by function in the PDF (tagging/decay-time resolution). The parameters indicated by (*) are constrained to external measurements in the fit.*

following Eq. 6.12, is shown in Fig. 6.14. No oscillation is observed due to the fact that ϕ_s is found to be zero in the fit and Δm_s is large. In addition, there is extra dilution due to the fact that $|A_\perp|^2 \neq 0$ and D_{eff} is small.

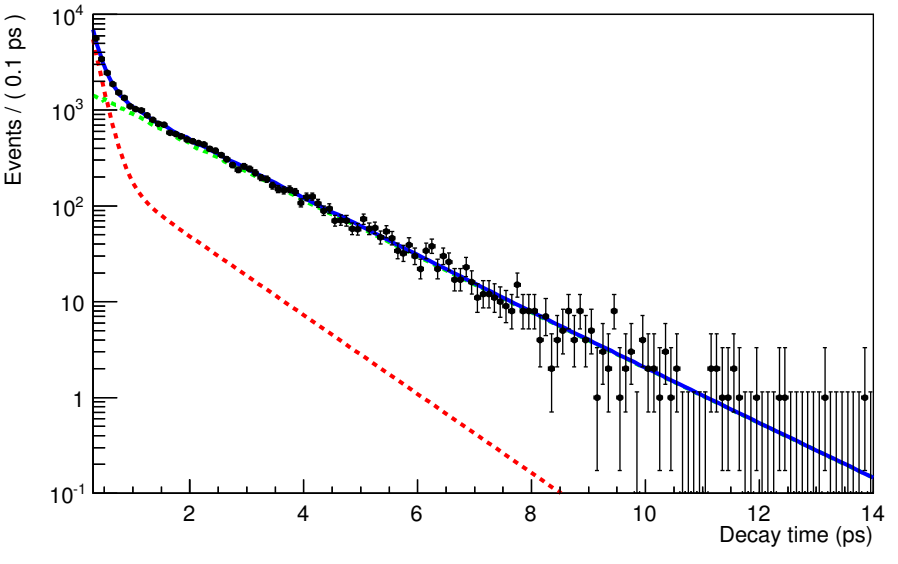

Figure 6.12: *Projection of the fitted PDF on the decay time. The data is indicated by the black points. The PDF signal component is the green dotted line and the PDF background component is the red dotted line. The sum of the two components is the full PDF, indicated by the solid blue line.*

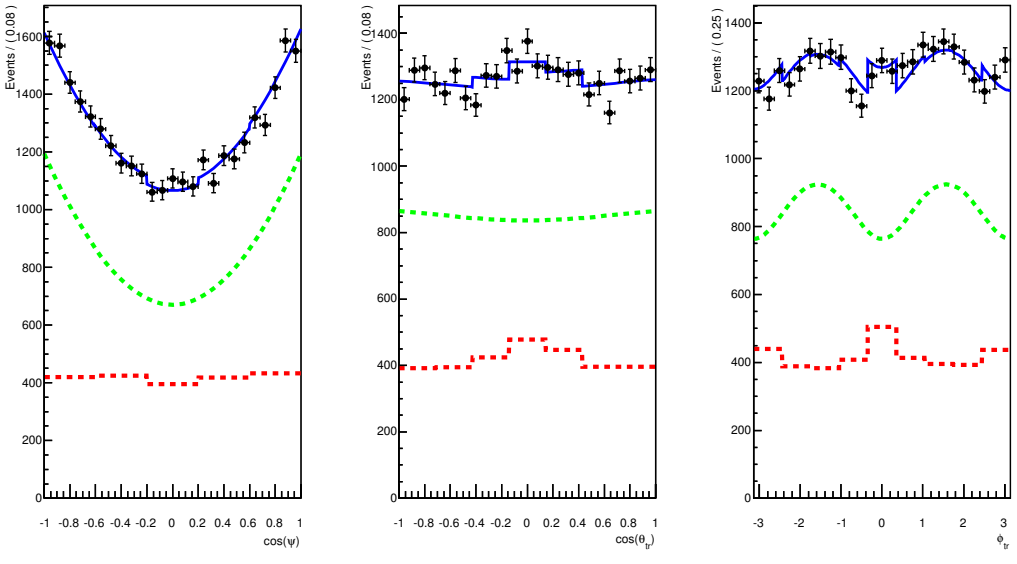

Figure 6.13: *Projection of the fitted PDF on the decay angles* $\cos\psi$, $\cos\theta$ *and* ϕ, *from left to right. The data is indicated by the black points. The PDF signal component is the green dotted line and the PDF background component is the red dotted line. The sum of the two components is the full PDF, indicated by the solid blue line.*

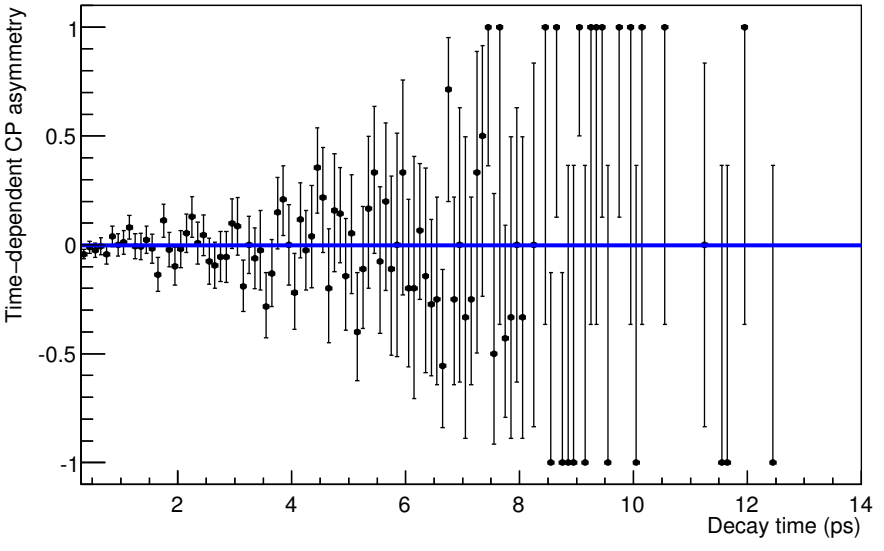

Figure 6.14: *Observed time-dependent CP asymmetry and the corresponding projection of the fitted signal PDF. No oscillation is observed due to the fact that ϕ_s is found to be zero and Δm_s is large. In addition, there is extra dilution due to the fact that $|A_\perp|^2 \neq 0$ and $D_{\rm eff}$ is small. The data shown in this figure is the weighted data that represents the signal component.*

6.7.2 Scans of Profile-Likelihood Ratios

The fit results for the physics parameters were presented in Table 6.5 and Table 6.6. The profile-likelihood ratio is defined as the ratio of the negative log-likelihood function, when one parameter is fixed and the negative log-likelihood function is minimized as a function of the remaining parameters, to the minimized negative log-likelihood function when all parameters are free (i.e. the best fit). A scan of the profile-likelihood ratio is a plot of the profile-likelihood ratio as a function of the parameter of interest. In the limit of a large number of events and no correlations between fit parameters, all the profile-likelihood ratio scans are expected to be parabolic and the statistical uncertainty on the parameter estimate is obtained from the $\Delta \log L = 0.5$ point.

1-Dimensional Scans

The scans of the profile-likelihood ratio for the physics parameters ϕ_s, Γ_s and $\Delta\Gamma_s$ are shown in Fig.6.15. In addition, the scans of the profile-likelihood ratio for the transversity amplitudes $|A_0|^2$, $|A_\perp|^2$, f_S and the strong phases $\delta_\perp$, $\delta_\parallel$ and δ_S are shown in Fig.6.16.

The profile-likelihood ratio scan for f_S is non-parabolic due to the choice of parameterization of f_S, an effect that is discussed in Sec. 6.7.5. In addition, the profile-likelihood for $\delta_\parallel$ is non-parabolic due to the fact that the fitted value is close to its degenerate value, as will be explained in Sec. 6.7.3.

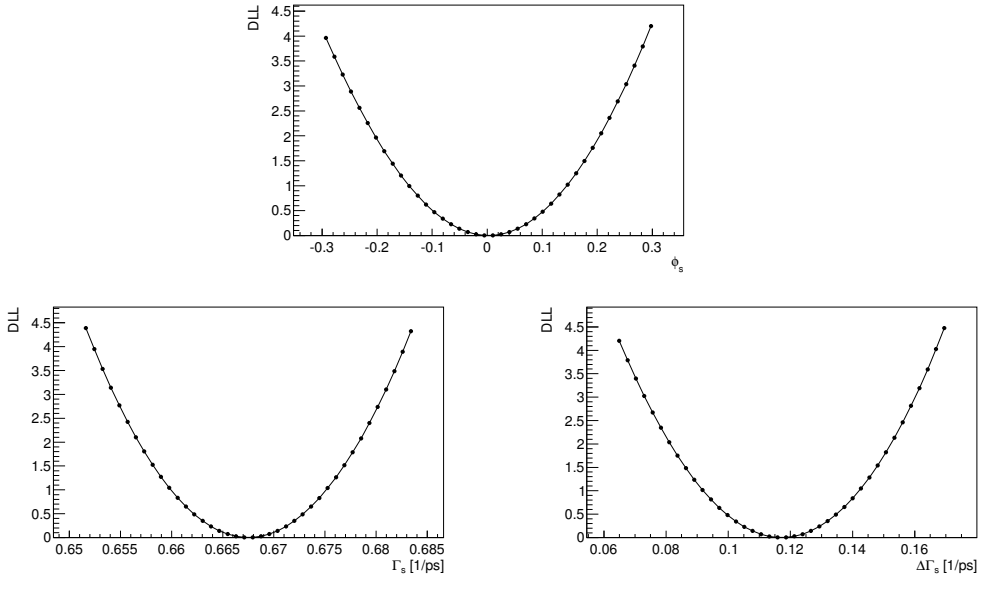

Figure 6.15: *Profile-likelihood scans for ϕ_s, Γ_s, and $\Delta\Gamma_s$.*

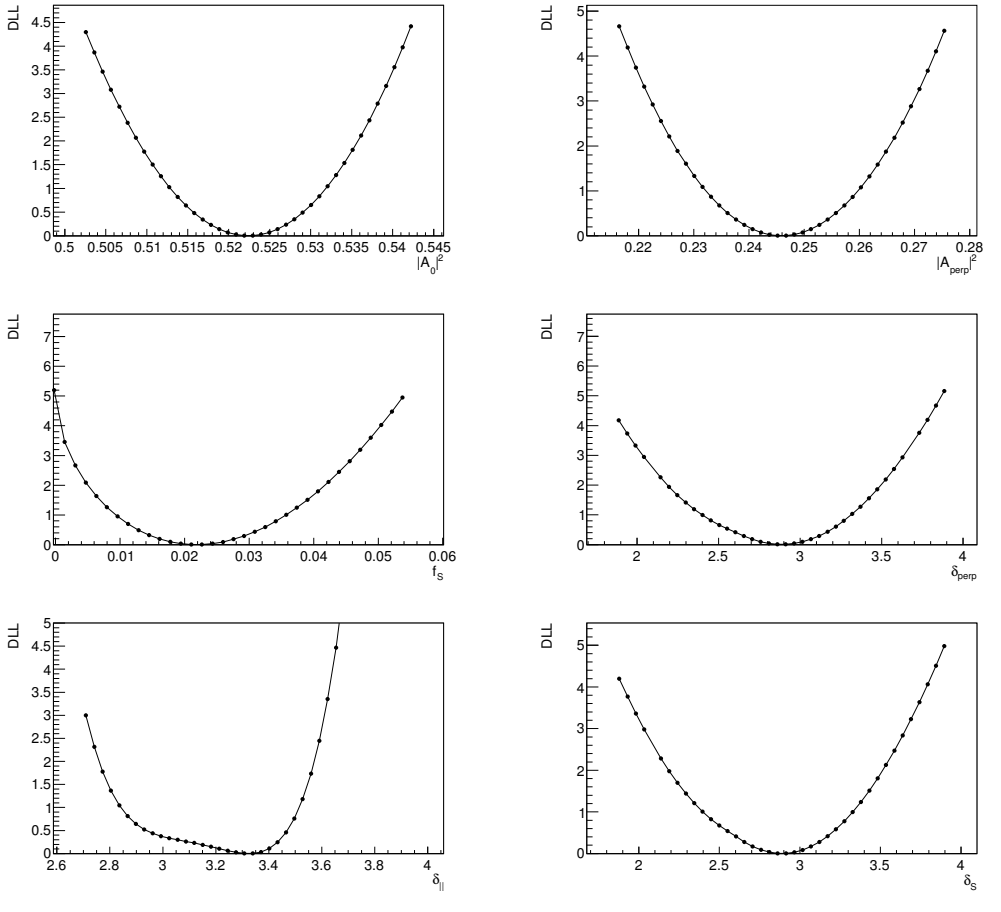

Figure 6.16: *Profile-likelihood scans for* $|A_0|^2$, $|A_\perp|^2$, f_S, $\delta_\perp$, $\delta_{\|}$ *and* δ_S.

2-Dimensional Scans

Historically, the ϕ_s analysis is presented using a two-dimensional contour plot of the profile-likelihood ratio for ϕ_s and $\Delta\Gamma_s$[14]. This contour plot is shown in Fig. 6.17. In addition, the

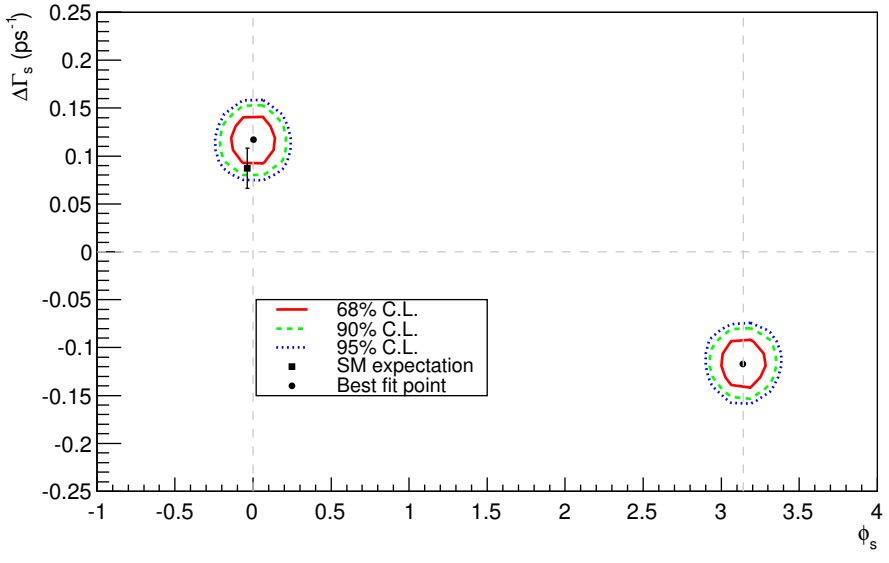

Figure 6.17: *Two-dimensional contour plot of the profile-likelihood ratio of $\Delta\Gamma_s$ versus ϕ_s. The black square indicates the SM point ($\phi_s = -0.036 \pm 0.002$, $\Delta\Gamma_s = 0.087 \pm 0.021\,\mathrm{ps}^{-1}$, see [51]) and the black dot indicates the fitted value as presented in Table 6.5. The confidence levels (CL) drawn correspond to 68% (solid red line), 90% (green dashed line) and 95% (blue dotted line). Note that systematic uncertainties are not included. Systematic uncertainties are treated in Sec. 6.7.5 and are not expected to have a big influence on this figure, since they are relatively small for ϕ_s and $\Delta\Gamma_s$.*

profile-likelihood ratio contours determined here are overlaid with the corresponding data from the CDF and D0 experiments and is presented in Fig. 6.18.

6.7.3 Solving the Ambiguity

Fig. 6.17 and Fig. 6.18 show that two disjoint solutions for $\Delta\Gamma_s$ and ϕ_s are found. This can be understood by noting that the signal PDF as presented in Appendix D is invariant under the following transformations:

$$(\phi_s, \Delta\Gamma_s, \delta_\parallel, \delta_\perp, \delta_S) \to (\pi - \phi_s, -\Delta\Gamma_s, -\delta_\parallel, \pi - \delta_\perp, -\delta_S) \quad . \tag{6.29}$$

[14] For a two-dimensional profile-likelihood ratio, the 68%, 90% and 95% confidence regions are given by a delta-log-likelihood of 2.30/2, 4.61/2 and 5.99/2, respectively [71].

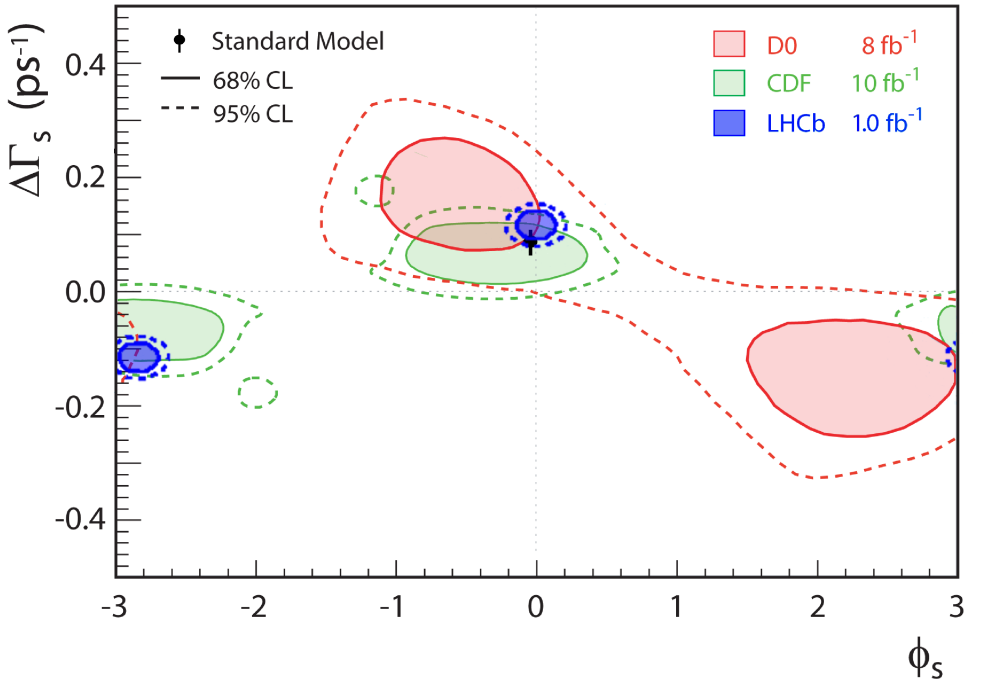

Figure 6.18: *Two-dimensional contour plots of the profile-likelihood ratios in the* $(\Delta\Gamma_s, \phi_s)$*-plane for the D0 collaboration [59] (red), the CDF collaboration [72] (green) and the values found here (blue). The black square indicates the SM point* ($\phi_s = -0.036 \pm 0.002, \Delta\Gamma_s = 0.087 \pm 0.021\,\mathrm{ps}^{-1}$)*. Only the 68% confidence levels (solid lines) and 90% confidence levels (dotted lines) are indicated. Note that systematic uncertainties are not included. Systematic uncertainties are treated in Sec. 6.7.5 and are not expected to have a big influence on this figure, since they are small compared to the statistical uncertainties for* ϕ_s *and* $\Delta\Gamma_s$*.*

This explains the appearance of a second minimum in the profile-likelihood ratio scans and it also explains the non-parabolic likelihood scan of the parameter $\delta_\parallel$ in Fig. 6.16, since the fitted value of $\delta_\parallel = 3.33 \pm 0.21$ is close to its degenerate solution $\delta_\parallel \to -\delta_\parallel$, modulo 2π.

However, this ambiguity can be resolved by measuring the phase difference between the S-wave and P-wave amplitudes as a function of the K^+K^- invariant mass, m_{KK}. The phase of the P-wave amplitude, which can be described by a spin-1 Breit-Wigner function of m_{KK}, rises rapidly through the m_{KK} region. The phase of the S-wave amplitude, on the other hand, is expected to vary relatively slowly for both an $f_0(980)$ meson S-wave contribution and a non-resonant S-wave contribution. As a result, the phase difference $\delta_S - \delta_\perp$ between the S-wave and P-wave amplitudes falls rapidly with increasing m_{KK}. By measuring this phase difference as a function of m_{KK}, and taking the solution with a decreasing trend when going through the ϕ meson mass pole from low to high masses, the ambiguity is resolved. In particular, the sign of $\Delta\Gamma_s$, which is a priori unknown, as mentioned in Sec. 1.4, is determined

by solving the ambiguity.

To solve the ambiguity, a dataset with a wider m_{KK} range is used, as compared to the range that was given in Table 6.1. Subsequently, this m_{KK} region is divided in four bins and the phase difference $\delta_{S\perp} \equiv \delta_S - \delta_\perp$ is fitted in every bin. This is shown in Fig. 6.19, which indicates that the solution with $\Delta\Gamma_s > 0$ is the physical solution, in agreement with the SM prediction [21]. A zoomed-in version of the profile-likelihood ratio contours in the

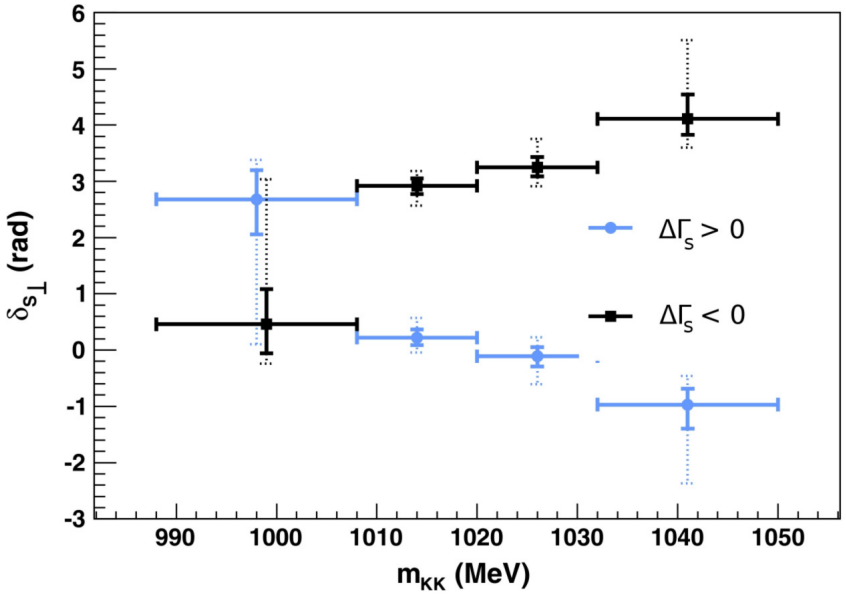

Figure 6.19: *Measured phase differences $\delta_{S\perp}$ between S-wave amplitudes and perpendicular P-wave amplitudes in four bins of m_{KK} for the solution with $\Delta\Gamma_s > 0$ (blue circles) and the solution with $\Delta\Gamma_s < 0$ (black squares). The dotted and solid asymmetric error bars correspond to different confidence levels of the fitted difference, $\delta_{S\perp}$. Figure taken from [21].*

$(\Delta\Gamma_s,\, \phi_s)$-plane showing the physical solution is presented in Fig. 6.20.

6.7.4 Δm_s Measurement

Although Δm_s is constrained in the fit, the PDF that is used in the ϕ_s analysis presented here, does contain terms that are sensitive to Δm_s[15]. With the current size of the dataset,

[15]When inspecting the separate terms of the PDF, some of the terms proportional to $\sin(\Delta m_s t)$ and $\cos(\Delta m_s t)$ are not multiplied by $C = 0$ or $S = -\sin\phi_s \simeq 0$ and are thus sensitive to Δm_s (for example, the terms proportional to Δm_s in Eq. D.6 are not multiplied by C or S, while the terms proportional to Δm_s in Eq. D.1 are).

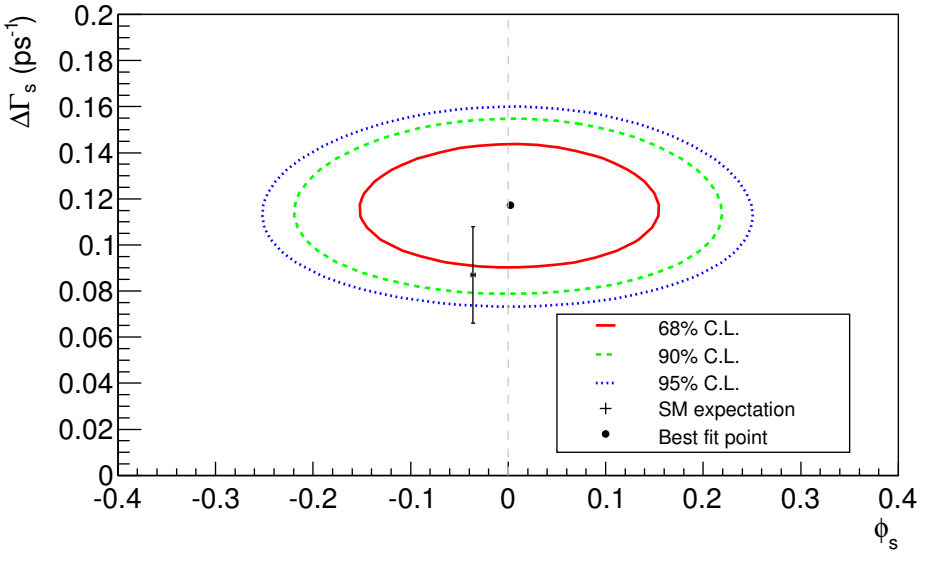

Figure 6.20: *Two-dimensional contours of the profile-likelihood ratio of $\Delta\Gamma_s$ versus ϕ_s: a zoom-in on the solution of the ambiguity shown in Fig. 6.17 that corresponds to the SM prediction. The confidence levels (CL) drawn correspond to 68% (solid red line), 90% (green dashed line) and 95% (blue dotted line).*

it is possible to float the parameter Δm_s. The best fit result is

$$\Delta m_s = 17.51 \pm 0.15\,\mathrm{ps}^{-1} \quad , \tag{6.30}$$

which is in good agreement with the LHCb measurement performed in [70], $\Delta m_s = 17.63 \pm 0.11\,\mathrm{ps}^{-1}$ [70]. In this fit, $\phi_s = 0.00 \pm 0.10$. This value is the same as found when Δm_s is constrained, see Table 6.5. The profile-likelihood ratio scan for Δm_s is shown in Fig. 6.21.

6.7.5 Systematic Uncertainties

Systematic uncertainties are assigned by studying possible sources of systematic effects. These studies are summarized here and finally the systematic uncertainties for all parameters are summarized.

S-Wave Fraction

By construction, the fraction of the S-wave contribution, f_S, can never be smaller than zero. If f_S is close to zero, this leads to non-parabolic profile-likelihood ratio scans and biases in fit parameters. Since f_S is determined to be small ($f_S = 0.022 \pm 0.011$), the scan of the profile-likelihood ratio of f_S in Fig. 6.16 is not parabolic.

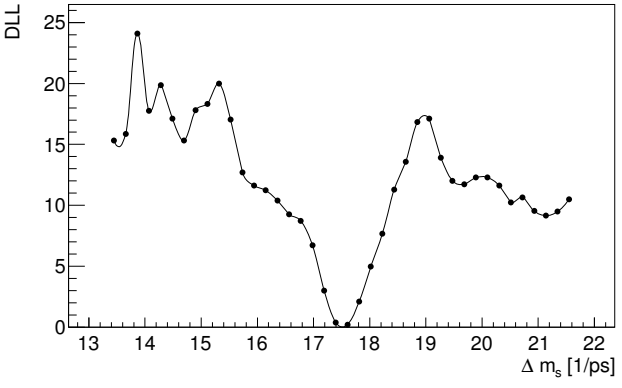

Figure 6.21: *Profile-likelihood scan for* Δm_s.

To study the effect of possible biases, toy datasets are generated at $f_S = 0.0$, $f_S = 0.02$ and finally $f_S = 0.04$. For all parameter biases, no dependence on the generation value of f_S is observed, where a parameter bias is defined as the difference between the fitted parameter and the value of the parameter that was used for generation. Therefore, no systematic uncertainty is assigned due to this effect.

Fit Bias

To estimate the parameter biases as a result of the limited data size, toy studies are performed in which 500 toys are generated that are representative for the actual dataset. The events in the toy datasets are generated using the values of the parameters that are extracted from the real data.

For every parameter, the bias is defined as $p_{\rm fit} - p_{\rm generated}$, where $p_{\rm generated}$ is the value of the parameter at which the toy dataset was generated and $p_{\rm fit}$ is the fitted parameter value. For each parameter, the mean bias and its error is given in Table 6.7, as well as the statistical uncertainty of the original fit. Only for ϕ_s no significant bias is observed (mean bias consistent with zero within 2σ) and therefore no systematic uncertainty is assigned to ϕ_s. For all other parameters, the absolute value of the mean bias is assigned as systematic uncertainty. In all cases the assigned systematic error is small compared to the statistical uncertainty of the original measurement.

Background Description

The fit model described in Sec. 6.6 (called the 'baseline fit' onwards) contains a signal component and a background component. In addition to this fit configuration, a fit of only the signal component PDF on the s-weighted data representing the signal component (as explained in Sec. 6.6.3) is performed. By construction, there is no background component in this dataset and therefore no background PDF is needed. The fit result for this fit

parameter	mean bias in toys	statistical error from measurement
ϕ_s	$(-0.2 \pm 0.5) \cdot 10^{-2}$	0.10
$\Gamma_s\,[\mathrm{ps}^{-1}]$	$(3.44 \pm 0.25) \cdot 10^{-3}$	0.005
$\Delta\Gamma_s\,[\mathrm{ps}^{-1}]$	$(-2.2 \pm 0.8) \cdot 10^{-3}$	0.018
$\lvert A_0\rvert^2$	$(-2.99 \pm 0.30) \cdot 10^{-3}$	0.007
$\lvert A_\perp\rvert^2$	$(2.9 \pm 0.4) \cdot 10^{-3}$	0.010
f_S	$(-5.0 \pm 0.5) \cdot 10^{-3}$	0.011
$\delta_\perp$	$(-3.1 \pm 1.5) \cdot 10^{-2}$	0.34
$\delta_\parallel$	$(9.8 \pm 0.8) \cdot 10^{-2}$	0.21
δ_S	$(-4.7 \pm 1.7) \cdot 10^{-2}$	0.34

Table 6.7: *Mean bias and mean bias error obtained from toy studies, and the original statistic uncertainty for all parameters. Only ϕ_s shows a bias that is consistent with zero within 2σ and therefore does not have an assigned systematic uncertainty.*

configuration (called the sFit, after the sPlot method) and the difference with the baseline fit is given in Table 6.8.

The differences between the baseline fit and the sFit can only be caused by the background description. Therefore, the difference between these two fit configurations is taken as the systematic uncertainty due to the background parameterization for each parameter. For ϕ_s this amounts to 10% of its statistical uncertainty, while for $\Delta\Gamma_s$ this is 20%.

parameter	baseline fit value	sFit value	absolute difference
ϕ_s	0.00 $\pm$ 0.10	-0.01 $\pm$ 0.10	0.01
$\Gamma_s\,[\mathrm{ps}^{-1}]$	0.658 $\pm$ 0.005	0.659 $\pm$ 0.005	0.001
$\Delta\Gamma_s\,[\mathrm{ps}^{-1}]$	0.115 $\pm$ 0.018	0.112 $\pm$ 0.017	0.003
$\lvert A_0\rvert^2$	0.522 $\pm$ 0.007	0.523 $\pm$ 0.006	0.001
$\lvert A_\perp\rvert^2$	0.247 $\pm$ 0.010	0.247 $\pm$ 0.009	-
f_S	0.022 $\pm$ 0.011	0.024 $\pm$ 0.010	0.002
$\delta_\perp$	2.89 $\pm$ 0.34	2.84 $\pm$ 0.29	0.05
$\delta_\parallel$	3.33 $\pm$ 0.21	3.36 $\pm$ 0.16	0.03
δ_S	2.89 $\pm$ 0.34	2.83 $\pm$ 0.29	0.06

Table 6.8: *Absolute difference in fit results between the baseline fit and the sFit. A hyphen '-' indicates a negligible effect.*

Angular Acceptance

A source of systematic uncertainty arising from angular acceptance is the observed difference in the kaon momentum spectra between simulated and real data. It turns out that the kaon

momentum and the decay angle $\cos\psi$ are related[16] and thus that the kaon momentum spectra must be properly simulated. As a systematic check, the angular acceptance is determined from a reweighted MC dataset that by construction matches the observed kaon momentum spectra. The assigned systematic uncertainties are the absolute differences in fitted values between the baseline fit and the fit where the angular acceptance is obtained from the reweighted MC dataset and are summarized in Table 6.9. The systematic uncertainties are rounded to the same number of digits as the baseline fit result for each parameter.

parameter	absolute difference
ϕ_s	-
$\Gamma_s\,[\mathrm{ps}^{-1}]$	0.001
$\Delta\Gamma_s\,[\mathrm{ps}^{-1}]$	0.001
$\lvert A_0\rvert^2$	0.032
$\lvert A_\perp\rvert^2$	0.018
f_S	-
$\delta_\perp$	0.02
$\delta_\parallel$	0.03
δ_S	0.02

Table 6.9: *Assigned systematic uncertainties indicating the absolute difference in fit results between the baseline fit and a fit with the angular acceptance as determined from a reweighted MC dataset that matches the observed kaon momentum spectra in data. The numbers are rounded to the same number of digits as the baseline fit result for each parameter. A hyphen '-' indicates a negligible effect.*

In addition, the limited size of the MC dataset that was used to determine the angular acceptance is taken into account. This is done by performing additional fits in which the calculated coefficients of the expansion of the angular-acceptance function, c_{00}^0, c_{22}^0, c_{20}^0 and c_{00}^2 (see Eq. 6.2), are varied by $\pm\,1\sigma$. For each coefficient, the absolute biases from the $\pm\,1\sigma$ fits are averaged and finally the averages for each coefficient are summed quadratically. The assigned systematic uncertainties are summarized in Table 6.10 for all parameters.

Acceptance for small decay time

To estimate the systematic uncertainty on the determination of the decay-time acceptance histogram, the baseline fit is repeated without multiplying the signal PDF with this histogram. The differences in the fit results are assigned as systematic uncertainties and are summarized in Table 6.11.

[16] This can be understood as follows: when $\cos\psi = 1$ ($\cos\psi = -1$), the K^+ is emitted in the direction of (opposite to) the B meson, i.e. with a relatively low (high) p_T (see Fig. 5.1). For the K^- meson, the relationships are opposite. This indicates that (implicit) cuts on the p_T of the kaons induce acceptance effects in $\cos\psi$ [64].

parameter	absolute difference
ϕ_s	-
$\Gamma_s\,[\mathrm{ps}^{-1}]$	0.001
$\Delta\Gamma_s\,[\mathrm{ps}^{-1}]$	0.001
$\lvert A_0\rvert^2$	0.001
$\lvert A_\perp\rvert^2$	0.002
f_S	0.001
$\delta_\perp$	0.01
$\delta_\parallel$	0.02
δ_S	0.01

Table 6.10: *Assigned systematic uncertainties due to the finite size of the MC dataset. These numbers are obtained by varying the four coefficients of the expansion of the angular-acceptance function within $\pm1\sigma$ and summing the fit biases quadratically for the four coefficients. A hyphen '-' indicates a negligible effect.*

parameter	baseline fit value	fit without decay-time acceptance	absolute difference
ϕ_s	0.00 ± 0.10	0.00 ± 0.10	-
$\Gamma_s\,[\mathrm{ps}^{-1}]$	0.658 ± 0.005	0.656 ± 0.005	0.002
$\Delta\Gamma_s\,[\mathrm{ps}^{-1}]$	0.115 ± 0.018	0.117 ± 0.018	0.002
$\lvert A_0\rvert^2$	0.522 ± 0.007	0.522 ± 0.007	-
$\lvert A_\perp\rvert^2$	0.247 ± 0.010	0.246 ± 0.010	0.001
f_S	0.022 ± 0.011	0.022 ± 0.011	-
$\delta_\perp$	2.89 ± 0.34	2.89 ± 0.34	-
$\delta_\parallel$	3.33 ± 0.21	3.32 ± 0.21	0.01
δ_S	2.89 ± 0.34	2.89 ± 0.35	-

Table 6.11: *Absolute differences in fit results between the baseline fit including decay-time acceptance and the fit without taking the decay-time acceptance into account. A hyphen '-' indicates a negligible effect.*

Acceptance for large decay time

In Sec. 6.3.2, the acceptance function for large decay time was found to be $\epsilon(t) = 1 + \beta\, t$, with $\beta = -0.0112 \pm 0.0013\,\mathrm{ps}$. The assigned systematic uncertainty is half the value of β [69], i.e. 0.006. Since this decay-time acceptance influences Γ_s only, this is directly translated as a systematic uncertainty of 0.006 ps^{-1} on Γ_s.

Length Scale and Momentum Scale

The determination of the parameters $\Delta\Gamma_s$ and Γ_s is a measurement of the lifetimes of the two mass eigenstates $B^0_{s,H}$ and $B^0_{s,L}$. The B meson lifetime t is determined from the distance between the primary vertex (PV) and the B meson decay vertex: $\frac{mp\cdot d}{p^2}$, with d the

decay distance, m the reconstructed B mass and p the B momentum. From this relation, it follows that $(\frac{\delta t}{t})^2 = (\frac{\delta p}{p})^2 + (\frac{\delta d}{d})^2$. The length scale $(\frac{\delta d}{d})$ is the accuracy by which the z-coordinate position of each of the VELO modules is known and is estimated to be at most 0.1%, whereas the momentum scale $(\frac{\delta p}{p})$ is determined from the shift in reconstructed masses of known resonances and is determined to be at most 0.15% [69]. From these, the relative error $(\frac{\delta t}{t}) = 0.18\%$ and the assigned systematic uncertainty is 0.001 ps^{-1} for Γ_s, while there is a negligible effect for $\Delta\Gamma_s$. The fit parameters other than Γ_s and $\Delta\Gamma_s$ are not affected by the length scale and momentum scale uncertainties.

Nuisance CP Asymmetries

A measurement of the asymmetry that results from CP violation in the interference between $B_s^0 - \overline{B}_s^0$ mixing and decay (parameterized by ϕ_s) is affected by several other (CP) asymmetries or nuisance asymmetries:

- CP violation in decay and/or mixing: in the ϕ_s analysis presented here, it is assumed that there is neither direct CP violation, nor CP violation in mixing. This is reflected in the statement $|\lambda| = 1$ in Sec. 5.7. The effect of this assumption is checked by performing toy studies in which events are generated with $|\lambda|^2 = 0.95$ and $|\lambda|^2 = 1.05$. These datasets are subsequently fitted with the assumption $|\lambda|^2 = 1$. The differences in the fit results are assigned as systematic uncertainties to the various parameters. The effect depends on the actual value of ϕ_s and is found to be negligible for both Γ_s and $\Delta\Gamma_s$, and 0.02 for ϕ_s.

- production asymmetry between B_s^0 and $\overline{B}_s^0$ mesons: in the ϕ_s analysis, it is assumed that there is no production asymmetry between B_s^0 and $\overline{B}_s^0$ mesons. Toy studies are performed by generating datasets with events that are generated with a generous $\pm 10\%$ production asymmetry. These datasets are fitted with the assumption of no production asymmetry. Again, the differences in the fit results are assigned as systematic uncertainties to the various parameters. The effect depends on the value of ϕ_s and is found to be (for the fitted value of ϕ_s) negligible for both Γ_s and $\Delta\Gamma_s$, and 0.01 for ϕ_s.

- difference in tagging efficiency for B_s^0 and $\overline{B}_s^0$ mesons: as indicated in Table 6.6, the signal tagging asymmetry $\delta_{T,\mathrm{signal}} = 0.000 \pm 0.012$, therefore, this possible source of nuisance asymmetry is ignored.

- difference in mistag probability between B_s^0 and $\overline{B}_s^0$ mesons: the effect of this nuisance asymmetry is absorbed in the constraints on the parameters p_0 and p_1 as indicated in Sec. 6.4.

Decay-Time Resolution, Tagging and Δm_s

The uncertainties related to the decay-time resolution, the tagging calibration and Δm_s are taken into account by constraining the related parameters in the fit:

- the scale factor of the decay-time resolution model is constrained in the fit to $S_{\sigma_t} = 1.45 \pm 0.06$, as mentioned in Sec. 6.6.4,

- the tagging calibration parameters p_0 and p_1 are constrained in the fit to $p_0 = 0.392 \pm 0.009$ and $p_1 = 1.035 \pm 0.024$, as mentioned in Sec. 6.4,
- the $B_s^0 - \overline{B}_s^0$ oscillation frequency Δm_s is constrained in the fit to $\Delta m_s = 17.63 \pm 0.11\,\mathrm{ps}^{-1}$, as measured by LHCb, see Sec. 6.7.

As a consequence, for these parameters, the uncertainties are (implicitly) included in the quoted statistical uncertainty.

Bias from Peaking Backgrounds

The only identified source of peaking background is from $B^0 \to J/\psi K^*$ events. The fraction of these events is estimated to be at most 2% and is estimated to be negligible compared to statistical uncertainties [69].

6.7.6 Summary of Systematic Uncertainties

All the mentioned systematic uncertainties are summarized for each parameter in Table 6.12. The total systematic uncertainty for each parameter is taken to be the quadratic sum of all the individual systematic uncertainties.

	ϕ_s	Γ_s $[\mathrm{ps}^{-1}]$	$\Delta\Gamma_s$ $[\mathrm{ps}^{-1}]$	$\lvert A_0\rvert^2$	$\lvert A_\perp\rvert^2$	f_S	$\delta_\perp$	$\delta_\parallel$	δ_S
stat. uncert.	0.10	0.005	0.018	0.007	0.010	0.011	0.34	0.21	0.34
fit bias	-	0.003	0.002	0.003	0.003	0.005	0.03	0.10	0.05
bkg. modelling	0.01	0.001	0.003	0.001	-	0.002	0.05	0.03	0.06
ang. acc. rew.	-	0.001	0.001	0.032	0.018	-	0.02	0.03	0.02
ang. acc. stat.	-	0.001	0.001	0.001	0.002	0.001	0.01	0.02	0.01
small time acc.	-	0.002	0.002	-	0.001	-	-	0.01	-
large time acc.	-	0.006	-	-	-	-	-	-	-
length + mom. scale	-	0.001	-	-	-	-	-	-	-
CPV mix + dec.	0.02	-	-	-	-	-	-	-	-
prod. asymm.	0.01	-	-	-	-	-	-	-	-
total syst. uncert.	0.02	0.007	0.004	0.032	0.018	0.005	0.06	0.11	0.08

Table 6.12: *Summary of systematic uncertainties. The total systematic uncertainty for every parameter is the quadratic sum of all the sources of systematic uncertainties. A hyphen '-' indicates no or negligible effect.*

6.8 Final Results including Systematic Uncertainties

A time-dependent angular analysis is performed on approximately 21 200 $B_s^0 \to J/\psi\,\phi$ candidates, obtained from $1\,\mathrm{fb}^{-1}$ of pp collisions collected during the 2011 LHCb runs at $\sqrt{s} = 7\,\mathrm{TeV}$. With an effective decay-time resolution of 46 fs and an effective tagging efficiency of $\epsilon_T D^2_{\mathrm{eff}} = (2.3 \pm 0.3)\%$, the following results for ϕ_s, Γ_s and $\Delta\Gamma_s$ are found:

$$\begin{aligned}\phi_s &= 0.00 \pm 0.10\,(\text{stat.}) \pm 0.02\,(\text{syst.}) \\ \Gamma_s &= 0.658 \pm 0.005\,(\text{stat.}) \pm 0.007\,(\text{syst.})\ \text{ps}^{-1} \\ \Delta\Gamma_s &= 0.115 \pm 0.018\,(\text{stat.}) \pm 0.004\,(\text{syst.})\ \text{ps}^{-1}\end{aligned}$$

In addition, for the transversity amplitudes the following values are found:

$$\begin{aligned}|A_0|^2 &= 0.522 \pm 0.007\,(\text{stat.}) \pm 0.032\,(\text{syst.}) \\ |A_\perp|^2 &= 0.247 \pm 0.010\,(\text{stat.}) \pm 0.018\,(\text{syst.}) \\ f_S &= 0.022 \pm 0.011\,(\text{stat.}) \pm 0.005\,(\text{syst.}) \quad .\end{aligned}$$

The parameter $|A_\parallel|^2$ is not a fit parameter, since the sum of the P-wave amplitudes is normalized to one, see Eq. 6.25. Finally, for the strong phases it is found that

$$\begin{aligned}\delta_\perp &= 2.89 \pm 0.34\,(\text{stat.}) \pm 0.06\,(\text{syst.}) \\ \delta_\parallel &= 3.33 \pm 0.21\,(\text{stat.}) \pm 0.11\,(\text{syst.}) \\ \delta_S &= 2.89 \pm 0.34\,(\text{stat.}) \pm 0.08\,(\text{syst.}) \quad .\end{aligned}$$

6.9 Discussion and Outlook

The measurement of $\phi_s = 0.00 \pm 0.10\,(\text{stat.}) \pm 0.02\,(\text{syst.})$ is the world's most precise measurement of ϕ_s. In addition, the measurement of $\Delta\Gamma_s = 0.115 \pm 0.018\,(\text{stat.}) \pm 0.004\,(\text{syst.})\ \text{ps}^{-1}$ is the first direct observation of a non-zero value of $\Delta\Gamma_s$. These results are all in good agreement with the Standard Model.

For most of the parameters, the uncertainties are still statistics-dominated. This is not the case for $|A_0|^2$ and $|A_\perp|^2$, where the systematic uncertainty is dominated by the angular acceptance correction. In addition, for Γ_s, the dominating uncertainty is the systematic uncertainty on the large decay-time acceptance.

Several improvements on the measurement of ϕ_s are foreseen. First of all, inclusion of the same-side tagger will improve the effective tagging power and thus the sensitivity to ϕ_s. In addition, a different trigger strategy can increase the event yields.

The weak phase ϕ_s is measured in other decays as well, for instance in $\overline{B}_s^0 \to J/\psi\,\pi^+\pi^-$ decays [73], which also allows for the combination of the results from separate independent analyses. Finally, to ensure that the zero value of ϕ_s is a genuine SM effect, instead of possible New Physics effects that are cancelled by penguin contributions, the latter should be taken into account as described in Sec. 5.9.

APPENDIX

A

In-situ Irradiations of OT Modules

In laboratory tests on OT modules, it was found that the maximum observed gain loss varies, depending on parameters such as high voltage, irradiation source type, source intensity, gas flow, gas mixture, irradiation time or flushing time prior to irradiation. Based on these observations, several beneficial treatments were devised, tested and finally applied to the installed OT modules, in order to prevent or reduce possible gain loss in the OT. The effects of these treatments were quantified by deliberately irradiating and scanning the modules, using the dedicated scanning setup as described in Chap. 4.

A.1 Beneficial Treatments

The following treatments were applied to the installed OT modules to prevent gain loss or reduce the ageing rate:

1. Flushing: given the fact that outgassing of the glue used in the construction of OT modules causes gain loss, long term flushing is expected to transport away these vapours. All OT modules have been flushed continuously since the completion of installation in the LHCb experimental cavern, in spring 2007. In addition, it was observed that a lower gas flow during irradiation is beneficial for the ageing rate. The gas flow in the OT is set to about 760 l/hr, corresponding to approximately 0.2 volume exchanges per hour.

2. Heating: in addition to continuous flushing, heating the modules at 40° C accelerates the outgassing of the glue, although the effect on the ageing rate differs from module to module. Before the LHC startup at the end of 2009, all modules in the experiment were heated for two weeks at 35° C while flushed at 0.5 volume exchanges per hour.

3. Additives in gas mixture: adding oxygen to the counting gas has been used in other HEP experiments to avoid irradiation damage in gas detectors [74, 75]. Tests on OT modules [76] show that the gain loss for gas mixtures with O_2 is reduced by approximately a factor two. The OT gas mixture was changed at the beginning of

2010 from the design composition of Ar/CO_2 (70%/30%) to a drift gas with an oxygen component, $Ar/CO_2/O_2$ (70%/28.5%/1.5%).

The positive effect of using oxygen as an additive to the gas mixture is probably due to an increased production of ozone [77]. The production of ozone under the source is presumably the reason that no gain loss is observed directly under and downstream of the source. One hypothesis is that instead of creating carbon deposits on the anode wire, the produced ozone radicals chemically bind to the outgassing vapours to form harmless stable gas molecules. This is consistent with the observation that the gain loss is higher when the gas flow is increased, since in that case the produced beneficial ozone radicals are removed from the source region faster.

A.2 In-situ Scans

The amount of gain loss in a module is determined by measuring the response of the module before and after irradiation with a 74 MBq ^{90}Sr source. During irradiation the source is centered on the middle of a module (around wire 32) using a special source holder and is collimated with a diameter of 6 mm at a distance of 4 cm from the module. The source is then moved up using a stepping motor to the desired location on the module and subsequently the high voltage of 1600 V is supplied to the wires. The typical irradiation time is 15 hours. The detector response is determined by scanning a module using a stepping motor and a source holder that holds two 74 MBq ^{90}Sr sources (identical to the irradiation source). The scan is performed by moving up the sources in steps of 1 cm (roughly 5 seconds per cm). At every measuring point the current through the wires induced by the sources is measured with a dedicated current meter.

The position of the scanning frame which accommodates the sources is limited to two C-frames on the A-side (positive LHCb x-coordinate) of the detector: C-frame T1-Q13-XU and C-frame T2-Q13-XU. The locations of these C-frames as well as the modules that were irradiated for gain stability tests are shown in Fig. A.1.

A.2.1 Quantifying Gain Loss

The gain loss is quantified by comparing the 2-dimensional current profiles before and after irradiation by taking the ratio of the two. This profile ratio is expected to be close to unity everywhere, except for the irradiated area.

Since the atmospheric pressure influences the gas conditions in the OT modules, the induced currents in the wires change from scan to scan. As a result, the absolute current measured before and after irradiation differ, even on a day-to-day basis. To correct for different values of the atmospheric pressure, the normalization of the profile ratio is performed in a region outside the irradiated region.

The gain loss is quantified in the following way: in the irradiated region, the two points with largest gain losses are found. The average of these two values is called the maximal gain loss (MGL). The damage of the module expressed in a percentage is then defined as $(1 - \mathrm{MGL}) \times 100\%$.

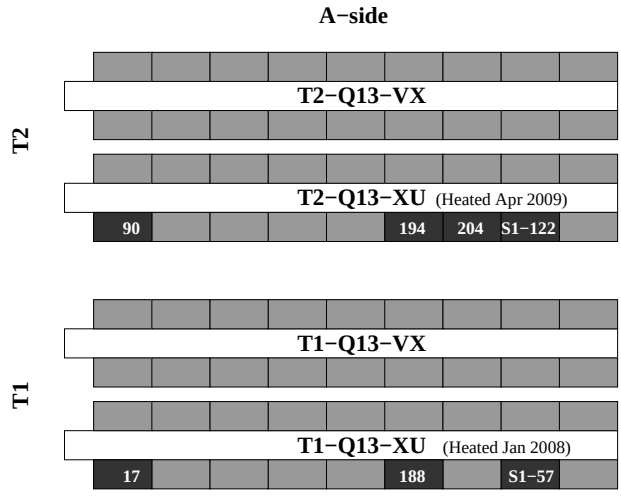

Figure A.1: *Schematic top view of the A side of the OT. Indicated are the unique serial numbers of the irradiated modules and the dates of heating of the C-frames.*

A.3 Results of in-situ Scans

A.3.1 C-frame T2-Q13-XU

Modules in this C-frame were irradiated and scanned before the C-frame was heated using heating blankets, allowing for a comparison of the behavior of the modules before, and after heating in-situ. The results for the irradiation tests performed on modules in C-frame T2-Q13-XU are summarized in Table A.1, which, for every irradiated module, shows the module type, irradiation date, total irradiation time and the maximal gain loss as defined in Sec A.2.1. Notice that no significant difference is observed between modules irradiated before and after module heating, whereas addition of O_2 does seem to have a beneficial effect on the ageing rate, since, in almost all cases, no clear irradiation damage is observed after the addition of O_2. The damage of 38% in module 122-125, after 84 hours of irradiation, is the location that was cured using the LHC beam as shown in Fig. 5 in Chap. 4.

A.3.2 C-frame T1-Q13-XU

The results for the irradiation tests performed on modules in C-frame T2-Q13-XU are summarized in Table A.2. No major differences in module behavior are observed as compared to C-frame T2-Q13-XU.

A

module	type	date	irr. time (hrs.)	max. damage	comment
90	F (NI)	08-20-08	14 (+14)	7% (9%)	before heating
90	F (NI)	02-24-09	66	9%	before heating
90	F (NI)	04-29-09	18	8%	after heating
90	F (NI)	10-22-09	16	7%	after heating
90	F (NI)	01-25-10	17	6% *	after addition of O_2
90	F (NI)	01-13-11	14	7% *	after addition of O_2
90	F (NI)	Jan 2012	353	6% *	after addition of O_2
122-125	S1 (WS)	02-25-09	14 (+70)	16% (38%)	before heating
122-125	S1(WS)	04-28-09	15	16%	after heating
122-125	S1 (WS)	10-21-09	19	13%	after heating
122-125	S1 (WS)	01-27-10	17	7%	after addition of O_2
122-125	S1 (WS)	07-19-10	14	10% *	after addition of O_2
122-125	S1 (WS)	01-11-11	16.5	7%	after addition of O_2
122-125	S1 (WS)	07-05-11	17 (+19)	7% (6%) *	after addition of O_2
194	F (HD)	02-27-09	21	8%	before heating
194	F (HD)	04-30-09	18	7%	after heating
194	F (HD)	07-20-10	13	5% *	after addition of O_2
204	F (HD)	02-26-09	18	9%	before heating

Table A.1: *Gain stability scan results for C-frame T2-Q13-XU. The maximal damage in brackets in case of a second irradiation is the total damage after the two irradiations. The acronym in parentheses in the type column indicates the production site: WS = Warsaw, NI = Nikhef Amsterdam, HD = Heidelberg. *: no clear irradiation spot could be discerned in the profile ratio.*

module	type	date	irr. time (hrs.)	max. damage
17	F (NI)	03-24-09	14	12%
57-18	S1 (WS)	03-25-09	14	6%
57-18	S1 (WS)	03-26-09	42	6%
188	F (HD)	03-31-09	21	7%

Table A.2: *Irradiation results for OT C-frame T1-Q13-XU. The second irradiation of 57-18 (42 hours) was at a different position on the module than the irradiation that lasted for 14 hours.*

APPENDIX

B

Gain Stability Monitoring using ^{90}Sr Scans

The ^{90}Sr scans are also used to monitor gain stability after periods of LHC operation. The lower half of eight modules located in C-frame T2-Q13-XU (see Fig. A.1) have been scanned in the summer of 2008, the winter shutdown of 2010/2011 and the winter shutdown of 2011/2012. This appendix summarizes the results of these scans.

B.1 Atmospheric Pressure Correction

In Appendix A, it was explained that atmospheric pressure effects were corrected by normalizing the current ratio to a region that was not irradiated by the ^{90}Sr source. However, when using the module scans to monitor gain stability over time, the region of interest consists of the entire module and thus an absolute pressure correction must be applied. Therefore the air pressure at the moment of the individual scans must be known.

B.1.1 Atmospheric Pressure in the Summer of 2008

No atmospheric pressure data is available for the LHCb pit during the summer of 2008. However, using meteorological data[1], recorded at Geneva airport at an elevation of 420 m, the atmospheric pressure in the LHCb pit can be estimated. The values for the atmospheric pressure p_0 at sea level were $p_0 = 1015.8\,\mathrm{hPa}$, $p_0 = 1015.6\,\mathrm{hPa}$ and $p_0 = 1019.2\,\mathrm{hPa}$, on August 18, 19 and 20 (the dates of the ^{90}Sr scans in 2008), respectively. We assume the LHCb pit is located 100 m below the surface, at 320 m above sea level. The atmospheric pressure at this height can be calculated from the atmospheric pressure at sea level:

$$p = p_0 \left(1 - \frac{Lh}{T_0}\right)^{\frac{gM}{RL}} \quad , \tag{B.1}$$

where $L = 0.0065\,\mathrm{K/km}$, $T_0 = 288.15\,\mathrm{K}$, $g = 9.81\,\mathrm{m/s^2}$, $M = 0.0289644\,\mathrm{kg/mol}$, $R = 8.31447\,\mathrm{J/(mol\ K)}$ and h is the elevation in meters. Using Eq. B.1, the values for the air

[1] http://www.wunderground.com/history/airport/LSGG/2008/8/19/DailyHistory.html

pressure in the LHCb pit at $h = 320\,\mathrm{m}$ are calculated and the average of 978.8 hPa is taken as the atmospheric pressure for all the scans recorded during the summer of 2008, as indicated in Table B.1. This table shows the scanning dates and the corresponding atmospheric pressure for every scanned module in C-frame T2-Q13-XU.

Table B.2 shows the results of two sets of scan comparisons. One comparison is between winter 2011/2012 and winter 2010/2011, while the other one is the comparison between winter 2011/2012 and summer 2008. The pressure correction factor is obtained from the difference in atmospheric pressure as found in Table B.1, using the relation

$$\frac{\Delta G}{G} = -5.18 \frac{\Delta p}{p_0} \quad , \tag{B.2}$$

with $\frac{\Delta G}{G}$ the relative gain and $\frac{\Delta p}{p_0}$ the relative atmospheric pressure, as explained in Chap. 4.

Table B.1: *Summary of ^{90}Sr scans. (*): estimates as explained in the text.*

	summer 2008		winter shutdown 2010/2011		winter shutdown 2011/2012	
module	date	pressure (*)	date	pressure	date	pressure
90A	2008-8-19 19:18	978.8	2011-1-11 14:47	972.9	2012-1-10 17:46	977.7
90B	2008-8-20 9:44	978.8	2011-2-2 22:36	989.3	2012-1-10 17:13	977.7
91A	2008-8-20 15:25	978.8	2011-1-12 18:29	984.8	2012-1-11 12:53	972.9
91B	2008-8-20 14:57	978.8	2011-1-12 18:01	984.8	2012-1-11 12:06	972.9
92A	2008-8-20 16:35	978.8	2011-1-12 17:16	984.3	2012-1-11 11:30	972.9
92B	2008-8-20 16:08	978.8	2011-1-12 16:45	984.3	2012-1-11 10:51	973.4
93A	2008-8-18 18:34	978.8	2011-1-12 15:44	984.0	2012-1-10 16:34	977.7
93B	2008-8-18 18:09	978.8	2011-1-12 14:57	984.0	2012-1-10 16:00	977.7
94A	2008-8-19 11:21	978.8	2011-1-12 14:21	984.0	2012-1-10 15:09	977.9
94B	2008-8-19 10:47	978.8	2011-1-12 12:48	984.0	2012-1-10 14:44	977.9
194A	2008-8-19 15:49	978.8	2011-1-12 12:12	984.3	2011-12-20 17:07	976.4
194B	2008-8-19 14:46	978.8	2011-1-12 11:41	984.3	2011-12-20 16:41	975.9
204A	2008-8-19 17:18	978.8	2011-1-12 11:01	984.0	2012-1-10 13:07	979.2
204B	2008-8-19 16:48	978.8	2011-1-12 10:24	984.3	2012-10 12:38	979.2
122-125A	2008-8-20 14:22	978.8	2011-1-11 15:53	973.4	2011-12-20 14:59	975.4
122-125B	2008-8-20 12:32	978.8	2011-1-12 9:43	984.0	2011-12-20 14:22	975.4

Table B.2: *Results of gain stability monitoring using ^{90}Sr scans.*

	winter 2011/2012 - winter 2010/2011			winter 2011/2012 - summer 2008		
module	relative gain	pressure correction factor	pressure corrected relative gain	relative gain	pressure correction factor	pressure corrected relative gain
90A	0.84	1.03	0.87	0.83	0.99	0.82
90B	0.94	0.94	0.88	0.84	0.99	0.83
91A	0.89	0.94	0.84	0.84	0.97	0.81
91B	0.88	0.94	0.83	0.85	0.97	0.82
92A	0.88	0.94	0.83	0.84	0.97	0.81
92B	0.88	0.95	0.84	0.84	0.97	0.81
93A	0.91	0.97	0.88	0.85	0.99	0.84
93B	0.91	0.97	0.88	0.86	0.99	0.85
94A	0.90	0.97	0.87	0.83	1.00	0.83
94B	0.90	0.97	0.87	0.83	1.00	0.83
194A	1.00	0.96	0.96	0.91	0.99	0.90
194B	1.01	0.96	0.97	0.93	0.98	0.91
204A	0.91	0.98	0.89	0.83	1.00	0.83
204B	0.91	0.97	0.88	0.82	1.00	0.82
122-125A	0.96	1.01	0.97	0.97	0.98	0.95
122-125B	1.03	0.96	0.99	0.97	0.98	0.95

APPENDIX

C

Gain Loss Monitoring using Threshold Scans: Conditions

This chapter summarizes operational conditions for all the OT threshold layer scans that were recorded during 2010 and 2011.

Table C.1 contains the recording dates and links to OT logbook entries for all threshold scans and some additional comments relevant for particular scans. Table C.2 contains the total delivered integrated luminosity at the moment of the individual scans, the number of thresholds that were recorded per layer and the atmospheric pressure at the time of the scans. Table C.3 summarizes run conditions during the various threshold scans. For every scan, the number of the LHC fill, the LHCb runs and the average number of visible pp interactions per bunch crossing, μ, is given. In addition, for every run, the total number of events per run, the number of recorded steps and the number of events per step are given.

Table C.1: *Additional information on threshold layer scans. On 15 May 2011 the readout gate was changed for station T1, T2 and T3 and an updated t_0 calibration was released. However, in the threshold scan recipes the readout gate is unchanged and a dedicated t_0 calibration database needs to be used in the analysis.*

date	logbook entry	remarks
Jul. 4 2010	https://lblogbook.cern.ch/OT/1129	only layer 0
Aug. 14 2010	https://lblogbook.cern.ch/OT/1214	full OT
Oct. 27 2010	https://lblogbook.cern.ch/OT/1339	non-conventional stepping definition
Mar. 13 2011	https://lblogbook.cern.ch/OT/1508	HV scan layer 4 in addition
May 16 2011	https://lblogbook.cern.ch/OT/1636	need dedicated t_0 database from here onward, see caption
Jun. 11 2011	https://lblogbook.cern.ch/OT/1711	
Jul. 29 2011	https://lblogbook.cern.ch/OT/1825	
Sep. 7 2011	https://lblogbook.cern.ch/OT/1921	
Oct. 12 2011	https://lblogbook.cern.ch/OT/2058	

Table C.2: *Threshold layer scan conditions. (*): numbers for total delivered lumi from https://lbrundb.cern.ch/rundb/fill*

date	total delivered luminosity [pb^{-1}] (*)	thresholds per layer	atmospheric pressure	pressure correction factor wrt Aug. 14 2010
Jul. 4 2010	0.6	8	981.0	-
Aug. 14 2010	1.2	8	975.0	1.0 (definition)
Oct. 27 2010	34.4	8	971.5	0.98
Mar. 13 2011	41.8	8	971.0	0.98
May 16 2011	137.8	8	987.8	1.08
Jun. 11 2011	331.4	10	978.0	1.02
Jul. 29 2011	584.8	10	977.2	1.01
Sep. 7 2011	809.2	10	979.0	1.02
Oct. 12 2011	1239.5	10	985.3	1.06

Table C.3: *Run conditions during threshold layer scans. (*): numbers from https://lbweb.cern.ch/groups/online/OperationsPlots/OperationsDashboard.htm. (**): numbers from private communication with Richard Jacobsson.*

date	LHC fill	LHCb runs	average μ (*)	average μ (**)	total events in run	number of steps in run	number of events per step	remarks
Jul. 4 2010	not in RunDB	77043	?	?	14.7M	96	153k	only OT in
Aug. 14 2010	1283	77555	?	0.6	14.1M	100	140k	all but RICH1 & RICH2
Oct. 27 2010	1436	81329	?	1.52	6.1M	40	150k	
	1436	81330	?	1.49	8.8M	$\sim$50	176k	
	1436	81331	?	1.46	4.1M	27	150k	
Mar. 13 2011	1613	87115	1.10	1.14	5.0M	35	143k	
	1613	87120	1.10	1.11	9.9M	66	150k	
May 16 2011	1785	91638	1.77	1.91	17.8M	42	424k	all but RICH1 & RICH2
	1785	91646	1.77	1.86	12.6M	30	420k	all but RICH1 & RICH2
	1785	91650	1.77	1.82	13.9M	33	421k	all but RICH1 & RICH2
Jun. 11 2011	1863	93394	1.26	0.09	32.7M	110	297k	
	1863	93396	1.26	0.08	4.6M	15	307k	
Jul. 29 2011	1991	97471	0.89	0.14	28M	87	322k	
	1991	97475	0.89	0.12	10.5M	36	292k	
Sep. 7 2011	2083	101346	1.30	1.74	22.9M	76	301k	all but RICH1 & RICH2
	2083	101349	1.30	1.62	4.5M	13	346k	all but RICH1 & RICH2
	2083	101350	1.30	1.61	9.2M	27	341k	all but RICH1 & RICH2
	2083	101354	1.30	1.57	5.4M	16	338k	all but RICH1 & RICH2
Oct. 12 2011	2204	103332	1.11	0.56	36.2M	124	292k	

C

C

APPENDIX

D

$B_s^0 \to J/\psi\,\phi$ PDF

The full $B_s^0 \to J/\psi\,\phi$ signal PDF with $q_T = 1$ is the sum of the following ten terms:

$$\begin{aligned} T_1(t) f_1(\vec{\Omega}) &= \cos^2\psi(1-\sin^2\theta\cos^2\phi)\cdot\frac{|a_0|^2 e^{-\Gamma_s t}}{1+C} \\ &\left(\cosh\left(\frac{\Delta\Gamma_s}{2}t\right) + C\cos(\Delta m_s t)\right. \\ &\left. -D\sinh\left(\frac{\Delta\Gamma_s}{2}t\right) - S\sin(\Delta m_s t)\right) \end{aligned} \tag{D.1}$$

$$\begin{aligned} T_2(t) f_2(\vec{\Omega}) &= \frac{1}{2}\sin^2\psi(1-\sin^2\theta\sin^2\phi)\cdot\frac{|a_\parallel|^2 e^{-\Gamma_s t}}{1+C} \\ &\left(\cosh\left(\frac{\Delta\Gamma_s}{2}t\right) + C\cos(\Delta m_s t)\right. \\ &\left. -D\sinh\left(\frac{\Delta\Gamma_s}{2}t\right) - S\sin(\Delta m_s t)\right) \end{aligned} \tag{D.2}$$

$$\begin{aligned} T_3(t) f_3(\vec{\Omega}) &= \frac{1}{2}\sin^2\psi\sin^2\theta\cdot\frac{|a_\perp|^2 e^{-\Gamma_s t}}{1+C} \\ &\left(\cosh\left(\frac{\Delta\Gamma_s}{2}t\right) + C\cos(\Delta m_s t)\right. \\ &\left. +D\sinh\left(\frac{\Delta\Gamma_s}{2}t\right) + S\sin(\Delta m_s t)\right) \end{aligned} \tag{D.3}$$

$$
\begin{aligned}
T_4(t)f_4(\vec{\Omega}) &= \frac{1}{2\sqrt{2}}\sin(2\psi)\sin^2\theta\sin(2\phi)\cdot\frac{|a_0||a_\parallel|e^{-\Gamma_s t}}{1+C} \\
&\quad \cos(\delta_\parallel-\delta_0)\left(\cosh\left(\frac{\Delta\Gamma_s}{2}t\right)+C\cos(\Delta m_s t)\right. \\
&\quad \left.-D\sinh\left(\frac{\Delta\Gamma_s}{2}t\right)-S\sin(\Delta m_s t)\right) \qquad \text{(D.4)} \\
T_5(t)f_5(\vec{\Omega}) &= \frac{1}{2\sqrt{2}}\sin(2\psi)\sin(2\theta)\cos\phi\cdot\frac{|a_0||a_\perp|e^{-\Gamma_s t}}{1+C} \\
&\quad \left(\sin(\delta_\perp-\delta_0)[C\cosh\left(\frac{\Delta\Gamma_s}{2}t\right)+\cos(\Delta m_s t)]\right. \\
&\quad \left.+\cos(\delta_\perp-\delta_0)[S\sinh\left(\frac{\Delta\Gamma_s}{2}t\right)-D\sin(\Delta m_s t)]\right) \qquad \text{(D.5)} \\
T_6(t)f_6(\vec{\Omega}) &= -\frac{1}{2}\sin^2\psi\sin(2\theta)\sin\phi\cdot\frac{|a_\parallel||a_\perp|e^{-\Gamma_s t}}{1+C} \\
&\quad \left(\sin(\delta_\perp-\delta_\parallel)[C\cosh\left(\frac{\Delta\Gamma_s}{2}t\right)+\cos(\Delta m_s t)]\right. \\
&\quad \left.+\cos(\delta_\perp-\delta_\parallel)[S\sinh\left(\frac{\Delta\Gamma_s}{2}t\right)-D\sin(\Delta m_s t)]\right) \qquad \text{(D.6)} \\
T_7(t)f_7(\vec{\Omega}) &= \frac{1}{3}(1-\sin^2\theta\cos^2\phi)\cdot\frac{|a_S|^2e^{-\Gamma_s t}}{1+C} \\
&\quad \left(\cosh\left(\frac{\Delta\Gamma_s}{2}t\right)+C\cos(\Delta m_s t)\right. \\
&\quad \left.+D\sinh\left(\frac{\Delta\Gamma_s}{2}t\right)+S\sin(\Delta m_s t)\right) \qquad \text{(D.7)} \\
T_8(t)f_8(\vec{\Omega}) &= \frac{2}{3}\sqrt{3}\cos\psi(1-\sin^2\theta\cos^2\phi)\cdot\frac{|a_0||a_S|e^{-\Gamma_s t}}{1+C} \\
&\quad \left(\cos(\delta_0-\delta_S)[C\cosh\left(\frac{\Delta\Gamma_s}{2}t\right)+\cos(\Delta m_s t)]\right. \\
&\quad \left.+\sin(\delta_0-\delta_S)[S\sinh\left(\frac{\Delta\Gamma_s}{2}t\right)-D\sin(\Delta m_s t)]\right) \qquad \text{(D.8)} \\
T_9(t)f_9(\vec{\Omega}) &= \frac{1}{6}\sqrt{6}\sin\psi\sin^2\theta\sin(2\phi)\cdot\frac{|a_\parallel||a_S|e^{-\Gamma_s t}}{1+C} \\
&\quad \left(\cos(\delta_\parallel-\delta_S)[C\cosh\left(\frac{\Delta\Gamma_s}{2}t\right)+\cos(\Delta m_s t)]\right. \\
&\quad \left.+\sin(\delta_\parallel-\delta_S)[S\sinh\left(\frac{\Delta\Gamma_s}{2}t\right)-D\sin(\Delta m_s t)]\right) \qquad \text{(D.9)}
\end{aligned}
$$

D

$$
\begin{aligned}
T_{10}(t) f_{10}(\vec{\Omega}) \quad = \quad & -\frac{1}{6}\sqrt{6}\sin\psi\sin(2\theta)\cos\phi \cdot \frac{|a_\perp||a_S|e^{-\Gamma_s t}}{1+C} \\
& \sin(\delta_\perp - \delta_S)\left(\cosh\left(\frac{\Delta\Gamma_s}{2}t\right) + C\cos(\Delta m_s t)\right. \\
& \left. + D\sinh\left(\frac{\Delta\Gamma_s}{2}t\right) + S\sin(\Delta m_s t)\right) \quad . \qquad \text{(D.10)}
\end{aligned}
$$

The PDF for $q_T = -1$ is found by making the following substitutions in the equations above:

$$
B_s^0 \leftrightarrow \overline{B}_s^0 \quad \Leftrightarrow \quad (S \leftrightarrow -S, C \leftrightarrow -C, a_\perp \leftrightarrow -a_\perp) \quad . \qquad \text{(D.11)}
$$

D

D

APPENDIX

E

Angular Distribution: Basis Functions

The angular dependence of the $B_s^0 \to J/\psi\,\phi$ PDF is coded up in terms of associated Legendre polynomials $P_l^m(\cos\psi)$ and spherical harmonics $Y_l^m(\theta,\phi)$, where ψ, θ and ϕ are the decay angles in the transversity frame.

E.1 Associated Legendre Polynomials

$$P_l(x) = \frac{1}{2^l l!}\frac{d^l}{dx^l}(x^2-1)^l \tag{E.1}$$

$$P_l^m(x) = \frac{(-1)^m}{2^l l!}(1-x^2)^{\frac{1}{2}m}\frac{d^{l+m}}{dx^{l+m}}(x^2-1)^l \tag{E.2}$$

$$P_l^{-m}(x) = (-1)^m\frac{(l-m)!}{(l+m)!}P_l^m(x) \tag{E.3}$$

$$P_0^0(\cos\psi) = 1 \tag{E.4}$$

$$P_1^0(\cos\psi) = \cos\psi \tag{E.5}$$

$$P_2^0(\cos\psi) = \frac{1}{2}(3\cos^2\psi - 1) \tag{E.6}$$

$$P_1^1(\cos\psi) = -\sin\psi \tag{E.7}$$

$$P_2^1(\cos\psi) = -3\cos\psi\sin\psi \tag{E.8}$$

$$P_2^2(\cos\psi) = 3\sin^2\psi \tag{E.9}$$

Inverting these results in

$$\cos\psi = P_1^0(\cos\psi) \tag{E.10}$$
$$\sin\psi = -P_1^1(\cos\psi) \tag{E.11}$$
$$\cos^2\psi = \frac{2}{3}(P_2^0(\cos\psi) + \frac{1}{2}P_0^0(\cos\psi)) \tag{E.12}$$
$$\sin^2\psi = \frac{1}{3}P_2^2(\cos\psi) \tag{E.13}$$
$$\sin 2\psi = -\frac{2}{3}P_2^1(\cos\psi) \tag{E.14}$$

E

E.2 Spherical Harmonics

$$Y_l^m(\theta,\phi) = N_{lm}P_l^m(\cos\theta)e^{im\phi} \text{ with } N_{lm} = \sqrt{\frac{2l+1}{4\pi}\frac{(l-m)!}{(l+m)!}} \tag{E.15}$$
$$Y_l^{-m}(\theta,\phi) = (-1)^m N_{lm}P_l^m(\cos\theta)e^{-im\phi} \tag{E.16}$$

$$Y_{lm}(\theta,\phi) = \begin{cases} Y_l^0(\theta,\phi) & (m=0) \\ \frac{1}{\sqrt{2}}\left(Y_l^m + (-1)^m Y_l^{-m}\right) & (m>0) \\ \frac{1}{i\sqrt{2}}\left(Y_l^{|m|} - (-1)^{|m|}Y_l^{-|m|}\right) & (m<0) \end{cases} \tag{E.17}$$
$$= \begin{cases} N_{l0}P_l^0(\cos\theta) & (m=0) \\ \sqrt{2}N_{lm}P_l^m(\cos\theta)\cos(m\phi) & (m>0) \\ \sqrt{2}N_{l|m|}P_l^{|m|}(\cos\theta)\sin(|m|\phi) & (m<0) \end{cases} \tag{E.18}$$

This results in

$$1 = \sqrt{\frac{4\pi}{9}}\left(3Y_{00}(\cos\theta,\phi)\right) \tag{E.19}$$

$$\cos^2\theta = \sqrt{\frac{4\pi}{9}}\left(Y_{00}(\cos\theta,\phi)+\sqrt{\frac{4}{5}}Y_{20}(\cos\theta,\phi)\right) \tag{E.20}$$

$$\sin^2\theta = \sqrt{\frac{4\pi}{9}}\left(2Y_{00}(\cos\theta,\phi)-\sqrt{\frac{4}{5}}Y_{20}(\cos\theta,\phi)\right) \tag{E.21}$$

$$\sin^2\theta\cos^2\phi = \sqrt{\frac{4\pi}{9}}\left(Y_{00}(\cos\theta,\phi)-\sqrt{\frac{1}{5}}Y_{20}(\cos\theta,\phi)+\sqrt{\frac{3}{5}}Y_{2,2}\ (\cos\theta,\phi)\right) \tag{E.22}$$

$$\sin^2\theta\sin^2\phi = \sqrt{\frac{4\pi}{9}}\left(Y_{00}(\cos\theta,\phi)-\sqrt{\frac{1}{5}}Y_{20}(\cos\theta,\phi)-\sqrt{\frac{3}{5}}Y_{2,2}\ (\cos\theta,\phi)\right) \tag{E.23}$$

$$\sin^2\theta\cos\phi\sin\phi = \sqrt{\frac{4\pi}{9}}\left(\sqrt{\frac{3}{5}}Y_{2,-2}(\cos\theta,\phi)\right) \tag{E.24}$$

$$\sin\theta\cos\theta\cos\phi = \sqrt{\frac{4\pi}{9}}\left(-\sqrt{\frac{3}{5}}Y_{2,1}(\cos\theta,\phi)\right) \tag{E.25}$$

$$\sin\theta\cos\theta\sin\phi = \sqrt{\frac{4\pi}{9}}\left(-\sqrt{\frac{3}{5}}Y_{2,-1}(\cos\theta,\phi)\right) \tag{E.26}$$

E

E.3 Angular Distributions in Terms of Basis Functions

The P-wave angular distributions in Table 5.1 and the S-wave angular distributions in Table 5.3 are rewritten using spherical harmonics and associated Legendre polynomials and summarized in Table E.1.

E.4 Integrals

The integrals of products of P_i^j and Y_l^m are calculated as

$$\int_{-1}^{1} d\cos\theta \int_0^{2\pi} d\phi\ \ Y_l^m(\theta,\phi)Y_{l'}^{m'*}(\theta,\phi) = \delta_{ll'}\delta_{mm'} \tag{E.27}$$

$$\int_{-1}^{1} dx P_k^m P_l^m = \frac{2}{2l+1}\frac{(l+m)!}{(l-m)!}\delta_{kl} \tag{E.28}$$

$$P_2^2(x) = 3(1-x^2) = 2(P_0-P_2) \tag{E.29}$$

$$P_2^1(x) = -3x(1-x^2)^{1/2} = \tag{E.30}$$

$$= -3x(1-...x^2+...x^4+...x^6+...) \tag{E.31}$$

$$= ...P_1+...P_3+...P_5+...P_7+... \tag{E.32}$$

$$P_1^1(x) = -1(1-x^2)^{1/2} \tag{E.33}$$

$$= ...P_0+...P_2+...P_4+...P_6+... \tag{E.34}$$

(E.35)

	$P_i^j(\cos\psi)Y_{lm}(\cos\theta,\phi)$
$\|A_0(t)\|^2$	$(P_0^0+2P_2^0)\left(2Y_{00}+\sqrt{\frac{1}{5}}Y_{20}-\sqrt{\frac{3}{5}}Y_{22}\right)$
$\|A_\parallel(t)\|^2$	$P_2^2\left(Y_{00}+\frac{1}{2}\sqrt{\frac{1}{5}}Y_{20}+\frac{1}{2}\sqrt{\frac{3}{5}}2Y_{22}\right)$
$\|A_\perp(t)\|^2$	$P_2^2\left(Y_{00}-\sqrt{\frac{1}{5}}Y_{20}\right)$
$\mathrm{Re}(A_0^*(t)A_\parallel(t))$	$P_2^1\left(-\sqrt{\frac{6}{5}}Y_{2,-2}\right)$
$\mathrm{Im}(A_0^*(t)A_\perp(t))$	$P_2^1\left(\sqrt{\frac{6}{5}}Y_{2,1}\right)$
$\mathrm{Im}(A_\parallel^*(t)A_\perp(t))$	$P_2^2\left(\sqrt{\frac{3}{5}}Y_{2,-1}\right)$
$\|A_s(t)\|^2$	$P_0^0\left(2Y_{00}+\sqrt{\frac{1}{5}}Y_{20}-\sqrt{\frac{3}{5}}Y_{22}\right)$
$\mathrm{Re}(A_0^*(t)A_S(t))$	$P_1^0\left(4\sqrt{3}Y_{00}+2\sqrt{\frac{3}{5}}Y_{20}-6\sqrt{\frac{1}{5}}Y_{22}\right)$
$\mathrm{Re}(A_\parallel^*(t)A_S(t))$	$P_1^1\left(-3\sqrt{\frac{2}{5}}Y_{2,-2}\right)$
$\mathrm{Im}(A_\perp^*(t)A_S(t))$	$P_1^1\left(-3\sqrt{\frac{2}{5}}Y_{2,1}\right)$

Table E.1: *The angular dependence of the six P-wave and four S-wave terms in the $B_s^0 \to J/\psi\,\phi$ PDF, expressed in terms of spherical harmonics and associated Legendre polynomials. A common factor $\frac{2}{9}\sqrt{\pi}$ for every term has been omitted for clarity.*

APPENDIX

F

Angular Acceptance Correction: Comparing two Methods

In Sec. 6.2.3 it is shown how the coefficients c^i_{lm} can be calculated when expressing the acceptance function as an expansion in terms of the same basis functions as the $B^0_s \to J/\psi\,\phi$ signal PDF. Another method to correct for angular acceptance is to calculate ten normalization weights corresponding to the ten angular functions $f_i(\vec{\Omega})$, using the concept of likelihood maximization [64]. Here it is shown how to reconstruct these ten normalization weights from the coefficients of the expansion of the angular acceptance function.

The ten normalization weights ξ_i are calculated from a generated Monte Carlo dataset as

$$\xi_i(t) = \int f_i(\vec{\Omega})\epsilon(t,\vec{\Omega})\mathrm{d}\vec{\Omega} = \frac{1}{N_{\mathrm{gen}}} \sum_{e\in\{\mathrm{accepted}\}} \frac{f_i(\vec{\Omega}_{\mathrm{e}})}{g(\vec{\Omega}_{\mathrm{e}}|t_{\mathrm{e}})} \quad , \tag{F.1}$$

where $g(\vec{\Omega},t)$ is the theoretical PDF with which events are generated.

Writing the angular acceptance function as an expansion in terms of associated Legendre polynomials and spherical harmonics,

$$\epsilon(\psi,\theta,\phi) = c^i_{jk} P_i(\cos\psi) Y_{jk}(\theta,\phi) \quad , \tag{F.2}$$

the integral of the product of the acceptance function and the signal PDF (which is the

normalization integral for the resulting PDF), becomes

$$
\begin{aligned}
N(q_T,t) &= \int \mathrm{d}\cos\psi \int \mathrm{d}\cos\theta \int \mathrm{d}\phi\epsilon(\psi,\theta,\phi)|[\vec{A}(t,q_T)+\frac{1}{\sqrt{3}}\vec{S}(t,q_T)]\wedge\hat{n}|^2 \\
&= \frac{2}{9}\sqrt{\pi}\,c^i_{jk}\int \mathrm{d}\cos\psi P_i(\cos\psi)\int \mathrm{d}\cos\theta\mathrm{d}\phi Y_{jk}(\theta,\phi)\Bigg[\\
&\quad |A_0(t)|^2(P_0^0(\cos\psi)+2P_2^0(\cos\psi))\left(2Y_{00}+\sqrt{\frac{1}{5}}Y_{20}-\sqrt{\frac{3}{5}}Y_{22}\right) \\
&\quad +|A_\parallel(t)|^2P_2^2(\cos\psi)\left(Y_{00}+\sqrt{\frac{1}{20}}Y_{20}+\sqrt{\frac{3}{20}}Y_{22}\right) \\
&\quad +|A_\perp(t)|^2P_2^2(\cos\psi)\left(Y_{00}-\sqrt{\frac{1}{5}}Y_{20}\right) \\
&\quad -\mathrm{Re}(A_0^*(t)A_\parallel(t))\sqrt{\frac{6}{5}}P_2^1(\cos\psi)Y_{2,-2} \\
&\quad +\mathrm{Im}(A_0^*(t)A_\perp(t))\sqrt{\frac{6}{5}}P_2^1(\cos\psi)Y_{2,1} \\
&\quad +\mathrm{Im}(A_\parallel^*(t)A_\perp(t))\sqrt{\frac{3}{5}}P_2^2(\cos\psi)Y_{2,-1} \\
&\quad +|A_S(t)|^2P_0^0(2Y_{00}+\sqrt{\frac{1}{5}}Y_{20}-\sqrt{\frac{3}{5}}Y_{22}) \\
&\quad +\mathrm{Re}(A_0^*(t)A_S(t))P_1^0(4\sqrt{3}Y_{00}+2\sqrt{\frac{3}{5}}Y_{20}-6\sqrt{\frac{1}{5}}Y_{22}) \\
&\quad -\mathrm{Re}(A_\parallel^*(t)A_S(t))3\sqrt{\frac{2}{5}}P_1^1Y_{2,-2} \\
&\quad -\mathrm{Im}(A_\perp^*(t)A_S(t))3\sqrt{\frac{2}{5}}P_1^1Y_{2,1}\Bigg] \quad .
\end{aligned}
$$

F

Using the integrals of products of P_i^j and Y_l^m as defined in Appendix E.4 the integrals over $\cos\theta$ and ϕ are calculated:

$$
\begin{aligned}
N(q_T,t) \;=\; & \frac{2}{9}\sqrt{\pi}\int \mathrm{d}\cos\psi P_i(\cos\psi)\Big[\\
& |A_0(t)|^2 2(\frac{1}{2}P_0^0(\cos\psi)+P_2^0(\cos\psi))\left(2c_{00}^i+\sqrt{\frac{1}{5}}c_{20}^i-\sqrt{\frac{3}{5}}c_{22}^i\right) \\
& +|A_\parallel(t)|^2 2(P_0^0(\cos\psi)-P_2^0(\cos\psi))\left(c_{00}^i+\sqrt{\frac{1}{20}}c_{20}^i+\sqrt{\frac{3}{20}}c_{22}^i\right) \\
& +|A_\perp(t)|^2 2(P_0^0(\cos\psi)-P_2^0(\cos\psi))\left(c_{00}^i-\sqrt{\frac{1}{5}}c_{20}^i\right) \\
& -\mathrm{Re}(A_0^*(t)A_\parallel(t))\sqrt{\frac{6}{5}}P_2^1(\cos\psi)c_{2,-2}^i \\
& +\mathrm{Im}(A_0^*(t)A_\perp(t))\sqrt{\frac{6}{5}}P_2^1(\cos\psi)c_{2,1}^i \\
& +\mathrm{Im}(A_\parallel^*(t)A_\perp(t))2\sqrt{\frac{3}{5}}(P_0^0(\cos\psi)-P_2^0(\cos\psi))c_{2,-1}^i \\
& +|A_S(t)|^2 P_0^0(2c_{00}^i+\sqrt{\frac{1}{5}}c_{20}^i-\sqrt{\frac{3}{5}}c_{22}^i) \\
& +\mathrm{Re}(A_0^*(t)A_S(t))P_1^0(4\sqrt{3}c_{00}^i+2\sqrt{\frac{3}{5}}c_{20}^i-6\sqrt{\frac{1}{5}}c_{22}^i) \\
& -\mathrm{Re}(A_\parallel^*(t)A_S(t))3\sqrt{\frac{2}{5}}P_1^1 c_{2,-2}^i \\
& -\mathrm{Im}(A_\perp^*(t)A_S(t))3\sqrt{\frac{2}{5}}P_1^1 c_{2,1}^i\Big] \quad .
\end{aligned}
$$

F

Finally, calculating the integral over $\cos\psi$:

$$
\begin{aligned}
N(q_T,t) &= 4\,\frac{2}{9}\sqrt{\pi}\Big[\\
&\quad |A_0(t)|^2\left(c^0_{00}+\frac{2}{5}c^2_{00}+\sqrt{\frac{1}{20}}(c^0_{20}+\frac{2}{5}c^2_{20})-\sqrt{\frac{3}{20}}(c^0_{22}+\frac{2}{5}c^2_{22})\right) \\
&+ |A_\parallel(t)|^2\left(c^0_{00}-\frac{1}{5}c^2_{00}+\sqrt{\frac{1}{20}}\left(c^0_{20}-\frac{1}{5}c^2_{20}\right)+\sqrt{\frac{3}{20}}\left(c^0_{22}-\frac{1}{5}c^2_{22}\right)\right) \\
&+ |A_\perp(t)|^2\left(c^0_{00}-\frac{1}{5}c^2_{00}-\sqrt{\frac{1}{5}}\left(c^0_{20}-\frac{1}{5}c^2_{20}\right)\right) \\
&+ \mathrm{Re}(A^*_0(t)A_\parallel(t))\sqrt{\frac{6}{5}}\frac{3\pi}{32}\left(+c^1_{2,-2}-\frac{1}{4}c^3_{2,-2}-\frac{5}{128}c^5_{2,-2}-\frac{7}{512}c^7_{2,-2}\right. \\
&\quad \left.-\frac{105}{16384}c^9_{2,-2}+\ldots\right) \\
&- \mathrm{Im}(A^*_0(t)A_\perp(t))\sqrt{\frac{6}{5}}\frac{3\pi}{32}\left(+c^1_{2,1}-\frac{1}{4}c^3_{2,1}-\frac{5}{128}c^5_{2,1}-\frac{7}{512}c^7_{2,1}\right. \\
&\quad \left.-\frac{105}{16384}c^9_{2,1}+\ldots\right) \\
&+ \mathrm{Im}(A^*_\parallel(t)A_\perp(t))\sqrt{\frac{3}{5}}\left(c^0_{2,-1}-\frac{1}{5}c^2_{2,-1}\right) \\
&+ |A_S(t)|^2\frac{1}{2}\left(2c^0_{00}+\sqrt{\frac{1}{5}}c^0_{20}-\sqrt{\frac{3}{5}}c^0_{22}\right) \\
&+ \mathrm{Re}(A^*_0(t)A_S(t))\frac{1}{6}\left(4\sqrt{3}c^1_{00}+2\sqrt{\frac{3}{5}}c^1_{20}-6\sqrt{\frac{1}{5}}c^1_{22}\right) \\
&- \mathrm{Re}(A^*_\parallel(t)A_S(t))3\sqrt{\frac{2}{5}}\frac{\pi}{8}\left(c^0_{2,-2}-\frac{1}{8}c^2_{2,-2}-\frac{1}{64}c^4_{2,-2}-\frac{5\pi}{1024}c^6_{2,-2}\right. \\
&\quad \left.-\frac{35\pi}{16384}c^8_{2,-2}-\ldots\right) \\
&- \mathrm{Im}(A^*_\perp(t)A_S(t))3\sqrt{\frac{2}{5}}\frac{\pi}{8}\left(c^0_{2,1}-\frac{1}{8}c^2_{2,1}-\frac{1}{64}c^4_{2,1}-\frac{5\pi}{1024}c^6_{2,1}\right. \\
&\quad \left.-\frac{35\pi}{16384}c^8_{2,1}-\ldots\right)\Big] \quad .
\end{aligned}
$$

F

At this point, it is possible to identify the equivalence of the following combinations of Fourier coefficients of the acceptance function, and the normalization weights:

$$
\begin{aligned}
\xi_{00} &= \frac{8}{9}\sqrt{\pi}\left(c_{00}^{0}+\frac{2}{5}c_{00}^{2}+\sqrt{\frac{1}{20}}(c_{20}^{0}+\frac{2}{5}c_{20}^{2})-\sqrt{\frac{3}{20}}(c_{22}^{0}+\frac{2}{5}c_{22}^{2})\right)\\
\xi_{\|\|} &= \frac{8}{9}\sqrt{\pi}\left(c_{00}^{0}-\frac{1}{5}c_{00}^{2}+\sqrt{\frac{1}{20}}\left(c_{20}^{0}-\frac{1}{5}c_{20}^{2}\right)+\sqrt{\frac{3}{20}}\left(c_{22}^{0}-\frac{1}{5}c_{22}^{2}\right)\right)\\
\xi_{\perp\perp} &= \frac{8}{9}\sqrt{\pi}\left(c_{00}^{0}-\frac{1}{5}c_{00}^{2}-\sqrt{\frac{1}{5}}\left(c_{20}^{0}-\frac{1}{5}c_{20}^{2}\right)\right)\\
\xi_{0\|} &= \frac{8}{9}\sqrt{\pi}\sqrt{\frac{6}{5}}\frac{3\pi}{32}\left(+c_{2,-2}^{1}-\frac{1}{4}c_{2,-2}^{3}-\frac{5}{128}c_{2,-2}^{5}-\frac{7}{512}c_{2,-2}^{7}-\frac{105}{16384}c_{2,-2}^{9}+...\right)\\
\xi_{\perp 0} &= -\frac{8}{9}\sqrt{\pi}\sqrt{\frac{6}{5}}\frac{3\pi}{32}\left(+c_{2,1}^{1}-\frac{1}{4}c_{2,1}^{3}-\frac{5}{128}c_{2,1}^{5}-\frac{7}{512}c_{2,1}^{7}-\frac{105}{16384}c_{2,1}^{9}+...\right)\\
\xi_{\|\perp} &= \frac{8}{9}\sqrt{\pi}\sqrt{\frac{3}{5}}\left(c_{2,-1}^{0}-\frac{1}{5}c_{2,-1}^{2}\right)\\
\xi_{SS} &= \frac{8}{9}\sqrt{\pi}\frac{1}{2}\left(2c_{00}^{0}+\sqrt{\frac{1}{5}}c_{20}^{0}-\sqrt{\frac{3}{5}}c_{22}^{0}\right)\\
\xi_{S0} &= \frac{8}{9}\sqrt{\pi}\frac{1}{6}\left(4\sqrt{3}c_{00}^{1}+2\sqrt{\frac{3}{5}}c_{20}^{1}-6\sqrt{\frac{1}{5}}c_{22}^{1}\right)\\
\xi_{S\|} &= -\frac{8}{9}\sqrt{\pi}3\sqrt{\frac{2}{5}}\frac{\pi}{8}\left(c_{2,-2}^{0}-\frac{1}{8}c_{2,-2}^{2}-\frac{1}{64}c_{2,-2}^{4}-\frac{5\pi}{1024}c_{2,-2}^{6}-\frac{35\pi}{16384}c_{2,-2}^{8}-...\right)\\
\xi_{S\perp} &= -\frac{8}{9}\sqrt{\pi}3\sqrt{\frac{2}{5}}\frac{\pi}{8}\left(c_{2,1}^{0}-\frac{1}{8}c_{2,1}^{2}-\frac{1}{64}c_{2,1}^{4}-\frac{5\pi}{1024}c_{2,1}^{6}-\frac{35\pi}{16384}c_{2,1}^{8}-...\right)
\end{aligned}
$$

As a cross-check, if the efficiency is uniform and unity for all the angles:

$$\epsilon(\psi,\theta,\phi)=1 \Rightarrow c_{00}^{0}=2\sqrt{\pi}; c_{jk}^{i}=0(i\neq 0, j\neq 0, k\neq 0) \quad . \tag{F.3}$$

In that case the normalization weights reduce to

$$\xi_{\|\|}=\xi_{00}=\xi_{\perp\perp}=\xi_{SS}=\frac{16\pi}{9} \tag{F.4}$$

$$\xi_{\|\perp}=\xi_{\perp 0}=\xi_{0\|}=\xi_{S\|}=\xi_{S\perp}=\xi_{S0}=0 \quad , \tag{F.5}$$

as expected from the original normalization integral without efficiency

$$
\begin{aligned}
N(q_T,t) &= \int \mathrm{d}\cos\psi \int \mathrm{d}\cos\theta \int \mathrm{d}\phi |[\vec{A}(t,q_T)+\frac{1}{\sqrt{3}}\vec{S}(t,q_T)]\wedge\hat{n}|^2\\
&= \frac{16\pi}{9}\left(|A_0(t)|^2+|A_{\|}(t)|^2+|A_{\perp}(t)|^2+|A_S(t)|^2\right) \quad .
\end{aligned} \tag{F.6}
$$

In the likelihood fit for parameter estimations, only the relative normalization of the ten normalization weights matters. This means that only a subset of the Fourier components

F

angular function $f_i(\vec{\Omega})$	normalization weight	reconstructed weight from acceptance expansion	ratio
$f_1(\vec{\Omega})$	27.7686	13.8843	0.5000
$f_2(\vec{\Omega})$	29.1998	14.5999	0.5000
$f_3(\vec{\Omega})$	29.2655	14.6327	0.5000
$f_4(\vec{\Omega})$	0.1002	0.05008	0.5000
$f_5(\vec{\Omega})$	0.0025	0.0012	0.5055
$f_6(\vec{\Omega})$	0.0296	0.01467	0.4959
$f_7(\vec{\Omega})$	28.1541	14.0770	0.5000
$f_8(\vec{\Omega})$	0.0076	0.0040	0.5284
$f_9(\vec{\Omega})$	-0.0087	-0.0044	0.5027
$f_{10}(\vec{\Omega})$	-0.2212	-0.1106	0.5000

Table F.1: *Table comparing two methods of angular acceptance correction: using normalization weights and normalization weight reconstruction from coefficients in the angular acceptance expansion method. There is an overall factor between the corresponding columns, expressed by the last column with the ratio of the two. Since this ratio is constant for all 10 functions, it is shown that the ten normalization weights can properly be reconstructed from the coefficients in the expansion method.*

needs to be known to perform the fit. Of course additional terms will improve the visual results when plotting differential distributions.

F.1 Comparison

To reconstruct the ten normalization weights from the coefficients in the angular acceptance expansion, the coefficients up to and including ninth order as expressed in the previous section were considered here. The results are given in Table F.1.

Bibliography

[1] C. S. Wu, E. Ambler, R. W. Hayward, D. D. Hoppes, and R. P. Hudson, "Experimental test of parity conservation in beta decay," *Phys. Rev.*, vol. 105, pp. 1413–1415, Feb 1957.

[2] R. L. Garwin, L. M. Lederman, and M. Weinrich, "Observations of the failure of conservation of parity and charge conjugation in meson decays: the magnetic moment of the free muon," *Phys. Rev.*, vol. 105, pp. 1415–1417, Feb 1957.

[3] C. A. Baker *et al.*, "Improved experimental limit on the electric dipole moment of the neutron," *Phys. Rev. Lett.*, vol. 97, p. 131801, Sep 2006.

[4] J. H. Christenson, J. W. Cronin, V. L. Fitch, and R. Turlay, "Evidence for the 2π decay of the K_2^0 meson," *Phys. Rev. Lett.*, vol. 13, pp. 138–140, Jul 1964.

[5] N. Cabibbo, "Unitary symmetry and leptonic decays," *Phys. Rev. Lett.*, vol. 10, pp. 531–533, Jun 1963.

[6] M. Kobayashi and T. Maskawa, "CP-violation in the renormalizable theory of weak interaction," *Progress of Theoretical Physics*, vol. 49, no. 2, pp. 652–657, 1973.

[7] J. J. Aubert *et al.*, "Experimental observation of a heavy particle J," *Phys. Rev. Lett.*, vol. 33, pp. 1404–1406, Dec 1974.

[8] J. E. Augustin *et al.*, "Discovery of a narrow resonance in e^+e^- annihilation," *Phys. Rev. Lett.*, vol. 33, pp. 1406–1408, Dec 1974.

[9] S. W. Herb *et al.*, "Observation of a dimuon resonance at 9.5 GeV in 400-GeV proton-nucleus collisions," *Phys. Rev. Lett.*, vol. 39, pp. 252–255, Aug 1977.

[10] F. Abe *et al.*, "Observation of top quark production in $\overline{p}p$ collisions with the Collider Detector at Fermilab," *Phys. Rev. Lett.*, vol. 74, pp. 2626–2631, Apr 1995.

[11] S. Abachi *et al.*, "Search for high mass top quark production in $p\overline{p}$ collisions at $\sqrt{s} =$ 1.8 TeV," *Phys. Rev. Lett.*, vol. 74, pp. 2422–2426, Mar 1995.

[12] B. Aubert *et al.*, "Observation of CP violation in the B^0 meson system," *Phys. Rev. Lett.*, vol. 87, p. 091801, Aug 2001.

[13] K. Abe *et al.*, "Observation of large CP violation in the neutral B meson system," *Phys. Rev. Lett.*, vol. 87, p. 091802, Aug 2001.

[14] V. M. Abazov *et al.*, "Evidence for an anomalous like-sign dimuon charge asymmetry," *Phys. Rev. Lett.*, vol. 105, p. 081801, Aug 2010.

[15] R. Aaij *et al.*, "Evidence for CP violation in time-integrated $D^0 \to h^- h^+$ decay rates," *Phys. Rev. Lett.*, vol. 108, p. 111602, Mar 2012.

[16] A. J. Buras, M. E. Lautenbacher, and G. Ostermaier, "Waiting for the top quark mass, $K^+ \to \pi^+ \nu\overline{\nu}$, $B_s^0 - \overline{B}_s^0$ mixing, and CP asymmetries in B decays," *Phys. Rev. D*, vol. 50, pp. 3433–3446, Sep 1994.

[17] J. Charles *et al.*, "CP violation and the CKM matrix: assessing the impact of the asymmetric B factories," *European Physical Journal C*, vol. 41, pp. 1–131, May 2005. Updated results and plots available at: http://ckmfitter.in2p3.fr.

[18] I. I. Bigi and A. I. Sanda, *CP Violation*. Cambridge monographs on particle physics, nuclear physics, and cosmology, Cambridge Univ. Press, 1999.

[19] I. Dunietz, R. Fleischer, and U. Nierste, "In pursuit of new physics with B_s decays," *Phys. Rev. D*, vol. 63, p. 114015, Dec 2000.

[20] V. Weisskopf and E. P. Wigner, "Calculation of the natural brightness of spectral lines on the basis of Dirac's theory," *Z. Phys.*, vol. 63, pp. 54–73, 1930.

[21] R. Aaij *et al.*, "Determination of the sign of the decay width difference in the B_s^0 system," *Phys. Rev. Lett.*, vol. 108, p. 241801, Jun 2012.

[22] U. Nierste, "Three lectures on meson mixing and CKM phenomenology." arXiv:0904.1869, 2009.

[23] J. Beringer *et al.* (Particle Data Group), "The review of particle physics," *Phys. Rev. D*, vol. 86, no. 1, 2012.

[24] G. C. Branco, L. Lavoura, and J. P. Silva, *CP Violation*. Internat. Ser. Mono. Phys., Oxford: Clarendon Press, 1999.

[25] Y. Amhis *et al.*, "Averages of b-hadron, c-hadron, and tau-lepton properties as of early 2012." arXiv:1207.1158, Jul 2012.

[26] A. A. Alves *et al.*, "The LHCb Detector at the LHC," *JINST*, vol. 3, p. S08005, 2008.

[27] R. Aaij *et al.*, "Measurement of J/ψ production in pp collisions at $\sqrt{s} = 7\,\mathrm{TeV}$," *Eur. Phys. J.*, vol. C71, p. 1645, 2011.

[28] R. W. Forty and O. Schneider, "RICH pattern recognition," Tech. Rep. LHCb-98-040, CERN, Geneva, Apr 1998.

R

[29] The LHCb Collaboration, "LHCb reoptimized detector design and performance," Tech. Rep. LHCb-TDR-9, CERN, 2003.

[30] S. Bachmann *et al.*, "Ageing in the LHCb Outer Tracker: Phenomenon, culprit and effect of oxygen," *Nuclear Instruments and Methods in Physics Research Section A*, vol. 617, no. 1-3, pp. 202 – 205, 2010.

[31] F. Sauli, *Principles of operation of multiwire proportional and drift chambers*. CERN-1977-9, 1977. p.9.

[32] L. B. A. Hommels, *The Tracker in the Trigger of LHCb.* PhD thesis, Universiteit van Amsterdam, Amsterdam, 2006.

[33] H. Deppe, U. Stange, U. Trunk, and U. Uwer, "The OTIS reference manual," Tech. Rep. CERN-LHCb-2008-010, CERN, Geneva, Feb 2008.

[34] F. Jansen, *Unfolding single-particle efficiencies and the Outer Tracker in LHCb*. PhD thesis, Vrije Universiteit, Amsterdam, 2011.

[35] Y. Gouz. Private communication, see also internal note LHCb-2004-120.

[36] M. Deissenroth. Private communication, see also presentation during LHCb week in November 2005: *Multi-Hit Studies at 5m Modules with the ASDBLR Readout*.

[37] V. Suvorov, G. W. van Apeldoorn, I. Gouz, and T. Sluijk, "Avalanche and streamer production in Ar/CO_2 mixtures," Tech. Rep. LHCb-2005-038, CERN, Geneva, Jul 2005.

[38] A. Bien. Private communication, see also presentation during LHCb week in November 2011: *Simulation of OT Double Pulse*.

[39] A. Kozlinskiy. Private communication, thesis in preparation.

[40] R. M. Van der Eijk, *Track reconstruction in the LHCb experiment*. PhD thesis, Universiteit van Amsterdam, Amsterdam, 2002.

[41] H. Tanja, *Alterungsstudien und Studium der Betriebseigenschaften des Outer Trackers des LHCb Detektors*. PhD thesis, Universität Heidelberg, 2007. Section 9.2 (in German).

[42] I. Mous, "Aging in the LHCb Outer Tracker," Master's thesis, Vrije Universiteit, Amsterdam, 2007.

[43] G. Krämer, T. Mannel, and W. F. Palmer, "Angular correlations in the decays $B \to VV$ using heavy quark symmetry," *Z. Phys. C*, vol. 55, pp. 497–502, Mar 1992.

[44] G. Valencia, "Angular correlations in the decay $B \to VV$ and CP violation," *Phys. Rev. D*, vol. 39, pp. 3339–3345, Dec 1988.

[45] A. S. Dighe, I. Dunietz, and R. Fleischer, "Extracting CKM phases and $B_s - \overline{B}_s$ mixing parameters from angular distributions of non-leptonic B decays," *Eur. Phys. J. C*, vol. 6, pp. 647–662, Apr 1998.

[46] A. S. Dighe, I. Dunietz, H. J. Lipkin, and J. L. Rosner, "Angular distributions and lifetime differences in $B_s \to J/\psi\phi$ decays." arXiv:hep-ph/9511363, Nov 1995.

[47] R. Knegjens. Private communication.

[48] R. Aaij *et al.*, "Measurement of the CP violating phase ϕ_s in $\overline{B}^0_s \to J/\psi f_0(980)$," *Phys. Lett. B.*, vol. 707, pp. 497–505, 2012.

[49] R. Fleischer, R. Knegjens, and G. Ricciardi, "Anatomy of $B^0_{s,d} \to J/\psi f_0(980)$," *Eur.Phys.J.*, vol. C71, p. 1832, 2011.

[50] A. Lenz, "Theoretical status of B_s-mixing and lifetimes of heavy hadrons," *Nucl. Phys. B, Proc. Suppl.*, vol. 177-178, pp. 81–86, May 2007.

[51] A. Lenz and U. Nierste, "Numerical updates of lifetimes and mixing parameters of B mesons." arXiv:1102.4274, 2011.

[52] A. Lenz and U. Nierste, "Theoretical update of $B_s - \overline{B}_s$ mixing," *J. High Energy Phys.*, vol. 06, p. 72, Dec 2006.

[53] S. Faller, R. Fleischer, and T. Mannel, "Precision physics with $B^0_s \to J/\psi\phi$ at the LHC: The quest for new physics," *Phys. Rev. D*, vol. 79, p. 014005, Jan 2009.

[54] R. Fleischer and T. Mannel, "General analysis of new physics in $B \to J/\psi K$," *Phys. Lett. B*, vol. 506, pp. 311–322, Jan 2001.

[55] F. Abe *et al.*, "Observation of the decay $B^0_s \to J/\psi\phi$ in $\bar{p}p$ collisions at $\sqrt{s} = 1.8$ TeV," *Phys.Rev.Lett.*, vol. 71, pp. 1685–1689, 1993.

[56] F. Abe *et al.*, "Ratios of bottom meson branching fractions involving J/ψ mesons and determination of b quark fragmentation fractions," *Phys. Rev. D*, vol. 54, pp. 6596–6609, Dec 1996.

[57] R. Louvot, "Υ(5S) Results at Belle." arXiv:0905.4345v2, 2009.

[58] T. Aaltonen *et al.*, "Measurement of the CP-violating phase $\beta_s^{J/\psi\phi}$ in $B^0_s \to J/\psi\phi$ decays with the CDF II detector," *Phys. Rev. D*, vol. 85, p. 072002, Apr 2012.

[59] V. M. Abazov and other, "Measurement of the CP-violating phase $\phi_s^{J/\psi\,\phi}$ using the flavor-tagged decay $B^0_s \to J/\psi\,\phi$ in $8\ \mathrm{fb}^{-1}$ of $p\overline{p}$ collisions," *Phys. Rev. D*, vol. 85, p. 032006, Feb 2012.

[60] R. Aaij *et al.*, "Measurement of the CP-Violating Phase ϕ_s in the Decay $B^0_s \to J/\psi\phi$," *Phys. Rev. Lett.*, vol. 108, p. 101803, Mar 2012.

[61] R. Aaij and J. Albrecht, "Muon triggers in the high level trigger of LHCb." LHCb-PUB-2011-017, Sep 2011.

[62] W. D. Hulsbergen, "Decay chain fitting with a kalman filter," *Nucl. Instrum. Methods Phys. Res., A*, vol. 552, pp. 566–575, Mar 2005.

R

[63] B. Aubert *et al.*, "Measurement of the $B \to J/\psi\, K^*(892)$ decay amplitudes," *Phys. Rev. Lett.*, vol. 87, p. 241801, Nov 2001.

[64] T. du Pree, *Search for a Strange Phase in Beautiful Oscillations*. PhD thesis, Vrije Universiteit, Amsterdam, 2010.

[65] R. Aaij. Private communication.

[66] R. Aaij *et al.*, "Opposite-side flavour tagging of B mesons at the LHCb experiment," *Eur. Phys. J. C*, vol. 72, p. 2022, Feb 2012.

[67] W. Verkerke and D. Kirkby, "The RooFit toolkit for data modeling." arXiv:physics/0306116v1, 2003.

[68] M. Pivk and F. R. Le Diberder, "sPlot: a statistical tool to unfold data distributions," *Nucl. Instrum. Meth.*, vol. A555, pp. 356–369, 2005.

[69] Private communication, LHCb internal note LHCb-ANA-2012-004-v2, "Tagged time-dependent angular analysis of $B_s^0 \to J/\psi\, \varphi$ decays with 1.03 fb^{-1}."

[70] R. Aaij *et al.*, "Measurement of the $B_s^0 - \overline{B}_s^0$ oscillation frequency Δm_s in $B_s^0 \to D_s^-(3)\pi$ decays," *Physics Letters B*, vol. 709, no. 3, pp. 177 – 184, 2012.

[71] G. Cowan, *Statistical Data Analysis*. Oxford Science Publications, Oxford University Press, 1998.

[72] T. Aaltonen *et al.*, "Measurement of the B_s^0 Mixing Phase using $B_s^0 \to J/\psi\, \varphi$ Decays from the Full Run II Dataset." CDF note 10778, March 2012.

[73] R. Aaij *et al.*, "Measurement of the CP-violating phase ϕ_s in $\overline{B}_s^0 \to J/\psi\pi^+\pi^-$ decays." arXiv:1204.5675, April 2012.

[74] M. Capéans-Garrido *et al.*, "Recent aging studies for the ATLAS transition radiation tracker," *IEEE Trans. Nucl. Sci.*, vol. 51, pp. 960–967, 2004.

[75] D. Allspach *et al.*, "Aging in the large CDF axial drift chamber," *IEEE Trans. Nucl. Sci.*, vol. 52, pp. 2956–2962, 2005.

[76] M. R. Blom, "Ageing of the LHCb Outer Tracker," Master's thesis, Vrije Universiteit, Amsterdam, 2009.

[77] C. Färber. Private communication, see also presentation during LHCb week in September 2008: *New Results from Ageing Studies*.

[78] The ATLAS Collaboration, "Observation of a new particle in the search for the Standard Model Higgs boson with the ATLAS detector at the LHC." arXiv:1207.7214, CERN-PH-EP-2012-218, submitted to *Phys. Lett. B.*, Aug 2012.

[79] The CMS Collaboration, "Observation of a new boson at a mass of 125 GeV with the CMS experiment at the LHC." arXiv:1207.7235, CMS-HIG-12-028, CERN-PH-EP-2012-220, submitted to *Phys. Lett. B.*, Jul 2012.

[80] K. G. Begeman, A. H. Broeils, and R. H. Sanders, "Extended rotation curves of spiral galaxies - Dark haloes and modified dynamics," *Monthly Notices of the Royal Astronomical Society*, vol. 249, pp. 523–537, Apr. 1991.

Summary

This thesis marks the finalization of my PhD research. During the four years of my research, people frequently asked me about my work. I was surprised to notice that especially people from outside the work field of particle physics are very much interested in the work we do as particle physicists. I think their interest originates from questions that everyone asks themselves from time to time, such as 'what is matter made of?' and 'how did the universe begin and how will it end?'. These questions are essentially the motivation for our work. My hope is, that all the people that I have talked to in the last four years can enjoy reading at least parts of my thesis. Therefore, I will first start with a general introduction to particle physics, to explain the research I performed. After this, I will summarize the results of my analyses, guided by the title of my thesis. I will start with time-dependent CP violation using $B_s^0 \to J/\psi\,\phi$ (to be pronounced as *b sub s to jay psi fi*) events and conclude with the radiation hardness of the LHCb Outer Tracker.

Particle Physics and the LHC

The LHC is a particle accelerator that accelerates and collides protons in a circular underground tunnel. It stretches over 27 kilometers and is situated 100 meters below the surface. The protons collide millions of times per second in four distinct points along the LHC ring. Large particle detectors are installed surrounding the collision points to record the collisions or events. In this case, 'to record' means that the information about the passage of particles through the different subdetectors of the experiments is stored on computers. In the early days of particle physics, 'to record' would have meant to take a photograph of the event, as can be seen in Fig. S.1.

I performed my PhD research for the LHCb experiment, one of the four major experiments on the LHC accelerator ring. LHCb is a dedicated B physics experiment, as indicated by the additive 'b'. In B physics experiments, properties of B mesons are studied. To understand what these B mesons and their properties are, it is instructive to first have a look at the so-called Standard Model of elementary particles.

The Standard Model

The Standard Model (SM) describes our current knowledge of elementary particles and their interactions. It can be represented by a mathematical formula, but for the sake of simplicity it can be thought of as the set of all building blocks of nature, as shown in Fig. S.2.

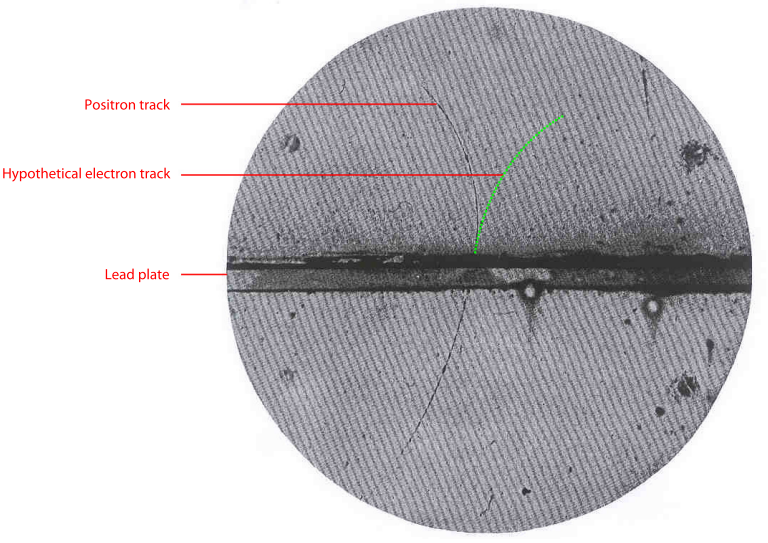

Figure S.1: *Photograph showing the discovery of an anti-electron, a so-called positron, recorded in 1932 by Carl D. Anderson. The identity of the positron is inferred from its direction of curvature, since it is opposite to the direction that is expected for an electron, indicated here by the dashed green line. The lead plate is used to slow down the incoming particle to deduce its direction of motion (upward or downward in the figure) from the difference in the radius of curvature on both sides of the plate.*

The SM is a theory that accurately predicts the many measurements that have been performed during the last decades. However, there are several known problems associated with it. One of these problems is well-known and was one of the reasons the LHC was built in the first place: to prove the existence of the Higgs boson.

Although I did not work on the Higgs search itself, the work that I performed on CP asymmetries is linked to Higgs particles. This is because the so-called Yukawa terms in the SM that express the couplings between the Higgs field and fermions to generate mass, are exactly the terms from which CP asymmetries arise, as explained in Chap. 1. I will now briefly elaborate on the Higgs search, since this puzzle might have been solved very recently.

The Higgs Boson

The Higgs particle was predicted in 1964 by, among others, Peter Higgs and is a necessary ingredient of the SM, since its presence generates mass for all other fundamental particles. It is being searched for in the ATLAS and CMS detectors, which are two other experiments on the LHC ring. July 4 2012 the ATLAS and CMS collaborations announced the discovery of a new boson whose properties are in agreement with the SM Higgs boson. This extraordinary finding was presented in a press conference held at CERN and was broadcasted worldwide

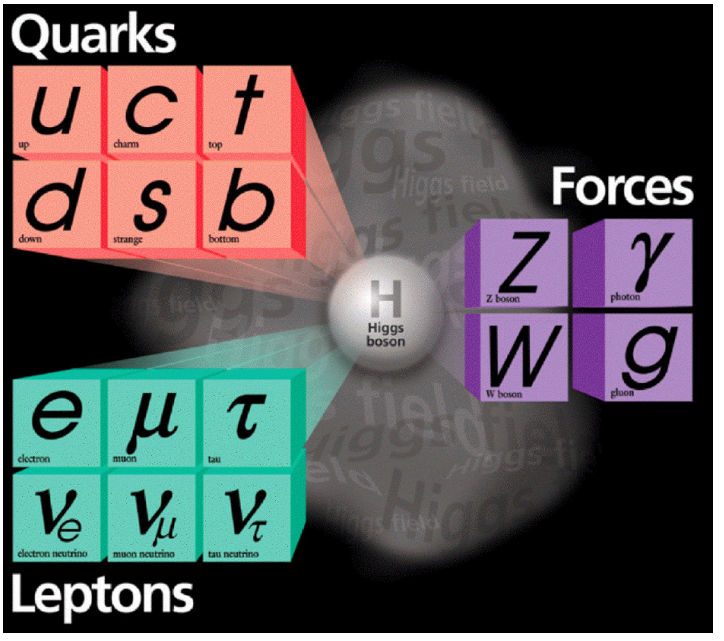

Figure S.2: *Schematic representation of the Standard Model, showing all the fundamental particles currently known. The Higgs boson (or, officially, a boson consistent with the SM Higgs boson) has been discovered on July 4, 2012.*

in the presence of Peter Higgs himself. The goal was not only observing the Higgs boson, but also to determine its mass. The ATLAS collaboration discovered a new boson with a mass of $126.0 \pm 0.6\,\mathrm{GeV}/c^2$ [78], whereas the CMS collaboration independently observed a new boson with a mass of $125.3 \pm 0.6\,\mathrm{GeV}/c^2$ [79]. In the coming years, at the LHC the properties of this new fundamental particle will be studied in order to test the SM. Whatever the results of those studies, the discovery of this new boson marks the end of a longstanding open question in the SM and in particle physics in general.

Fundamental Forces in the SM

The SM describes all elementary particles and their interactions. An interaction of a particle with one of the so-called force-carrier particles (Z, W, g and γ in Fig. S.2) is the manifestation of nature's fundamental forces. There are four fundamental forces in nature. Two of them can actually be observed in daily life. These are gravitation and the electromagnetic force (for example electricity). The two other fundamental forces of nature are the so-called weak force and the strong force. These two forces are less well-known, because their influence is only noticeable on very small (nuclear) scales. The weak force is involved in many radioactive decays, while the strong force acts as the proverbial glue that keeps quarks together to form protons or other bound quark states; so-called hadronic particles. The SM incorporates the strong, the weak and the electromagnetic forces. It does so through gluon particles (g), the

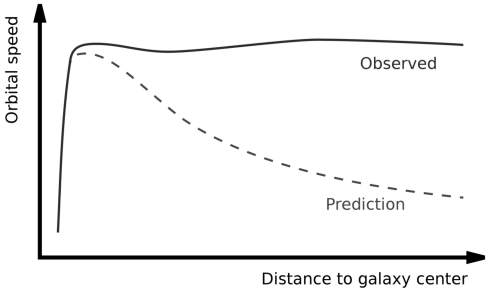

Figure S.3: *Stellar orbital speed as a function of distance to a galaxy center. Newtonian gravity predicts that the orbital speed decreases as a function of distance to the center, but observations prove otherwise. An explanation for this problem is dark matter, an unknown substance that does however feel gravity.*

Z and W particles and photons (γ particles) respectively. However, until now, physicists have been unable to incorporate gravity into the SM.

The Contents of our Universe

I have described two problems with the SM, namely the search for the Higgs boson and the incorporation of gravity. Another striking problem in particle physics deals with the content of our universe itself and arises from cosmological observations. When studying the orbital speed of stars at the outskirts of spiral galaxies, Newtonian gravitation predicts that the orbital speed decreases inversely with the square root of the radius of the orbit. However, observations [80] show that the orbital speed remains almost constant as a function of distance to the galaxy center, as indicated qualitatively in Fig. S.3. The best explanation so far is that there is some sort of invisible matter (here, 'matter' is a substance that is subject to gravity) in addition to visible matter, like that in stars. The ratio of known visible matter to this unknown so-called dark matter can be derived from the orbital-speed observations and amounts to a stunning one to five. Within the SM, there are no particles that can explain dark matter. Thus, the SM can account for only 20% of all the matter in the universe.

New Physics

To solve part of the problems associated with the SM mentioned above, theoretical physicists are trying to devise new mathematical models that incorporate and extend the SM. Such New Physics (NP) models make predictions for new types of particles, like dark matter candidates and new types of interactions. The experiments at the LHC are a unique environment for scientists to search for these new particles and interactions. These searches can be performed both in a direct way and in an indirect way. The former approach is used by the ATLAS and CMS detectors, by searching for the hypothetical particles in the decay products from the proton-proton collisions. In LHCb, however, the search for NP is performed indirectly, as

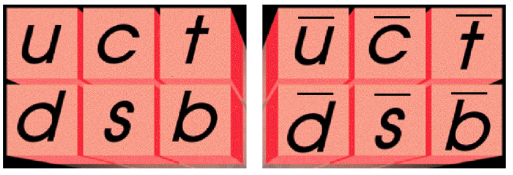

Figure S.4: *In 1928, Paul Dirac predicted that every fundamental particle has its own antiparticle associated with it. This is illustrated here for the six different types of quarks. For example, the up quark u, indicated on the left, has the anti-up quark as its associated antiparticle, indicated on the right by $\overline{u}$.*

LHCb measures parameters that are affected if new particles contribute to certain processes. When a significant deviation from the SM prediction is found, this could be an indication of New Physics. The measurement of such a parameter is the subject of my thesis and is denoted symbolically as ϕ_s. To explain what this parameter represents, another ingredient is needed: antimatter.

Antimatter

The schematic picture of the SM depicted in Fig. S.2 is actually incomplete. In 1928 the physicist Paul Dirac predicted the existence of so-called antimatter on mathematical grounds. This implied that every particle in the SM should have an antiparticle partner, as indicated for the quarks in Fig. S.4. Dirac was proven right in 1932, when the positron was discovered. A positron is the antiparticle of the well-known negatively charged electron, which means that it carries a positive charge. The photograph in Fig. S.1 shows one of the first positrons ever observed. Its identity was deduced from the direction of curvature in a magnetic field, since this was opposite to the direction that was expected for an electron, as indicated in the picture. When matter and antimatter particles meet, they 'destroy' or annihilate each other, producing photons. In the next paragraph I will explain B mesons and anti-B mesons, what CP violation means and how this relates to the parameter ϕ_s.

B mesons, CP Violation and ϕ_s

Mesons are quasi-stable particles that consist of two quarks. B mesons are mesons that contain one b or $\overline{b}$ (this denotes an anti-b) quark. These b quarks are sometimes called beauty quarks and, correspondingly, B mesons are occasionally referred to as beauty mesons. Here, since I have studied the decay of a beauty meson, we have arrived at the title of my thesis: The Decay of Beauty. The quark content of a B_s^0 meson is $(\overline{b}s)$, while the decay products in $B_s^0 \to J/\psi\,\phi$ decays are the J/ψ meson $(c\overline{c})$ and the ϕ meson $(s\overline{s})$, as indicated in Fig. S.5.

The final ingredient that is needed to explain the parameter ϕ_s is a property of B mesons called mixing. Mixing means that B mesons can oscillate back and forth to their own antiparticle. This happens at an incredibly high frequency, roughly 18 trillion times per second. When two protons collide in LHCb, B_s^0 mesons and their antiparticles, $\overline{B}_s^0$ mesons, are produced in equal amounts. Due to mixing, the decay to the state $J/\psi\,\phi$ can take

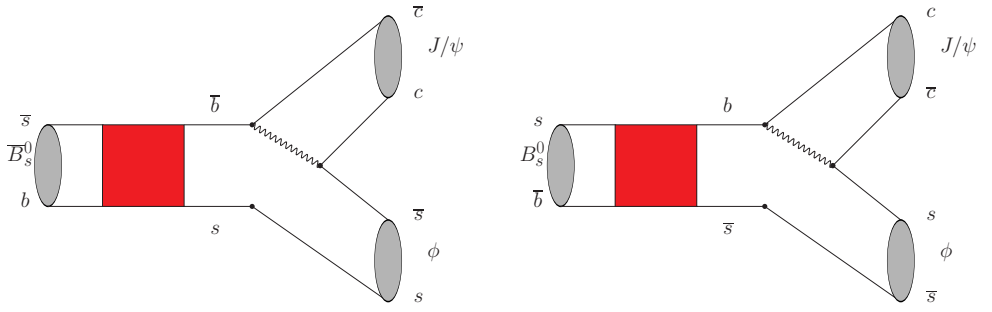

Figure S.5: *Left: schematic representation of a $\overline{B}^0_s$ meson oscillating to a B^0_s meson (a process indicated by the red box) before decaying into the final state $J/\psi\,\phi$. Right: schematic representation of a B^0_s meson oscillating to a $\overline{B}^0_s$ meson (again indicated by the red box) before decaying into the final state $J/\psi\,\phi$. Depending on the decay time of the B meson that was produced in the proton-proton collision, there is a possible difference in the decay rate of these two processes, which would be an indication of CP violation. The amount of CP violation is measured by ϕ_s and can be enhanced with respect to the SM prediction by NP processes in the red boxes.*

place at a moment when the parent particle was a B^0_s particle, a $\overline{B}^0_s$ particle or even a quantum-mechanical superposition of the two.

Depending on the decay time of the B meson, there could be a difference in decay rate between decays where the originally produced particle was a B^0_s meson and where the produced particle was a $\overline{B}^0_s$ meson. This effect is called time-dependent CP violation[1], represented graphically in Fig. S.5. The parameter ϕ_s is a measure of the amount of time-dependent CP violation in $B^0_s \to J/\psi\,\phi$ decays. In the SM, ϕ_s is predicted to be very small, whereas NP models can enhance its value. Therefore, any significant deviation in ϕ_s from the SM prediction could be an indication of a New Physics discovery. In the next section, I will present the results of my ϕ_s measurement.

The Decay of Beauty: Time-Dependent CP Violation using $B^0_s \to J/\psi\,\phi$ Decays

In the SM, ϕ_s is predicted to be $\phi_s = -0.036 \pm 0.002$ [17]. Any significant deviation from this prediction is an indication of New Physics. The value I measured is $\phi_s = 0.00 \pm 0.10\,(\text{stat.}) \pm 0.02\,(\text{syst.})$, which is in perfect agreement with the value as predicted by the SM. The result of my analysis can be presented and compared to earlier experiments by drawing contours in the $\phi_s - \Delta\Gamma_s$ plane as shown in Fig. S.6, where $\Delta\Gamma_s$ is the lifetime difference between two types of B^0_s mesons. The smaller these contours, the more precise the measurement, therefore the measurement presented here is currently the most precise.

[1] The 'C' and 'P' in CP violation stand for charge and parity respectively. For more information, see Chap. 1.

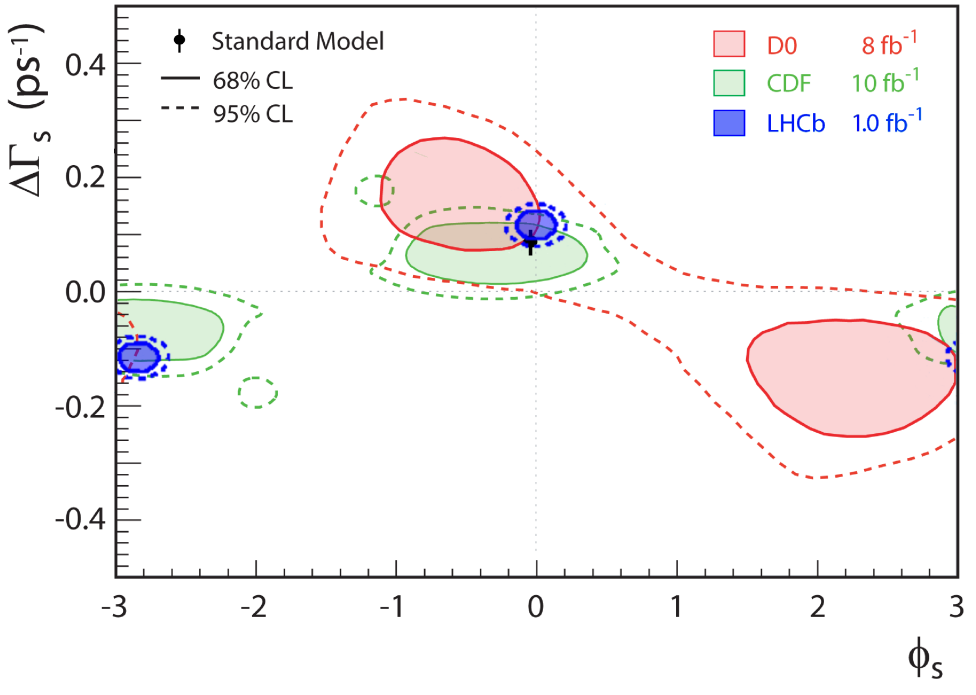

Figure S.6: *Two-dimensional confidence contours in the $\phi_s - \Delta\Gamma_s$ plane for the D0 collaboration [59] (red), the CDF collaboration [72] (green) and the values found in this analysis (blue). The black square indicates the SM point ($\phi_s = -0.036 \pm 0.002$, $\Delta\Gamma_s = 0.087 \pm 0.021\,\mathrm{ps}^{-1}$).*

Although the measured value for ϕ_s is in agreement with the SM, it is important to continue this analysis by adding more data and different decay channels that are sensitive to this parameter. This will reduce the uncertainty on the measurements and allow the observation of possible deviations from the SM. In the next section, I will summarize the second part of my thesis, which is related to the radiation hardness of the LHCb Outer Tracker.

Ageing: Radiation Hardness of the LHCb Outer Tracker

The Outer Tracker (OT) is one of the subdetectors of the LHCb experiment. It is used to reconstruct the trajectories of charged particles through the detector originating from proton-proton collisions. To detect a traversing particle, the OT uses straw tubes filled with an ionization gas that act as cathodes with a central anode wire. It consists of three detection stations and each station comprises 4 detection layers. The OT has a modular design, meaning that it consists of 432 modules of 128 straw tubes, leading to a total of roughly 55 000 straw tubes in the entire OT. The modules are constructed by glueing the

straws to the module panels.

After construction and prior to installation of the modules in the LHCb experiment, laboratory tests [30] proved that outgassing of the glue that was used in the module construction reduced the performance of the detector modules. In the context of particle detector technology, effects that gradually reduce detector performance, such as outgassing, are collectively called ageing effects.

The modules that were installed in the LHCb cavern were subjected to several treatments to reduce or prevent ageing effects [41, 30, 42]. My thesis summarizes the results of tests that monitor the behavior of the OT modules after installation in the LHCb cavern. The effects of the beneficial treatments were tested by deliberately irradiating and scanning modules using a dedicated scanning setup which is installed in front of the modules. Before adding an oxygen component to the counting gas, several modules showed severe radiation damage after relatively small received dose, although large module-to-module variations were observed. After adding O_2 to the OT gas mixture, few to no radiation damage was observed.

To monitor the behavior of the OT modules after the startup of the LHC in 2009, two methods were devised. The first method uses the same scanning setup as described above to regularly perform reference scans of a subset of the modules. These scans are performed manually in the LHCb pit and can therefore only be performed during technical shutdowns of the LHC. The second method uses charged particle tracks produced by LHC collisions to study hit efficiency as a function of the amplifier threshold of the OT electronics. These so-called threshold scans are performed while the LHC is operational and producing collisions with tracks in the LHCb detector.

Both methods to monitor the performance of the OT modules were applied in my research. In this thesis, I conclude that neither method has shown any significant gain loss in the OT so far. Both types of tests are and will continue to be performed regularly to monitor the radiation hardness of the OT.

Nederlandse Samenvatting

Veroudering en het Verval van Schoonheid
Stralingshardheid van de LHCb Outer Tracker en Tijdsafhankelijke CP-Schending in Vervallen van het Type $B_s^0 \to J/\psi\,\phi$

Dit proefschrift markeert het einde van mijn promotie. Gedurende de vier jaar van mijn onderzoek hebben veel mensen me gevraagd naar mijn werk als deeltjesfysicus. Tot mijn verbazing waren dat vooral mensen van buiten het vakgebied. Ik denk dat hun interesse voortkomt uit vragen die iedereen zichzelf wel eens stelt, zoals 'waar bestaat materie uit?' en 'hoe is ons universum ontstaan en hoe zal het eindigen?'. Dit soort vragen vormen de motivatie voor fundamenteel natuurkundig onderzoek. Mijn hoop is dat al die mensen met wie ik de afgelopen vier jaar heb gesproken in ieder geval delen van dit proefschrift kunnen lezen en begrijpen. Daarom zal ik nu eerst beginnen met een algemene introductie over deeltjesfysica, om uiteindelijk mijn eigen onderzoek te kunnen uitleggen. Daarna zal ik de resultaten van mijn onderzoek samenvatten, waarbij ik de titel van mijn proefschrift als leidraad neem: ik begin met tijdsafhankelijke CP-schending in vervallen van het type $B_s^0 \to J/\psi\,\phi$ (uitspraak: *bee es naar jee psie fie*) en eindig met de stralingshardheid van de LHCb Outer Tracker.

Deeltjesfysica en de LHC

De LHC is een deeltjesversneller die protonen versnelt en laat botsen in een cirkelvormige tunnelbuis van 27 kilometer lang en die zich 100 meter onder de grond bevindt. De protonen botsen miljoenen keren per seconde op vier verschillende locaties langs de omtrek van de versneller. Op die locaties zijn grote deeltjesdetectoren gebouwd rondom het botsingspunt om de botsingen of zogenoemde *events* te detecteren. Informatie over de passage van deeltjes door de verschillende subdetectoren van zo'n experiment wordt opgeslagen op computers, zodat de botsingen later met speciale software gereconstrueerd en geanalyseerd kunnen worden. In de begindagen van de deeltjesfysica daarentegen werd de informatie over dit soort botsingen opgeslagen door simpelweg een foto te nemen, zoals te zien is in Figuur S.1 in de Engelstalige samenvatting (bijschriften derhalve in het Engels).

Ik heb mijn onderzoek uitgevoerd bij het LHCb-experiment, één van de vier grote experimenten van de LHC. LHCb is een experiment dat zich richt op B-fysica, vandaar de toevoeging 'b'. Bij dit soort experimenten worden de eigenschappen van zogeheten B-mesonen bestudeerd. Om te begrijpen wat dit voor deeltjes zijn en wat voor eigenschappen

ze hebben is het belangrijk om eerst te kijken naar het zogenoemde Standaardmodel van de deeltjesfysica.

Het Standaardmodel

Het Standaardmodel beschrijft onze huidige kennis van de elementaire deeltjes en hun onderlinge interacties. Er zijn meerdere manieren om over dit model na te denken. In principe is het een wiskundige formule, maar je zou het ook kunnen beschouwen als de verzameling van alle fundamentele bouwstenen van de natuur, zoals te zien is in Figuur S.2.

Het Standaardmodel is een theorie die zeer nauwkeurige en juiste voorspellingen doet voor vele metingen die de afgelopen decennia zijn uitgevoerd. Maar er zijn ook verscheidene problemen met dit model. Eén van deze problemen is eigenlijk de 'raison d'être' voor de LHC en is vrij goed bekend bij het algemene publiek: het vinden van het Higgsdeeltje. Ondanks dat ik tijdens mijn promotie zelf niet heb meegewerkt aan deze zoektocht, is het werk dat ik heb gedaan aan CP-assymetrieën gerelateerd aan het Higgsdeeltje. Dit komt doordat de zogenoemde Yukawa-termen in het Standaardmodel, die de koppelingen tussen het Higgsveld en de fermionen beschrijven om massa te genereren, juist die termen zijn die CP-assymetrieën kunnen genereren, zoals wordt uitgelegd in Hoofdstuk 1. Ik besteed hier enige aandacht aan de zoektocht naar de Higgs, omdat deze puzzel zeer recent lijkt te zijn opgelost.

Het Higgsdeeltje

Het Higgsdeeltje werd voorspeld in 1964 door onder andere Peter Higgs en is een noodzakelijk onderdeel van het Standaardmodel, omdat het massa genereert voor alle andere fundamentele deeltjes. Er wordt naar gezocht in de ATLAS- en de CMS-detector, twee andere van de vier grote experimenten bij de LHC. Zeer recent, op 4 juli 2012, hebben deze twee onderzoekscollaboraties de ontdekking aangekondigd van een nieuw boson dat in overeenstemming lijkt te zijn met een Higgsboson zoals wordt verwacht in het Standaardmodel. Deze bijzondere vondst werd bekend gemaakt in een wereldwijd uitgezonden persconferentie die werd gehouden op CERN in het bijzijn van Peter Higgs zelf. Het doel van de metingen was niet alleen om het Higgsdeeltje te vinden, maar ook om de massa ervan te bepalen. De ATLAS-collaboratie heeft een massa gemeten van $126.0 \pm 0.6\,\text{GeV}/c^2$ [78], en de CMS-collaboratie heeft in een onafhankelijke meting een massa van $125.3 \pm 0.6\,\text{GeV}/c^2$ gevonden [79]. In de komende jaren zullen de eigenschappen van dit nieuwe fundamentele deeltje bestudeert worden om het Standaardmodel verder te testen. Wat de resultaten van deze studies ook zullen zijn, met de ontdekking van dit nieuwe boson lijkt een einde gekomen te zijn aan een langlopende zoektocht binnen het Standaardmodel en in de deeltjesfysica in het algemeen.

Fundamentele Krachten in het Standaardmodel

Zoals gezegd beschrijft het Standaardmodel alle elementaire deeltjes en hun interacties. In de natuur komen vier fundamentele krachten voor. Zo'n fundamentele kracht laat zich gelden door de interactie van een deeltje met één van de zogeheten krachtdragers (Z, W, g en γ in Figuur S.2). Van deze vier fundamentele krachten zijn er twee die in het alledaagse leven

voelbaar zijn: de zwaartekracht en de elektromagnetische kracht (bijvoorbeeld elektriciteit). De twee overgebleven natuurkrachten zijn de zogeheten zwakke kernkracht en de sterke kernkracht. Deze twee zijn niet direct voelbaar voor ons, omdat deze krachten zich alleen op zeer kleine (subatomaire) schaal doen gelden. De zwakke kernkracht is betrokken bij veel radioactieve vervallen en de sterke kernkracht werkt als de spreekwoordelijke lijm die quarks bij elkaar houdt om protonen of andere gebondenquarktoestanden, zogenaamde hadronen, te vormen. Het Standaardmodel verenigt de sterke en zwakke kernkracht en de elektromagnetische kracht, respectievelijk door middel van gluondeeltjes (g), Z- en W-deeltjes en fotonen (γ-deeltjes). Het is tot nu toe echter onmogelijk gebleken om ook de zwaartekracht in te lijven in het Standaardmodel.

De Inhoud van ons Universum

Naast de al beschreven problemen is er nog een andere opvallende puzzel in de deeltjesfysica, die volgt uit kosmologische observaties en te maken heeft met de inhoud van ons universum. Bij het bestuderen van baansnelheden van sterren in de buitenste regionen van melkwegstelsels, verwacht men op grond van de wetten van Newton dat deze omgekeerd evenredig afneemt met de wortel van de afstand tot het centrum van het melkwegstelsel. Observaties laten echter zien [80] dat deze snelheid nagenoeg constant blijft als een functie van de afstand tot het centrum, zoals geschetst in Figuur S.3. De beste verklaring tot nu toe is dat er naast de normale, zichtbare materie zoals in sterren (met materie wordt een substantie bedoeld die onderhevig is aan de zwaartekracht) een bepaalde vorm van onzichtbare materie bestaat. Uit de eerdergenoemde observaties van baansnelheden kan worden afgeleid dat de fractie van bekende zichtbare materie ten opzichte van onbekende zogeheten donkere materie ongeveer één op vijf is. Het Standaardmodel beschrijft geen deeltjes die deze donkere materie kunnen verklaren, en derhalve verklaart het Standaardmodel slechts 20% van alle materie in ons universum.

Nieuwe Fysica

Teneinde de beschreven problemen van het Standaardmodel op te lossen, hebben theoretisch fysici nieuwe wiskundige modellen opgesteld die het Standaardmodel omvatten en uitbreiden. Deze zogeheten Nieuwe Fysicamodellen voorspellen nieuwe soorten deeltjes en interacties, waarbij de nieuwe deeltjes bijvoorbeeld kandidaat zouden kunnen zijn voor donkere materie. De experimenten bij de LHC vormen voor wetenschappers een unieke omgeving waar naar deze nieuwe deeltjes en interacties gezocht kan worden. Deze zoektochten worden grofweg op twee manieren uitgevoerd: direct en indirect. Bij de ATLAS- en de CMS-detector wordt direct naar de hypothetische deeltjes gezocht in de vervalproducten van de proton-protonbotsingen. Bij LHCb daarentegen wordt indirect naar Nieuwe Fysica gezocht door parameters te meten die worden beïnvloed als nieuwe deeltjes zouden bijdragen aan bepaalde processen. Als een significante afwijking wordt gemeten ten opzichte van de voorspelling zoals gedaan door het Standaardmodel, zou dat een aanwijzing zijn voor Nieuwe Fysica. Het onderwerp van mijn proefschrift is de meting van zo'n soort parameter die symbolisch wordt weergegeven door ϕ_s. Om uit te leggen wat deze parameter precies voorstelt, is nog een ander ingrediënt nodig: antimaterie.

Antimaterie

Het schematische plaatje van het Standaardmodel, zoals weergegeven in Figuur S.2, is eigenlijk incompleet. In 1928 voorspelde de natuurkundige Paul Dirac namelijk op wiskundige gronden dat er zoiets als antimaterie moest bestaan. Dit betekende dat elk deeltje in het Standaardmodel een antideeltje als partner zou hebben. In Figuur S.4 staan bijvoorbeeld de quarks aangeduid met hun bijbehorende antideeltjes of antiquarks. Met de ontdekking van het positron in 1932 kreeg Dirac zijn gelijk. Een positron is het antideeltje van het welbekende negatief geladen elektron, en draagt daarom een positieve lading. De foto in Figuur S.1 laat het eerste positron zien dat ooit is waargenomen. De identiteit van het deeltje werd afgeleid uit de richting van de kromming van de baan in een magnetisch veld, aangezien die tegengesteld was aan de richting die werd verwacht voor een elektron, zoals aangegeven in de foto. Als een materiedeeltje en een antimateriedeeltje elkaar tegenkomen, zullen ze elkaar in een flits 'vernietigen' of annihileren. Dat doen ze letterlijk, omdat bij dit proces een foton (een lichtdeeltje) wordt uitgezonden. In het laatste deel van deze introductie op mijn onderzoek, zal ik uitleggen wat B-mesonen precies zijn, wat CP-schending betekent en hoe dit gerelateerd is aan de parameter ϕ_s.

B-mesonen, CP-schending en ϕ_s

Mesonen zijn quasi-stabiele deeltjes die bestaan uit twee quarks. B-mesonen zijn mesonen waarvan één quark een b-quark of een $\overline{b}$-quark (zo wordt een anti-b aangegeven) is. Deze b-quarks hebben als bijnaam 'schoonheidsquarks', naar de 'b' van *beauty*. Evenzo worden B-mesonen ook wel 'schoonheidsmesonen' genoemd. En daarmee zijn we aangekomen bij de titel van mijn proefschrift, omdat ik het verval van een schoonheidsmeson heb bestudeerd. De precieze inhoud van een B_s^0-meson is $(\overline{b}s)$ en de vervalproducten in vervallen van het type $B_s^0 \to J/\psi\,\phi$ zijn het J/ψ meson $(c\overline{c})$ en het ϕ meson $(s\overline{s})$.

Het laatste ingrediënt dat nodig is om uit te leggen wat de parameter ϕ_s nou precies betekent, is een eigenschap van B-mesonen die menging wordt genoemd: B-mesonen oscilleren heen en terug naar hun eigen antideeltje, een proces dat razendsnel verloopt, ongeveer 18 biljoen keer per seconde. Bij een botsing tussen twee protonen in LHCb, worden in principe evenveel B_s^0-mesonen als $\overline{B}_s^0$-mesonen geproduceerd. Als gevolg van menging zal het verval naar de vervalproducten J/ψ en ϕ plaatsvinden op een moment waarop het zogenoemde moederdeeltje ofwel een B_s^0-meson, of een $\overline{B}_s^0$-meson, of zelfs een kwantummechanische superpositie van de twee is.

Afhankelijk van de vervaltijd van het B-meson kan er een verschil zijn in de vervalsnelheid tussen vervallen waarbij het oorspronkelijk geproduceerde deeltje een B_s^0-meson en een $\overline{B}_s^0$-meson was. Dit effect heet tijdsafhankelijke CP-schending[1] en wordt geïllustreerd in Figuur S.5. De parameter ϕ_s is een maat voor de hoeveelheid tijdsafhankelijke CP-schending in vervallen van het type $B_s^0 \to J/\psi\,\phi$. In het Standaardmodel is de voorspelling dat de waarde van ϕ_s zeer klein is, terwijl sommige Nieuwe Fysicamodellen een aanzienlijk hogere waarde voorspellen. Elke significante afwijking van de voorspelling van het Standaardmodel in de gemeten waarde van ϕ_s kan daarom een aanwijzing zijn voor Nieuwe Fysica. In de

[1] De 'C' en de 'P' in CP-schending staan respectievelijk voor lading (*charge*) en pariteit (*parity*). Voor meer informatie, zie Hoofdstuk 1.

volgende alinea zal ik mijn meting van ϕ_s presenteren.

Het Verval van Schoonheid: Tijdsafhankelijke CP-Schending in Vervallen van het Type $B_s^0 \to J/\psi\,\phi$

Het Standaardmodel voorspelt dat $\phi_s = -0.036 \pm 0.002$ [17]. Elke significante afwijking van dit getal is een aanwijzing voor Nieuwe Fysica. De waarde die ik gemeten heb is $\phi_s = 0.00 \pm 0.10\,(\text{stat.}) \pm 0.02\,(\text{syst.})$, wat binnen de foutenmarge in overeenstemming is met de voorspelling van het Standaardmodel. Het resultaat van de analyse die ik heb uitgevoerd kan ook gepresenteerd worden en vergeleken met eerdere experimenten door contouren te tekenen in het $(\phi_s, \Delta\Gamma_s)$-vlak, waar $\Delta\Gamma_s$ het verschil in levensduur is tussen twee typen B_s^0-mesonen. Dit staat aangegeven in Figuur S.6. De breedte van de contouren zegt iets over de precisie van de meting en dit figuur laat daarom zien dat de meting in dit proefschrift op dit moment de meest precieze is.

Ondanks dat de gemeten waarde van ϕ_s op dit moment in overeenstemming is met het Standaardmodel, is het belangrijk om deze meting te verfijnen. Dat kan door meer data toe te voegen en meerdere vervalkanalen te bestuderen die gevoelig zijn voor deze parameter. Op deze manier wordt de onzekerheid van de meting verkleind en kunnen mogelijke afwijkingen van het Standaardmodel geobserveerd worden. Ik zal nu het tweede deel van mijn onderzoek bespreken, waarin ik me heb bezig gehouden met de stralingshardheid van de LHCb Outer Tracker.

Veroudering: Stralingshardheid van de LHCb Outer Tracker

De Outer Tracker (OT) is één van de subdetectoren van het LHCb-experiment en wordt gebruikt om de sporen van geladen deeltjes door de detector te reconstrueren die ontstaan bij de proton-protonbotsingen. Om passerende deeltjes te detecteren, gebruikt de OT rietjes gevuld met een ionisatiegas die als cathode dienen met een centrale anodedraad. De OT bestaat uit drie detectiestations, waarbij elk station weer uit vier detectielagen bestaat. Verder heeft de OT een modulair ontwerp, wat betekent dat de OT is opgebouwd uit 432 modules met 128 rietjes, ofwel zo'n 55000 rietjes in totaal. Een module wordt gebouwd door de rietjes aan de modulepanelen te lijmen.

Na de constructie en voor het installeren van de modules in het LHCb-experiment bleek uit laboratoriumproeven [30] dat de prestatie van bepaalde modules achteruit ging als gevolg van uithardingsgassen afkomstig van de lijm die gebruikt werd bij de moduleconstructie. In de context van deeltjesdetectortechnologie wordt de vermindering van detectorprestaties, bijvoorbeeld door uithardingsgassen, ook wel veroudering genoemd.

Na installatie in het LHCb-experiment zijn de modules onderworpen aan verscheidene behandelingen om veroudering te verminderen of tegen te gaan [41, 30, 42]. Mijn proefschrift vat de resultaten samen van testen die zijn uitgevoerd om de prestaties van de OT-modules na installatie in het LHCb-experiment te controloren. Deze testen werden uitgevoerd door modules opzettelijk te bestralen en te scannen met een opstelling die aan de voorkant van de

modules kan worden geplaatst. Voordat er een zuurstofcomponent aan het ionisatiegas was toegevoegd lieten enkele modules ernstige stralingsschade zien. Dit effect werd zelfs geobserveerd na relatief kleine ontvangen doses, hoewel er ook sterke variaties tussen verschillende modules voorkwamen. Na de toevoeging van O_2 aan het ionisatiegas was er slechts kleine of helemaal geen stralingsschade.

Om het gedrag van OT-modules te blijven controloren na het starten van de LHC in 2009, zijn twee methoden verzonnen. De eerste methode gebruikt dezelfde scanopstelling die hierboven is beschreven om regelmatig referentiescans te maken van een aantal modules. Deze scans worden handmatig uitgevoerd bij het LHCb-experiment en kunnen daarom alleen gedaan worden tijdens technisch onderhoud aan de LHC als er geen botsingen plaatsvinden. De tweede methode gebruikt de sporen van geladen deeltjes die geproduceerd worden bij de LHC-botsingen door de treffingsefficiëntie te bestuderen als een functie van de versterkingsdrempel van de electronica van de OT. Deze zogeheten drempelscans worden uitgevoerd als de LHC operationeel is en botsingen maakt in de LHCb-detector.

Ik heb beide methodes om de prestaties van OT-modules te controleren toegepast in mijn onderzoek. In mijn proefschrift concludeer ik dat geen van beide methodes significante stralingsschade aan de OT hebben kunnen aantonen. Beide methodes zullen echter regelmatig worden herhaald om de stralingshardheid van de OT te controleren.

Acknowledgements

Although the only name that is written on the cover of this thesis is mine, I could not have finished writing this book without the help, support and encouragement of a number of people that I would like to address here. This final section will be partly in Dutch and partly in English.

Allereerst wil ik mijn twee promotoren bedanken, Marcel Merk en Gerhard Raven. Marcel, het is ongelooflijk hoe efficiënt jij werkt. Ik zie continu PhD-studenten bij je binnenlopen om hoofdstukken in te leveren die jij voor ze moet lezen. Op de één of andere manier weet jij dat razendsnel voor elkaar te krijgen en ook nog eens altijd goede slimme vragen op het juiste moment te stellen. Gerhard, ik zal maar eerlijk zijn: onze manier van werken verschilt nogal. Waar ik voor een oplossing ga die simpelweg werkt, zal jij altijd naar een elegantere of meer algemene oplossing zoeken. Dat leverde me vooral problemen op bij het coderen, maar je filosofie heeft me veel geleerd, en zonder jouw hulp zou het niet gelukt zijn.

De volgende op de lijst is Niels Tuning, mijn copromotor. Niels is echt een rasoptimist. Ik denk dat ik in vier jaar tijd vooral geleerd heb om in te schatten of een door jou gegeven tijdsplanning echt realistisch is, of vooral om de moed erin te houden. Het maakte eigenlijk niet uit want dat laatste lukte altijd. Bedankt voor alle steun en aanmoediging en vooral tijdens het schroeven en het werk in de pit heb ik ontzettend veel van je kennis en manier van werken geleerd.

De analyse van $B_s^0 \to J/\psi\,\phi$ -vervallen is veelomvattend en zou ik daarom nooit alleen hebben kunnen uitvoeren. Daarom wil ik hier Jeroen, Roel en Tristan bedanken en ook Rob Knegjens voor zijn bijdrage aan het theoretische deel van het $B_s^0 \to J/\psi\,\phi$ -formalisme.

I started working for Nikhef in 2007 as a master's student and I have always considered myself lucky to be surrounded by so many nice and smart people. A big thanks to all of you and also to the supporting personnel.

I would also like to thank my paranimfs, Robin and Serena and of course my 'guest of honor', Chiara, for you are more than just colleagues.

Over vrienden gesproken: bedankt dat jullie er waren in mijn leven naast het proefschrift.

In vele opzichten de belangrijksten zijn uiteraard mijn ouders en mijn zussen. Dank jullie wel voor jullie liefde en steun.

En dan natuurlijk mijn lieve Isolde: bedankt dat je er was al die jaren. Ik bewonder je om je scherpe blik op de wereld en hoop daar nog veel van te kunnen leren. Tevens wil ik je bedanken voor alle proeflezingen en correcties.

Daan van Eijk, augustus 2012